N° d'ordre NNT : 2026ECDL0015

THESE de DOCTORAT DE L'ECOLE CENTRALE DE LYON
Membre de l'Université de Lyon

Ecole Doctorale N°160
Ecole Doctorale Electronique Electrotechnique et Automatique (EEA)
Spécialité de doctorat : **Ingénierie pour le vivant**

Soutenue publiquement le 09/06/2026, par :

Fryni Skorda

Modification of zirconia dental implants to promote soft tissue adhesion and limit bacteria colonisation

Devant le jury composé de :

Falentin-Daudré, Céline Professeure, Université Sorbonne Paris Nord, Institut Galilée	**Rapportrice**
Boulmedais, Fouzia Directrice de Recherche CNRS, Institut Charles Sadron	**Rapportrice**
Rimondini, Lia Professeure de Technologie Médicale Appliquée et de Méthodologie, Università del Piemonte Orientale, Directrice du département des Sciences de la Santé (DiSS),	**Examinatrice**
Ploux, Lydie Directrice de Recherche CNRS, Université de Strasbourg, Biomaterials and Bioengineering Institute (CRBS)	**Examinatrice**
Chevalier, Jérôme Professeur, INSA de Lyon, MATEIS	**Co-Directeur**
Chevolot, Yann Directeur de Recherche CNRS, Institut des Nanotechnologies de Lyon (INL)	**Directeur**
Gremillard, Laurent Directeur de Recherche CNRS, INSA de Lyon, MATEIS	**Invité**
Laurenceau, Emmanuelle Maîtresse de conférences, École Centrale de Lyon, Institut des Nanotechnologies de Lyon (INL)	**Invitée**

Acknowledgements

I would like to express my sincere gratitude to the members of my thesis committee and jury for accepting to evaluate this work, and for the time and attention they will dedicate to the careful reading of this manuscript. I am particularly grateful for their expertise and for the insightful comments and discussions that will undoubtedly contribute to enriching this work.

My sincere thanks also go to Pr. Bruno Masenelli, Director of the Institut de Nanotechnologies de Lyon and Pr. Ségolène Callard, for their support and for fostering a dynamic and stimulating research environment. I am also grateful to the DSE team at the Institut de Nanotechnologies de Lyon and to all colleagues who contributed, directly or indirectly, to this project. The collaborative spirit of the laboratory created an environment in which scientific curiosity could truly thrive. In particular, I am especially grateful to Isabel and Thomas for their technical assistance, their patience, and the many discussions that made the long hours in the lab feel manageable.

I would also like to acknowledge the collaborators within the NOMAD project. This European collaboration not only enriched the scientific scope of this work but also gave me the opportunity to travel, exchange ideas, and witness the dedication of remarkable teams across Europe. These experiences broadened my perspective both scientifically and personally. This research wouldn't have been possible without funding and for that, I am thankful for the funding received from the NOMAD project

I would like to express my deepest gratitude to my supervisor, Dr. Yann Chevolot, for his constant guidance throughout this project. His scientific rigor, clarity of thought, and attention to detail have been inspiring, and played a fundamental role in shaping both the quality of this work and my growth as a researcher. I am especially grateful for his availability, patience, and encouragement, which helped me navigate challenges with confidence and curiosity.

I am equally thankful to my co-supervisor, Pr. Jérôme Chevalier, for his insightful advice, constructive feedback, and continuous support throughout this research. I am especially grateful for the trust he placed in me from the very beginning, which allowed me to approach this work with confidence and independence. His constant encouragement and availability were particularly valuable in overcoming challenges and maintaining perspective. His expertise, critical insight, and ability to position this research within a broader scientific context have greatly strengthened both its direction and its impact. His guidance has played a key role in shaping my scientific reasoning and development.

I would also like to thank Dr. Emmanuelle Laurenceau and Dr. Laurent Gremillard for their contribution as part of the team that made this project possible.

To my friends at INL, thank you for the laughter, the coffee breaks, the shared frustrations, and the countless small moments that made this journey lighter. Over the years, I had the chance to meet incredible people who brought warmth, humor, and perspective into everyday lab life.

Some of you have moved on, but the memories we created and the support we shared remain an important part of this experience.

During this time, I formed friendships that grew far beyond companionship in the lab. They became a second family, and I carry them with me well beyond this thesis. You know who you are. I am lucky enough to have met you.

To my family, I owe more than words can express. Thank you for your unconditional love, your patience, and your unwavering belief in me, especially during moments when I doubted myself. Your support has been the quiet strength behind every achievement.

Finally, to my friends back home, thank you for your constancy, your encouragement, and for reminding me who I am beyond academia. No matter the distance, you have always been present.

This thesis is as much yours as it is mine.

Contributions

Time-of-flight secondary ion mass spectrometry (ToF-SIMS) measurements and data analysis were carried out at the University of Siegen, and the contributions of Prof. Dr.-Ing. Manuela S. Killian, Dr. Swathi Naidu Vakamulla Raghu, and Setareh Orangpour are gratefully acknowledged.

X-ray photoelectron spectroscopy (XPS) measurements and analysis were performed by Dr. Vincent Humblot, and this subset of the XPS measurements and analyses was conducted at Franche-Comté Électronique Mécanique Thermique et Optique (FEMTO-ST). Additional XPS measurements and analyses were carried out at Laboratoire de Tribologie et Dynamique des Systèmes (LTDS), and the contribution of Dr. Jules Galipaud is gratefully acknowledged.

Cytotoxicity was evaluated using a direct-contact cell viability assay conducted within the I2B team of MATEIS, and the contribution of Sandra Balvay is gratefully acknowledged.

Another set of cytotoxicity and wound healing assays using a direct-contact cell viability assay was conducted at the University Medical Center Groningen, and the contributions of Prof. Henny C. van der Mei and Dr. Lu Yuan, who also managed the data, are gratefully acknowledged.

I further gratefully acknowledge the NOMAD project partners and all collaborators who contributed to this work through experimental assistance, scientific discussions, or support at any stage of the project.

Finally, I gratefully acknowledge the contribution of Anthogyr to the project, for providing the samples, and performing the mechanical stressors tests, as well as the sterilization with EtO.

All of the collaborators, that contributed through experimental work and/or scientific discussions made this work possible.

Contents

Acknowledgements ..... **iii**

Contributions ..... **v**

Contents ..... **vii**

List of Figures ..... **xi**

List of Tables ..... **xix**

List of Acronyms ..... **xxi**

Introduction ..... **xxiii**

I. State of the Art **1**

I.1. Abstract 1

I.2. General Introduction 1

I.3. Zirconia (ZrO_2) 4

I.3.1. Iono-Covalent Character 4

I.3.2. Discussion 7

I.4. Cross-Linkers 7

I.4.1. Organosilanes 7

I.4.2. Other Cross-Linkers 13

I.4.3. Discussion 14

I.5. Covalent Bonding for Immobilization of Biomolecules 15

I.5.1. Amine-based reactions 15

I.5.2. Thiol-based reactions 18

I.5.3. Other strategies 21

I.5.4. Discussion 22

I.6. Bioactive molecules for cell-matrix interactions 23

I.6.1. Extracellular Matrix (ECM)–Derived Peptides 24

I.6.2. Other Bioactive Molecules 26

I.7. Conclusion 27

II. Surface Pre-treatment **29**

II.1. Abstract 29

II.2. General Introduction 29

II.3. Materials & Methods 30
II.3.1. Materials and Reagents 30
II.3.2. Samples Preparation 30
II.3.3. Characterization Techniques 32
II.4. As-Received Samples Characterization 36
II.4.1. Crystallinity & Phase Content 36
II.4.2. Surface State & Chemical Composition 37
II.4.3. Conclusion 41
II.5. Surface Modifications for Contamination Removal 41
II.5.1. Hydrofluoric Acid (HF) Etching 41
II.5.2. Mechanical Polishing 45
II.6. Organic Contamination Removal and Surface Activation 49
II.7. Conclusion 51
III. Silanization of Yttria Doped Zirconia 53
III.1. Abstract 53
III.2. Introduction 53
III.3. Materials and Methods 56
III.3.1. Materials and Reagents 56
III.3.2. Surface Preparation 56
III.3.3. Experimental Design 57
III.3.4. Optimized Reaction Protocol 58
III.3.5. Characterization Methods 58
III.3.6. Biological Assays Protocols 62
III.4. Results & Discussion 62
III.4.1. Optimization of Silanization Reaction Parameters 63
III.4.2. Application of the Silanization Protocol to PFPTES 72
III.4.3. Characterization of PFPTES-grafted layer 73
III.5. Biological Evaluation 80
III.6. Conclusions 82
IV. Biomolecule Attachment 85
IV.1. Abstract 85
IV.2. Introduction 85
IV.3. Materials and Methods 87
IV.3.1. Materials and Reagents 87

IV.3.2. Surface Preparation ... 87
IV.3.3. Mechanical Stressors (Brushing) Test ... 90
IV.3.4. Characterization Methods ... 92
IV.3.5. Biological Assays Protocols ... 94
IV.4. Results & Discussion ... 96
IV.4.1. Optimization of Peptide Conjugation Parameters ... 96
IV.4.2. Characterization of the RGDC grafted layer ... 106
IV.4.3. Robustness to Sterilization ... 116
IV.4.4. Robustness to Mechanical Stressors ... 119
IV.5. Biological Activity ... 121
IV.5.1. Cytotoxicity Assays ... 122
IV.5.2. Proliferation and Wound Healing Assays ... 126
IV.6. Conclusion ... 128
V. Conclusions & Perspectives ... 129
V.1. Conclusions ... 129
V.1.1. Surface Pre-treatment ... 129
V.1.2. Silanization of Yttria stabilized zirconia ... 130
V.1.3. Biomolecule Attachment ... 130
V.2. Perspectives ... 131
A. Synthèse en français ... 133
A.1 Introduction ... 133
A.2 État de l'art ... 134
A.2.1 La zircone dans le contexte implantaire ... 134
A.2.2 Structure cristalline et propriétés physicochimiques de la zircone ... 134
A.2.3 Stratégies générales de biofonctionnalisation de la zircone ... 135
A.2.4 Chimies de couplage covalent ... 135
A.2.5 Molécules bioactives pour l'ingénierie de surface ... 136
A.2.6 Limites et enjeux actuels ... 136
A.3 Prétraitement de surface de la zircone ... 137
A.3.1 État initial des échantillons commerciaux ... 137
A.3.2 Stratégies d'élimination des contaminants inorganiques ... 137
A.3.3 Elimination de la contamination organique et activation de surface ... 138
A.3.4 Choix de l'état de surface pour la fonctionnalisation ... 138
A.4 Silanisation de la zircone stabilisée à l'yttrium ... 139

A.4.1 Enjeux de la silanisation sur zircone....139
A.4.2 Optimisation du greffage de l'APTES....139
A.4.3 Confirmation spectroscopique du greffage de la couche d'APTES....140
A.4.4 Transposition au silane activé PFPTES....140
A.4.5 Caractérisation multi-technique de la couche PFPTES....141
A.4.6 Cytocompatibilité des couches intermédiaires et bioactives....141
A.5 Greffage covalent du peptide RGDC sur zircone fonctionnalisée 142
A.5.1 Stratégie chimique et principe du greffage....142
A.5.2 Optimisation des paramètres de greffage....142
A.5.3 Caractérisation physicochimique du greffage du peptides RGDC....143
A.5.4 Activité biologique des surfaces biofonctionnalisées....145
A.6 Conclusion.... 146
VI. References.... 149

List of Figures

Figure I-1. Overall strategy of the biofunctionalization of zirconia..... 6

Figure I-2. Illustration of the silanization reaction pathway employing mono- and multifunctional silanes..... 9

Figure I-3. Schematic representation of EDC/NHS coupling chemistry, showing carbodiimide-mediated activation of carboxyl groups and subsequent amide bond formation with primary amines. R_1 and R_2 denote the reacting functional groups..... 17

Figure I-4. Schematic representation of glutaraldehyde-mediated coupling between R_1 and R_2 functional groups..... 18

Figure I-5. Schematic overview of maleimide-based surface functionalization strategies: (a) direct reaction of N-phenyl maleimide with amine-terminated surfaces, potentially via a Michael-type addition; (b) thiol–maleimide coupling involving electron-deficient alkenes ('enes') enabling mild, one-pot crosslinking of thiol-containing molecules; (c) introduction of surface-bound maleimide groups using heterobifunctional reagents such as N-succinimidyl-3-maleimidopropionate (SMP) reacting with amine-functionalized surfaces..... 20

Figure II-1. Schematic representation of the different zirconia surface states investigated and their corresponding nomenclature..... 31

Figure II-2. Schematic representation of the water contact angle (WCA) measurement principle, illustrating the droplet–surface interaction used to assess surface wettability..... 32

Figure II-3. Principle of X-ray Photoelectron Spectroscopy (XPS). Monochromatic X-rays excite core electrons, which are emitted from the sample surface. *Reproduced from Bagus et al.* [189] 33

Figure II-4. X-Ray Diffraction scheme, reproduced by *Britannica Editors. "X-ray diffraction." Encyclopedia Britannica, August 2, 2024. https://www.britannica.com/science/X-ray-diffraction.*..... 34

Figure II-5. X-ray diffraction (XRD) pattern of the untreated zirconia disk (ZR-AR)..... 36

Figure II-6. SEM micrograph of the Zr-AR zirconia surface acquired at 1,000× magnification. Scale 50μm. 37

Figure II-7. SEM micrographs of the Zr-AR zirconia surface acquired in backscattered electron (BSE) mode at magnifications of 3,000× and 6,000×. Scale 20 and 10μm. 38

Figure II-8. EDS elemental analysis of surface contaminants on the Zr-AR zirconia sample, indicating their composition and distribution. Scale 5µm..... 39

Figure II-9. XPS survey spectrum of an Zr-AR zirconia sample, showing the elemental composition at the surface. The unexpected presence of Al and Si peaks is highlighted here..... 40

Figure II-10. SEM images of zirconia surfaces (ZR-HF) after HF etching: left, 2% HF for 5 min; right, 10% HF for 60 min, illustrating the effect of etching severity on surface morphology. Scale 50µm. 44

Figure II-11. High-magnification SEM image of the Zr-P zirconia surface in BSE mode, showing individual zirconia grains and embedded alumina particles within the zirconia matrix. Scale 5µm. 46

Figure II-12. EDS elemental analysis of a ZR-P disk, highlighting the presence of aluminum-containing particles. Scale 5µm..... 47

Figure II-13. X-ray photoelectron spectroscopy (XPS) survey spectrum of the ZR-P sample..... 48

Figure II-14. AFM measurements before (left) and after (right) polishing. (note the 20 times smaller z-scale (color scale) after polishing) 49

Figure II-15. XPS survey spectra, stacked, of ZR-AR samples treated with NaOH + UV/O_3 (green) and Piranha solution + UV/O_3 (red) 51

Figure III-1. Schematic representation of silanization of oxide surfaces. Reproduced from Pujari *et al.* (2014) [204] 54

Figure III-2. Molecular structures of 3-aminopropyltriethoxysilane (APTES) and 11-pentafluorophenylundecanoatetriethoxysilane (PFPTES)..... 55

Figure III-3. Molecular structures of N-Hydroxysuccinimide (NHS) and Pentafluorophenyl (PFP) esters. 55

Figure III-4. Schematic representation of the parameter screening strategy used to optimize organosilane grafting onto zirconia surfaces. For APTES, the influence of silane concentration (0.5, 1, 2 and 5 mM), immersion time (1, 2, 4 and 8 h), curing time (1, 2, 16, and 24 h), and solvent (anhydrous ethanol or dichloromethane, DCM) was systematically investigated. Based on this parametric study, optimal conditions were identified for PFPTES functionalization, corresponding to a 2 h immersion in a 1 mM solution prepared in anhydrous DCM, followed by 1 h curing. The scheme summarizes the stepwise selection of parameters leading to the final optimized protocol..... 58

Figure III-5. Schematic representation of the ADECA colorimetric assay. S1: Reaction between surface-bound amine groups and the activated dye; S2: Washing step to remove unreacted dye;

S3: Dye release in acidic conditions for colorimetric quantification. The dotted line indicates an electrostatic interaction rather than a covalent bond. This figure summarizes the full workflow of the assay, from dye coupling to final absorbance measurement. 59

Figure III-6. (a) Mean water contact angle and (b) amine density values measured at different immersion times of ZR-P for an APTES concentration of 0.5 mM (in EtOH), after annealing at 110°C. 64

Figure III-7. (a) Mean water contact angle and (b) amine density values measured at different immersion times of ZR-P for an APTES concentration of 1 mM (in EtOH), after annealing at 110°C. 65

Figure III-8. (a) Mean water contact angle and (b) amine density values measured at different immersion times of ZR-P for an APTES concentration of 2 mM (in EtOH), after annealing at 110°C. 65

Figure III-9. (a) Mean water contact angle and (b) amine density values measured at different immersion times of ZR-P for an APTES concentration of 5 mM (in EtOH), after annealing at 110°C 65

Figure III-10. Mean amine density values measured at different immersion times (2h and 8h) of ZR-P for different APTES concentrations (1mM and 5 mM) in EtOH, after annealing at 110°C. 67

Figure III-11. (a) Water contact angle (WCA) and (b) mean amine surface density (ADECA) measured as a function of curing time for zirconia samples functionalized with 1 mM APTES and 2 h immersion in dry ethanol. Curing was performed at 110°C. Amine density values represent the average of triplicate measurements, with error bars indicating standard deviation. 68

Figure III-12. XPS survey spectra of zirconia surfaces before and after APTES functionalization. (a) Bare zirconia substrate and (b) zirconia functionalized with APTES under the optimized conditions (1 mM, 2 h immersion, 110°C curing). The emergence of the C 1s peak at 285 eV and the Si 2p signal around 100 eV after treatment confirms the presence of the grafted organosilane layer..... 70

Figure III-13. High-resolution O 1s XPS spectra of zirconia surfaces before and after APTES functionalization. (a) Bare zirconia substrate and (b) zirconia functionalized with APTES under optimized conditions (1 mM, 2 h immersion, 110°C curing). Deconvolution of the O 1s region reveals contributions from lattice oxygen (Zr–O) and surface hydroxyl or siloxane-related species. After functionalization, changes in the relative intensity of the higher binding energy component indicate the formation of Si–O–Zr and/or Si–O–Si bonds associated with the grafted silane layer. 71

Figure III-14. High-resolution Si 2p XPS spectra of zirconia surfaces before and after APTES functionalization. (a) Bare zirconia substrate, showing no detectable Si 2p signal, and (b) zirconia functionalized with APTES under optimized conditions (1 mM, 2 h immersion, 110°C curing). The

appearance of a distinct Si 2p peak around 102–103 eV after treatment confirms the presence of silicon-containing species associated with the grafted silane layer. 71

Figure III-15. Survey spectra of polished zirconia disks for the control sample (red) and after PFPTES treatment (green). Following functionalization, characteristic fluorine signals appear at F 1s (~689 eV) together with the F KLL Auger feature (~832 eV). Silicon-related peaks are observed at Si 2s (~153 eV) and Si 2p (~102–103 eV), confirming the presence of the grafted silane layer. An increase in the C 1s signal (~285 eV) is also detected, consistent with the formation of an organic fluorinated overlayer. 74

Figure III-16. High-resolution XPS spectra of PFPTES-functionalized zirconia. a) F 1s region showing components centered at approximately 685 eV and 688 eV, corresponding to inorganic fluoride species and aromatic C–F bonds from the pentafluorophenyl group, respectively. (b) Si 2p region displaying a peak at ~102–103 eV, characteristic of silicon in siloxane environments (Si–O–Si and/or Si–O–Zr), confirming covalent attachment of the PFPTES layer to the zirconia surface. Experimental conditions of III.3.5..... 75

Figure III-17. (a) TOF-SIMS analysis of the $Si_2C_3^+$ fragment intensity for the control (blue) and PFPTES-functionalized (green) zirconia samples. The markedly higher signal observed for the functionalized surface reflects the presence of silane-derived silicon–carbon fragments, in contrast with the low background level of the control. (b) TOF-SIMS analysis showing the Si^+ and $C_2H_4^+$ fragment intensities for the control (blue) and PFPTES-functionalized (green) zirconia samples. Both ions display significantly higher signals on the functionalized surface compared to the control, consistent with the introduction of the organic silane layer. (c) TOF-SIMS analysis of the $Si_2H_3^+$ fragment intensity for the control (blue) and PFPTES-functionalized (green) zirconiasamples. The functionalized surface exhibits a notably higher signal than the control, reflecting the presence of silane-derived silicon-containing species. (d) TOF-SIMS analysis of the $C_2H_7F_2^+$ fragment intensity for the control (blue) and PFPTES-functionalized (green) zirconia samples. The increase in signal for the functionalized sample indicates the presence of fluorinated organic fragments associated with the PFPTES layer 77

Figure III-18. ATR-FTIR spectra of the control zirconia surface (purple), PFPTES-functionalized zirconia (red), and the reference PFPTES compound (black). The functionalized surface exhibits vibrational features that correspond to those of the PFPTES reference, confirming the presence of the grafted fluorinated silane layer. 79

Figure III-19. Cytotoxicity assessment of MG-63 osteoblast-like cells after 24 h of direct contact with ZrO_2 surfaces. Cell metabolic activity was quantified using the PrestoBlue assay (excitation 535 nm, emission 610 nm, gain 40). PFPTES-functionalized ZrO_2 surfaces were compared to non-functionalized ZrO_2 (ZrO_2 control) and tissue culture plastic, "témoin plastique" (positive control). Data are shown for three independent replicates. 80

Figure III-20. Relative cell metabolic activity of MG-63 osteoblast-like cells after 24 h of direct contact with ZrO_2 surfaces, expressed as a percentage of the tissue culture plastic control (témoin

plastique). Fluorescence values obtained from the PrestoBlue assay were normalized to the plastic control, set to 100%. PFPTES-functionalized ZrO_2 and non-functionalized ZrO_2 (control ZrO_2) exhibited metabolic activity levels comparable to the reference material. 81

Figure IV-1. Chemical structure of the RGDC peptide (Arg–Gly–Asp–Cys), highlighting the integrin-binding RGD motif and the N-terminal primary amine used for covalent immobilization onto the activated zirconia surface. 86

Figure IV-2. Experimental setup for the brushing test, in the facilities of our NOMAD partner, Anthogyr..... 91

Figure IV-3. Surface density versus input concentration of RGD peptides grafted on bone cartilage, *reproduced by* [236]..... 97

Figure IV-4. High-resolution XPS N 1s spectrum of ZR-REC samples functionalized with RGDC at 500 μg/mL (≈ 1.15 mM). The N 1s signal appears at very low intensity and close to the noise level, indicating minimal detectable nitrogen at the surface. This weak signal suggests a low peptide surface coverage and/or nitrogen concentration near the XPS detection limit under these conditions. 99

Figure IV-5. Stacked FTIR spectra of 3Y-TZP ZrO_2 powder (ZR-PW) after different surface treatments: control powder immersed in dichloromethane (DCM) and carbonate buffer (blue), PFPTES-functionalized powder after silanization in 1 mM PFPTES in anhydrous DCM (2 h) followed by 1h annealing (red), and PFPTES-functionalized powder after exposure to RGDC peptide (1 mg·mL^{-1}, 2.2 mM) in carbonate buffer for 2 h (green)..... 100

Figure IV-6. Stacked FTIR spectra of 3Y-TZP ZrO_2 powder after successive surface treatments. The control powder immersed in dichloromethane (DCM) is shown in blue, the PFPTES-functionalized powder obtained after silanization in 1 mM PFPTES in anhydrous DCM by annealing is shown in red, and the PFPTES-functionalized powder after exposure to RGDC peptide (1 mg·mL^{-1}, 2.2 mM) in DI H_2O (pH 8) for 2 h is shown in green. 102

Figure IV-7. Recorded FT-IR spectra of the bare silver colloidal particles (line 1), the unbound peptide (line 3) and the AgNP- peptide systems (line 2) for $RGD(GC)_2$, *reproduced from* [248]. 103

Figure IV-8. Comparison of the RGDC peptide vibrational features obtained in this work with literature FTIR spectra of the free (unreacted) RGDC peptide (line 3 in red) and RGDC-functionalized silver nanoparticles (line 2 in blue), *reproduced from* [248]. The spectrum labeled "Control" corresponds to 3Y-TZP ZrO_2 powder subjected to the complete experimental protocol in the absence of PFPTES and RGDC. The spectrum labeled "RGDC" corresponds to PFPTES-functionalized ZrO_2 powder after immersion in an RGDC peptide solution (2.2 mM) prepared in pH 8 buffer for 2 h. This comparison highlights similarities and differences in vibrational features between free, grafted, and zirconia-supported RGDC systems. 104

Figure IV-9. Stacked FTIR spectra of 3Y-TZP ZrO_2 powder following successive surface treatments and RGDC grafting experiments performed at different pH values. The spectrum labeled Control corresponds to ZrO_2 powder immersed sequentially in dichloromethane (DCM) and buffer without silane or peptide. The PFPTES spectrum corresponds to powder functionalized with PFPTES (1 mM in anhydrous DCM, 2 h immersion) followed by annealing at 110 °C for 1 h. The PFPTES control spectrum corresponds to PFPTES-functionalized powder subsequently immersed in buffer in the absence of RGDC. The remaining spectra correspond to PFPTES-functionalized powders exposed to RGDC peptide solutions (2.2 mM) prepared in HEPES buffer, with the pH adjusted to 7.6, 8.6, or 9.6 using 0.1 mM NaOH. The spectra are presented to compare changes in vibrational features as a function of surface treatment and peptide grafting pH, particularly in the 1800–1100 cm^{-1} region where peptide-related modes are expected. 105

Figure IV-10. (a) High-resolution XPS F 1s spectra of PFPTES- and (b) RGDC-functionalized zirconia surfaces. The PFPTES-modified surface (a) exhibits a well-defined F 1s signal centered around ~688 eV, characteristic of the pentafluorophenyl group. After RGDC grafting (b), the F 1s signal markedly decreases to near-background level, consistent with nucleophilic substitution of the activated ester and loss of the fluorinated moiety. Peak fitting components and background are shown for the PFPTES surface, while only background-level signal is observed after peptide coupling. 108

Figure IV-11. Positive ToF-SIMS spectra of selected secondary ion fragments acquired for bare Zr-KU ZrO_2, PFPTES-functionalized ZR-KU ZrO_2, and PFPTES + RGDC Zr-KU surfaces: (a) ZrO^+ substrate-related fragment, (b) carbon- and silicon-containing fragments in the low mass range, (c) organosilane- and organic-related fragments in the higher mass range, and (d) nitrogen-containing fragments characteristic of the peptide-grafted surface. All spectra were acquired under identical experimental conditions and normalized to total secondary ion counts. 109

Figure IV-12. Positive-ion ToF-SIMS characterization of ZR-DOC surfaces before and after PFPTES functionalization and RGDC grafting: (a) attenuation of the substrate-related Zr^+ fragment (m/z ≈ 89.91) following PFPTES treatment; (b) fluorinated silane-related signal in the m/z ≈ 79 region; (c) enhancement of siloxane- and nitrogen-containing fragments in the m/z ≈ 114 region after PFPTES functionalization and RGDC grafting; and (d) appearance of the peptide-derived fragment $C_{21}H_{38}N^+$ (m/z ≈ 304.3) exclusively after RGDC immobilization, confirming successful peptide grafting. 113

Figure IV-13. Fluorescence microscopy images of ZrO_2 disks. *Left:* control sample consisting of ZR-DOC immersed in the FITC–RGDC solution to assess nonspecific adsorption. *Right:* silanized ZR-DOC functionalized with FITC-labeled RGDC peptide using the optimized grafting protocol. Both images are displayed using the same fluorescence intensity scale. 114

Figure IV-14. Fluorescence microscopy images of FITC-labeled RGDC-functionalized zirconia disks. The functionalized surface (right) exhibits a homogeneous green fluorescence signal across the disk area, indicating successful immobilization and spatial distribution of the peptide. In

contrast, the control sample (left), consisting of a zirconia disk immersed in the fluorescent peptide solution without prior silanization, shows only weak and localized fluorescence, consistent with limited nonspecific adsorption. 115

Figure IV-15. Positive (b), (d), (f), (g), (h) and negative (a), (c), (e) ToF-SIMS spectra acquired for bare Zr-DOC zirconia (control) and RGDC-functionalized surfaces (sterilized and non-sterilized), highlighting differences in surface chemical composition across selected mass regions. All spectra were acquired under identical experimental conditions and normalized to total secondary ion counts. 117

Figure IV-16. Fluorescence microscopy images of zirconia (ZR-DOC) disks before and after simulated tooth brushing. A bare zirconia disk (control_bare) is shown as a negative control, alongside a functionalized disk prior to brushing (control_before). Functionalized samples exposed to 100, 1,000, and 22,500 brushing cycles are also presented. The decrease in fluorescence intensity reflects the progressive loss or degradation of the RGDC-FITC bioactive layer under mechanical stress, with 22,500 cycles corresponding to approximately six months of daily tooth brushing. 120

Figure IV-17. Quantitative analysis of fluorescence intensity on RGDC-FITC functionalized ZR-DOC disks before and after simulated tooth brushing. Mean fluorescence intensities were extracted from three linear regions of interest (ROIs) of 3.739 μm, 3.963 μm, and 4.674 μm in length, defined across each sample. The values represent the average intensity along each line, while error bars correspond to the standard deviation of the three ROI measurements, reflecting local surface heterogeneity. The evolution of the fluorescent signal is shown as a function of the number of brushing cycles (100, 1,000, and 22,500 cycles), in comparison to the functionalized control prior to brushing. 121

Figure IV-18. Representative fluorescence microscopy images of fibroblasts cultured on bare ZrO_2 (ZR-DOC), PFPTES-modified ZR-DOC (ZR-DOC-PFPTES), and RGDC-functionalized silanized ZR-DOC (ZR-DOC-RGD) after 1 and 3 days of culture. Actin cytoskeleton was stained with phalloidin (F-actin, green) and cell nuclei with DAPI (blue). Scale bar: 50 μm 122

Figure IV-19. Cytocompatibility of ZrO_2 surfaces assessed using human gingival fibroblasts. Quantitative cell viability results obtained by XTT assay are shown, expressed as percentage relative to the tissue culture plastic positive control. Data are presented as mean ± standard deviation. 123

Figure IV-20. Quantitative cell viability results obtained by the XTT assay are shown, expressed as a percentage relative to the tissue culture plastic positive control. The effects of ethylene oxide (EtO) sterilization and surface pre-treatment by etching with 2% hydrofluoric acid (HF) for 5 min were also evaluated. Data are presented as mean ± standard deviation. 124

Figure IV-21. Representative fluorescence microscopy images of fibroblasts cultured on sterilized bare ZrO_2 (ZR-DOC), sterilized PFPTES-modified ZrO_2 (ZR-DOC-PFPTES), and sterilized RGDC-

functionalized ZrO2 (ZR-DOC-RGDC), after EtO sterilization, and with (ZR-DOC-HF) and without HF 2% acid treatment (ZR-DOC), after 1 day of culture. Actin cytoskeleton was stained with phalloidin (F-actin, green) and cell nuclei with DAPI (blue). Scale bar: 50 μm 124

Figure IV-22. Representative fluorescence microscopy images of fibroblasts cultured on sterilized bare ZrO_2 (ZR-DOC), sterilized PFPTES-modified ZrO_2 (ZR-DOC-PFPTES), and sterilized RGDC-functionalized ZrO2 (ZR-DOC-RGDC), after EtO sterilization, and with (ZR-DOC-HF) and without HF 2% acid treatment (ZR-DOC), after 3 days of culture. Actin cytoskeleton was stained with phalloidin (F-actin, green) and cell nuclei with DAPI (blue). Scale bar: 50 μm 125

Figure IV-23. Endothelial tube formation assay performed using extracts from differently modified ZR-DOC disks. Representative optical microscopy images of human umbilical vein endothelial cells cultured with material extracts show the formation of capillary-like networks. Tube formation was quantitatively analyzed using ImageJ software, with nodes (branching points) identified in red and meshes (enclosed network areas) highlighted in yellow. Quantitative analysis of network parameters is presented below for each condition. Scale bar: 100 μm. 127

Figure IV-24. Quantitative wound healing assay results showing the evolution of wound closure over time for the different surface conditions. 128

List of Tables

Table I-1. A summary of examples of physicochemical modifications of zirconia found in literature 3

Table I-2. Overview of reported silanization approaches, including reaction conditions, for the functionalization of zirconia surfaces..... 13

Table II-1. Overview of the different acid etching conditions tested, showing variations in etching time and acid concentration 31

Table II-2. Atomic percentages of the untreated zirconia surface (ZR-AR) determined by X-ray photoelectron spectroscopy (XPS) 40

Table II-3. XPS analysis: Atomic percentage of Al 2p as a function of HF etching parameters of ZR-HF samples..... 43

Table II-4. Summary of wettability measurements: Water contact angles (WCA in °) as a function of HF etching (Zr-HF sample) parameters..... 43

Table II-5. Mean surface roughness (Sa) and standard deviation (SD) of zirconia samples before and after HF etching under different concentrations and etching times, measured by optical interferometry (three measurements per sample). 45

Table II-6. The atomic percentages of an ZR-AR sample, analyzed by XPS..... 48

Table II-7. Summary of the cleaning methods evaluated and their corresponding water contact angle values, reflecting the surface energy of the samples after treatment. 50

Table III-1. Atomic percentages obtained from XPS survey spectra for bare zirconia (control) and zirconia functionalized with APTES under optimized conditions (1 mM, 2 h immersion, 110°C curing)..... 69

Table III-2. Water contact angle values measured on polished zirconia disks before and after surface functionalization with PFPTES 73

Table III-3. Atomic percentages obtained from XPS survey spectra for polished zirconia before and after PFPTES treatment using the optimized protocol. The appearance of Si 2p and F 1s signals, together with the increase in C 1s and attenuation of Zr 3d and Y 3d contributions, confirms successful grafting of the fluorinated silane layer. 76

Table IV-1. Definition, origin, geometry, and processing history of the ZrO_2-based samples used in this study. Sample identifiers are constructed to encode the material form (bulk, powder, or thin film), supplier or fabrication route, and any additional surface treatment, enabling clear and consistent referencing throughout the manuscript. 89

Table IV-2. Mean atomic percentages (n = 3) obtained by XPS for ZrO_2 samples functionalized with RGDC peptides at different solution concentrations in carbonate buffer following a 1 h grafting reaction. When indicated, n = 1 or n = 2 denotes that the corresponding element was detected in only one or two of the three analyzed samples..... 98

Table IV-3. Surface elemental composition (atomic percentage, At%) of ZR-KU zirconia disks determined by X-ray photoelectron spectroscopy (XPS) after successive surface treatments. Prior to functionalization, all ZR-KU disks were cleaned using a series of organic solvents to remove fabrication-related contaminants. PFPTES-functionalized and RGDC-grafted samples were prepared according to the protocols described in Sections 4.3.2.2 and 4.3.2.3. The control sample was subjected to the same solvent and buffer exposures, consisting of immersion in anhydrous dichloromethane (DCM) and HEPES buffer, but without PFPTES or RGDC..... 107

Table IV-4. Surface elemental composition (atomic percentage, At%) of ZR-DOC zirconia disks determined by X-ray photoelectron spectroscopy (XPS) after successive surface treatments. Prior to functionalization, all ZR-DOC disks were cleaned using a series of organic solvents to remove fabrication-related contaminants. PFPTES-functionalized and RGDC-grafted samples were prepared according to the protocols described in Sections 4.3.2.2 and 4.3.2.3. The control sample was subjected to the same solvent and buffer exposures, consisting of immersion in anhydrous dichloromethane (DCM) and HEPES buffer, but without PFPTES or RGDC..... 111

List of Acronyms

3Y-TZP	3mol% Yttria- Tetragonal Zirconia Polycrystal
ADECA	Amine Density Estimation Colorimetric Assay
AFM	Atomic Force Microscopy
APDMES	(3-AminoPropyl)DiMethylethoxySilane
APTES	(3-AminoPropyl)TriEthoxySilane
CBB	Coomassie Brilliant Blue
CuAAC	Copper-Catalyzed Azide–Alkyne Cycloaddition
DBCO	DiBenzoCycloOctyne
DCM	DiChloroMethane
EDC	1-Ethyl-3-(3-Dimethylaminopropyl)Carbodiimide
EDS	Energy Dispersive x-ray Spectrometry
FTIR	Fourier Transform Infrared Spectroscopy
HF	Hydrofluoric Acid
MDP	MethacryloyloxyDecyldihydrogen Phosphate
NHS	N-HydroxySuccinimide
PDA	PolyDopAmine
PEG	PolyEthylene Glycol
PFP	PentaFluoroPhenyl
PFPTES	PentaFluoroPhenylTriEthoxySilane
SAM	Self Assembled Monolayer
SEM	Scanning Electron Microscopy
SPAAC	Strain-Promoted Azide-Alkyne Cycloaddition
ToF-SIMS	Time-of-Flight Secondary Ion Mass Spectrometry
WCA	Water Contanct Angle
XPS	X-Ray Photoelectron Spectroscopy
XRD	X-Ray Diffraction

Introduction

Dental implants have revolutionized modern dentistry by providing a durable and functional solution for tooth replacement. Their long-term clinical success, however, depends not only on mechanical stability but also on effective biological integration with the surrounding tissues. Inadequate integration with either hard tissue (bone) or soft tissue (epithelium and connective tissue) can compromise implant performance and ultimately lead to premature failure. While osseointegration ensures anchorage of the implant within the bone, the peri-implant soft tissue plays a critical protective role by forming a biological seal against the quite aggressive oral environment. Failure of this seal facilitates bacterial infiltration and inflammation, increasing the risk of peri-implant diseases such as peri-implantitis, which remains one of the leading causes of implant failure.

In response to these challenges, surface modification has become a central strategy for improving implant performance. By tailoring surface properties, it is possible to influence protein adsorption, cell adhesion, and tissue organization at the implant–tissue interface. Historically, surface engineering efforts have focused primarily on modifying surface roughness and topography to enhance bone integration. However, it is now well established that surface chemistry plays a critical role in modulating biological responses. As a result, increasing attention has been directed toward chemical and bioactive surface modifications capable of actively guiding cellular behavior rather than relying solely on passive physical cues.

Titanium has long been considered the reference material for dental implants due to its mechanical reliability and favorable biological response. Nevertheless, zirconia has emerged as a promising alternative, particularly for aesthetic reasons and in response to concerns related to metal sensitivity. Zirconia exhibits high strength, corrosion resistance, and a tooth-like color. Clinical studies have demonstrated osseointegration levels comparable to those of titanium and, additionally, lower plaque adhesion. Despite these advantages, zirconia presents specific challenges from a surface chemistry perspective. Its chemical inertness and limited surface reactivity complicate the development of advanced and reproducible surface functionalization strategies, particularly when compared to titanium.

To date, most reported surface modifications of zirconia rely on physical or physicochemical treatments aimed at modifying surface roughness, wettability, or surface energy. While such approaches can influence cellular responses, they remain indirect and do not introduce specific biochemical signals at the implant surface. In contrast, biofunctionalization strategies seek to directly immobilize biologically active molecules onto implant surfaces in order to promote targeted interactions with surrounding tissues. Although biofunctionalization has been widely explored for metallic implants, its application to zirconia remains relatively limited, despite its strong potential to improve both hard and soft tissue integration.

Biofunctionalization approaches typically involve the immobilization of biomolecules involved in cell adhesion, proliferation, or differentiation, such as extracellular matrix (ECM) proteins, growth factors, or short bioactive peptide sequences. However, the successful implementation of peptide-based biofunctionalization requires stable and well-defined anchoring strategies. Simple physisorption generally leads to weakly bound and poorly reproducible coatings, making covalent immobilization approaches based on surface cross-linkers more suitable for long-term biomedical applications.

Considering the complexity of zirconia surfaces, the development of reliable chemical functionalization strategies is particularly critical. Surface modification protocols must ensure strong and stable anchoring of the organic layer while maintaining reproducibility and compatibility with practical constraints such as processing time, solvent choice, and scalability. In this context, silane-based chemistries represent a promising route for introducing reactive functional groups onto oxide surfaces, provided that their implementation on zirconia can be carefully controlled and characterized.

Within this framework, the objective of this thesis is to develop and characterize controlled chemical strategies for the biofunctionalization of zirconia surfaces intended for dental implant applications. More specifically, this work aims to:

- establish well-defined and reproducible zirconia surface states prior to functionalization,
- investigate and optimize silane-based surface modification protocols suitable for zirconia,
- control key parameters influencing the formation and reproducibility of the silane layer,
- enable the covalent immobilization of bioactive peptides onto functionalized zirconia surfaces,
- assess grafting efficiency using complementary surface-sensitive characterization techniques.
- evaluate the biological response to the modified zirconia surfaces in order to assess their potential to promote favorable cellular interactions,
- investigate the robustness and stability of the functionalized layers under clinically relevant stressors, with particular emphasis on conditions relevant to translation and scale-up

By addressing these objectives, this thesis seeks to contribute to the development of chemically tailored zirconia surfaces capable of supporting stable and biologically relevant implant–tissue interactions.

This manuscript is organized as follows: The first chapter presents a comprehensive state of the art, reviewing the current knowledge on zirconia surface modification, organosilane chemistry, and biofunctionalization strategies relevant to dental implant applications. Particular attention is given to the challenges associated with reproducibility, and biomolecule immobilization. The second chapter describes the preparation and characterization of zirconia surfaces prior to functionalization, with emphasis on surface state control and activation. The third chapter focuses on the development and optimization of silane-based surface modification strategies, including the influence of processing parameters on surface chemistry and

reproducibility. Subsequent chapters investigate the covalent grafting of a bioactive peptide onto functionalized zirconia surfaces and the evaluation of grafting efficiency using complementary analytical techniques. The final surfaces are evaluated for their biocompatibility and cell-adhesive properties, as well as their ability to withstand sterilization and mechanical stress, ensuring their relevance for practical applications. Finally, the concluding chapter discusses the relevance of these surface functionalization strategies for dental implant applications and outlines perspectives for future research.

I. State of the Art

I.1. Abstract

In this first chapter, the current state of the art in zirconia surface functionalization for biomedical applications is outlined. Zirconia is first introduced as a material, highlighting its iono-covalent character, mechanical robustness, chemical stability, and relevance in dental implantology. The overall strategy for the chemical modification of its surface is then presented. The role of molecular crosslinkers is examined next, with particular emphasis on organosilanes, which enable the formation of stable covalent Si–O–Zr bonds and create reactive platforms for subsequent modification. The main covalent bonding mechanisms used to attach functional molecules to zirconia surfaces are then described, including nucleophilic substitution, amide coupling and other chemo-selective reactions tailored for aqueous or physiological environments. Finally, the range of bioactive molecules that can be grafted onto modified zirconia is explored, such as adhesive peptides, antimicrobial sequences, and other biologically derived motifs designed to promote soft tissue sealing and prevent peri-implant complications. Together, these elements establish the conceptual framework for understanding how zirconia can be transformed into an active, biologically instructive surface.

I.2. General Introduction

Dental implants have revolutionized modern dentistry, offering a durable and functional solution for tooth replacement. Dental implant treatment is typically performed in several stages. First, the damaged tooth is extracted if necessary, and the implant site is prepared by drilling a cavity in the alveolar bone. The implant fixture is then surgically inserted into the bone and covered by the gingival tissue or fitted with a healing abutment, depending on the clinical protocol. During the following healing period, which generally lasts several weeks to a few months, osseointegration occurs, allowing the implant to become firmly anchored within the surrounding bone. Once sufficient healing has been achieved, an abutment is connected to the implant and extends through the soft tissue to support the prosthetic restoration. Finally, a custom-made crown, bridge, or denture is attached to the abutment, restoring both function and aesthetics.

However, long-term success depends not only on the mechanical stability of the implant but also on its biological integration with surrounding tissues. Yet, poor integration with either the

hard tissue (bone) or soft tissue (epithelium and connective tissue) can lead to complications. Hard tissue supports the implant through osseointegration, while soft tissue forms a seal that protects against bacterial invasion. The inadequate integration of these tissues can increase the risk of infections such as peri-implantitis, a major cause of implant failure. To address these challenges, surface modification of dental implants has emerged as a critical strategy to enhance their performance by enhancing interactions with both tissue types. By modifying surface chemistry, topography, and bioactivity, the goal is to promote osseointegration, improve soft tissue attachment, and increase the implant lifetime.

Aside from titanium, that remains the material of choice, zirconia has been studied and accepted as a credible alternative for dental implants due to its mechanical and aesthetic properties [1–5]. The Statement of the ESCI 2021 (European Society for Ceramic Implantology) supports this by concluding that the zirconia implant concept is appropriate for clinical application. This conclusion is based on several key findings: recently developed two-piece zirconia implants offer advantages over one-piece designs in terms of prosthetic flexibility and broader clinical indications, while also demonstrating sufficient resistance to clinical masticatory forces. However, the fracture resistance and mechanical stability of these implants can vary depending on manufacturing processes, material properties, implant geometries, and prosthetic connection designs. Importantly, both one- and two-piece zirconia implants show comparable levels of osseointegration and biological integrity. Despite limited current literature on surface modification of zirconia ceramics, with most studies focusing on physical or chemical methods (**Table I-1**) to adjust surface roughness, wettability for influencing cell behavior, some different approaches to enhance zirconia adhesion ability have been reported [6]. Nevertheless, its biofunctionalization remains scarcely investigated and involves grafting organic layer(s) on its surfaces to attach the bioactive molecules. Such an approach could make zirconia surfaces more attractive to cells with osteogenic or tissue regenerative potential.

Method Type	Method Name	Description / Effect on Zirconia Surface	References
Physical	Sandblasting (Air Abrasion)	Abrasion with alumina or silica particles creates micro-roughness to improve mechanical retention	7
Physical	Grinding / Polishing	Mechanical abrasion to smooth or roughen the surface depending on grit size; affects roughness and surface defects	8,9
Physical	Laser Treatment	Uses laser pulses to selectively ablate or pattern the surface, creating micro/nano structures	10,11
Physical	UV (ultraviolet) light treatment	Photocatalytic cleaning, increases hydrophilicity, enhances protein adsorption	12
Chemical	Acid Etching	Etch surface to create uniform micro-roughness and clean contamination after blasting	13

Chemical	Alkaline Treatment	Use of bases like NaOH to induce surface roughening and increase hydroxyl groups	14
Chemical / Physical	Heat Treatment (Thermal Etching)	Electrochemical oxidation or molten salt hot etching to increase retention or surface topography	15
Chemical	Chemical coatings (e.g., polydopamine, MDP primers or bioactive films)	Apply chemical layer to enhance cellular responses or bonding to resin cements	16

Table I-1. A summary of examples of physicochemical modifications of zirconia found in literature

To promote healing of peri-implant bone and gingiva, interactions between biomaterials and biomolecules involved in cell adhesion and growth play a crucial role. However, the direct grafting of biomolecules onto raw implant surfaces is challenging, as it generally depends on physisorption via weak interactions. Physisorption is expected to lead to low stability coatings [17]. To overcome this, several strategies have been proposed including the layer by layer approach [18], surface polymer grafting [19] or hetero-bifunctional cross-linkers. Hetero-bifunctionnal cross-linkers are often used to introduce reactive chemical groups onto the material surface. These cross-linkers contain one group that specifically binds to the substrate, and another that can later react with biomolecules for functionalization [20].

Over the years, a significant amount of research has focused on grafting organic layers onto materials like titanium and other metal oxides to improve their biological performance [21,22]. A particularly promising strategy involves incorporating extracellular matrix (ECM) proteins, growth factors or short peptide sequences onto implant surfaces. These molecules provide cells with recognizable sites, helping to guide and enhance cellular responses.

When it comes to modifying dental implants, and especially zirconia, it is essential to ensure that biomolecules such as peptides and proteins are securely anchored to the crosslinker layer. For this reason, multiple chemistries are used to confirm a chemically and mechanically stable and successful grafting.

Many research efforts are devoted in exploring which specific peptides are most effective for use in dentistry and how to successfully attach them to zirconia surfaces. Peptides used in dentistry are reported in a scoping review [23] where the objective was to examine current scientific literature pertaining to the classifications, utilizations, and applications of peptides in the field of dentistry at present. In an interesting paper by Morra [24], biochemical modifications of titanium with peptides and ECM proteins, various modifications are discussed with some being relevant to similar research on biomodification of zirconia.

I.3. Zirconia (ZrO_2)

Zirconia may exhibit three different crystalline phases: monoclinic (m), cubic (c), and tetragonal (t). Among these, tetragonal zirconia is the preferred phase for dental implants due to its superior mechanical properties, related to its ability to present phase transformation toughening [25]. Indeed, in the vicinity of a pre-existing defect, or a crack, high local stresses can trigger the transformation of tetragonal grains to the monoclinic symmetry and lead to a process zone which shield the applied stress intensity factor, with certain analogy to the plastic zone in metals [26]. However, the tetragonal phase is unstable at body temperature leading to the transition to monoclinic phase (t → m) and requires stabilization through the addition of yttria (Y_2O_3) or ceria (CeO_2) (Y-TZP, Ce-TZP). Adding approximately 2%-3% mol of yttria as a stabilizing agent, enables the sintering of fully tetragonal, fine-grained zirconia ceramic materials (3Y-TZP), that can transform under stress [27].

However, surface preparation can significantly alter the phase distribution [28–31]:

- Polishing and low-temperature aging (e.g., in humid environments) may induce t→m transformation at the surface, increasing roughness and potentially affecting its chemical properties (**II.2**) and consequently silane or peptide attachment.
- Sandblasting and acid etching can also promote t → m phase change, depending on their severity.
- Sintering conditions, especially at high temperatures, can lead to partial formation of the cubic phase (c-ZrO_2), which lacks transformation and leads to questions about low-temperature aging due to microstructural heterogeneities.

The performance of zirconia, both mechanical and biological, is intrinsically linked to its microstructure. Grain size, which is influenced by the sintering conditions (temperature, time, and atmosphere), plays a crucial role in determining surface roughness, mechanical stability, and phase stability. Typically, 3Y-TZP should display grain sizes ranging from 200 to 500 nm after sintering. Excessive grain growth (>1 μm) can destabilize the tetragonal phase, leading to spontaneous transformation into the monoclinic phase and resulting in undesirable aging effects or surface degradation, while too small grains would not be able to present transformation under stresses [32,33].

I.3.1. Iono-Covalent Character

3Y-TZP (3 mol% yttria-stabilized tetragonal zirconia polycrystal), which is mostly used in dental implants, exhibits a mixed ionic and covalent bonding character that directly contributes to its mechanical strength, chemical stability, and toughness. The primary bonds in zirconia are between zirconium (Zr^{4+}) and oxygen (O^{2-}), which show strong ionic character due to the significant electronegativity difference, yet also exhibit covalent traits due to orbital hybridization

between Zr 4d and O 2p orbitals. This results in an estimated bond character of roughly 60% ionic and 40% covalent [34]. When yttrium oxide (Y_2O_3) is added to stabilize the tetragonal phase at room temperature, Y^{3+} ions substitute for Zr^{4+} in the lattice, forming oxygen vacancies for charge compensation. These vacancies increase ionic mobility and influence the material's phase behavior (they help to stabilize the tetragonal phase) and sintering characteristics [26,35]. While Y–O bonds are somewhat less ionic than Zr–O, they still contribute to the overall mixed bonding character of the system [36]. The stabilization of the tetragonal phase, responsible for the material's transformation toughening, relies on both ionic interactions that define lattice dynamics and covalent contributions that impart structural rigidity [37].

At the surface, zirconium atoms act as Lewis acid sites, while oxygen atoms serve as Lewis base sites, with their surface densities typically ranging from 4 to 5 μmol/m². Because of these Lewis acid-base pairs, water molecules tend to adsorb and dissociate, leading to the formation of surface hydroxyl groups. Literature reports estimate the density of these hydroxyl groups at approximately 20 μmol/m² [38]. Their acidity likely depends on crystallinity, as observed for titania, suggesting that it may vary across tetragonal, cubic, and monoclinic zirconia. Several studies have reported such phase-dependent differences in surface acidity. For instance, Busca *et al.* [39] used infrared spectroscopy with pyridine adsorption and showed that tetragonal zirconia tends to exhibit stronger Lewis acidity than the monoclinic phase, likely due to a higher concentration of coordinatively unsaturated Zr^{4+} sites. Additionally, Jung and Bell [40] investigated the effects of zirconia phase on methanol synthesis over Cu/ZrO_2 catalysts, finding that the monoclinic phase exhibited higher activity than the tetragonal phase under identical conditions.

Nevertheless, zirconia surface hydroxyl groups behave as Brønsted bases, in contrast to those on silica that are Brønsted acids [41]. Surface hydroxyl groups are key reactive species on zirconia surfaces and vary significantly with crystal phase and thermal treatment. Early studies by Yamaguchi *et al.*, identified two distinct O–H stretching bands at 3780 cm^{-1} and 3680 cm^{-1}, corresponding to different types of hydroxyl groups on dehydrated ZrO_2 surfaces, formed upon evacuation at 500°C (773K) [42]. Trunschke *et al.* later showed that the nature of the ZrO_2 phase also influences the ν(OH) region: monoclinic ZrO_2 presents a band near 3650 cm^{-1}, while tetragonal ZrO_2 shows a higher-frequency band at 3730 cm^{-1}, reflecting different coordination environments of surface OH groups [43]. Bensitel and co-workers (2009) studied thermally treated ZrO_2 (723 K) and observed two OH bands at 3775 cm^{-1} and 3670 cm^{-1}, corresponding to terminal (type I) and bridged (type II) hydroxyls, respectively [44]. At even higher temperatures (~1170 K), the number of hydroxyls decreases, and the remaining bands become sharper and more isolated, as reported by Audry *et al.* in their FTIR study of hydroxylation under oxidative conditions[45]. Additionally, computational and spectroscopic work by Korhonen *et al.* revealed that hydroxyls on different monoclinic ZrO_2 surface (such as (111) and (101)) exhibit distinct vibrational frequencies, with single, bridged, and tribridged OH species contributing to complex FTIR signatures [46].

The reactivity of zirconia is strongly influenced by its surface sites, including Lewis acid/base sites and Brønsted hydroxyl groups, making its physicochemical properties complex and variable. For example, its isoelectric point has been reported to range from 2.7 to 12.07 depending on

synthesis and hydration state [47]. Additionally, zirconia has an exceptionally high affinity for fluoride and phosphate, though phosphate adsorption is pH-dependent and can be reversed at pH values above 8 [47].

Most of the studies focus on monoclinic zirconia in catalytic or chromatographic applications, where zirconia is typically in powder form with a high specific surface area, while Y-TZP implants are mostly in their tetragonal form. To the best of our knowledge, little to no research has been conducted on these reactive surface sites in dense tetragonal Y-TZP used for dental implants. In particular, the role of these reactive sites in cell-material interactions remains largely unexplored.

I.3.1.1. *Overall Strategy for the Biofunctionalization of Zirconia*

The functionalization of zirconia surfaces typically follows a multi-step strategy designed to ensure effective and stable attachment of biomolecules. It begins with a crucial surface pretreatment step, often involving cleaning and mild activation methods in order to generate surface hydroxyls. These hydroxyl groups serve as reactive sites for subsequent grafting of an organic intermediate layer with a crosslinker, commonly bearing functional groups. The crosslinker forms stable covalent bonds with the zirconia surface while providing a tailored chemical handle for further modification. In the final step, the desired biomolecule is covalently grafted onto the crosslinker via its complementary functional group, ensuring robust anchoring of bioactive compounds on the zirconia substrate **(Figure I-1**).

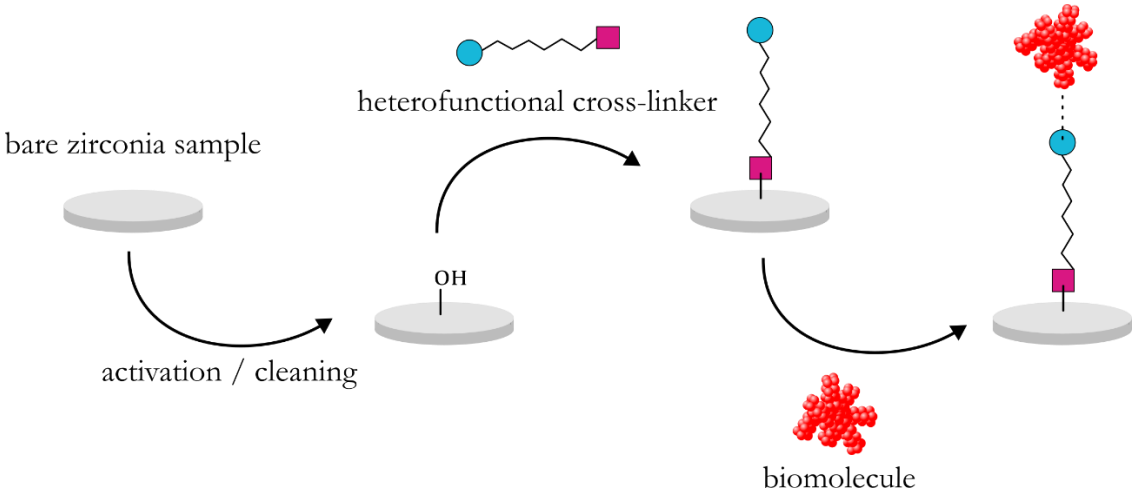

Figure I-1. Overall strategy of the biofunctionalization of zirconia

As mentioned, surface pretreatments of zirconia are essential for removing surface contamination and introducing hydroxyl groups, necessary for the subsequent attachment of a cross-linker [48]. The selection of a cleaning method is primarily based on its efficiency and its impact on surface morphology. However, the need to remove contaminants while preserving the properties of the 3-YTP zirconia surface limits the available cleaning methods. Surface cleaning

alone is often insufficient to ensure stable and functional modification of zirconia; effective pretreatment protocols must also promote surface activation, notably through hydroxylation or roughening. Depending on the intended surface chemistry, pretreatments can be mechanical (e.g., airborne-particle abrasion) [49,50], chemical (e.g., etching, oxidative solutions) [51], or physico-chemical (e.g., oxygen plasma, UV/O_3) [52,53]. Each method affects the surface energy, morphology, and reactivity differently, with varying implications for reproducibility and long-term stability of grafted layers.

I.3.2. Discussion

The role of the crystalline structure and the iono-covalent character of zirconia surfaces remains largely underexplored in the context of surface biofunctionalization. While these physicochemical properties have been extensively studied in other fields, their influence on surface reactivity and functionalization efficiency has not been thoroughly investigated. To the best of our knowledge, a systematic examination and optimization of zirconia's surface reactivity, specifically destined for biofunctional applications, is still lacking in the current literature. This may be due to the difficulties to titrate the reactive sites of bulk sintered zirconia as opposed to zirconia powder where infrared spectroscopy combined with chemical probes can be applied.

I.4. Cross-Linkers

To enhance both mechanical and biochemical stability of bioactive layers containing peptides or other biomolecules, diverse chemical functionalization strategies have been investigated. In the following chapter, the chemical reactions of these cross-linkers are first discussed as well as the key parameters influencing the reactions. Then, the specific case of zirconia is emphasized.

I.4.1. Organosilanes

Surface functionalization with organosilanes involves first a surface pretreatment (**II.2**), followed by silanization reaction in either a solvent or gas phase, then a curing step, and a final washing step to remove weakly bonded molecules

Organosilanes are composed of three essential components – the silyl head group ($-SiR_nX_{4-n}$), where:

→ R: is a hydrocarbon chain consisting of an aliphatic chain or polyethylene oxide/polyethylene glycol chain (spacer chain) eventually bearing an organic reactive group (tail group) typically located at the terminus.

→ a non-hydrolyzable organic group such as methyl or ethyl,

→ X: a hydrolyzable group such as chlorine (Cl) or alkoxy (e.g., methoxy $–OCH_3$ or ethoxy $–OC_2H_5$) and

→ n: 0, 1, 2 or 3 depending on the functionality

The reactivity and physicochemical properties of the obtained layers depend on these three components as well as the experimental conditions under which the silanization reaction is carried out. Silanization is a versatile reaction that has been employed on various oxide substrates or oxide thin films such as silica, titanium, or other metal oxides. However, despite its widespread use, only a limited number of studies have applied this strategy to zirconia surfaces. The vast majority of the literature focuses on silica-based systems, and many of the references often cited in the context of zirconia actually report data on silica or titania, not zirconia itself.

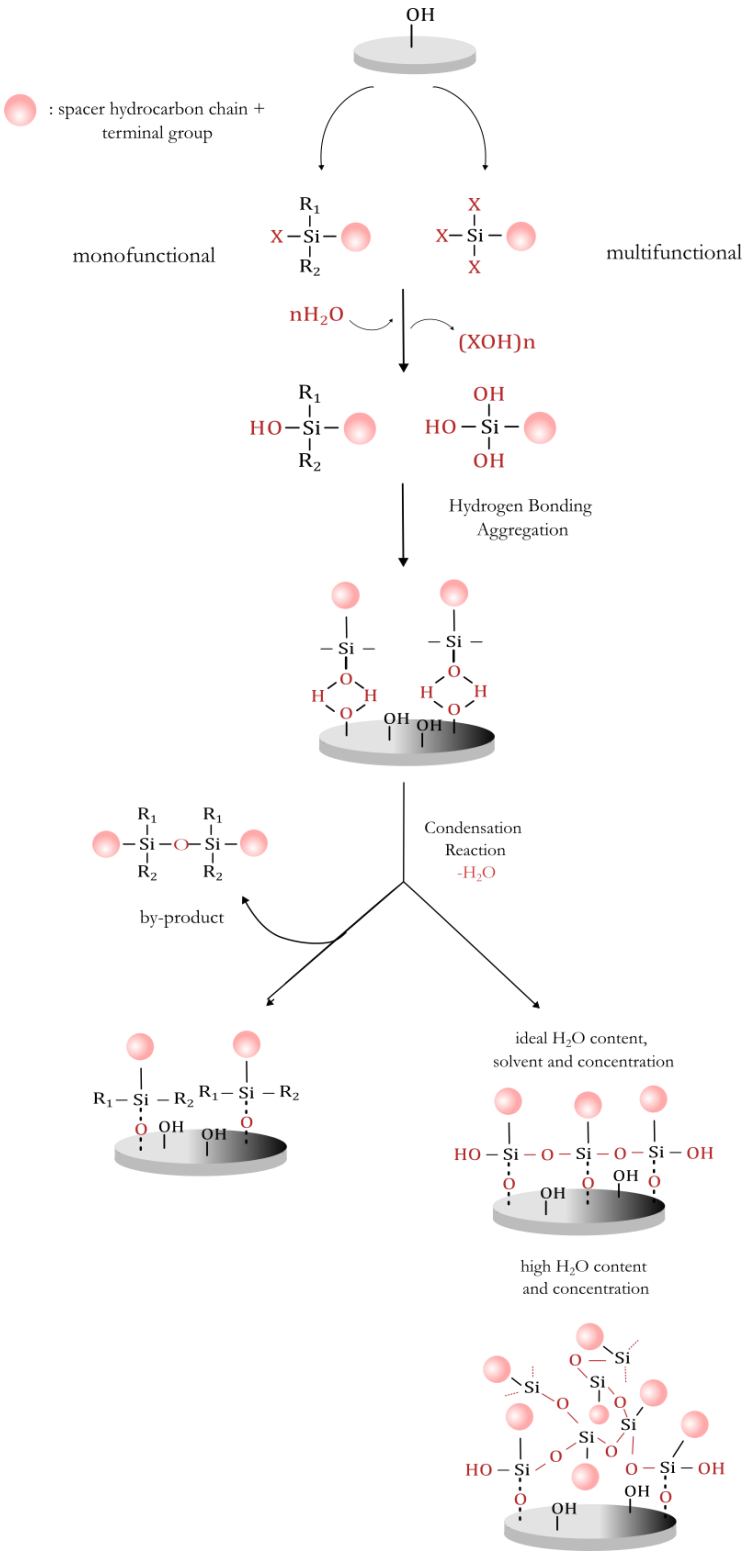

Figure I-2 Illustration of the silanization reaction pathway employing mono- and multifunctional silanes

The silyl head group undergoes a reaction with surface hydroxyl groups, establishing a siloxane bond between the organosilane molecule and the substrate. Subsequently, the organic

functionalities facilitate the immobilization of biological probes through either covalent or electrostatic interactions. (**Figure I-2**)

The classification of organosilanes is determined by the number of reactive sites present in the silyl groups (leading to distinguish between monofunctional and multifunctional), by the nature of these reactive site (chlorosilanes, alkoxysilanes, …) and the terminal organic group (amine, mercapto, carboxyl, …).

The spacer chain is typically an alkyl chain or a polyethylene glycol chain (PEG). This chain plays a key role in both the structure of the layer as well as its physicochemical properties. In the case of alkyl chains, increasing number of carbons increases lateral Van der Waals interactions leading to more ordered layers. Some authors have included urea function within the chain to promote lateral hydrogen bonding [54]. PEG chains have the advantage of reducing non-specific adsorption of proteins but are prone to oxidative degradation (in the presence of oxygen when heated) or enzymatic cleavages [55]. These chains, due to their flexibility and lack of strong lateral interactions, tend to form disordered or brush-like structures rather than crystalline monolayers. The conformation and organization of PEG layers depend largely on the grafting density and molecular weight. At low densities, PEG adopts a mushroom-like configuration, while at high grafting densities, it forms a more extended brush structure, which is key to its antifouling properties [55].

In Dugas *et al.* [56], the kinetics and the mechanisms of the silanization reaction on silicon surface have been reviewed. Two primary mechanisms are commonly outlined: (1) the direct reaction of silane with surface hydroxyl groups, and (2) a two-step process in which the silane undergoes hydrolysis to form silanol groups, which then react with the surface hydroxyls of the substrate leading to the formation of a siloxane bridge. For monofunctional silanes, the organosilyl headgroup can react with either surface silanols or another organosilane, leading to the formation of an inert dimer. The resulting dimer byproducts can be easily washed away from the surface, leaving only on the surface organosilanes grafted by a single siloxane bond. The advantage is that uncontrolled condensation reaction does not occur but the density of the layer is usually lower than the one obtained with multifunctional silanes. Conversely, multifunctional silane headgroups can undergo poly-condensation reaction between organosilanols in solution. The properties of the resulting silane layer vary depending on the reaction conditions such as silane type, duration, water content, temperature, solvent.

In two publications, published a decade apart, the same research group [57,58] reviewed the surface chemistry of silane monolayers and showed how progress in silane chemistry has enabled better-controlled self-assembled monolayers (SAMs), expanding their range of applications.

Brzoska *et al.* [59] studied the influence of temperature of silanization on the quality of monolayers in the scope of reproducibility. High-quality, densely packed, and homogeneous monolayers are only obtained when silanization is performed below a specific threshold temperature (Tc), which depends on the chain length of the trichlorosilane in question. Above Tc, the resulting layers are disordered and less reproducible. This temperature-dependent behavior

is linked to the molecular organization during grafting and mirrors phase transitions seen in Langmuir monolayers, emphasizing the importance of controlled low-temperature conditions for achieving reproducible silanization.

Howarter and Youngblood [60] studied various parameters in the silanization reaction with 3-aminopropyltriethoxy silane (APTES) and demonstrated that controlling reaction conditions is crucial for achieving desired APTES films on silica. Reaction time strongly influences film thickness, with longer times producing thicker films, while concentration and temperature primarily affect roughness and wettability. Low concentrations (1%) yield smooth, thin films (<3 nm) only under time-limited conditions (1h), with minimal temperature dependence. Optimal conditions for thick, smooth films with measurable receding contact angles include higher concentrations (10–33%), longer times (24–72h), and elevated temperatures (75°C). Curing conditions must be carefully optimized, as elevated temperatures can degrade sensitive terminal groups. For instance, in the case of PEG, which contains ether linkages (–CH_2–CH_2–O–), exposure to elevated temperatures in the presence of oxygen can lead to oxidation, producing peroxides and other degradation products. This can alter the chemical nature of the surface, potentially reducing hydrophilicity, biofunctionality, or binding capacity if PEG or similar chains are part of the grafted film [61].

Several studies suggest that gas-phase silanization results in less polycondensation of multifunctional silanes compared to liquid-phase methods. According to Fiorilli *et al.* [62], vapor-phase deposition on silicon reduces poly-condensation of the silane precursor due to the lower molecular density in the gas phase. Similarly, Duleba *et al.* [62] investigated the reproducibility and stability of silane layers in nanopipettes, comparing APTES and 3-aminopropyltrimethoxysilane (APTMS) silanization in ethanol and vapor-phase to identify improved protocols and highlight potential issues and reported that gas-phase silanization improves reproducibility and stability of silane layers compared to liquid-phase methods. These studies highlight the advantages of gas-phase silanization in achieving more controlled and uniform surface functionalization. However, gas phase silanization is not applicable is the silane molecule cannot be evaporated under heating or vacuum. Some other authors have developed silanization using spin coating as a deposition method with good reproducibility [64].

Some differences are to be expected in this work, as monoclinic zirconia is predominantly used as a chromatography stationary phase, whereas the tetragonal phase is employed in implant applications. As described in **I.3.1**, different reactivity is expected from the different phases of zirconia. Nevertheless, the silanization reaction occurs between the silanol groups of the silanes and the hydroxyl groups of zirconia leading to the formation of heterosiloxane bond Si-O-Zr. The stability of the resulting layers is primarily determined by the silane's functionality, with multifunctional silanes (e.g., trialkoxysilanes) forming more cross-linked and hydrolytically stable networks than monofunctional variants [65–67]. It may well be that this improve stability is due to polycondensation reaction leading to a polymer layer at the surface of zirconia. The stability to hydrolysis of the heterosiloxane bond Si-O-Zr seems to be less than Si-O-Si but better than Si-O-Ti and Si-O-Al [66]. Also, for yttriated zirconia, formation of Si-O-Y bound cannot be

excluded. In **Table I-2** are summarized parameters found in the literature for the silanization of zirconia. Mainly, silanization of zirconia was carried out using aminosilane APTES or Aminopropyldimethylethoxysilane (APDMES). The amino terminal groups of these silanes facilitate the formation of a covalent bond with Y-TZP and act as a catalyst of the silanization as described in the literature [68,69].

Silanization of zirconia has been widely studied in the field of chromatography [70–72] but fewer reports can be found in the literature concerning the silanization of zirconia for biomedical applications. Zirconia's high strength and biocompatibility make it ideal for dental crowns and bridges, but its inert surface resists bonding with resin cements [73]. Unlike silica-based ceramics, zirconia has fewer and less reactive surface hydroxyl groups, limiting direct silanization [65]. Silanization addresses this through γ-MPS silane coupling agents that bridge zirconia and resin when combined with silica-coating pretreatments like tribochemical blasting [74,75]. The process creates siloxane (Si-O-Si) bonds with embedded silica while the methacrylate end copolymerizes with resin cement [76]. For simplified bonding, 10-methacryloyloxydecyldihydrogen phosphate (MDP) primers chemically bond to zirconia's Zr-OH groups without silica coating [76,77]. These primers chemically interact directly with zirconia's surface hydroxyls (Zr-OH), forming stable bonds without the need for silica-coating, which simplifies clinical protocols.

Publication	**Silane**	**Pre-treatment**	**Solvent**	**Temperature**	**Concentration**	**Time**	**Washing Step**	**pH**	**Comments**
Hsu et. al (2014)	APTES	Hydrothermal treatment in DI water at 134 °C at 0.2mPa for 0, 1, 3 ,6 ,12h	acetone	• Immersion: 40°C • Curing: 40°C	5%	• Immersion: 48h • Curing: 8h	ultrasonically washed with • chloroform • acetone • methanol • DI water	-	-
Caravacas et. al (2016)	APDMES	• O_2 plasma • O_2 plasma + DI water 4h	Dry pentane	• Immersion: rt • Curing: 147°C	0.1% v/v	• Immersion: 1h • Curing: overnight	no	-	Under N_2
Liu et. al (2016)	APTES	-	ethanol	• Immersion: 40°C • Curing: 60°C	-	• Immersion: 2h • Curing: 24h	Washed with ethanol	5	Nanoparticles Dried under vacuum
Hong *et al.* (2021)[68]	γ-MPS, MTMS, MTPS, APTES	5M NaOH 60°C overnight	ethanol	• Immersion: 37°C • Curing: 65°C	2%	Immersion : 24h	ultrasonically rinsed with absolute ethanol and double-distilled water for 10 min each	-	

Zhou et. al (2022) [79]	APTES	5M NaOH 60°C 24h	methylbenzene	• Immersion: 80°C	5%	• Immersion: 24h	-	-	No curing, directly into SMP for peptide coupling
Palkowitz *et al.* (2024)[80]	APDS	Piranha (3:1)	Anhyd toluene	• Immersion: 120°C	5%	Immersion : 3h	Toluene DI H2O 3min each	-	Dried overnight in r.t.

Table I-2. Overview of reported silanization approaches, including reaction conditions, for the functionalization of zirconia surfaces

I.4.2. Other Cross-Linkers

Phosphonic acids (PA) constitute a well-established class of anchoring molecules for the modification of metal oxide surfaces, forming relatively strong metal–oxygen–phosphorus bonds and offering significant chemical versatility for further functionalization [81,82]. Their surface attachment typically occurs through mono-, bi-, or tridentate coordination modes, which influence grafting density, molecular orientation, and interfacial stability [83]. Compared with silane-based strategies, PA layers are often reported to exhibit improved hydrolytic stability on certain oxides, which has motivated their investigation for zirconia surface functionalization [22]. Several studies have demonstrated PA-based modification of ZrO_2, including phosphonic acid functionalization of zirconia nanoparticles [84], phosphonate monolayers used for peptide immobilization [85], carbamoyl phosphonic acid grafting with spectroscopic validation [86], and ligand grafting on porous zirconia supports [87]. Classical hydrolytic stability studies further suggest that PA monolayers on zirconia can be more stable than silane analogues under aqueous conditions [88]. However, systematic investigations isolating reaction parameters or evaluating long-term stability and clinical durability on zirconia remain scarce, and most reported protocols rely on empirical optimization rather than mechanistic understanding.

L-3,4-dihydroxyphénylalanine (L-dopa) has been efficiently used as a cross-linker on zirconia for immobilization of peptides while minimizing the reliance on organic solvents [89]. Under alkaline conditions (typically pH > 7.5) and in the presence of oxygen, L-dopa undergoes spontaneous oxidative polymerization, leading to the formation of a dark brown to black, melanin-like layer known as polydopamine (PDA). This process is driven by the autoxidation of catechol groups in L-dopa or dopamine, resulting in the formation of quinones, which subsequently undergo intramolecular cyclization and cross-linking reactions to form PDA, a polymer structurally analogous to eumelanin [90–92]. The resulting PDA adheres strongly to a wide range of surfaces including metals, oxides, and polymers, due to its rich chemical functionality and ability to form covalent and non-covalent interactions [90–92]. In contrast, under oxygen-depleted conditions, catechol groups can directly coordinate with oxide surfaces (e.g., TiO_2, Fe_2O_3), and although this has not yet been explicitly reported for zirconia, it is highly plausible by analogy [93–

[95]. Although this property is often exploited in materials science and surface modification, the resulting dark coloration can be considered aesthetically unappealing in certain biomedical or consumer applications [92].

Polydopamine has been utilized as coating on zirconia implant abutment surfaces as a potential soft tissue engineering method. Fibroblast behavior, antimicrobial activity and oral bacteria adhesion were evaluated to assess peri-implant soft-tissue seal success [96,97]. The PDA coating of zirconia surfaces was shown to enhance human gingival fibroblast adhesion and proliferation while reducing bacterial colonization *in vitro*, indicating its potential to improve peri-implant soft-tissue integration; however, further *in vivo* studies are necessary to confirm these effects under simultaneous bacterial and tissue interaction conditions [96,97].

I.4.3. Discussion

Despite its widespread use, the silanization reaction on 3-YTP zirconia surfaces remains incompletely understood in the context of biofunctionalization of implant and in particular on yttria-stabilized sintered zirconia. While organosilane chemistry has been extensively employed for surface modification, the specific interactions between silane molecules and the iono-covalent zirconia surface are not yet fully explored. Critical parameters such as solvent, pH, silane concentration, and annealing for the condensation reaction significantly influence the formation, stability, and uniformity of the silane layer, yet are often insufficiently addressed in the literature. Moreover, the effectiveness of silanization is highly dependent on appropriate surface pre-treatment strategies, such as hydroxylation, cleaning, and activation, which serve to increase surface reactivity and ensure the availability of reactive –OH groups for covalent silane attachment. A systematic investigation of both the surface preparation and reaction conditions is therefore essential to establish a controlled and reproducible silanization protocol for biomedical applications.

Other crosslinking systems based on alternative chemistries or bioinspired adhesion mechanisms have also been explored. While they may enable functionalization under mild or aqueous conditions, their interaction with zirconia surfaces remains insufficiently characterized in terms of binding efficiency, stability, and surface coverage. Further studies are required to better understand their surface reactivity and to develop reliable and reproducible modification protocols.

Finally, in the context of biomaterials, the stability of these organic layers when submitted to industrial sterilization compatible processes or mechanical stresses (i.e. when screwed in the bone or toothbrush brushing) remains unaddressed to the best of our knowledge.

I.5. Covalent Bonding for Immobilization of Biomolecules

One strategy to enhance tissue integration of dental implant is to functionalize the surface of the implant material with bioactive molecules (proteins, peptides) involved in cell-matrix interactions. To elaborate these bioactive surfaces, the choice of the bioactive molecules and the way they are immobilized on the surface are important parameters. There are two main immobilization methods on chemically functionalized surfaces: physical adsorption and covalent binding. The last one is often preferred because it allows stable binding depending on the terminal reactive group of the cross-linker grafted on the surface. In the following part, we will present and discuss the most common covalent binding reactions, then we will focus on peptides known to be involved in cell-matrix interactions.

In peptide, thiols, hydroxyls or/and amines are present on the amino acid side chains or at the N-terminal of the molecules. These chemical groups are potential reactive sites for their immobilization on functionalized material in particular Zirconia. Indeed, they can be reacted with aldehydes, cyanate esters, epoxide, isothiocyanate, thiols. These reactions have been reviewed in particular by Hermanson [98].

Some other coupling reaction may require the introduction of a specific reactive group in the peptide chain: For example, 1,3-Huisgen cycloaddition requires the derivatization of the molecules with either a propargyl or an azide.

I.5.1. Amine-based reactions

Amide formation is among the most widely employed strategies for covalently attaching peptides to surfaces. This reaction occurs via nucleophilic attack of an amine on a carboxyl group, resulting in the formation of a stable amide bond. To achieve appreciable reaction rates, the carboxyl group typically requires activation. When the amine is present on the surface rather than the peptide, activating the peptide's carboxyl group can lead to unwanted intra- or inter-peptide condensation, emphasizing the advantage of surface-bound carboxyl groups for controlled coupling via amide formation.

Several activation strategies have been developed, including pentafluorophenyl (PFP) esters, carbodiimides (DIC, DCC), and other reactive intermediates, but the most widely reported approach for biomolecule immobilization is EDC (1-ethyl-3-(3-dimethylaminopropyl)carbodiimide)/NHS (N-hydroxysuccinimide) chemistry, often combined with sulfo-NHS for improved solubility.

In this method, EDC activates surface carboxyl groups to form an unstable O-acylisourea intermediate. NHS or its water-soluble derivative, sulfo-NHS (sNHS), stabilizes this intermediate, generating a reactive NHS ester that readily reacts with primary amines on peptides to form amide bonds (**Figure I-3**). This reaction is favored for its mild conditions and broad compatibility with biomolecules, preserving peptide bioactivity. The method, strategies, and parameters of the three-step EDC/NHS reaction are discussed in detail by Fischer [99]. Fischer highlights that optimal reaction conditions are critical: reagent concentrations of ~0.4 M EDC and 0.1 M NHS are commonly employed, with pH between 5 and 7 to balance amine nucleophilicity and ester hydrolysis. Lower pH reduces amine nucleophilicity, while higher pH accelerates hydrolysis of the NHS ester.

Mechanistic studies have illustrated these effects. Nakajima and Ikada [100] showed that cyclizable carboxylic acids, such as maleic acid, form reactive intermediates in acidic conditions (pH 3.5–4.5), facilitating efficient amide formation, whereas noncyclizable acids are less reactive. Excess EDC can lead to N-acylurea formation, emphasizing the need for careful optimization. Further insights into EDC-mediated bioconjugation were provided by a systematic study by Totaro *et al.* [99] demonstrated that efficient conjugation is primarily driven by high amine nucleophile concentrations rather than sNHS itself, and highlighted peptide-sequence-dependent side reactions.

Reaction parameters also include pH, solvent, temperature, and time. According to Madler *et al.* [102], nucleophilic reactivity ranks as imidazole > ε-amino ~ α-amino ~ thiolate ~ phenolate. At pH 6–7.8, lysine residues are predominantly protonated and less nucleophilic, favoring reactions with tyrosine or hydroxyl-containing residues adjacent to histidine. At pH 9.1, primary amines react preferentially even in peptides containing multiple reactive sites.

Applications on zirconia surfaces have leveraged EDC/NHS chemistry for biofunctionalization in both biosensing and tissue engineering. For example, antibody-functionalized zirconia nanodot films enabled covalent immobilization of anti-CYFRA-21-1 antibodies for oral cancer biomarker detection [103]. In the context of bone tissue engineering, hydroxyapatite-coated zirconia substrates were further functionalized with type I collagen via EDC/NHS chemistry, significantly enhancing osteoblast adhesion and proliferation [104].

Combining EDC/NHS with amine-functionalized surfaces, such as APTES-modified zirconia, allowed grafting of sulfonated hydroxyapatite (S-HA) and peptides, with successful immobilization confirmed by X-ray photoelectron spectroscopy (XPS) [105–109]. On zirconia, for example, this approach was applied to graft sulfonated hydroxyapatite (S-HA) onto particles previously functionalized with primary amines via APTES silanization [104].

Reaction times typically range from 10 to 60 minutes, depending on ligand accessibility and surface properties. Controlling EDC stoichiometry is essential to avoid N-acylurea side products, which irreversibly modify surfaces and reduce reactive sites. Quenching residual activated esters with ethanolamine prevents nonspecific binding and improves assay specificity.

Preconditioning inert surfaces like zirconia via silanization or phosphonate linkers introduces reactive functional groups.

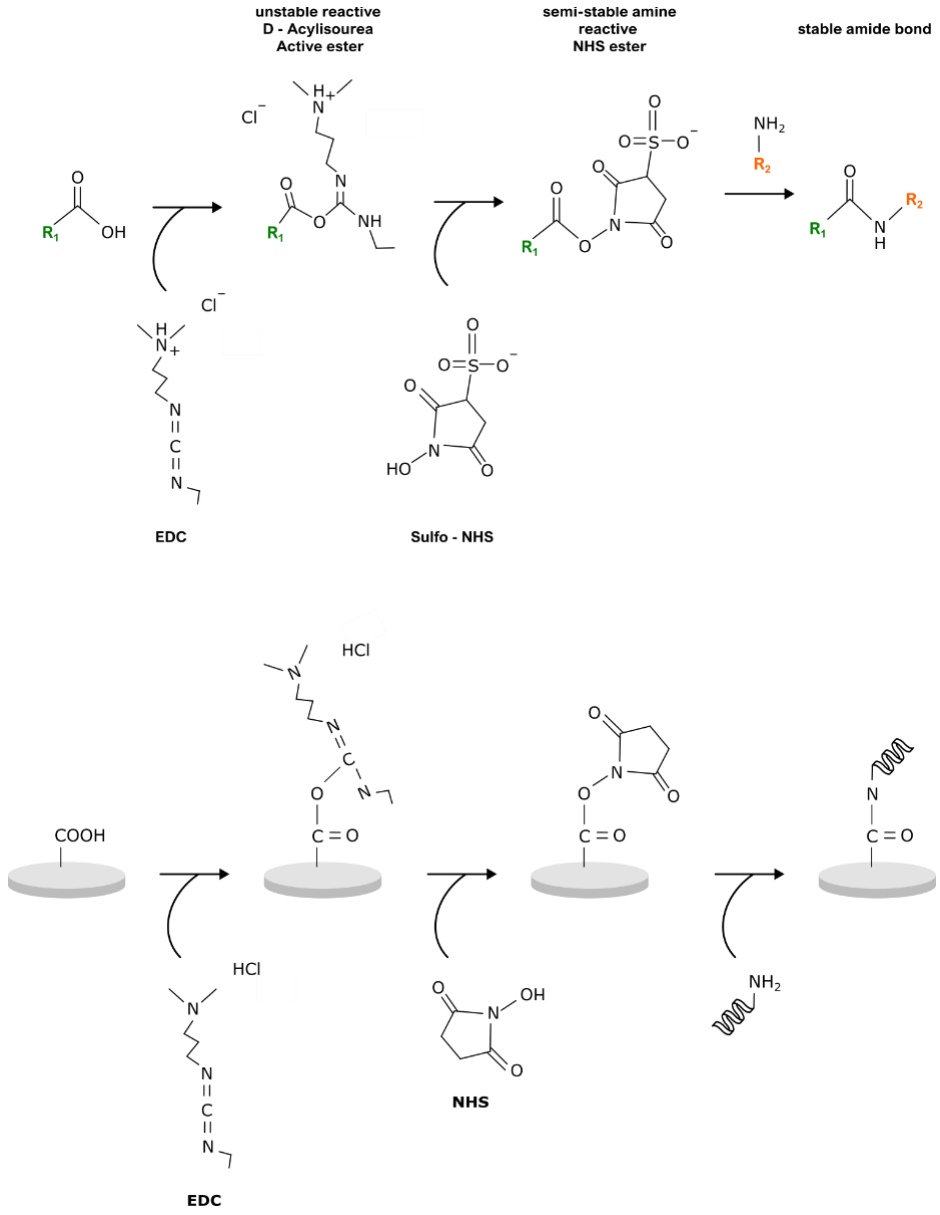

Figure I-3. Schematic representation of EDC/NHS coupling chemistry, showing carbodiimide-mediated activation of carboxyl groups and subsequent amide bond formation with primary amines. R_1 and R_2 denote the reacting functional groups.

PFP esters provide a complementary approach. Carboxyl groups on the surface or peptide can be converted into PFP esters, which react readily with primary amines under mild conditions. The electron-withdrawing pentafluorophenyl group enhances carbonyl electrophilicity, enabling efficient coupling even for sterically hindered peptides. PFP esters have been applied in peptide synthesis as intermediates [110], polymer–protein conjugation [111], inter-nanoparticle coupling [112], and mixed PFP/o-fluorophenyl esters for peptide conjugation and protein immobilization [113]. Their

high reactivity, mild reaction conditions, and broad solvent compatibility make them ideal for generating stable and bioactive peptide-functionalized zirconia surfaces.

Glutaraldehyde is a commonly used bifunctional crosslinker in bioconjugation due to its ability to form covalent bonds between amine groups, making it particularly useful for coupling peptides, proteins, and other biomolecules to surfaces or to each other (**Figure I-4**) [114–116]. After surface functionalization with aminosilanes like APTES, glutaraldehyde can form Schiff base linkages between its aldehyde groups and primary amines on proteins, peptides, or enzymes. Despite its effectiveness as a crosslinker, glutaraldehyde is known to exhibit cytotoxic and potentially mutagenic effects, and residual glutaraldehyde in biomaterials has been associated with inflammatory responses and reduced biocompatibility, which has raised concerns regarding its use in biomedical applications [117].

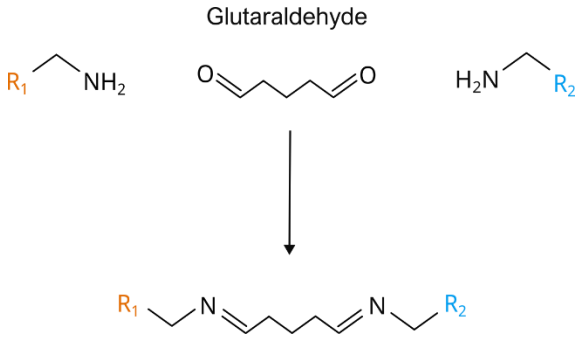

Figure I-4. Schematic representation of glutaraldehyde-mediated coupling between R_1 and R_2 functional groups.

For example, glucose oxidase has been successfully immobilized on APTES-functionalized magnetic zirconia nanoparticles using glutaraldehyde, resulting in stable covalent attachment and retention of enzymatic activity. Subsequently, for the immobilization of a cell promoting peptide, Tano de la Hoz *et al.* demonstrated the successful grafting of the biomolecules on anodized zirconium via APTES-glutaraldehyde chemistry [118].

I.5.2. Thiol-based reactions

Disulfide bridge formation arises from the oxidation of two thiol (–SH) groups—typically from cysteine residues—resulting in a covalent –S–S– linkage. This reaction can occur via mild oxidizing conditions or through thiol–disulfide exchange, in which a nucleophilic thiolate attacks an existing disulfide bond via an S_N2-like mechanism. In surface bioconjugation strategies, thiol-functionalized substrates are often prepared by silanization with organosilanes bearing thiol groups (e.g., MPTMS), which have been used extensively to functionalize metal-oxide and silica surfaces and enable subsequent S–S coupling with cysteine-bearing biomolecules [119]. This approach has been demonstrated across a range of surfaces (silica [120], titania [121], alumina [122]) and on copper nanoparticles [123], supporting the transferability of thiol-silane strategies to bulk or

coated ZrO_2 substrates after appropriate surface activation and control of hydrolysis/condensation conditions.

In this part, we will focus on the thiol implicating click reaction: the Michael addition. Since their introduction to bioconjugation over 50 years ago, maleimides have become indispensable tools for site-selective protein modification. Their reactivity is primarily utilized through thiol-Michael addition reactions, such as cysteine-containing molecules, enabling precise and stable conjugation. These versatile chemical properties have solidified maleimides as a cornerstone in the development of advanced bioconjugation strategies for diverse biomedical and biotechnological applications.

Maleimide-mediated thiol-Michael addition reactions are driven by the cis-conformation of the carbonyl groups and ring strain. These reactions are highly selective for thiols, enabling efficient conjugation with cysteine residues in peptides or proteins. Maleimide-based crosslinkers facilitate one-pot synthesis under mild conditions by linking thiols and primary amines. These reactions typically involve thiol-containing peptides reacting with electron-deficient alkenes ('enes') (**Figure I-5**). The mechanism, kinetics, and influence of various parameters in maleimide–thiol reactions were extensively evaluated in a study by Northrop *et al.* [124]. The article discusses three potential mechanisms: (a) thiolate-catalyzed addition of a thiol to an N-substituted maleimide, (b) thiolate anion formation through acid-base equilibrium, and (c) thiolate anion formation via a nucleophile-initiated pathway. These findings provided valuable insights into the underlying chemistry driving thiol-Michael addition reactions.

Typically carried out in polar solvents such as dimethylformamide or aqueous buffers (pH ~7.5), maleimide-thiol conjugation requires no catalyst, as solvent polarity promotes thiol ionization and enhances reactivity.

A comprehensive review by Renault *et al.* [125] highlights the wide-ranging applications of maleimides in bioconjugation, emphasizing their advantages, limitations, and recent strategies devised to overcome these challenges. One of its main advantages is that it proceeds under physiological conditions, minimizing potential denaturation or loss of activity of sensitive biomolecules. However, this strategy has notable limitations. Maleimide-thiol conjugates can undergo retro-Michael reactions or exchange with other thiols, leading to potential instability, and maleimide groups are also susceptible to hydrolysis, which can reduce their availability for conjugation and impact immobilization efficiency. To overcome these challenges, researchers have developed maleimide derivatives with enhanced stability, reducing their susceptibility to hydrolysis and thiol exchange, such as dibromomaleimides [126] and pyridyl-substituted maleimides [127].

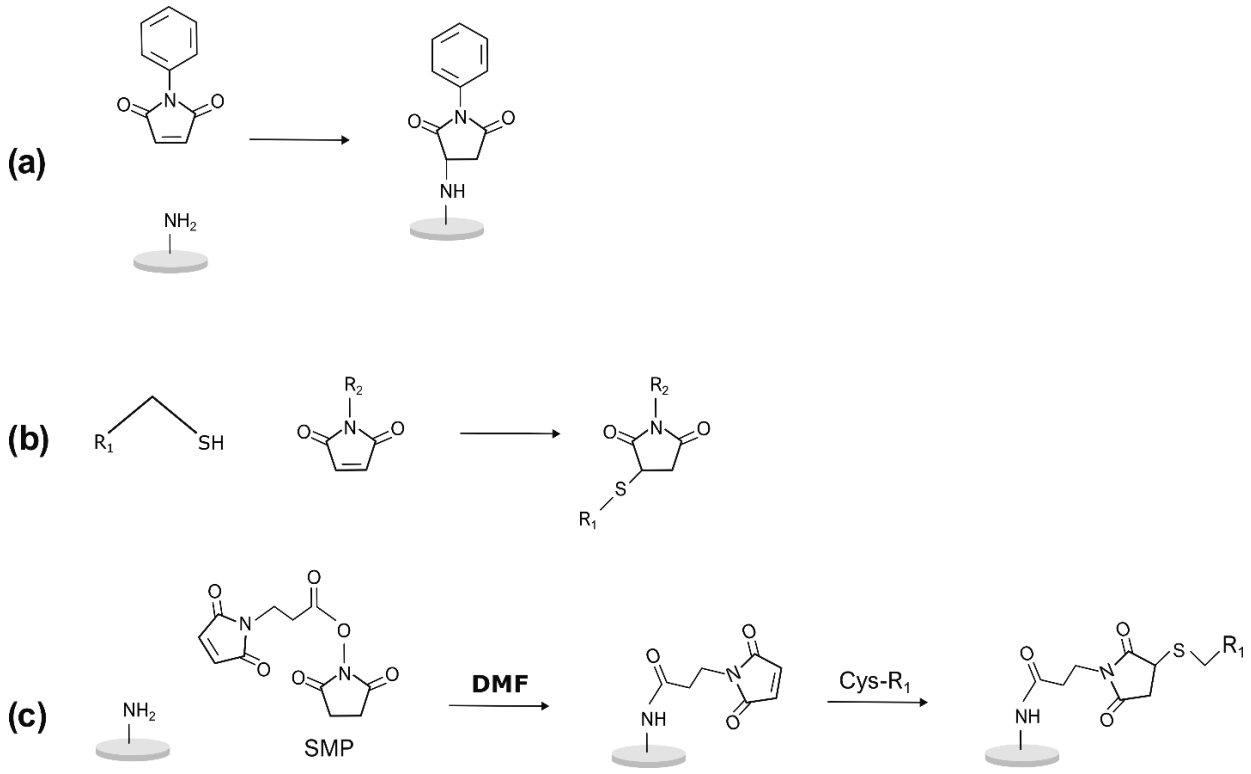

Figure I-5. Schematic overview of maleimide-based surface functionalization strategies: (a) direct reaction of N-phenyl maleimide with amine-terminated surfaces, potentially via a Michael-type addition; (b) thiol–maleimide coupling involving electron-deficient alkenes ('enes') enabling mild, one-pot crosslinking of thiol-containing molecules; (c) introduction of surface-bound maleimide groups using heterobifunctional reagents such as N-succinimidyl-3-maleimidopropionate (SMP) reacting with amine-functionalized surfaces.

Building on these mechanistic insights, Sun *et al.* [128] expanded the scope of thiol-Michael addition reactions by demonstrating their effectiveness and versatility in peptide–polymer conjugation. Their work showcased how this reaction can be applied under mild conditions to achieve efficient and selective coupling, emphasizing its potential for constructing functional polymer–peptide systems suitable for biomedical applications, particularly in gene delivery. Similarly, the reaction between N-phenyl maleimide and an aminosilane monolayer on silica was investigated by Shen *et al.* [129] suggesting a potential Michael addition mechanism (**Figure I-5**).

Introduction of the maleimide group on the surface can be done directly using maleimide containing silane. Alternatively, maleimide groups can be introduced onto surfaces using heterobifunctional reagents such as N-succinimidyl-3-maleimido-propionate (SMP), which react with APTES-functionalized surfaces like titanium [130] (**Figure I-5**).

Together, these studies underscore the versatility and efficiency of maleimide chemistry in bioconjugation, solidifying its role in site-specific bioactive modifications and peptide immobilization strategies across biomedical applications.

I.5.3. Other strategies

Click chemistry has emerged as a powerful and highly selective strategy for biomolecule conjugation, particularly in surface functionalization and biomedical applications [131–133]. The term encompasses a family of reactions including azide–alkyne cycloadditions, thiol–ene reactions, and thiol–Michael additions, the latter of which was already introduced in the previous section in the context of thiol-based coupling strategies. Click reactions enable the formation of covalent bond under mild conditions without interfering with biological systems. These reactions are characterized by their efficiency, bioorthogonality, and compatibility with aqueous environments. Several comprehensive reviews have summarized the applications of these chemistries in biomedical contexts, providing valuable insights into their mechanisms, comparative advantages, and emerging uses in bioconjugation strategies [134–136]. In the context of biomolecule immobilization, click chemistry offers selectivity, precise control over the orientation and density of surface-bound species, making it an attractive alternative to traditional coupling methods like EDC/NHS, particularly for applications requiring high stability and biocompatibility.

The copper(I)-catalyzed azide–alkyne cycloaddition (CuAAC) [131,137] -forms stable triazole linkages between azide- and alkyne-functionalized molecules. More recently, copper-free alternatives such as strain-promoted azide–alkyne cycloaddition (SPAAC) have gained popularity due to their compatibility with live-cell and *in vivo* applications [138,139].

Among the copper-free click reactions, SPAAC is well-suited for surface bioconjugation, and one of the most widely used cyclooctynes in this context is DBCO, due to its favorable reactivity and product stability. DBCO-based SPAAC chemistry has been successfully applied to a broad range of surface modification strategies, including those designed for cell adhesion, biosensing, and tissue engineering. Its efficiency and selectivity have enabled the functionalization of nanoparticles, vesicles, and monolayers with biomolecules such as peptides, antibodies, and PEG chains, while minimizing nonspecific interactions [140–143].

While SPAAC offers advantages in biological settings due to its metal-free nature, the copper(I)-catalyzed azide–alkyne cycloaddition (CuAAC) remains a widely adopted method for surface bioconjugation, especially when catalyst toxicity is not a concern [144]. This reaction has enabled the immobilization of peptides, proteins, and nucleic acids on a variety of azide- or alkyne-functionalized surfaces, including polymers, nanoparticles, and metal oxides. In addition to its efficiency, CuAAC allows for spatial and temporal control over surface modification when combined with techniques like photopatterning or microfluidics. A recent review details CuAAC applications for functionalizing surfaces with various biomolecules across biomedical contexts [145]. Although the presence of copper may limit its use in certain biological applications, CuAAC remains a gold standard for *in vitro* surface functionalization where stability and precision are paramount.

While extensively used on polymers, gold, silica, and titanium oxide surfaces, its direct application to zirconia (ZrO_2) has not yet been reported in the literature. However, successful examples on zirconium-based materials such as Zr-MOFs suggest that ZrO_2 surfaces could

support CuAAC chemistry under appropriate conditions [146]. This presents a promising, though still exploratory, avenue for covalently immobilizing biomolecules onto amine- or alkyne-modified zirconia substrates. In contrast, strain-promoted azide–alkyne cycloaddition (SPAAC), the copper-free variant of click chemistry, has already been demonstrated on zirconia surfaces. One study reported the successful application of multi-step vapor-phase SPAAC to zirconia nanopowders, enabling metal-free and solvent-free surface functionalization [147].

In conclusion, despite the widespread adoption of click chemistry for surface bioconjugation across various material platforms, its application on zirconia remains largely unexplored. Aside from a single report on vapor-phase SPAAC with zirconia nanopowders, no studies to date have demonstrated click-based biomolecule immobilization directly on bulk zirconia or zirconia-coated surfaces.

Genipin, derived from Gardenia jasminoides, is a natural crosslinking agent with significantly lower cytotoxicity and genotoxicity compared to glutaraldehyde that is also commonly used for the attachment of biomolecules [148]. It forms stable crosslinks through nucleophilic and Schiff reactions which resist enzymatic degradation.

Genipin was utilized by J.-Y. Chen and colleagues [148] to immobilize a protein critical for promoting bone and cartilage formation (BMP-2) on rough zirconia surfaces. After sandblasting and alkaline treatment of zirconia surface to introduce hydroxyl groups, genipin was employed to form bonds between the hydroxyl and aldehyde groups, allowing the protein to be grafted.

Tissue transglutaminase (tTG) is an enzymatic bioconjugation tool that catalyzes covalent bonds between glutamine and lysine residues, forming stable ε-(γ-glutamyl)lysine crosslinks. It has been used to crosslink collagen and other ECM proteins, enhancing mechanical strength while preserving integrin-binding sites crucial for cell adhesion and proliferation [149–151]. Unlike chemical crosslinkers such as EDC-NHS, tTG maintains native bioactivity and supports long-term cell viability.

While no studies have yet applied tTG directly to zirconia surfaces, strong precedents exist: for titanium, tTG-mediated collagen immobilization on silanized Ti6Al4V yields high stability and significantly improved osteogenic responses from mesenchymal stem cells [152]. Leveraging these insights, tTG-mediated conjugation on appropriately activated zirconia could provide a selective, covalent route to biofunctionalize the material.

I.5.4. Discussion

There is a comparative study by Malavika *et al.* [153], evaluating a variety of bioconjugation strategies used to modify the mechanical and biological properties of collagen-based scaffolds, with notable differences emerging between commonly used crosslinkers such as EDC-NHS, genipin, and tissue transglutaminase. EDC-NHS treatment yields constructs with high tensile stiffness but compromises long-term cell proliferation and integrin-mediated adhesion due to the

loss of glutamate residues critical for cell binding. In contrast, genipin achieves a comparable degree of mechanical reinforcement while preserving cell attachment and promoting sustained proliferation, positioning it as a favorable alternative where both structural integrity and bioactivity are essential. Tissue transglutaminase, while producing substrates with lower stiffness, enhances cell behavior by potentially modifying existing collagen networks in a way that maintains or improves biochemical signaling. These findings underscore the importance of selecting crosslinking chemistries not only to achieve desired mechanical performance but also to modulate cell–material interactions, ultimately enabling the design of collagen scaffolds with tunable biofunctionality for tissue engineering applications.

I.6. Bioactive molecules for cell-matrix interactions

Bioactive molecules for the surface bioengineering of dental implants include a wide range of agents such as growth factors (fibroblast growth factor, platelet-derived growth factor, enamel matrix components, epidermal growth factor, bone morphogenetic proteins), extracellular matrix (ECM) components (fibronectin, laminin, collagen), antimicrobial molecules (e.g., human β-defensins), antibodies (such as anti-sclerostin), and pharmacological agents (e.g., statins, antibiotics). Peptides have attracted particular attention, especially short sequences derived from ECM proteins, such as laminin fragments (RGD, YIGSR, Ln-5), collagen-derived P15, ameloblastin-derived motifs, antimicrobial peptides like GL13K, or receptor-targeting peptides such as the protease-activated receptor-4 (PAR4) agonist. Some of these peptides exhibit dual functionality, promoting both osseointegration and gingival tissue adhesion (e.g., RGD, YIGSR), whereas others display a more specific activity, favoring either soft tissue integration (e.g., PAR4) or bone regeneration (e.g., BMP-derived peptides). Compared to larger biomolecules, peptides offer notable advantages, including higher stability and, importantly, resistance to sterilization processes, making them particularly attractive candidates for clinical applications. For instance, the RGD peptide remains stable after ethylene oxide sterilization [154] whereas protein activity is often compromised by the same process [155]. This aspect is particularly relevant for zirconia implants, as gamma sterilization not only risks affecting biomolecule functionality but also induces undesirable color changes, making ethylene oxide the preferred industrial sterilization method.

Biomimetic surface modification of zirconia implants still has received little attention. In the following, we will focus on those covalently immobilized on zirconia.

I.6.1. Extracellular Matrix (ECM)–Derived Peptides

Research into the cell-binding capabilities of different proteins, like fibronectin, vitronectin, collagen, and fibrinogen, revealed that short peptide sequences such as Arg-Gly-Asp (RGD) can bind to specific cell receptors. Discovered 30 years ago [156], the Arg-Gly-Asp (RGD) tripeptide is the fundamental sequence within fibronectin, crucial for cell adhesion. This peptide has gained significant attention in biomaterial functionalization due to its ability to bind various integrins, facilitating cell adhesion and potentially promoting cell differentiation. Recently, more advanced variants like cyclic RGD (cRGD) peptides have been explored, as their three-dimensional structure is thought to offer enhanced receptor affinity.

Since the 1990s, RGD peptides have been widely used to enhance cell adhesion on various substrates, particularly for coating titanium implants [105,130,157–161]. However, their use on zirconia abutments or implants appears to be scarce and limited.

The RGD sequence binds to a broad family of integrin receptors on the cell surface, notably $\alpha v\beta 3$ and $\alpha 5\beta 1$, initiating focal adhesion formation. This engagement activates intracellular signaling cascades involving SMAD, p38 MAPK, and ERK pathways, which together regulate cytoskeletal reorganization, proliferation, and osteogenic differentiation. Importantly, RGD promotes cell adhesion without disrupting proliferation, making it well suited for implant surfaces. Advanced derivatives, such as cyclic RGD (cRGD), have been designed to stabilize the conformation of the peptide and improve receptor affinity, mimicking the three-dimensional presentation of the sequence in native proteins. Moreover, when RGD is combined with soluble growth factors such as BMP-7, synergistic effects are observed: osteogenic differentiation is significantly enhanced and bone repair accelerated in critical-sized defect models [162]. RGD-functionalized zirconia surfaces can guide tissue formation, making them valuable for applications such as dental implants and orthopedic implants, as well as, tissue engineering scaffolds [163–165]

As for the more complex structure of the linear RGD (l-RGD) peptide, the cyclic RGD (c-RGD), a comparative study was conducted on titanium surfaces by Kämmerer *et al.* [166]. While both variants supported endothelial cell (EC) attachment and proliferation, c-RGD-modified titanium surfaces demonstrated significantly greater cell coverage and proliferation after three days compared to l-RGD, silanized, or untreated controls. These findings suggest that cyclic RGD, due to its conformational stability and higher binding affinity, may provide more robust and sustained biological responses. Although promising, these *in vitro* results underscore the need for *in vivo* validation to confirm the long-term benefits of c-RGD coatings in implant applications.

Several immobilization chemistries have been reported for attaching RGD to zirconia. Zang *et al.* grafted RGD peptides to zirconia scaffolds via maleimide chemistry on an APTES-modified surface [167]. In the study, the immobilization of the RGD tripeptide onto hydrothermally treated Y-TZP surfaces significantly enhanced cellular responses. MG-63 osteoblasts showed improved adhesion, spreading, proliferation, and differentiation on RGD-functionalized zirconia compared to untreated surfaces. These effects are driven by specific interactions between the RGD motif and

integrin receptors on the cell membrane, promoting focal adhesion formation and activating osteogenic signaling pathways. Similarly, Fernandez *et al.* [168] showcased that the immobilization of a containing RGD peptide onto zirconia and zirconia/titanium cermets allowed the cellular spreading of MC3T3 osteoblasts.

Another immobilization route has been tested on anodized zirconium surfaces. The anodization process generates a porous oxide layer with a monoclinic crystalline structure, providing reactive sites for further modification. RGD peptides were covalently attached after silanization with APTES and crosslinking with glutaraldehyde [118]. While the study focuses on anodized zirconium, a similar strategy could be adapted for zirconia.

Furthermore, there is a lack of understanding about the antimicrobial properties of RGD coatings. While RGD peptides are not inherently antimicrobial, their incorporation into multifunctional biomaterials, such as co-delivery systems, hydrogels, and amphiphilic peptides, can impart antimicrobial properties [169–172]. These engineered systems leverage the cell-adhesive nature of RGD peptides while introducing antimicrobial functionalities, making them promising candidates for applications in tissue engineering and/or wound healing.

Chen *et al.* [173] applied an electrophoretic-fusion method to immobilize carboxydecylphosphonic acid on zirconia, followed by EDC/NHS coupling of the PAR4 agonist peptide. The modified surfaces induced strong platelet aggregation and PDGF release, and when seeded with gingival epithelial cells (OBA9), significantly enhanced cell attachment and laminin-5 deposition, promoting basal lamina formation.

In a study by Minguela *et al.* [163], zirconia surfaces were laser-patterned with microgrooves (3 μm or 10 μm periodicity) and biofunctionalized with the osteogenic DWIVA peptide, alone or in combination with RGD. This dual approach, combining physical topography and biochemical signaling, was shown to significantly promote human mesenchymal stem cell adhesion, cytoskeletal organization, and directional migration along the grooves. Furthermore, DWIVA-functionalized surfaces led to an upregulation of osteogenic genes such as RUNX2 and ALPL, indicating a strong potential for enhancing osseointegration around zirconia implants.

Laminin derived peptides, such as Laminin-5 (Ln-5), have been studied for their well-known role as an epithelial cell-adhesive protein with a site that binds to the extracellular matrix via integrins, potentially enhancing cell adhesion to the bioceramic surfaces [174]. A key *in vitro* study demonstrated that applying soluble laminin-5 to titanium alloy (Ti-6Al-4V) surfaces resulted in improved epithelial cell attachment and promoted the formation of hemidesmosomes [175]. Although the study was conducted on titanium and not zirconia, and the peptide was not covalently bound, laminin-5's strong cell-adhesive properties and its role in hemidesmosome formation make it a compelling candidate for future exploration on zirconia surfaces.

Another study investigated the interaction of laminin with alumina-zirconia composites of varying ZrO_2 content, discovering that laminin-functionalized composites, analyzed using X-ray photoelectron spectroscopy and atomic force microscopy, improved epithelial cell adhesion and migration, with Ln-5 enhancing cellular activation more on zirconia-rich composites and Ln-

1 on alumina-rich ones [176]. Although the laminin was not covalently immobilized in this case either, the findings highlight its potential to modulate epithelial responses depending on surface composition. These results further support laminin, particularly Ln-5, as a promising biomolecule to explore for enhancing soft tissue integration in zirconia-based dental materials.

Another laminin-derived peptidic sequence is the YIGSR (Tyr-Ile-Gly-Ser-Arg) and it was introduced for its cell spreading properties in 1993 [177]. In a 2005 tissue engineering study, the combination of YIGSR with RGD on PEG-hydrogels was found to significantly increase MVEC (cultured microvascular endothelial cells) migration rates relative to RGD alone [178]. To our knowledge, the covalent immobilization of YIGSR peptide (or with combination with the RGD sequence) onto dental zirconia and the evaluation of their cell promoting bioactivity related to the gingiva has not yet been explored.

Type I collagen has been successfully immobilized on sandblasted and alkaline-treated zirconia surfaces using the natural cross-linker procyanidin, forming a stable collagen layer confirmed by X-ray photoelectron spectroscopy (XPS) and surface analysis [179]. This covalent functionalization significantly enhanced mesenchymal stem cell adhesion, proliferation, and mineralization, with activation of focal adhesion kinase, AKT, and p38 signaling pathways, indicating strong cell–matrix interactions. While the study focused on osteogenic cells rather than soft tissue, the integrin-mediated adhesion promoted by collagen I highlights its potential as a versatile bioactive coating.

I.6.2. Other Bioactive Molecules

In 2020, the highly repetitive functional sequence, Ser-Asp-Ser-Ser-Asp (SDSSD) peptide, found in dentin phosphoprotein (DPP), was covalently binded bound to dental zirconia using an APTES crosslinker. This sequence is believed to activate osteoblast-specific pathways inducing their adhesion and mineralization and the *in vitro* tests showcased that the SDSSD immobilized Y-TZP surface augmented early cell adhesion and proliferation without cytotoxicity [79].

Bone morphogenetic proteins (BMPs) are the most frequently studied canonical growth factors for zirconia biofunctionalization: BMP-2 has been covalently immobilized on roughened ZrO_2 using the natural crosslinker genipin, which enhanced hMSC adhesion and mineralization *in vitro*, and similar BMP-2 incorporation into biomimetic calcium-phosphate coatings improved peri-implant bone formation *in vivo* [180,181]. Recombinant BMP-7 has also been combined with RGD on zirconia scaffolds, as mentioned in the previous chapter, to synergistically drive osteogenic differentiation of human dental pulp stem cells, showing dose-dependent effects [162].

Beyond BMPs, other osteoanabolic peptides and factors have been grafted to zirconia: abaloparatide (a PTHrP analog) has been reported in recent surface-engineering studies to boost osteogenesis when immobilized with nano-hydroxyapatite on zirconia substrates[182].

Growth and differentiation factor-5 has also been successfully immobilized on zirconia using click chemistry [183]. The resulting Zr/GDF-5 surfaces released the growth factor over 28 days and promoted enhanced osteogenic responses, including proliferation, ALP activity, calcium deposition, and upregulation of genes such as Runx2, Osterix, collagen I, and osteocalcin, in both *in vitro* and *in vivo* settings.

I.7. Conclusion

This chapter reviewed the main approaches reported for the covalent biofunctionalization of zirconia surfaces, including surface pretreatments, silanization strategies, coupling chemistries, and the types of biomolecules used. Together, these studies show that zirconia can be chemically modified to immobilize bioactive molecules, but they also reveal a high level of variability in methods and outcomes.

A key issue emerging from the literature is the specific nature of zirconia surface chemistry. Compared with more commonly studied oxides such as silica or titania, zirconia presents lower intrinsic reactivity and surface properties that depend on phase and treatment history. As a result, protocols transferred from other oxide systems often lead to inconsistent results or limited stability when applied to zirconia. This problem is amplified by the lack of standardized and well-documented functionalization procedures, particularly for silanization, making it difficult to compare studies or draw clear structure–property relationships.

In addition, many studies focus on demonstrating chemical attachment or short-term biological responses, while fewer address long-term stability, robustness under relevant conditions, or compatibility with industrial implant manufacturing. Although several works investigate cell interactions with functionalized zirconia, these studies most often evaluate general cytocompatibility or osteoblastic responses. In contrast, relatively limited attention has been given to soft-tissue-related cells such as fibroblasts and keratinocytes, which are critical for the establishment of a stable peri-implant soft tissue seal.

Overall, the current state of the art indicates that successful zirconia biofunctionalization depends not only on the choice of chemistry, but also on how surface preparation, processing parameters, and biological objectives are combined. This chapter therefore sets the basis for a more critical and rational approach to zirconia surface modification, which is explored in the following chapters.

II. Surface Pre-treatment

II.1. Abstract

This chapter describes the preparation and characterization of zirconia surfaces prior to functionalization. Commercial 3Y-TZP disks were first characterized to assess the surface state of the as-received samples and subsequently subjected to controlled surface treatments to obtain well-defined and reproducible surface states, including mechanically polished and chemically etched surfaces. Mechanical polishing and hydrofluoric acid etching were employed to remove manufacturing contamination. Mechanical polishing lead to producing a smooth and well-controlled topography. Hydrofluoric acid (HF) etching was also successful at removing surface contaminants, and induced surface morphological modifications. The effects of these treatments were evaluated using scanning electron microscopy (SEM), atomic force microscopy (AFM), energy-dispersive X-ray spectroscopy (EDS), X-ray diffraction (XRD), X-ray photoelectron spectroscopy (XPS), and water contact angle (WCA) measurements. In addition, several surface-cleaning and activation procedures were assessed based on their ability to remove organic contamination, with UV/ozone treatment selected for subsequent experiments due to its effectiveness and practicality. Overall, this work establishes a robust surface preparation strategy, providing well-characterized zirconia substrates suitable for subsequent surface functionalization and bioactive molecule grafting.

II.2. General Introduction

Prior to functionalization, zirconia surfaces require careful pretreatment to ensure reproducibility and effectiveness of subsequent chemical modifications using organo-silane (see **III**). As-received zirconia is inevitably covered by organic and inorganic contaminants originating for example from manufacturing, polishing, or handling, which can interfere with silane grafting or biomolecule immobilization [77,184]. In addition, surface roughness and crystallinity both play key roles in determining the mechanical stability of the substrate and biological responses. While controlled polishing or roughening is necessary to adjust the topography to the desired level, maintaining an appropriate crystalline structure of zirconia is equally important, as it governs the material's strength, resistance to phase transformation, and the adhesion of functional layers [28,29,31,32,73,185,186]. Beyond cleanliness and morphology, pretreatment also serves to activate the zirconia surface by generating hydroxyl groups, which act as essential anchoring sites for silane coupling reactions [187,188]. Together, these steps provide a clean, chemically active, and

topographically controlled substrate, forming a reliable foundation for reproducible surface functionalization and subsequent bioactive grafting.

II.3. Materials & Methods

II.3.1. Materials and Reagents

Commercially available 3Y-TZP disks (Ø 9 mm, thickness 2 mm; provided by Anthogyr, Sallanches, France) were used as the substrate material. The disks were manufactured by injection molding and supplied with a ground surface finish on one side, corresponding to an average arithmetic roughness Ra of approximately 0.2 μm.

Sodium Hydroxide pellets, Hydrogen Peroxide, sulfuric acid (H_2SO_4), ammonium hydroxide NH_4OH, hydrofluoric acid HF 48%, Ethanol 99,8%, 2-Propanol 99,5%, Acetone 99,5%, were purchased from Sigma-Aldrich. Deionised water (DI water) (, resistivity ≥ 18.2 MΩ·cm) was used for the preparation of all solutions and for rinsing the samples throughout the experimental procedure.

The UV–ozone cleaning was performed using a Novascan UV–Ozone Cleaner (PSD/PSDP series) operating under ambient conditions with a supplemental oxygen flow. The UV lamp operated at an irradiance of 28–32 mW/cm² at 254 nm and the samples were treated for 30 min.

Piranha solution, prepared by slowly adding hydrogen peroxide (H_2O_2, 30 %) to concentrated sulfuric acid (H_2SO_4, 98 %) in a 3:1 v/v ratio, was freshly made immediately before use. Samples were immersed in the piranha solution for a defined duration, then extensively rinsed with ultrapure water and dried under a nitrogen stream. For the SC-1 solution, it was prepared by mixing ammonium hydroxide (NH_4OH, 25 %), hydrogen peroxide (H_2O_2, 30 %), and ultrapure water in a 1:1:5 v/v/v ratio. Samples were immersed in the SC-1 solution at elevated temperature under gentle agitation, followed by thorough rinsing with ultrapure water and nitrogen drying.

II.3.2. Samples Preparation

Silicon carbide (SiC) abrasive papers (Type M, non-adhesive, Ø 200 mm, Presi) with grit sizes P180, P360, P600, and P1200 were used for progressive surface grinding of the as-received zirconia disks. Fine polishing was subsequently performed using polycrystalline diamond suspensions (6 μm, 3 μm, and 1 μm, Presi) and a colloidal silica (SiO_2) suspension (0.03 μm, Presi) applied on adhesive polishing cloths (Ø 250 mm, RAM, Presi), following a sequence from the coarsest to the finest particle size. After polishing, the samples were cleaned by successive sonication steps in acetone, ethanol, 2-propanol, and deionized water, each for 10 min, to remove polishing residues.

Hydrofluoric acid (HF) etching was also employed to remove surface contamination identified on the as-received zirconia disks. Etching was performed using aqueous HF solutions at concentrations of 2, 5, and 10 %, with immersion times of 5, 15, 30, and 60 min (**Table II-1**). Following etching, the samples were thoroughly rinsed with deionized water and dried under a nitrogen stream.

HF concentration %	**Time (min)**			
2	5	15	30	60
5	5	15	30	60
10	5	15	30	60

Table II-1. Overview of the different acid etching conditions tested, showing variations in etching time and acid concentration

For clarity, the different zirconia surface states investigated in this study are identified using the nomenclature shown in **Figure II-1** and are referred to accordingly in the following sections.



Figure II-1. Schematic representation of the different zirconia surface states investigated and their corresponding nomenclature.

After the relevant treatment, the zirconia disks were subjected to different cleaning procedures to remove organic contaminants.

- Exposure to UV/Ozone (UV/O_3) treatment for 30 min operating under ambient conditions with supplemental oxygen flow,
- Immersion in 1 M NaOH for 3 h,
- Immersion in piranha solution (H_2SO_4/H_2O_2, 3:1 v/v) for 30 min followed by 10 min sonication in deionized water,
- Immersion in solution (NH_4OH/H_2O_2, 2:1 v/v) for 30 min at 80 °C (it will be described as "basic piranha"),

Following each treatment, the samples were thoroughly rinsed with deionized water and dried under a nitrogen stream. In addition, combinations of these treatments with UV/O_3 for 30 min exposure were also tested (with supplemental oxygen flow).

II.3.3. Characterization Techniques

II.3.3.1. *Water contact angle (WCA)*

Water Contact Angle Measurement (WCA) is a technique based on the following principle: when a liquid droplet is placed on a solid surface, the shape of the droplet at equilibrium reflects the balance of interfacial forces at the three-phase contact line: solid–vapor (γSV), solid–liquid (γSL), and liquid–vapor (γLV) (**Figure II-2**). This relationship is described by Young's equation (**Equation II-1**),

$$\gamma SV = \gamma SL + \gamma LV \cos\theta$$

Equation II-1 Young's equation

where θ is the angle at the three-phase contact line between the surface and the tangent of the liquid droplet surface. This angle is called the contact angle. Its value provides insight into the relative surface energy of the solid: Using water as a liquid, hydrophilic surfaces exhibit low contact angles (<90°) due to strong solid–liquid interactions, whereas hydrophobic surfaces display high contact angles (>90°) as liquid–vapor interactions dominate. Extremely low angles (<10°) indicate near-complete wetting, while very high angles (>150°) are characteristic of superhydrophobic surfacesSince surface chemistry and functional groups determine surface energy, while surface topography can influence the measured contact angle, changes in WCA provide indication of surface modification, including the absence or presence of organic contamination or the grafting of organic molecules such as silanes or peptides.

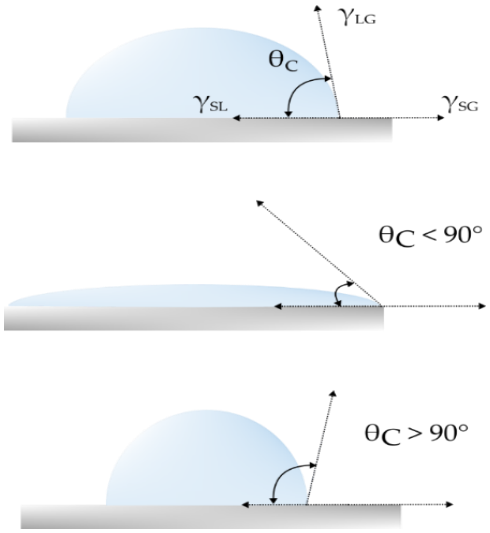

Figure II-2. Schematic representation of the water contact angle (WCA) measurement principle, illustrating the droplet–surface interaction used to assess surface wettability.

WCA measurements were performed with GBX-Digidrop MCAT goniometer (France) at room temperature, and at least three droplets were placed on different areas of each sample to

account for potential heterogeneities, with the average value reported. Contact angles θ were measured from sessile deionized water drops of 0.8 µL using the Visiodrop software.

II.3.3.2. *X-ray Photoelectron spectroscopy (XPS)*

X-ray Photoelectron Spectroscopy (XPS) is a surface-sensitive technique based on the photoelectric effect. When a material is irradiated with X-rays (1-3 kV), core electrons are ejected if the photon energy exceeds their binding energy. By measuring the kinetic energy of these emitted electrons, the binding energy of each electron can be determined using **Equation II-2.**

$$E_b = h\nu - E_k - \phi,$$

Equation II-2 XPS binding energy relationship

where E_b is the binding energy, $h\nu$ is the photon energy, E_k is the measured kinetic energy, and ϕ is the spectrometer work function. Since each element has characteristic binding energies, XPS spectra can be used to identify the elements present at the surface (**Figure II-3**). Additionally, small shifts in the binding energy, known as chemical shifts, provide information about the oxidation state and chemical environment of the atoms. The technique is highly surface-sensitive due to the limited escape depth of photoelectrons, typically around 1–10 nm, making it particularly useful for studying thin films, coatings, and surface modifications.

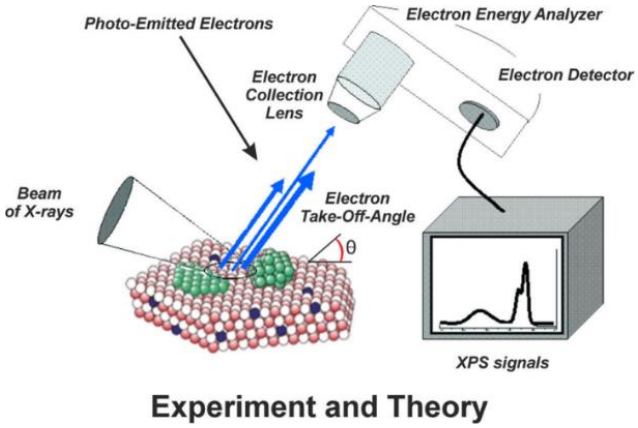

Figure II-3. Principle of X-ray Photoelectron Spectroscopy (XPS). Monochromatic X-rays excite core electrons, which are emitted from the sample surface. *Reproduced from Bagus et al.* [189]

XPS measurements and analyses were performed using a ULVAC PHI Versaprobe III photoelectron spectrometer, equipped with a standard AlKα monochromated source (hν = 1486.6 eV), operated at a 50 W electron beam power (with a circular spot size of 200 µm of diameter). The emission of photoelectrons from the sample was analyzed at a takeoff angle of 45° under ultra-high vacuum conditions of around 10^{-9} mbar. Spectra were carried out with 224 eV pass energy for the survey scan and 27 eV pass energy for elementary high-resolution regions. The spectra were fitted using CasaXPS software version 2.3.25. The C–C bond contribution of C1s peak at 285 eV was used as a binding energy reference. The background was subtracted using the Shirley method. Quantification was performed using the sensitivity factors provided by the

manufacturer considering the cross section of each element, the escaping depth of electrons and the spectrometer transmission as well as angular distribution correction. Peak shape was Gaussian/Lorentzian (70/30).

II.3.3.3. *X-Ray Diffraction (XRD)*

X-ray Diffraction (XRD) is a technique used to identify crystalline phases and evaluate the structural properties of materials. The principle is based on the constructive interference of monochromatic X-rays scattered by the periodic arrangement of atoms in a crystal lattice. When the conditions of Bragg's law $n\lambda = 2d\ sin\theta$ are satisfied, diffraction peaks are produced at specific angles corresponding to the interplanar spacings d. Each material exhibits unique diffraction patterns that serve as fingerprints of its crystal structure. By analyzing the position, intensity, and width of the peaks, information on phase composition, crystallinity and crystallite size, and possible lattice strains can be obtained (**Figure II-4**).

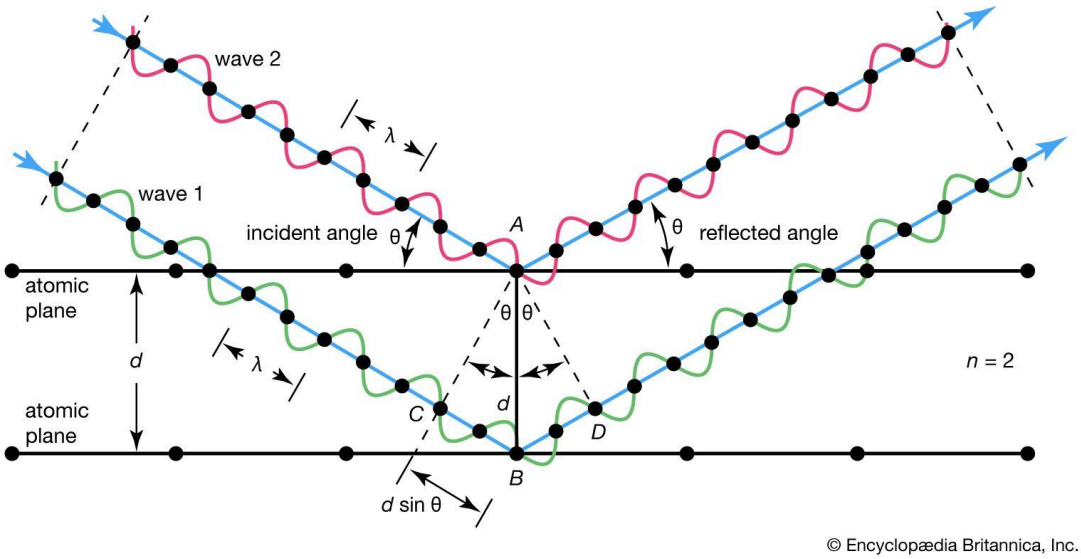

Figure II-4. X-Ray Diffraction scheme, reproduced by *Britannica Editors. "X-ray diffraction." Encyclopedia Britannica, August 2, 2024. https://www.britannica.com/science/X-ray-diffraction.*

The XRD diffractograms were acquired in Bragg-Brentano configuration with a D8 Advance Bruker A25 diffractometer (Bruker Co, Germany) placed at CITIUS and a D8 Advance Bruker AXS diffractometer (Billerica, USA) placed at MATEIS laboratory. All scans were recorded over a wide 2θ range (20° – 90°) or a reduced range (27° – 30°), with a step size of 0.015° or 0.02° and 0.1 or 1 s per step, respectively.

II.3.3.4. *Scanning electron microscopy (SEM)*

Scanning Electron Microscopy (SEM) is a surface imaging technique that provides high-resolution information on the morphology and topography of materials. The principle is based on scanning a focused beam of high-energy electrons across the sample surface. The interaction between the electron beam and the atoms of the specimen generates various signals, mainly

secondary and backscattered electrons, which are collected to form an image. Secondary electrons provide detailed topographical information, while backscattered electrons give contrast related to the atomic number of the elements present. SEM thus allows the visualization of surface features at the micro- and nanoscale, making it an essential tool for characterizing material surfaces and coatings. **Energy Dispersive X-ray Spectroscopy (EDS)** is used to analyze the elemental composition of the zirconia surfaces. EDS is based on the detection of characteristic X-rays emitted by atoms in the sample when they are excited by a high-energy electron beam, typically in a scanning electron microscope (SEM). When an incident electron ejects an inner-shell electron from an atom, an electron from a higher energy level fills the vacancy, releasing energy in the form of an X-ray. The energy of this X-ray is unique to each element, allowing qualitative and semi-quantitative identification of elements present on the surface.

The surface morphology of the samples was examined using a SEM Mira3 (Tescan®, Digital Microscopy Imaging®) on Nanolyon technological platform at INL laboratory. Prior to analysis, the samples were mounted on aluminum stubs using conductive carbon tape. Imaging was performed under high vacuum using an accelerating voltage typically ranging from 5 to 15 kV (0.5 to 3 μm depth analysis), depending on the surface conductivity and desired resolution. Secondary electron (SE) mode was used to visualize surface topography, while backscattered electron (BSE) imaging was employed when compositional contrast was required. All observations were conducted at room temperature without applying any conductive coating, as the zirconia substrates provided sufficient charge dissipation for imaging.

II.3.3.5. *Optical Interferometry*

Optical interferometry is a measurement technique that relies on the principle of interference of light waves to obtain precise information about surface topography, thickness, or refractive index variations. In this method, a coherent light source (usually a laser or a broadband light) is split into two beams: a reference beam and a measurement beam that interacts with the sample surface. When the two beams are recombined, they produce an interference pattern of alternating bright and dark fringes, resulting from constructive and destructive interference depending on the optical path difference between the beams. By analyzing these fringes, either through phase-shifting or white-light scanning techniques, one can reconstruct the surface profile with nanometer-scale vertical resolution. This non-contact approach makes optical interferometry particularly valuable for characterizing delicate or smooth surfaces, such as polished metals, semiconductors, or biomaterials, with high precision and minimal risk of altering the sample.

II.3.3.6. *Atomic Force Microscopy*

Atomic Force Microscopy (AFM) is a high-resolution technique used to characterize surface topography at the nanometer scale. A sharp tip mounted on a flexible cantilever scans the surface, and the interactions between the tip and the sample are used to generate a three-dimensional map of the surface. AFM is commonly used to measure surface morphology and quantify roughness parameters such as Ra or Sa.

Topographical images of the sample were acquired using the non-contact mode. FORTA cantilevers from AppNano were used. They are made of aluminum with a gold coating on the detector side, better for imaging in liquids than the aluminum classical coating. Their frequencies vary between 43 and 81 kHz in air, for a typical spring constant between 0.6 and 3.7 N/m.

II.4. As-Received Samples Characterization

II.4.1. Crystallinity & Phase Content

The X-ray diffraction (XRD) analysis of the as-received zirconia disk (ZR-AR) revealed sharp and well-defined diffraction peaks, indicative of high crystallinity (

Figure II-5). The main reflections observed correspond to the characteristic peaks ((101), (110), (112), (211), and (202)) of tetragonal zirconia (t-ZrO_2) for Cu Kα radiation. No additional peaks were detected, suggesting the absence of secondary phases. Notably, the distinctive monoclinic ZrO_2 peaks around 28° and 31° were not present, confirming the predominance of the tetragonal phase. These results are consistent with the expected structure of 3 mol% yttria-stabilized tetragonal zirconia (3Y-TZP). The diffraction pattern is characteristic of tetragonal ZrO_2.

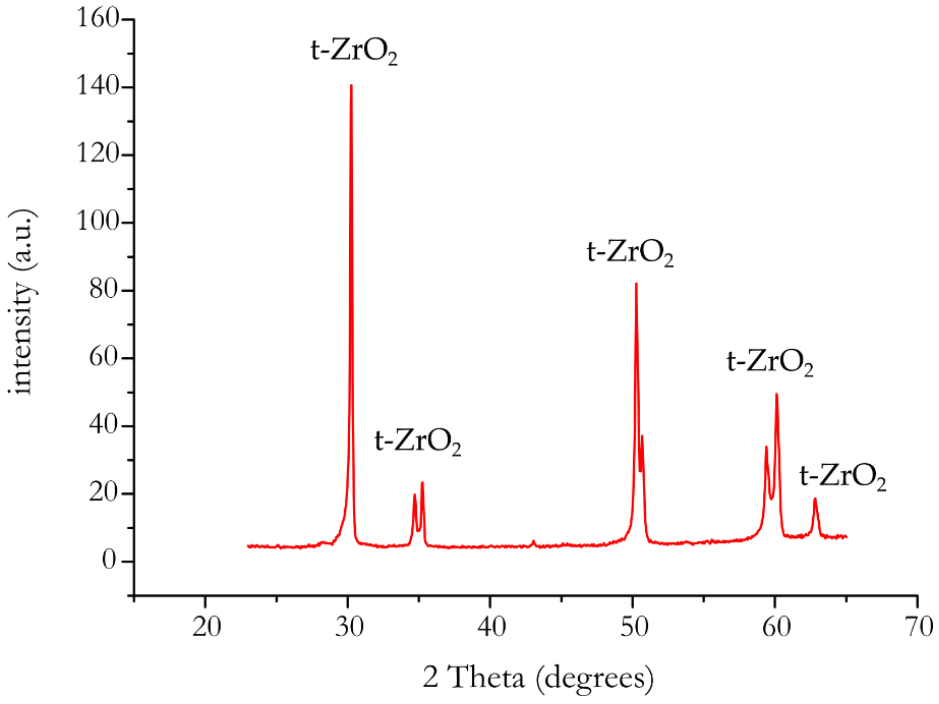

Figure II-5. X-ray diffraction (XRD) pattern of the untreated zirconia disk (ZR-AR).

II.4.2. Surface State & Chemical Composition

To evaluate the initial state of the zirconia disks upon reception (ZR-AR), Scanning Electron Microscopy (SEM) was performed. The surface observations revealed the presence of particulate contamination of unknown origin, with an average size of 20 µm (**Figure II-6**). To identify the chemical composition of these particles, Energy Dispersive X-ray Spectroscopy (EDS) and X-ray Photoelectron Spectroscopy (XPS) analyses were conducted.

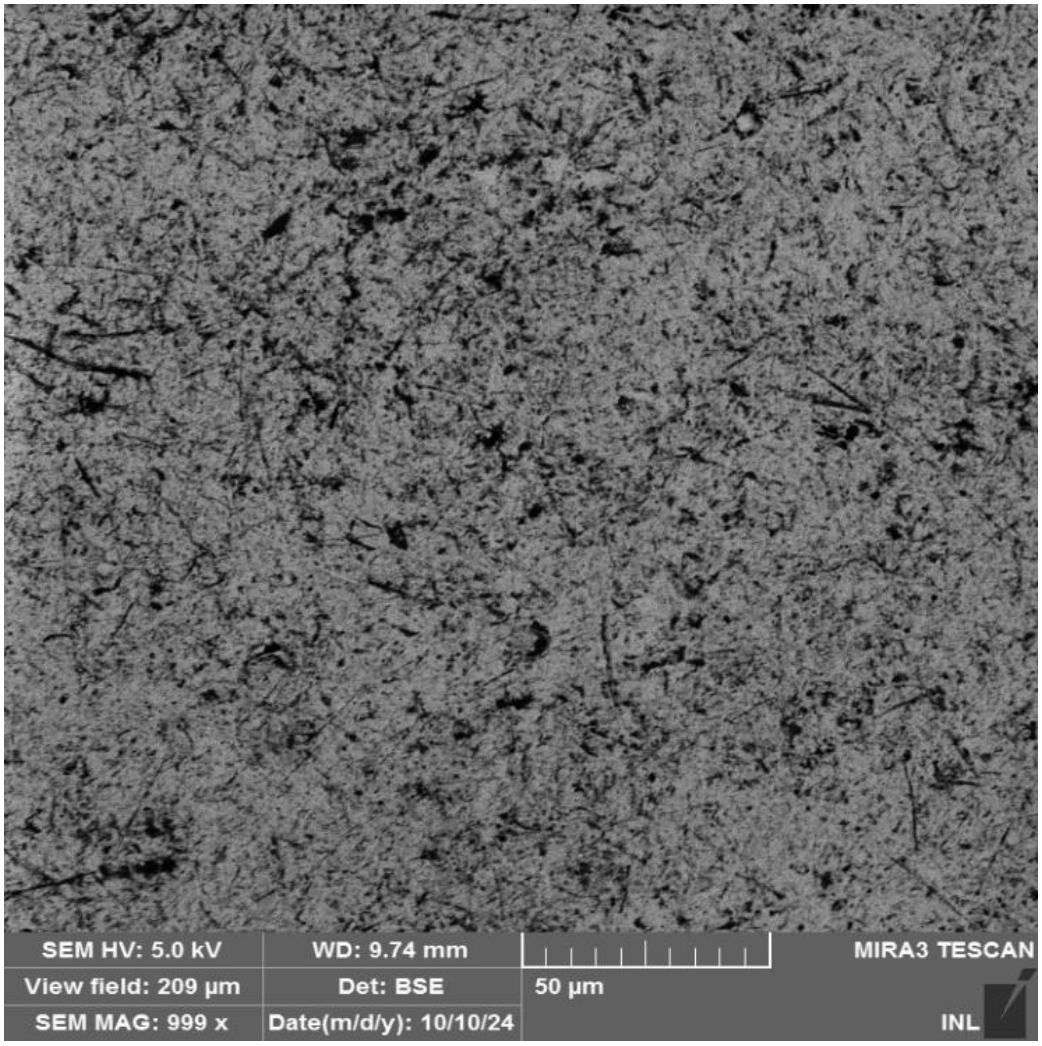

Figure II-6. SEM micrograph of the Zr-AR zirconia surface acquired at 1,000× magnification. Scale 50µm.

The backscattered electron mode observations, combined with EDS, confirmed the presence of aluminum oxide and silicon oxide, likely originating from the manufacturing process (**Figure II-7, Figure II-8)**

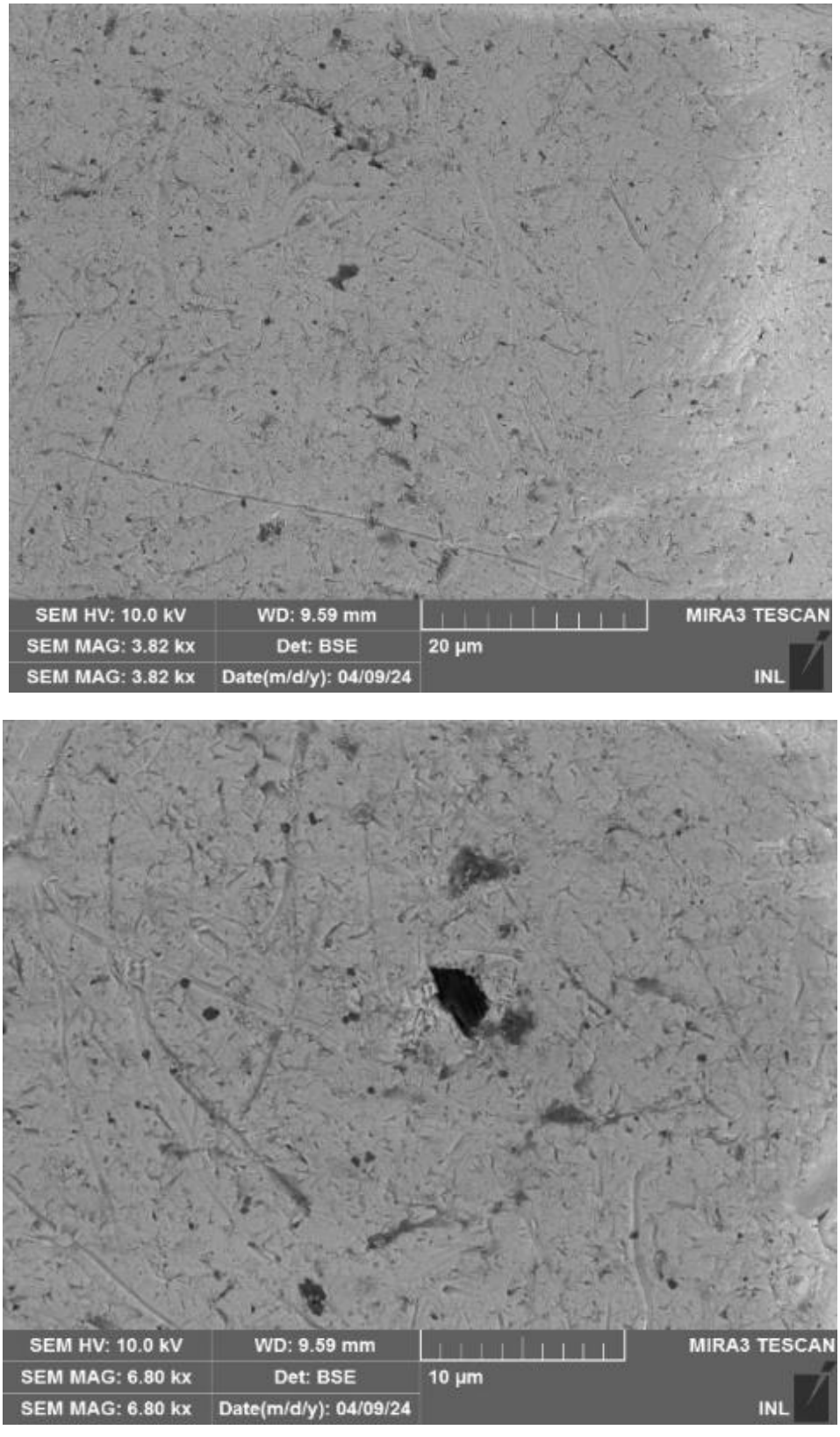

Figure II-7. SEM micrographs of the Zr-AR zirconia surface acquired in backscattered electron (BSE) mode at magnifications of 3,000× and 6,000×. Scale 20 and 10µm.

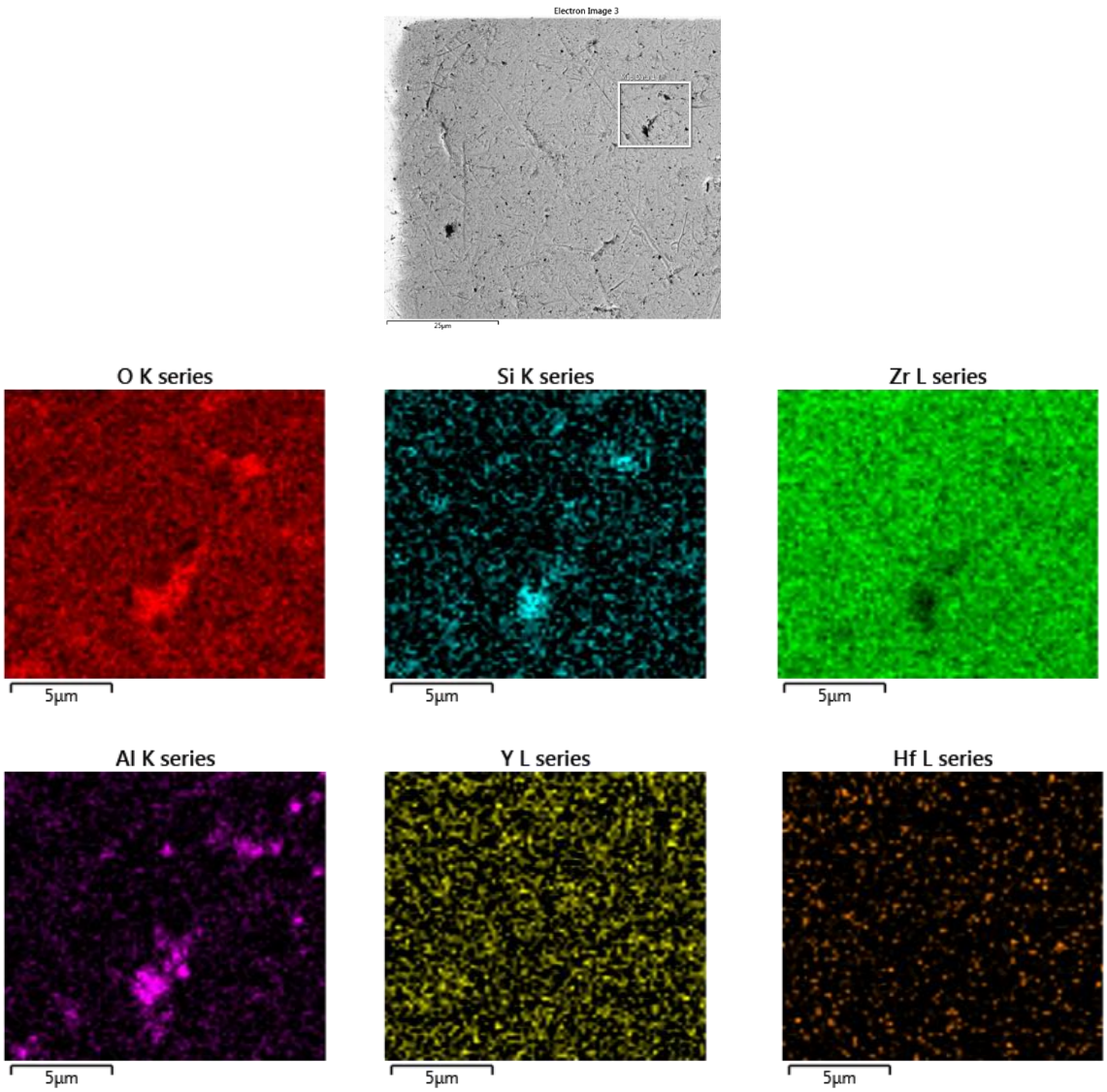

Figure II-8. EDS elemental analysis of surface contaminants on the Zr-AR zirconia sample, indicating their composition and distribution. Scale 5µm.

To assess the nature of the surface contamination on the as-received samples, the disks were cleaned using a sequence of solvents (acetone, IPA, ethanol, and DI water) and subsequently analyzed by XPS. The survey spectrum of the ZR-AR surface is shown in **Figure II-9**. Characteristic zirconia peaks were observed at 348 eV (Zr $3p_{1/2}$), 333 eV (Zr $3p_{3/2}$), 182.2 eV (Zr $3d_{5/2}$), and 184.6 eV (Zr $3d_{3/2}$), together with the O 1s peak at 532 eV and the Y 3d doublet at approximately 152 and 154 eV. A C 1s peak centered at 285 eV was also detected and is attributed to adventitious carbon from air exposure. The measured binding energies are consistent with literature values reported for 3Y-TZP zirconia [190].

In addition to the zirconia-related signals, peaks were detected at 154.0 eV, 118 eV, 102 eV, and 74 eV, corresponding to Si 2s, Al 2s, Si 2p, and Al 2p, respectively. The Si 2p peak at approximately 102 eV indicates silicon in an oxidized state (SiO_2 or SiO_x), while the Al 2p peak at 74 eV is characteristic of aluminum oxide. The concurrent presence of silicon- and aluminum-

containing oxides suggests residual contamination, likely originating from the manufacturing or processing environment [190–192].

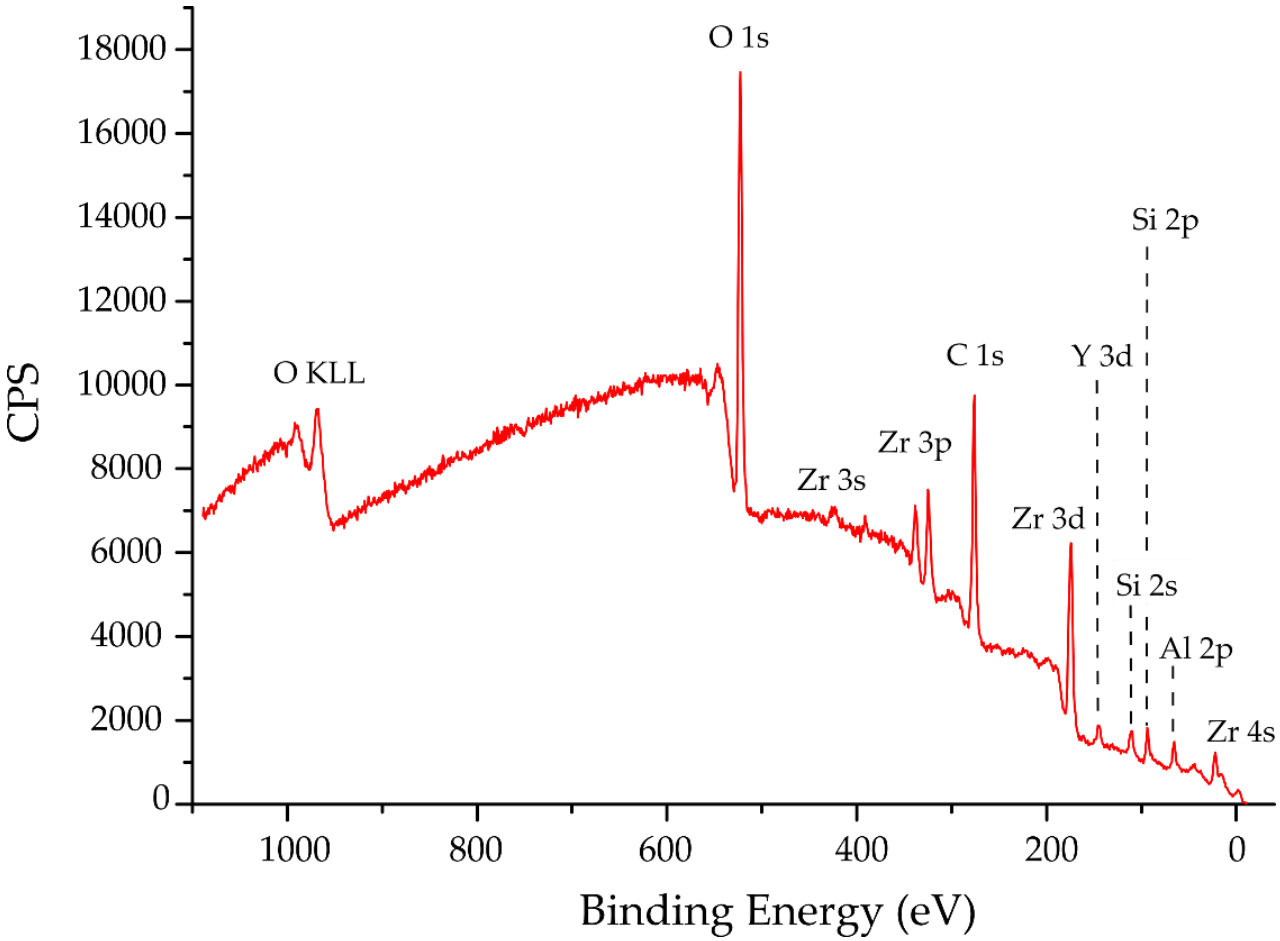

Figure II-9. XPS survey spectrum of an Zr-AR zirconia sample, showing the elemental composition at the surface. The unexpected presence of Al and Si peaks is highlighted here.

The atomic percentages of C 1s, O 1s, Zr 3d, Y 3d, Al 2p, and Si 2p are reported in **Table II-2**. The relatively low intensities of the Zr 3d and Y 3d signals indicate that the zirconia substrate is partially masked by surface contaminants. Although aluminum is intentionally added to the Y-TZP lattice to promote densification at lower sintering temperatures and improve resistance to low-temperature aging [193], its content should be minor (less than 0.5 wt.%). The detected Al 2p signal could thus be likely attributed to surface contamination.

Element	O 1s	C 1s	Zr 3d	Y 3d	Al 2p	Si 2p
At %	36.6	45.6	5	0.6	6.2	5.9

Table II-2. Atomic percentages of the untreated zirconia surface (ZR-AR) determined by X-ray photoelectron spectroscopy (XPS)

These contaminants significantly attenuate the X-ray signal and limit access to the underlying zirconia surface. More importantly, the presence of silicon- and aluminum-containing oxides is detrimental for subsequent surface functionalization. In particular, residual silicon species may interfere with organosilane grafting, leading to misleading surface analyses and inaccurate estimates of functionalization efficiency. Therefore, effective removal of these contaminants was considered as essential to ensure a clean, homogeneous oxide surface and reliable interpretation of surface modification results.

II.4.3. Conclusion

To ensure reproducible surface functionalization, the underlying topography and cleanliness of zirconia must be carefully controlled. Zirconia surfaces can be topographically modified through various treatments to enhance their suitability for functionalization. Reported methods include sandblasting, acid etching, polishing, and other mechanical or chemical approaches [194], which can alter surface roughness and morphology to influence subsequent chemical reactivity and cell interactions. Two approaches were selected to prepare the surfaces: hydrofluoric acid (HF) etching and mechanical polishing. HF etching creates controlled roughness and exposes reactive sites that can enhance chemical grafting, while polishing produces smooth, well-defined surfaces that facilitate surface characterization and reduce the influence of adventitious contaminants.

II.5. Surface Modifications for Contamination Removal

II.5.1. Hydrofluoric Acid (HF) Etching

Hydrofluoric acid (HF) as selected as a pre-functionalization cleaning step because of its ability to etch surface oxides on zirconia. By removing the outermost oxide layers, HF treatment indirectly eliminates weakly bound inorganic and organic surface contaminants, thereby exposing a cleaner and more reactive surface for subsequent silanisation. Mechanistically, the fluoride anion (F^-) acts as a nucleophile on metal–oxygen bonds (e.g., Zr–O) to form soluble metal-fluoride complexes (such as ZrF_6^{2-}), thereby selectively removing surface material and generating microscale/nanoscale irregularities and fresh hydroxylated sites. Because HF readily dissolves silica and glassy phases, it is widely used to etch glass-ceramics at relatively high etch rates (often tens to hundreds of nanometers per minute for silica-rich materials). In contrast, dense crystalline zirconia, which lacks a silica glass matrix, is much more resistant to HF attack, showing very slow etching and minimal surface change under similar conditions. Studies on zirconia

surfaces exposed to HF report that short exposures (e.g., tens of seconds) produce negligible roughening, and only prolonged etching (minutes) leads to measurable surface modification, consistent with the material's higher chemical stability compared to silica-based ceramics. In this context, "less aggressive" refers to the significantly lower material removal rate and limited surface dissolution of zirconia in HF relative to silica-rich glassy materials [195].

Studies on HF etching of 3Y-TZP zirconia show that, compared with silica or glass ceramics, zirconia is highly resistant to chemical attack. Aggressive treatments, such as 40 % HF for up to two hours, can increase surface roughness and induce some tetragonal-to-monoclinic (t → m) phase transformation, yet bulk flexural strength and low-temperature degradation remain largely unaffected [196]. In contrast, milder HF treatments, typically involving lower concentrations (5–10 %) and short exposure times (1–10 min at room temperature), result in minimal changes to surface topography while effectively removing surface contamination, including adventitious carbon [197]. More severe treatments combining higher HF concentrations with elevated temperature or auxiliary vibration have been shown to further increase nanoroughness and improve resin bonding, without compromising the structural integrity of the zirconia substrate [198]. Taken together, these studies demonstrate that HF etching of zirconia can be tuned over a wide range of conditions, from gentle surface cleaning to more pronounced topographical modification. Importantly, such controlled etching is particularly well suited for three-dimensional zirconia components, as it allows effective removal of surface contaminants without altering the overall geometry or inducing uncontrolled roughening of complex surfaces. Accordingly, in the present work, HF was employed primarily as a controlled chemical cleaning step to remove surface contaminants from dental zirconia disks, with the aim of exposing a clean, hydroxylated surface suitable for subsequent silanisation and functionalization while preserving the integrity of the substrate.

II.5.1.1. *Surface State Analysis*

The HF etching process was first evaluated for its ability to remove surface contaminants, particularly SiO_2 and Al_2O_3 particles. With the use of SEM, Al containing particles of 20µm size in average were observed and the Si contamination was visible through XPS analysis. HF etching was tested with HF concentration spanning from 2% to 10% with etching duration of 5 min to 60 min

XPS analysis showed that Si was eliminated under all tested conditions, including the mildest treatment of 2% HF for 5 min, whereas complete removal of Al, as indicated by the Al 2p peak, required more aggressive etching (60 min at 5% or 10% HF) (**Table II-3**). Corresponding water contact angle (WCA) measurements revealed that the most hydrophilic surfaces were obtained under these extended 5% or 10% HF treatments (**II.5.2.1**). Surface topography was subsequently examined by SEM to assess morphological changes induced by the etching (**II.5.2.2**).

HF concentration %	Al 2p %			
	5min	15min	30min	60min
2	8	8	5	8
5	8	7	9	**0**
10	8	9	9	**0**

Table II-3. XPS analysis: Atomic percentage of Al 2p as a function of HF etching parameters of ZR-HF samples

II.5.1.2. *Surface Wettability*

The WCA results are summarized in **Table II-4**. The values are the average of three different points on the sample.

HF concentration %	Mean WCA (°)			
	5min	15min	30min	60min
2	40	52	34	42
5	20	20	20	20
10	40	43	7	2

Table II-4. Summary of wettability measurements: Water contact angles (WCA in °) as a function of HF etching (Zr-HF sample) parameters

The analysis of water contact angle (WCA) data indicates that surface wettability was strongly influenced by both HF concentration and etching time. Treatment with 5 % HF resulted in hydrophilic surfaces (WCA ≈ 20°), consistent with effective surface cleaning and increased surface hydroxylation without pronounced surface alteration. In contrast, time-dependent wettability changes were observed for 2 % and 10 % HF, with extended etching at 10 % HF (30–60 min) yielding super-hydrophilic surfaces (WCA < 7°). As demonstrated by SEM analysis in the previous section (**II.5.1.1**), these aggressive etching conditions also lead to the development of a pronounced micro-scale surface morphology. The observed increase in wettability is therefore consistent with the combined effects of surface chemical modification and etching-induced morphological changes.

II.5.1.3. *Roughness Effect*

Figure II-10 compares SEM micrographs of zirconia surfaces etched under the mildest (2 % HF for 5 min) and the most aggressive (10 % HF for 60 min) conditions, acquired at the same magnification. While the surface treated under mild etching conditions shows only limited morphological changes (Sa = 0.1±0.03 µm) compared to the Zr-AR (Sa= 0.05±0.03 µm), the sample

exposed to the most aggressive treatment exhibits a clearly developed micro-topography, indicating a significant modification of the surface morphology (Sa = 0.3±0.16µm).

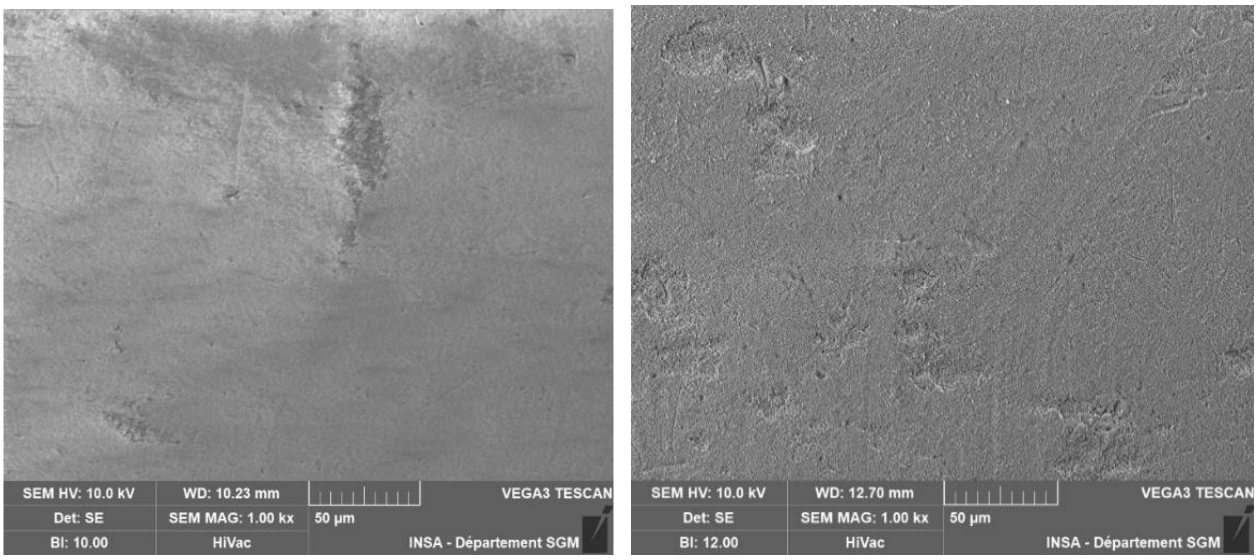

Figure II-10. SEM images of zirconia surfaces (ZR-HF) after HF etching: left, 2% HF for 5 min; right, 10% HF for 60 min, illustrating the effect of etching severity on surface morphology. Scale 50µm.

Surface roughness values obtained after HF etching are summarized in **Table II-5**. The control samples exhibited a low mean roughness (Sa = 0.05 ± 0.03 µm), while all HF-treated samples showed an increase in surface roughness, with Sa values ranging from approximately 0.10 to 0.37 µm depending on etching conditions. For each HF concentration, roughness generally increased with etching time, although no monotonic or reproducible trend could be established.

HF%	Time (min)	Mean Sa (µm)	SD (µm)
control	-	0,05	0,03
2	5	0,1	0,03
2	15	0,26	0,09
2	30	0,37	0,07
2	60	0,2	0,04
5	5	0,1	0,06
5	15	0,3	0,07
5	30	0,2	0,03
5	60	0,3	0,02
10	5	0,2	0,12

10	15	0,18	0,08
10	30	0,1	0,04
10	60	0,3	0,16

Table II-5. Mean surface roughness (Sa) and standard deviation (SD) of zirconia samples before and after HF etching under different concentrations and etching times, measured by optical interferometry (three measurements per sample).

II.5.2. Mechanical Polishing

Polishing Zr-AR disks was performed following the protocol described in the Materials and Methods chapter (**II.3.2**.). Large-grit SiC paper was initially used, as the samples were not completely flat, before progressing to finer grits to diamond suspensions to achieve the desired surface finish.

II.5.2.1. *Surface State Analysis*

On the polished disks (ZR-P), SEM/EDS analysis was performed to assess the presence of aluminum-containing features.

In the backscattered electron mode, the observations revealed isolated particles, which can be attributed to Al_2O_3. In backscattered electron (BSE) mode, image contrast arises from differences in atomic number (Z), with heavier elements appearing brighter and lighter elements appearing darker. This compositional contrast enables the distinction between phases within the material. In this context, the observed isolated particles can be attributed to Al_2O_3, as its average atomic number differs from that of the surrounding zirconia matrix, making these inclusions visible in BSE imaging.

This is consistent with the composition of biomedical-grade 3Y-TZP zirconia, which typically contains small amounts of alumina (≈0.2–0.5 wt.%) added to improve sintering behavior and enhance resistance to low-temperature degradation, as mentioned in **II.4.1** [29]. As the alumina content exceeds its solubility limit in zirconia, it is commonly present as discrete alumina grains dispersed within the zirconia matrix.

At higher magnification, particles in the range of 0.5–1 μm were observed embedded within the zirconia microstructure, supporting this interpretation. In addition, zirconia grains became clearly distinguishable (

Figure II-11), as extensive polishing removes the superficial surface layer and exposes the underlying crystalline microstructure. Contrast between grains arises from differences in crystallographic orientation and slight relief at grain boundaries, enabling grain visualization under SEM.

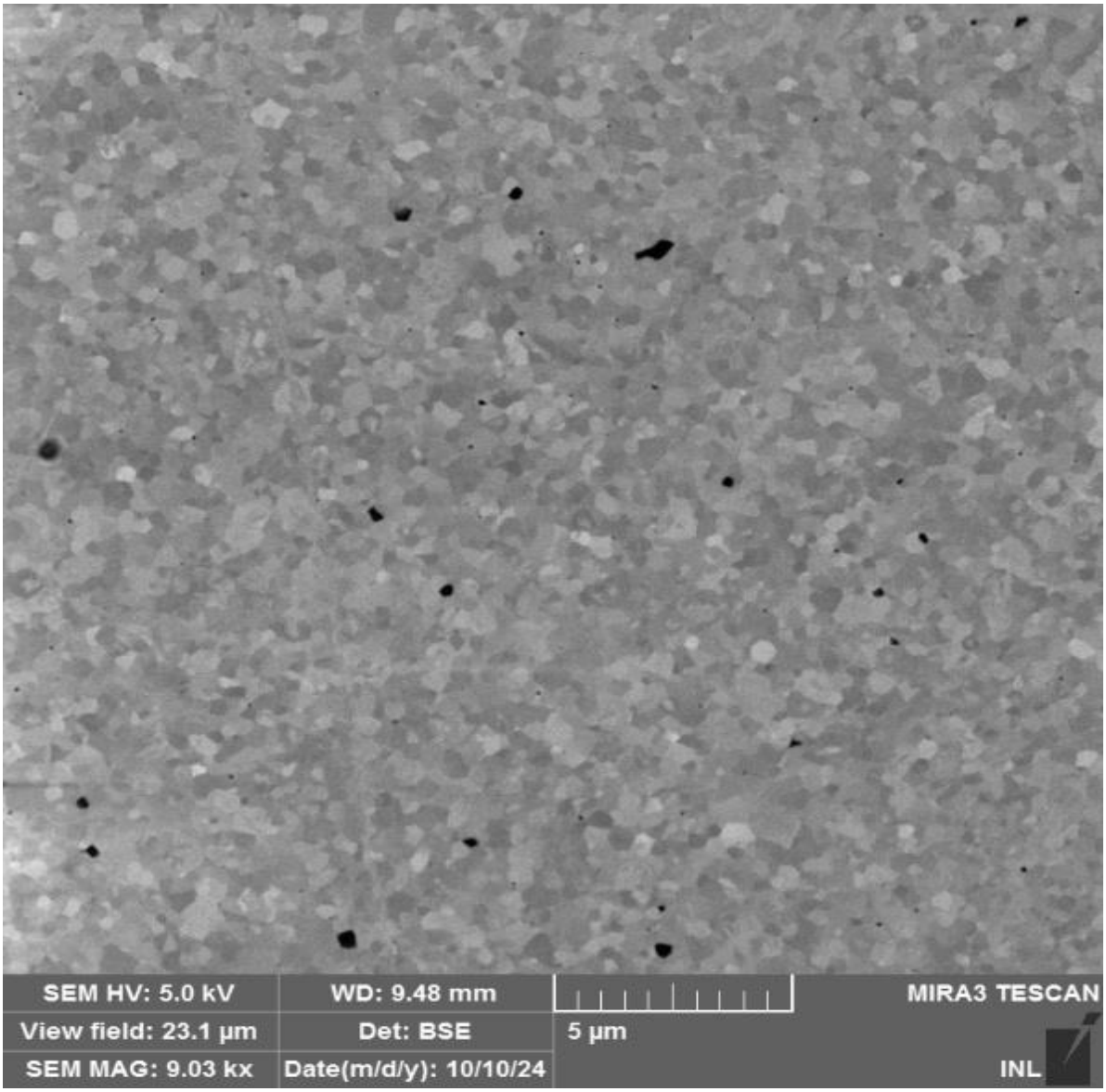

Figure II-11. High-magnification SEM image of the Zr-P zirconia surface in BSE mode, showing individual zirconia grains and embedded alumina particles within the zirconia matrix. Scale 5µm.

On the same scale, the EDS analysis confirmed the presence of aluminum or aluminum oxide particles on the surface, which are believed to originate from the bulk material, as discussed before (**Figure II-12**). The presence of Al in the lattice is consistent with medical grade zirconia.

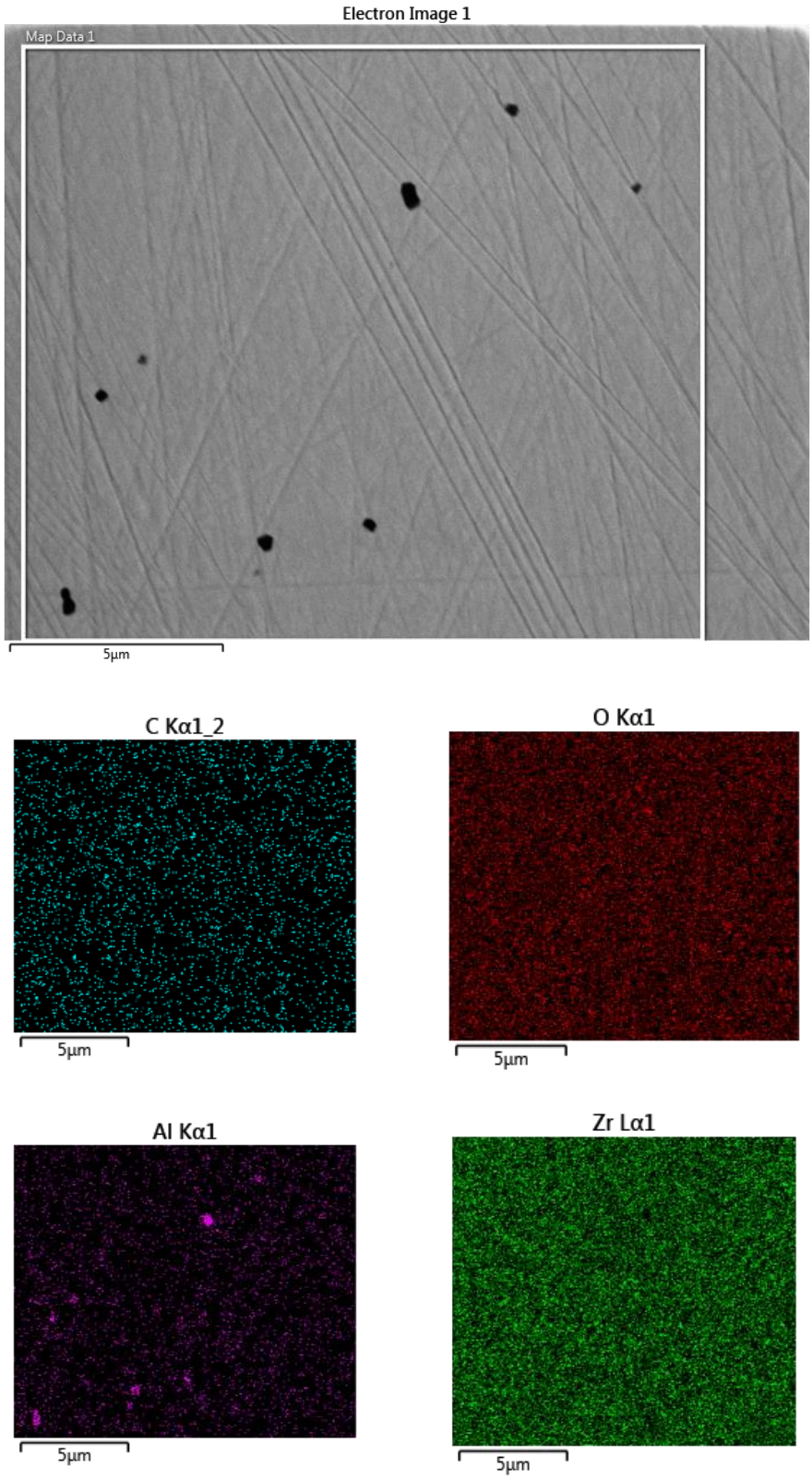

Figure II-12. EDS elemental analysis of a ZR-P disk, highlighting the presence of aluminum-containing particles. Scale 5µm.

XPS analysis of the ZR-P samples confirmed a clean and reproducible ZrO_2 surface, with no detectable Al or Si contamination (**Figure II-13** and **Table II-6**).

Element	O 1s	C 1s	Zr 3d	Y 3d	Al 2p	Si 2p
At %	50	29	20	1	-	-

Table II-6. The atomic percentages of an ZR-AR sample, analyzed by XPS.

Although the Al containing particles are detectable and visible with the microscopy techniques, after polishing the surface, it was never present in an XPS analysis of the ZR-P samples. The hypothesis for that, is that since they are embedded in the crystallographic structure of the substrate they are probably not detectable on the first 10 nm of the surface, which is the analysis depth of an XPS analysis or more simply, that the concentration of Al containing particles is below the detection threshold. The subsequent section discusses methodologies for the removal of residual organic contamination.

In **Figure II-13**, the surface of the ZR-P samples, as analyzed by XPS, reveals the presence of Zr 3s (~531 eV), Zr 3p (~333–353 eV), Zr 3d (~182–185 eV), Y 3d (~157–160 eV), O KLL (~980 eV), and O 1s (~530 eV) peaks, which are primarily associated with the zirconia substrate. A C 1s signal (~285 eV), attributed to unavoidable adventitious carbon contamination, is also observed. The absence of Si 2p (~101–103 eV) and Al 2p (~74 eV) peaks confirms the successful preparation of a clean, contamination-free zirconia surface suitable for subsequent functionalization.

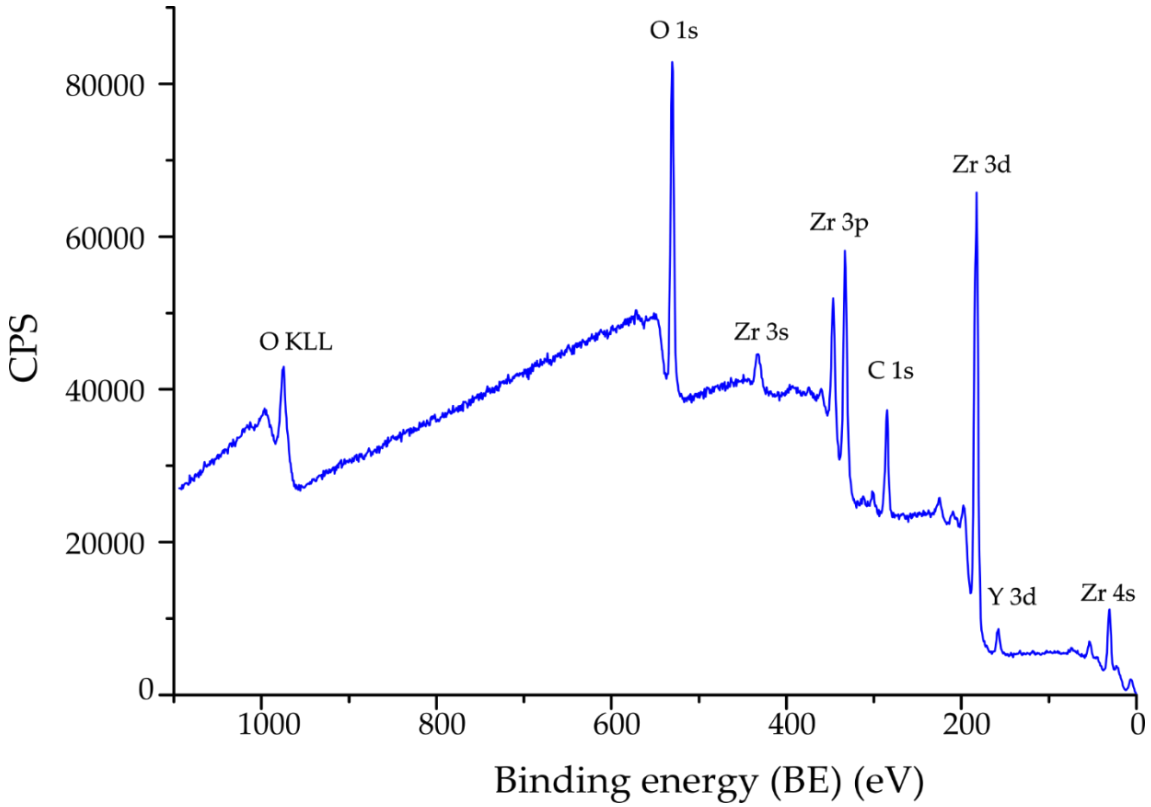

Figure II-13. X-ray photoelectron spectroscopy (XPS) survey spectrum of the ZR-P sample

II.5.2.2. *Roughness Effect*

AFM analysis of the ZR-AR disks revealed an average surface roughness Sa of approximately 0.2 µm, together with pronounced injection-molding lines and surface contamination features reaching heights of up to ~1 µm. Following manual polishing, a marked reduction in surface roughness was observed. As shown in **Figure II-14**, the ZR-P surfaces exhibit a significantly smoother topography, with an average roughness reduced to approximately 10 nm. Residual isolated alumina particles remain visible at the surface, consistent with the bulk composition of biomedical-grade 3Y-TZP zirconia. Owing to the manual nature of the polishing process and the initial non-planarity of the injection-molded disks, slight variations in polishing conditions were required between samples; nevertheless, the overall polishing treatment resulted in a substantial and reproducible decrease in surface roughness.

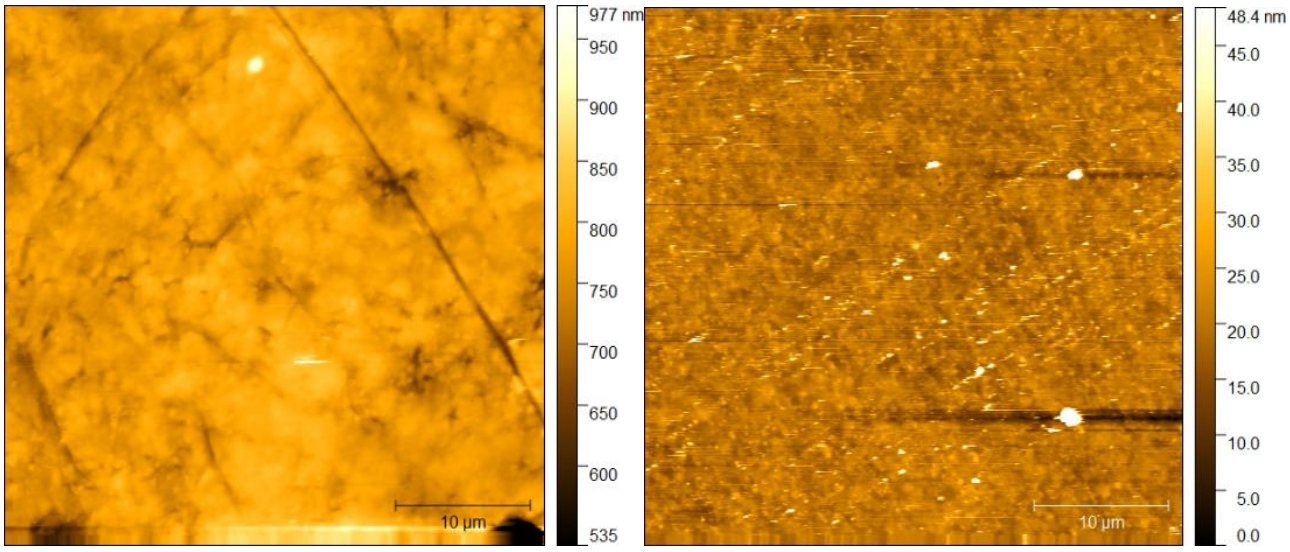

Figure II-14. AFM measurements before (left) and after (right) polishing. (note the 20 times smaller z-scale (color scale) after polishing)

II.6. Organic Contamination Removal and Surface Activation

Several surface-cleaning and activation methods were evaluated to assess their efficiency in removing organic surface contamination, as summarized in **Table II-7**. The effectiveness of these treatments was assessed by water contact angle (WCA) measurements, used here as an indirect indicator of surface cleanliness. Contact angles were measured both before and after each cleaning procedure, with at least three measurements performed at different locations on each disk, and averaged values are reported. For comparison, ZR-AR zirconia disks cleaned only with

organic solvents exhibited an average contact angle of approximately 72°. The study was performed on ZR-P disks.

Cleaning procedures that resulted in super hydrophilic surfaces (WCA ≤ 10°) were considered effective in removing organic contaminants. Among the tested methods, UV/O_3 treatment for 30 min was selected for subsequent experiments due to its effectiveness, simplicity, and compatibility with routine sample processing. Ultraviolet/ozone (UV/O_3) treatment is widely used for the removal of organic contaminants from material surfaces via photo-oxidation, producing clean surfaces under ambient conditions without the use of wet chemicals [199]. UV/O_3 exposure has also been shown to increase surface wettability while causing minimal alteration of surface topography and crystalline structure when compared to plasma treatments [200].

Method	**Contact Angle After (°)**
UV/O_3	10
NaOH	23
NaOH + UV/O_3	5
Piranha solution (H_2SO_4/H_2O_2, 3:1 v/v)	10
Piranha solution + UV/O_3	3
SC1	6
SC1 + UV/O_3	3

Table II-7 . Summary of the cleaning methods evaluated and their corresponding water contact angle values, reflecting the surface energy of the ZR-P samples after treatment.

In this work, the efficiency of surface activation was primarily evaluated through WCA measurements. Changes in surface roughness or crystallinity induced by the cleaning treatments were not directly quantified.

XPS analysis was performed on ZR-AR samples treated with NaOH + UV/O_3 and Piranha solution + UV/O_3. The survey spectra revealed no significant differences in surface chemical composition between the two treatments, and no variations were observed in the O 1s peak (**Figure II-15**).

Although surface activation could not be directly quantified with the available techniques, its effectiveness is supported by the successful and reproducible functionalization of the treated zirconia surfaces, as discussed in the following chapter. Consequently, while surface activation was achieved, further optimization of the activation procedure was not pursued, as the selected UV/O_3 treatment fulfilled the requirements for subsequent surface functionalization.

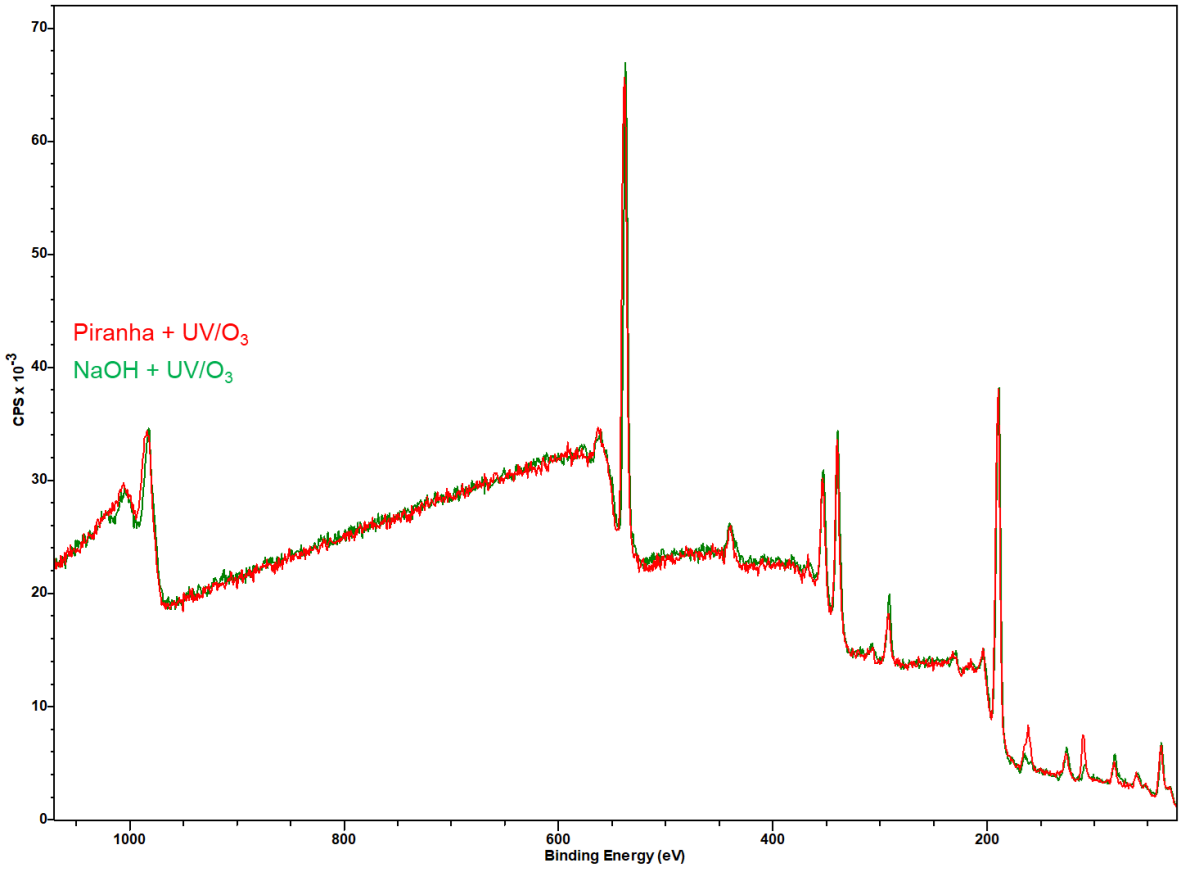

Figure II-15 XPS survey spectra, stacked, of ZR-AR samples treated with NaOH + UV/O_3 (green) and Piranha solution + UV/O_3 (red)

II.7. Conclusion

The importance of surface preparation for further functionalization has been highlighted in this chapter. To our knowledge, the pre-treatment of 3-YTP dental zirconia aimed at preparing a clean and active surface for the immobilization of organic layers has not been extensively evaluated and is often overlooked. After characterizing the as-received surface of the samples, Si- and Al-containing contamination was detected. For this reason, physicochemical cleaning methods were examined.

To achieve a homogeneous and clean surface prior to functionalization, two surface pre-treatment techniques were evaluated: mechanical polishing and acid etching. In addition, an activation method that was both practical and efficient was selected to promote the formation of surface hydroxyl groups.

The effect of mechanical polishing on the surface composition was also evaluated. Using the selected polishing protocol, the contamination detected on the as-received samples was effectively eliminated. XPS analysis confirmed the absence of both Si- and Al-containing surface

contaminants. However, observations at a larger scale using microscopy still indicated the presence of Al within the material, which is consistent with medical-grade zirconia where a subtle amount of alumina is incorporated into the bulk as a stabilizing phase.

The effect of HF etching on the zirconia surface was also therefore investigated. In addition to the increase in mean roughness, substantial variability was observed, particularly for higher HF concentrations and longer etching times, as reflected by the elevated standard deviations. This dispersion indicates significant surface inhomogeneity and suggests that the etching process is highly sensitive to local variations in the zirconia surface. Overall, despite its effectiveness in removing surface contaminants, HF etching does not provide reliable control over surface roughness for the initial surface state investigated. Consequently, polishing was selected as an alternative surface preparation method, as discussed in the following section.

Both approaches, polishing and HF 10% for 1 h etching, were effective in producing contamination-free surfaces. However, polishing was selected for the optimization of the grafting protocol of the first layer, as it yields a sufficiently smooth surface to enable reliable contact angle measurements, which cannot be performed on rougher surfaces. With a reproducible and clean surface thus established, the following chapter focuses on the silanization of the zirconia disks.

Based on these results, the 3-YTP disks provided by our partner were, in most cases, manually polished to an approximate roughness of 10 nm and further cleaned using a series of solvents followed by 30 min of UV/O_3 treatment prior to functionalization.

Although polishing was selected for the flat disks used in this work, this approach might be more challenging to apply to complex geometries. For 3D samples such as fixtures or abutments, acid etching could serve as an alternative cleaning method. When applied at low concentrations and for short durations, it effectively removes surface contaminants without altering the topography, thereby preserving a reproducible and desired roughness. However, if more intensive cleaning of the zirconia surface is required, etching with higher concentrations and longer exposure times can be employed, although this may compromise the surface roughness.

III. Silanization of Yttria Doped Zirconia

III.1. Abstract

This chapter focuses on developing and applying a reliable silanization method for zirconia surfaces. First, the silanization reaction is optimized using an amine group bearing trifunctional silane, with systematic evaluation of how concentration, immersion time, and curing duration affect layer formation, while minimizing unwanted polymerization. The optimized conditions are then applied to another trifunctional silane to form an activated ester–bearing platform suitable for subsequent peptide grafting. Comprehensive characterization of the resulting silane layers is carried out using water contact angle measurements (WCA), ToF-SIMS, XPS, FTIR and the Amine Density Estimation Colorimetric Assay (ADECA) colorimetric assay to assess surface chemistry, layer integrity, and functional group availability. Together, these experimental studies establish a reproducible silanization protocol tailored for zirconia functionalization.

III.2. Introduction

The immobilization of biomolecules onto material surfaces often requires the use of crosslinking agents to ensure a stable and specific attachment. Inorganic materials such as zirconia generally lack surface functional groups that can react directly with biomolecules, which typically present amino, carboxyl, or thiol functionalities. In the absence of a suitable interfacial coupling layer, the immobilization process relies predominantly on weak physical interactions such as van der Waals forces, electrostatic attraction, or hydrogen bonding. These non-covalent interactions are generally insufficient to withstand mechanical stress or long-term exposure to aqueous and biological environments, leading to detachment, loss of bioactivity, and poor reproducibility of functionalized surfaces. Crosslinkers address this limitation by introducing molecular bridges bearing complementary reactive groups that can form covalent bonds with both the substrate and the biomolecule. When suitable coupling chemistries are used, covalent attachment can enhance interfacial stability and reduce biomolecular denaturation, while offering the possibility of improved control over orientation and grafting density [201–204]. In contrast to simple adsorption, covalent immobilization also minimizes the uncontrolled release of biomolecules, which is particularly important for biomedical devices where the detachment and diffusion of bioactive

compounds into surrounding tissues could lead to reduced performance or unintended biological responses.

Among the various crosslinking strategies, silanization has emerged as one of the most effective and versatile methods for engineering hybrid organic–oxide interfaces. Organosilanes are bifunctional molecules with a hydrolyzable alkoxysilane group (–$Si(OR)_3$) or, in the case of chlorosilanes, a more reactive –$SiCl_x$ group, together with an organofunctional tail (e.g., –NH_2, –SH, –epoxy, or –COOH). Upon hydrolysis, both alkoxysilanes and chlorosilanes generate silanols, which can then undergo condensation with surface hydroxyl groups or self-condense to form siloxane (Si–O–Si) bonds. The silanization reaction is further discussed in Chapter 1. This process results in the formation of a covalently bonded silane layer on the oxide surface, forming a stable and tunable interface. The organic tail of the silane provides a reactive handle for further functionalization with biomolecules, peptides, or polymers through well-established coupling chemistries such as carbodiimide (EDC/NHS), glutaraldehyde, or click-type reactions [56,67,205–208].

A major advantage of silanization lies in its chemical tunability and process flexibility**.** The structure of the silane (chain length, number of reactive sites, and terminal functionality), the reaction environment (solvent, pH, humidity), and post-treatment conditions (curing time, temperature) can be adjusted to control the surface coverage, molecular organization, and accessibility of functional groups (

Figure III-1). This enables the formation of well-defined and reproducible surfaces tailored for specific biological interactions. Furthermore, the silane network contributes to the long-term chemical stability of the interface by preventing hydrolytic degradation and maintaining the covalent linkage between the substrate and the biomolecule [209–211].

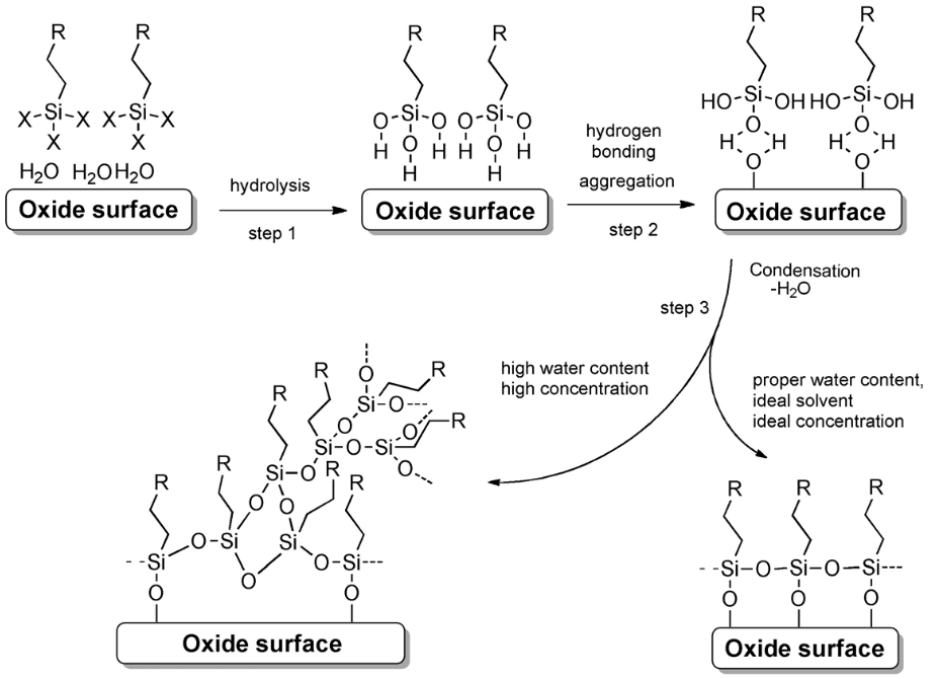

Figure III-1. Schematic representation of silanization of oxide surfaces. Reproduced from Pujari *et al.* (2014) [204]

In this chapter, we discuss the optimization of a silanization reaction using 3-aminopropyltriethoxysilane (APTES) on zirconia substrates. The -NH_2 end group of the APTES allowed the estimation of the amine density on the surface of the disks, through ADECA colorimetric assay (III.3.5.3.). optimized protocol was then applied to graft the selected pentafluorophenyl-terminated silane (PFPTES), both on disks and on zirconia powder, in preparation for subsequent peptide conjugation (**Figure III-2**). To confirm the successful surface modification, complementary characterization techniques were employed, providing both qualitative and semi-quantitative insights into the grafting efficiency.

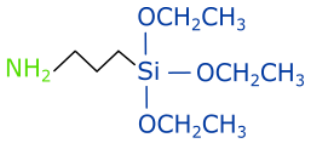

APTES

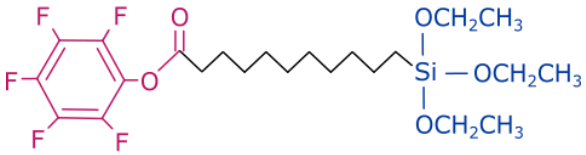

PFPTES

Figure III-2. Molecular structures of 3-aminopropyltriethoxysilane (APTES) and 11-pentafluorophenylundecanoatetriethoxysilane (PFPTES)

A key advantage of the PFP ester over the more commonly used N-hydroxysuccinimide (NHS) ester (**Figure III-3**) lies in its higher resistance to hydrolysis in aqueous or humid environments. NHS esters hydrolyze rapidly, with half-lives ranging from a few minutes at pH 8.6 to a few hours at pH 7, limiting their applicability for surface reactions [212]. In contrast, pentafluorophenyl (PFP) esters (**Figure III-3**) exhibit significantly enhanced hydrolytic stability, attributed to the strong electron-withdrawing effect of the fluorine atoms that stabilize the ester and make the leaving group less prone to nucleophilic attack [213,214]. As a result, PFP esters display improved shelf life and stability in humid or aqueous environments, allowing more controlled and reproducible bioconjugation reactions on the surface and that this enhanced robustness ensures that PFP-terminated silanes remain reactive and stable during functionalization, making them particularly suitable for subsequent peptide coupling under mild, aqueous conditions.

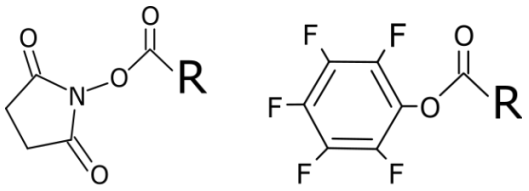

NHS PFP

Figure III-3. Molecular structures of N-Hydroxysuccinimide (NHS) and Pentafluorophenyl (PFP) esters.

III.3. Materials and Methods

III.3.1. Materials and Reagents

Commercially available 3Y-TZP zirconia (ZrO_2) substrates were used throughout this study in different physical forms in order to accommodate the requirements of surface-sensitive characterization techniques and biological assays. Bulk zirconia disks, zirconia powder, and zirconia thin films were employed depending on the experimental objective, as detailed below.

Bulk 3Y-TZP disks (Ø 9 mm, thickness 2 mm, provided by Anthogyr, Sallanches, France) and bulk 3Y-TZP disks (Ø 0.5 mm, thickness 2 mm, provided by DOCERAM, Dortmund, Germany) were supplied with a machined surface finish corresponding to a mean roughness of approximately 0.2 μm. Zirconia powder (3 mol% yttria-stabilized ZrO_2, TZ-3Y-E; Tosoh Corporation, Japan) was used for infrared spectroscopy measurements due to its high specific surface area, allowing enhanced sensitivity to surface-bound species.

Ethanol 99.8%, Ethanol dried (max 0.01% H_2O), Tetrahydrofurane 99% (THF), Acetone 99.5%, 2-Propanol 99.5%, Dichloromethane 99.8%, Methanol 99.9%, Acetic Acid (glacial) 100%, Sodium Hydroxide pellets, (3-Aminopropyl)triethoxysilane (APTES) 99% and Brilliant Blue G (≥80% purity) powder, were purchased from Sigma-Aldrich. 11-Pentafluorophenylundecanoatetriethoxysilane (PFPTES), was purchased from SIKEMIA. Dionised water (resistivity ≥ 18.2 MΩ) was produced using an Elga water production system from Veolia. This deionized water (DI Water) was used for the preparation of all solutions and for rinsing the samples throughout the experimental procedure.

Dichloromethane (DCM) was dried prior to use to eliminate residual moisture that could interfere with silanization reactions. To this aim, the solvent was stored over activated 4 Å molecular sieves for 48 hours under ambient conditions. The molecular sieves were activated by heating at 250 °C for a minimum of 12 hours to remove adsorbed water and allow to return to room temperature under reduced pressure.

III.3.2. Surface Preparation

The zirconia disks were manually polished using SiC abrasive papers with successive grit sizes (P180, P360, P600, and P1800) to progressively remove material. This was followed by polishing with diamond suspensions of decreasing particle size (6 μm, 3 μm, and 1 μm), and finally by a suspension of SiO_2 particles (0.03 μm) to achieve a smooth surface finish. The polishing sequence was performed from the coarsest to the finest grit. The achieved arithmetic roughness was measured around 10 nm.

The samples after polishing were cleaned with a series of solvents, for 10 min each, under sonication: acetone, 2-propanol, ethanol, Milli-Q H_2O and dried under N_2 stream.

The 3Y-TZP powder was first activated by UV/O_3 treatment for 30 min, then subjected to the procedure described in III.3.4. Since the substrate was in powder form, after immersion in the PFPTES solution, it was collected by vacuum filtration using a 47 mm Durapore PVDF membrane (0.45 μm) placed in a glass filter on top of a vacuum-equipped Erlenmeyer flask. The powder was washed three times with dry DCM and then dried in an oven at 110 °C for 5 minutes.

Samples were prepared as self-supporting pellets by weighing 20 mg of powder, which was pressed into circular pellets of 0.7 cm diameter. The mass was checked before and after pressing to ensure no loss. This corresponds to a surface loading of approximately 52 mg cm^{-2}, suitable for IR analysis.

The UV–ozone cleaning was performed using a Novascan UV–Ozone Cleaner (PSD/PSDP series) operating under ambient conditions with a supplemental oxygen flow. The UV lamp operated at an irradiance of 28–32 mW/cm^2 at 254 nm, and the samples were treated for 30 min.

III.3.3. Experimental Design

The purpose of this study was to determine how key reaction parameters influence the formation of the silane layer on zirconia surfaces, in order to define reproducible and efficient conditions for functionalization.

The factors investigated included the APTES concentration (0.5, 1, 2, and 5 mM), immersion time (1, 2, 4, and 8h), and curing time (1, 2, 16, and 24 h). In designing this study, particular attention was given to practicality, reaction time, and the potential scalability of the process for industrial applications. Therefore, shorter reaction times and lower silane concentrations were prioritized as desirable conditions. A factorial design was employed to systematically evaluate the combined effects of these parameters on surface amine density and change of wettability of the surface. Each condition was performed in triplicate to assess reproducibility. The experimental workflow is summarized in **Figure III-4**.

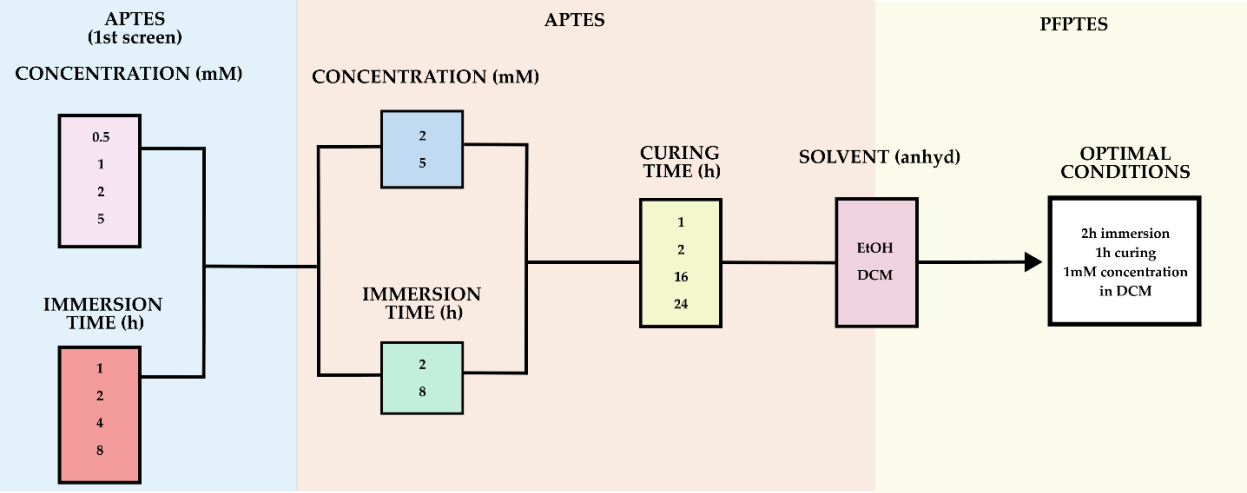

Figure III-4. Schematic representation of the parameter screening strategy used to optimize organosilane grafting onto zirconia surfaces. For APTES, the influence of silane concentration (0.5, 1, 2 and 5 mM), immersion time (1, 2, 4 and 8 h), curing time (1, 2, 16, and 24 h), and solvent (anhydrous ethanol or dichloromethane, DCM) was systematically investigated. Based on this parametric study, optimal conditions were identified for PFPTES functionalization, corresponding to a 2 h immersion in a 1 mM solution prepared in anhydrous DCM, followed by 1 h curing. The scheme summarizes the stepwise selection of parameters leading to the final optimized protocol.

III.3.4. Optimized Reaction Protocol

Functionalization was performed by immersing the activated substrates (III.3.2) in a freshly prepared 1 mM trifunctional silane solution in anhydrous dichloromethane (DCM) for 2 h at room temperature. The silane solution was prepared immediately before use by adding the silane to dried DCM, which had been stored over 4Å molecular sieves for at least 24 h. Following immersion, substrates were removed from the solution, and subjected directly, without rincing, to annealing at 110°C for 1 h to promote siloxane condensation and film stabilization. After annealing, samples were rinsed three times, in room temperature, with freshly dried DCM to remove physisorbed or polymerized species and then dried under nitrogen. Functionalized substrates were stored in dry conditions to avoid the hydrolysis of the activated ester, until characterization or further use.

III.3.5. Characterization Methods

III.3.5.1. *Water Contact Angle (WCA)*

For theoretical insight, see **II.3.3.1**.

WCA measurements were performed with GBX-Digidrop MCAT goniometer (France) at room temperature. Contact angles θ were measured from sessile deionized water drops of 0.8 µL

using the Visiodrop software and at least three droplets were placed on different areas of each sample to account for heterogeneity, with the average value reported.

III.3.5.2. *X-ray Photoelectron Spectroscopy (XPS)*

For theoretical insight, see **II.3.3.2**.

XPS measurements and analyses were performed using a ULVAC PHI Versaprobe III photoelectron spectrometer, equipped with a standard AlKa monochromated source (hν = 1486.6 eV), operated at a 50 W electron beam power (with a circular spot size of 200 µm of diameter). The emission of photoelectrons from the sample was analyzed at a takeoff angle of 45° under ultra-high vacuum conditions of around 10^{-9} mbar. Spectra were carried out with 224 eV pass energy for the survey scan and 27 eV pass energy for elementary high-resolution regions. The spectra were fitted using CasaXPS software version 2.3.25. The C–C bond contribution of C1s peak at 285 eV was used as a binding energy reference. The background was subtracted using the Shirley method. Quantification was performed using the sensitivity factors provided by the manufacturer considering the cross section of each element, the escaping depth of electrons and the spectrometer transmission as well as angular distribution correction. Peak shape was Gaussian/Lorentzian (70/30).

III.3.5.3. *Amine Density Estimation Colorimetric Assay (ADECA)*

Surface amine groups introduced during silanization were quantified using ADECA. The ADECA method is based on the electrostatic interaction between the positively charged ammonium on the surface and the negatively charged Coomassie Brilliant Blue (CBB). The amine groups are first turned into an ammonium salt by immersion in an acid solution. Next, after contact with the CBB solution, the CBB excess is removed with a first washing step prior immersion of the surfaces is a basic solution. Under this second washing step, the electrostatically bonded CBB molecules are released. The CBB are then titrated using Beer-Lambert Law [215] (**Figure III-5**).

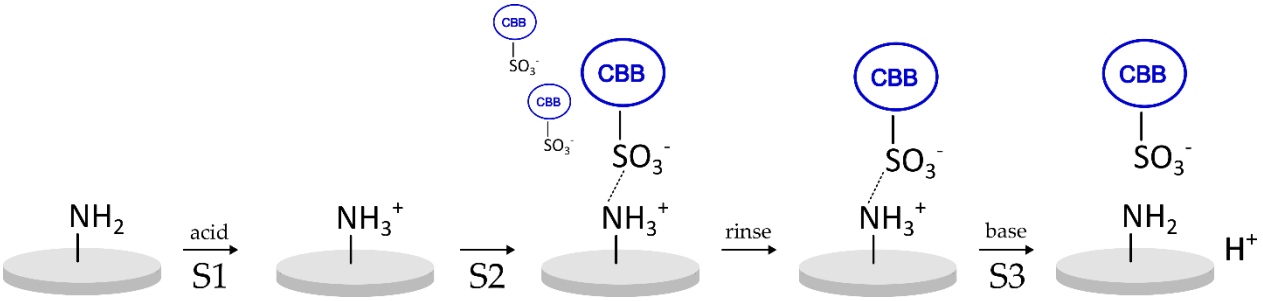

Figure III-5. Schematic representation of the ADECA colorimetric assay. S1: Reaction between surface-bound amine groups and the activated dye; S2: Washing step to remove unreacted dye; S3: Dye release in acidic conditions for colorimetric quantification. The dotted line indicates an electrostatic interaction rather than a covalent bond. This figure summarizes the full workflow of the assay, from dye coupling to final absorbance measurement.

Three solutions were prepared: S1, containing 100 mL of methanol, 50 mL of acetic acid, and 850 mL of deionized water for protonation and washing; S2, the staining solution, prepared by dissolving 125 mg CBB in 12.5 mL of acetic acid and 25 mL of methanol, then diluted with deionized water to a final volume of 500 mL; and S3, the desorption solution, consisting of 50 mL of 0.5 M carbonate buffer (pH=11.5) and 50 mL of methanol.

Aminated zirconia samples were first immersed in S1 for 10 minto protonate surface amines, then transferred to S2 for 30 minutes, with agitation, protected from light, to allow binding of CBB to the protonated amines. After staining, the samples were washed three times in S1 (10 min each) and once in deionized water (10 minutes) under stirring, then dried under a stream of nitrogen. Bound dye was subsequently released by immersion in 250µL of S3 for 5 min under stirring. Before measuring, 5 µL of 3 N HCl were added to the cuvette to acidify the solution and convert the released Coomassie dye back into its cationic form, as required in the ADECA protocol to ensure a stable and reproducible absorbance peak at 620 nm. Using the Beer–Lambert law, a quantitative estimate of surface amine density was provided.

Control samples consisting of bare, non-aminated zirconia were processed using the exact same protocol to account for any non-specific adsorption of CBB, and their absorbance values were subtracted from those of the functionalized samples.

The measured absorbance was transformed into molecular surface density according to the following equation (**Equation III-1**):

$$(A_{funct} - A_{control}) \cdot \frac{V}{\varepsilon \cdot l \cdot A_s} = \text{number of } NH_2/cm^2$$

Equation III-1 Determination of surface amine density by the ADECA colorimetric assay.

where:

- A_{funct} and $A_{control}$ are the absorbances of the functionalized and control samples, respectively,
- V is the reaction solution volume,
- ε is the molar extinction coefficient,
- l is the optical path length, and
- A_s is the surface area of the disk

In this work, the following values were used:

- ε = 82,243±221 L mol^{-1} cm^{-1} [215]
- l = 1 cm
- A_s = 184mm^2, corresponding to 1.84 cm^2 (9mm diameter, 2mm thickness)
- V = 0.5 mL, corresponding to 0.0005 L

III.3.5.4. *Time-of-flight secondary ion mass spectrometry (ToF-SIMS)*

Time-of-flight secondary ion mass spectrometry (ToF-SIMS) is a surface-sensitive analytical technique in which a pulsed primary ion beam sputters the outermost molecular layers of a material, producing secondary ions that are separated according to their time of flight. Because only the upper 1-2 nm of the surface are probed, ToF-SIMS is particularly suited for detecting subtle chemical differences, contamination, or molecular rearrangements at interfaces. The technique provides semi-quantitative mass spectral information, meaning that ion intensities reflect relative, but not absolute, surface concentrations. Positive and negative ion modes yield complementary chemical signatures, as different classes of fragments preferentially ionize in each polarity. Static SIMS conditions were used throughout to ensure that the chemical information reflects the native surface composition rather than beam-induced alterations.

ToF-SIMS was employed to characterize the surface chemical composition of the samples under these static conditions. Spectra were acquired in both positive and negative ion polarity to maximize chemical coverage and to detect both cationic and anionic fragments relevant to the studied system. All measurements were performed using a ToF-SIMS IV instrument (IONTOF GmbH) equipped with a 25 keV Bi^+ primary ion beam. The primary ion current was approximately 0.97 pA, with a pulse width below 0.8 ns. A total primary ion dose of ~5×10^{11} ions·cm^{-2} was applied, remaining well below the static limit of 1×10^{13} ions·cm^{-2} to minimize beam-induced surface modification and preserve the native chemical state. Spectra were collected from a 25×25 μm^2 analysis area positioned within a 100×100 μm^2 sputtered region. Each spot was measured for a minimum of 30 s in both polarities to ensure sufficient ion statistics for reliable comparison. Data processing and peak integration were performed using SurfaceLab 7.3. Ion-irradiated regions were considered locally altered and were excluded from subsequent analyses. All ion intensities were normalized to the total ion counts, enabling semi-quantitative comparison between samples and allowing differences in surface chemistry to be interpreted in a consistent and reproducible manner.

III.3.5.5. *Fourier-transform infrared spectroscopy (FTIR)*

Fourier-transform infrared spectroscopy (FTIR) is a technique that identifies chemical bonds and functional groups by measuring the absorption of infrared light at specific wavelengths corresponding to molecular vibrations. In this study, FTIR was used to qualitatively identify and semi-quantitatively assess the efficacy of the silanization protocols on zirconia powder.

Fourier-transform infrared (FTIR) spectra were collected at a resolution of 2 cm^{-1} using a Nicolet 6700 FT-IR Spectrometer (Thermo Fisher Scientific) equipped with a DTGS detector. The spectrometer was used in the transmission mode.

The measurements were taken with pressed pellets using ZR-PW. Samples were prepared as self-supporting pellets by weighing 20 mg of powder, which was pressed into circular pellets of 0.7 cm diameter. The mass was checked before and after pressing (1.5 Ton) to ensure no loss. This corresponds to a surface loading of approximately 52 mg cm^{-2}, suitable for IR analysis.

The spectra presented correspond to the raw absorbance data acquired by the instrument, as the background measurement was automatically recorded before each sample acquisition and substracted by the instrument software during data collection. No additional background subtraction or post-processing was applied to the FTIR spectra.

III.3.6. Biological Assays Protocols

III.3.6.1. *Cytotoxicity Assay*

Cytotoxicity was evaluated using a direct-contact cell viability assay conducted at the I_2B team of MATEIS, by Sandra Balvay. Human osteoblast-like MG-63 cells were used for this study. Prior to cell seeding, all ZrO_2 samples were sterilized using 70% ethanol. The bulk disks used for this test were ZR-REC. The number of samples tested are 9, per type of surface. The materials tested consisted of ZR-REC surfaces functionalized with the intermediate PFPTES layer. Two control conditions were included: a tissue culture–treated plastic control (TP), used as a positive reference for cell viability, and non-functionalized ZrO_2 disks (ZrO_2, REF), used as a negative material control.

Cells were detached from culture flasks by enzymatic treatment with Trypsin-EDTA, phenol red. After removal of the culture medium, RPMI 1640 Medium, cells were rinsed with trypsin to eliminate residual serum, followed by incubation with trypsin at 37 °C for a few minuntil complete detachment. The resulting cell suspension was collected and centrifuged (1800 rpm, 10 min, 4 °C). The supernatant was removed, and cells were resuspended in complete culture medium containing serum to neutralize residual trypsin. Mechanical dissociation by repeated aspiration was performed to ensure a homogeneous cell suspension.

Cell concentration was determined using an automatic cell counter and adjusted to obtain a seeding density of 5000 cells per well. A suspension containing 5000 cells was carefully deposited directly onto each material surface placed in a $_2$4-well culture plate, ensuring direct contact between the cells and the tested substrates. Samples were incubated at 37 °C for 24 h to allow cell adhesion and interaction with the materials.

III.4. Results & Discussion

This section presents the results of the systematic study performed to investigate how various reaction parameters influence the silanization of zirconia surfaces. The objective was to identify the optimal conditions that ensure the formation of a reproducible, homogeneous, and stable silane monolayer. The outcomes were assessed using water contact angle (WCA) measurements and the ADECA colorimetric assay, two complementary yet indirect techniques that helped identify qualitative trends linking surface wettability to the relative amine density. Finally, the

resulting layers were fully characterized using X-ray Photoelectron Spectroscopy (XPS) and Time-of-Flight Secondary Ion Mass Spectrometry (TOF-SIMS) to confirm their chemical composition and surface structure.

III.4.1. Optimization of Silanization Reaction Parameters

In the following section, the influence of each parameter is discussed in detail to evaluate its impact on grafting efficiency and reproducibility. The analysis combines water contact angle (WCA) measurements and ADECA quantification of surface amine density to identify correlations and determine optimal reaction conditions.

3-aminopropyltriethoxysilane (APTES) was selected for the optimization experiments due to its widespread use as a reference silane and its short three-carbon chain, which limits intermolecular interactions and favors the formation of relatively uniform monolayers. Although APTES and PFPTES share the same triethoxysilane anchoring group, differences in molecular size, polarity, and terminal functionality may influence hydrolysis, condensation kinetics, and surface packing. Nevertheless, since surface attachment is primarily governed by the reactivity of the alkoxy groups toward zirconia surface hydroxyls, optimization using APTES provides a rational framework for defining suitable reaction windows for PFPTES functionalization.

APTES also enables the use of the ADECA colorimetric assay for direct quantification of accessible primary amine groups. In contrast to XPS, which requires specialized instrumentation and limited access, ADECA offers a rapid and practical method for screening multiple reaction parameters. WCA measurements provide complementary information on changes in surface wettability and organic coverage, although they may also be influenced by contamination. For this reason, control zirconia samples subjected to the full protocol without APTES (C = 0 mM) were systematically included.

Literature reports indicate that APTES grafting densities on silica surfaces can reach high values, sometimes exceeding 10 molecules·nm^{-2}, while well-controlled monolayers on oxide substrates typically exhibit thicknesses of approximately 0.5–0.8 nm and grafting densities between 2 and 4 molecules·nm^{-2} [216–218]. However, lower grafting densities are generally reported for zirconia compared to silica, with reductions of approximately 30–40 % in some studies [219]. Surface treatments such as plasma or UV activation further influence hydroxyl density and wettability on zirconia [220], making direct comparison between studies difficult. These considerations establish a realistic framework for interpreting the experimental trends presented below.

However, lower grafting densities are generally reported for zirconia compared to silica, and surface pretreatments can significantly affect hydroxyl density and wettability (II.6). These considerations establish a realistic framework for interpreting the experimental trends observed in the present study. The following set of experiments was performed on ZR-P disks.

III.4.1.1. *Concentration & Immersion time*

For optimizing the silanization reaction, the first parameters studied were concentration and immersion time. For these experiments, the curing time and solvent were predetermined and selected: silanization was carried out in dry ethanol acidified with 0.14 % v/v acetic acid (pH ≈ 4.5). The addition of acetic acid serves to regulate hydrolysis and thereby hinder excessive self-condensation (polymerization) of the silane molecules [221]. The curing time was set to approximately 16 h (overnight) at 110°C, temperature previously employed by our group for surface functionalization.

Figure III-6 to Figure III-9 summarize the WCA and ADECA results obtained for the different concentrations and immersion times. WCA values correspond to the average of three measurements performed at different positions on each disk. Control samples were immersed in a solution containing 0 mM APTES and subjected to the same protocol. The mean WCA value of the control was 19°.

For the ADECA analysis, the amine density values of the control samples were used solely as baselines for the calculations and are therefore not displayed in the graphs. Due to the limited number of remaining samples and the instability of the technique during initial trials, measurements were performed with $n = 1$ for all conditions. During this period, efforts were also undertaken within the group to optimize the ADECA protocol reported in the literature and adapt it for application to zirconia surfaces. The obtained values should therefore be interpreted as indicative trends rather than statistically representative measurements. Despite these limitations, the results provide a preliminary estimation of amine density and enable qualitative comparison between the different functionalization conditions.

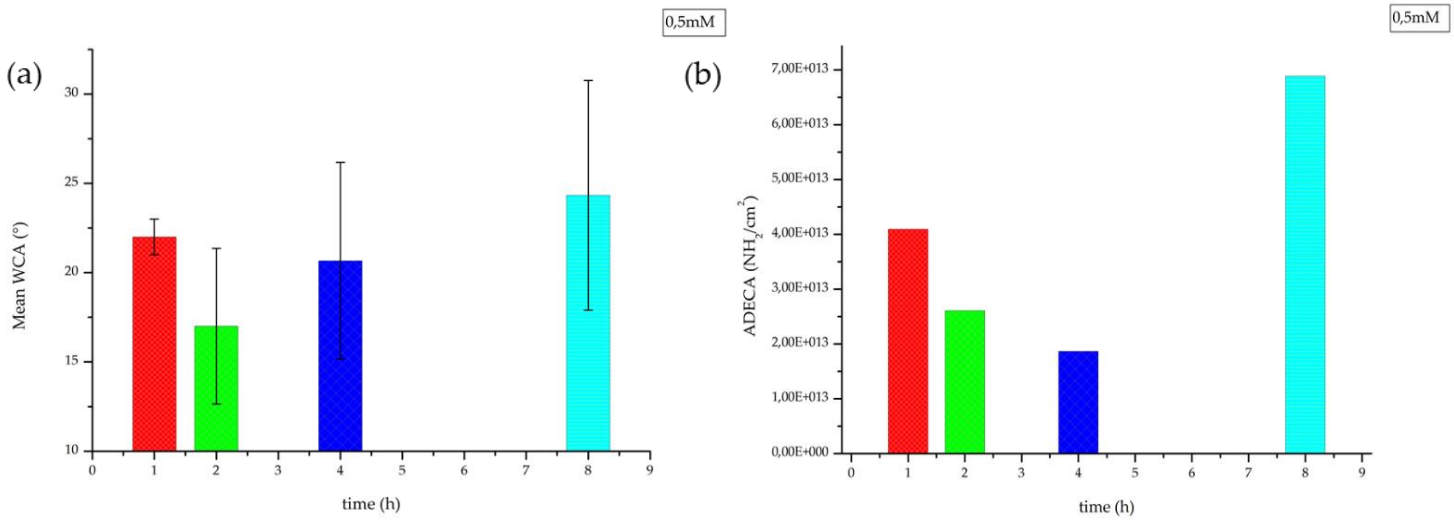

Figure III-6. (a) Mean water contact angle and (b) amine density values measured at different immersion times of ZR-P for an APTES concentration of 0.5 mM (in EtOH), after annealing at 110°C.

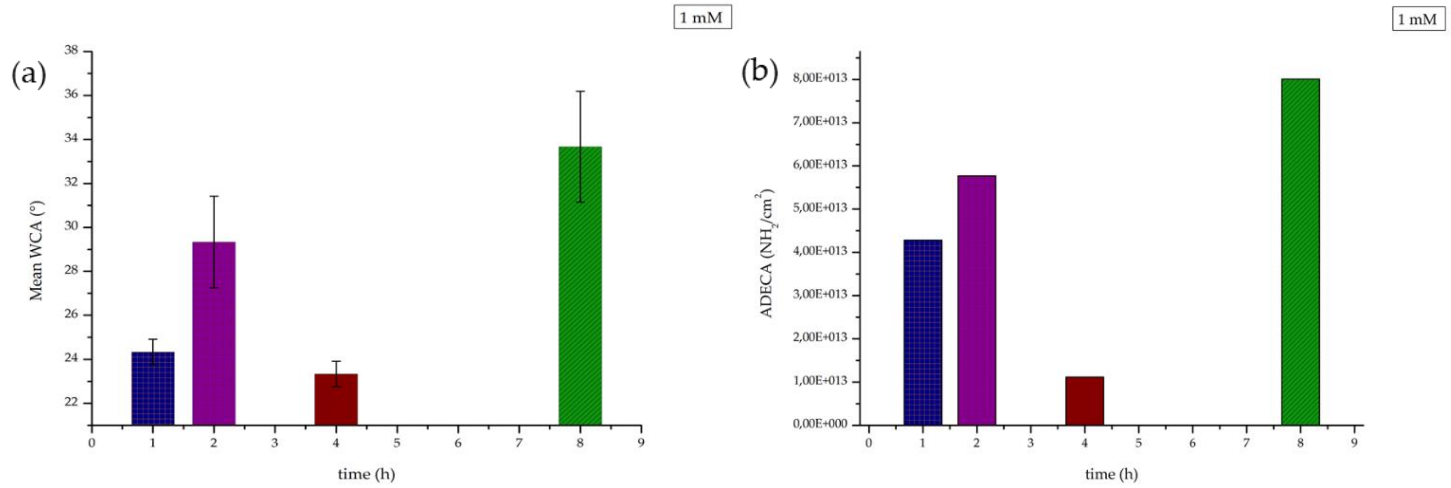

Figure III-7. (a) Mean water contact angle and (b) amine density values measured at different immersion times of ZR-P for an APTES concentration of 1 mM (in EtOH), after annealing at 110°C.

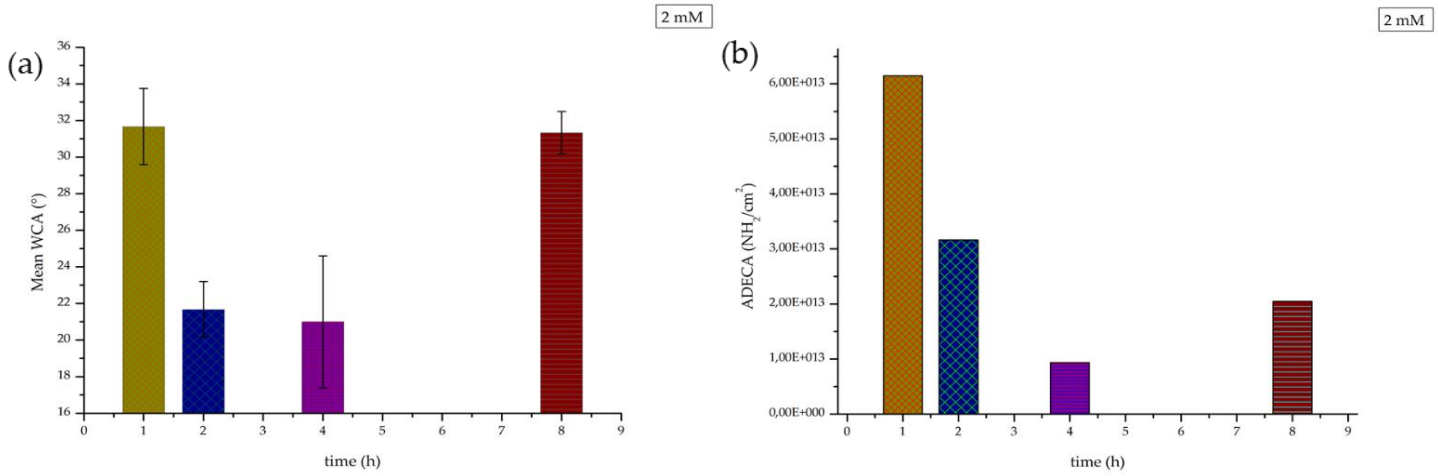

Figure III-8. (a) Mean water contact angle and (b) amine density values measured at different immersion times of ZR-P for an APTES concentration of 2 mM (in EtOH), after annealing at 110°C.

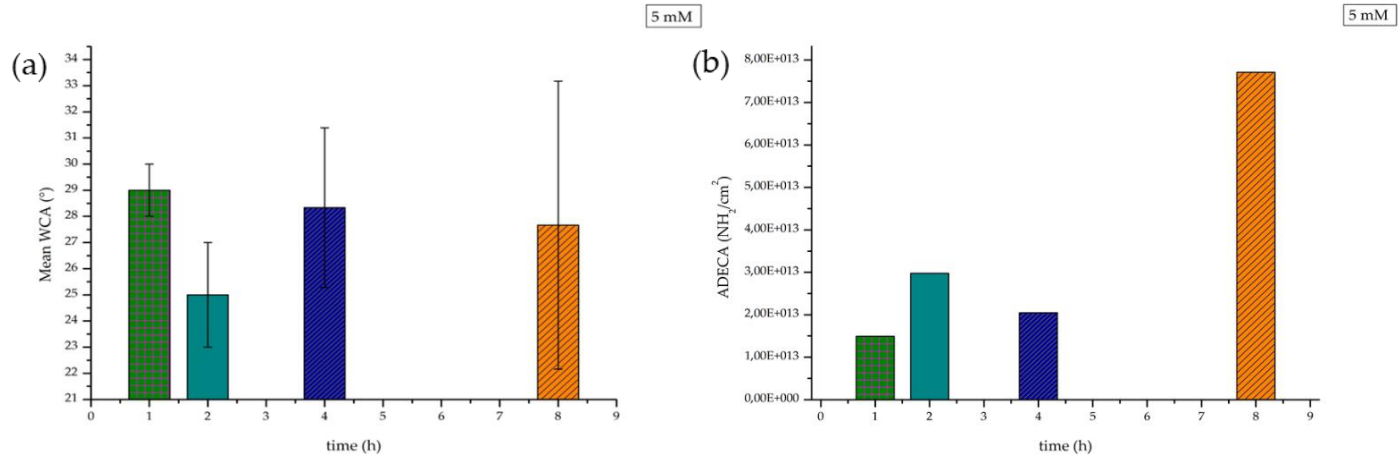

Figure III-9. (a) Mean water contact angle and (b) amine density values measured at different immersion times of ZR-P for an APTES concentration of 5 mM (in EtOH), after annealing at 110°C

Although absolute variations in WCA and amine density remain within a relatively narrow range, both techniques exhibit consistent trends across the tested conditions. For each condition, higher WCA values are generally accompanied by higher amine densities, indicating that changes in wettability reflect differences in organic surface coverage. However, at higher concentrations and longer immersion times, increases in amine density are not systematically matched by proportional changes in WCA. This suggests that surface wettability becomes less sensitive once a threshold surface coverage is reached, and that additional grafting does not translate linearly into macroscopic wettability changes.

From ADECA quantification, the measured amine densities fall approximately within the range of 0.1–1 molecule·nm^{-2}. These values are lower than typical dense monolayers reported for silica surfaces (2–4 molecules·nm^{-2}), but are consistent with literature describing reduced grafting densities on zirconia substrates.

Higher amine densities were generally observed at 1 mM and 5 mM, particularly after 8 h immersion. However, important differences emerge when reproducibility is considered. While 5 mM often produced elevated amine densities, especially at 2 h, this condition exhibited significantly higher standard deviations in repeated experiments (**Figure III-10**). The increased dispersion suggests greater sensitivity of the reaction to minor experimental variations, possibly reflecting less controlled condensation processes and the onset of partial multilayer formation at higher concentrations. In contrast, 2 h immersion consistently yielded lower variability across concentrations, indicating more controlled and reproducible surface organization.

The intermediate concentration (2 mM) showed an irregular variation with immersion time, suggesting that this condition does not provide a stable or predictable reaction regime. This behavior further supports the decision to prioritize reproducibility rather than simply selecting the condition that gives the highest apparent grafting density.

It is also important to note that ADECA provides an estimation of accessible primary amine groups rather than an exact molecular surface coverage. While the technique is well suited for comparing trends between samples, it does not capture subtle differences in silane organization or layer structure. For this reason, the optimization stage was treated as a screening step to identify a controlled and reproducible reaction window. The selected conditions were later validated using more surface-sensitive characterization techniques. Therefore, the ADECA results are interpreted in a comparative manner rather than as absolute values.

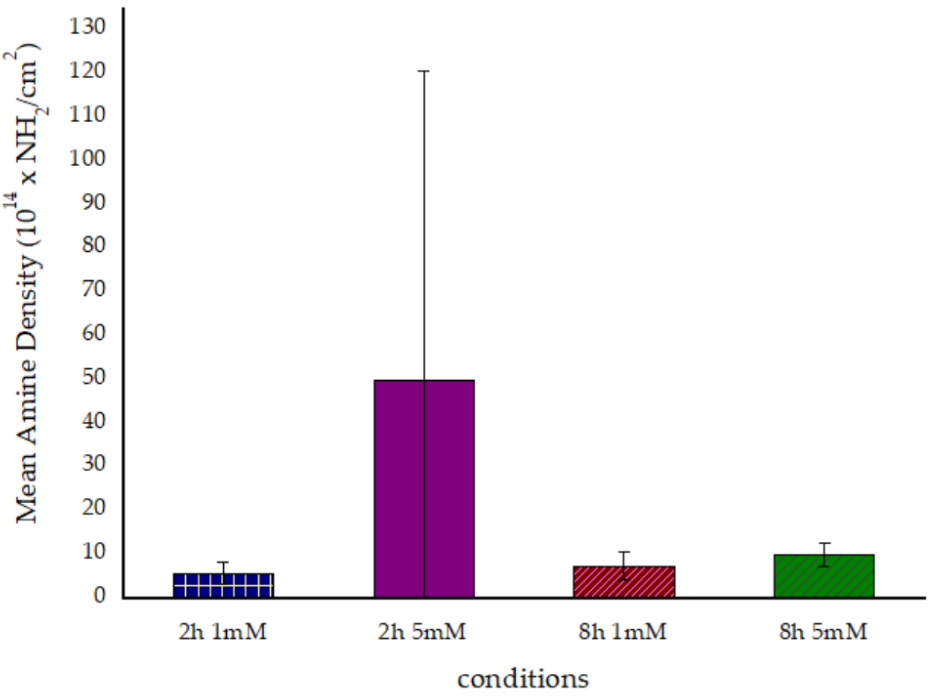

Figure III-10. Mean amine density values measured at different immersion times (2h and 8h) of ZR-P for different APTES concentrations (1mM and 5 mM) in EtOH, after annealing at 110°C.

Considering both grafting density and reproducibility, 1 mM APTES with 2 h immersion was selected as a good compromise between surface coverage, reaction control, experimental robustness, and practical feasibility. Although longer immersion (8 h) or higher concentration (5 mM) occasionally produced higher apparent amine densities, these gains were moderate relative to the increased variability or processing time. As an observation, the standard deviation for the mean amine density values appears to reach below zero. This can be explained by the standard deviation value being higher than the mean amine density itself and substracting the blank sample value issues. This can be considered as a significantly unreliable condition.

The behavior observed at low APTES concentrations (0.5–5 mM) is consistent with literature reports describing controlled monolayer formation under dilute conditions, where multilayer polymerization is minimized [222].

III.4.1.2. *Curing time*

Using the chosen immersion time (2h) and concentration (1mM) that were identified previously, the effect of curing time was then examined. The samples were prepared under the same conditions of the previous experiment while varying the curing duration (APTES in dry EtOH, curing time 110°C), and the resulting surfaces were analyzed using the ADECA colorimetric assay and WCA analysis. The amine surface density was plotted as a function of curing time, with each point representing the average of triplicate measurements.

No systematic variation in amine density was observed across the tested curing times (**Figure III-11**). Although minor fluctuations are present, the values remain within the experimental variability of the ADECA assay. WCA measurements likewise do not show a clear trend with increasing curing duration. These results indicate that under the selected conditions, surface condensation and stabilization occur efficiently within the shortest curing time tested.

Since prolonged curing did not result in a measurable increase in accessible amine density, the shortest effective curing duration was selected for subsequent experiments in order to reduce processing time while maintaining surface functionality.

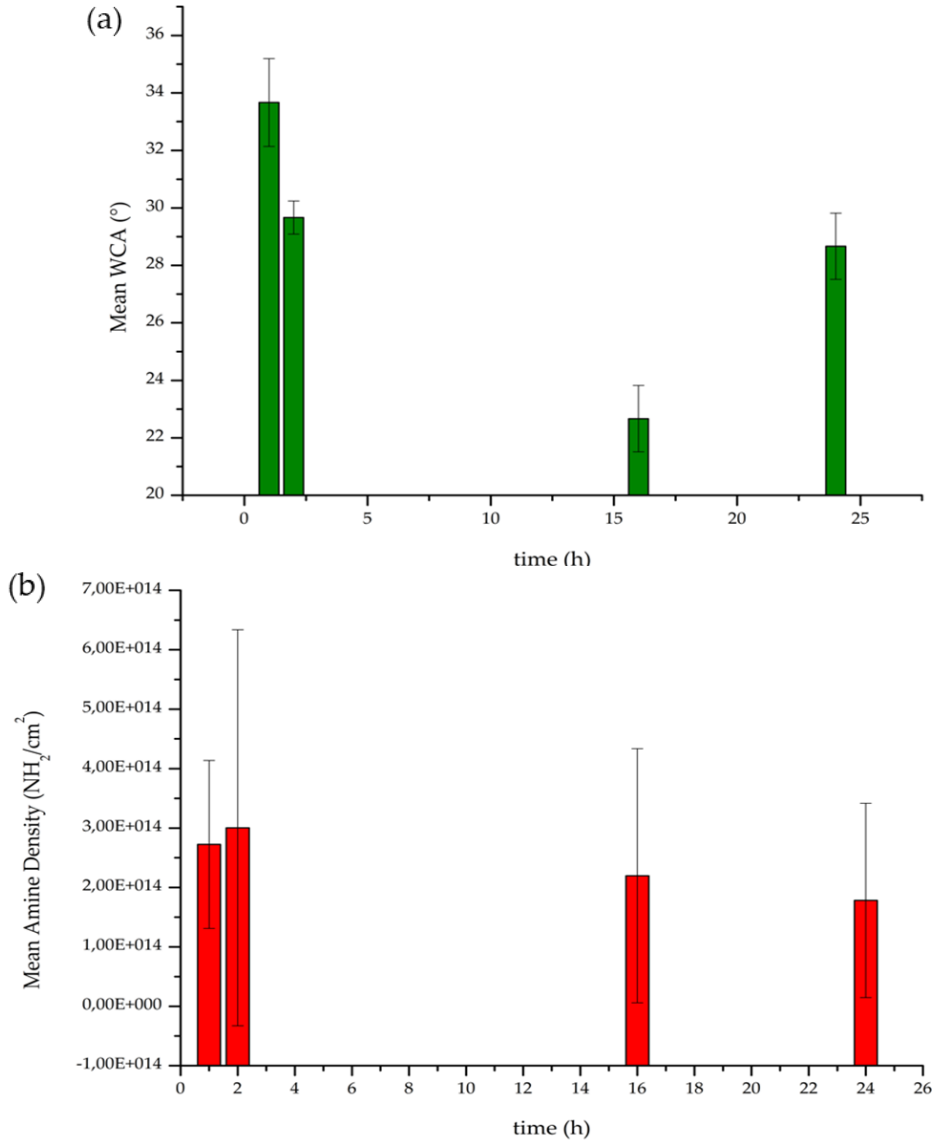

Figure III-11. (a) Water contact angle (WCA) and (b) mean amine surface density (ADECA) measured as a function of curing time for zirconia samples functionalized with 1 mM APTES and 2 h immersion in dry ethanol. Curing was performed at 110°C. Amine density values represent the average of triplicate measurements, with error bars indicating standard deviation.

III.4.1.3. *Chemical Composition*

The final optimized protocol was applied on polished zirconia disks and analyzed by XPS. The XPS survey spectra are presented in **Figure III-12** and the resulting atomic percentages are presented in **Table III-1**.

	XPS At%	
Element	control	APTES
Zr 3d	25 ± 1.15	19 ± 0.6
Y 3d	2 ± 0.2	1 ± 0.0
O 1s	57 ± 3	52 ± 1.5
C 1s	16 ± 7.2	25 ± 1.1
Si 2p	-	2.5 ± 0.0
N 1s	-	-

Table III-1. Atomic percentages obtained from XPS survey spectra for bare zirconia (control) and zirconia functionalized with APTES under optimized conditions (1 mM, 2 h immersion, 110°C curing).

The XPS atomic composition further confirms successful surface modification after APTES treatment (**Table III-1**). Compared to the control zirconia surface, the functionalized sample shows a decrease in the Zr 3d signal (from 25 at% to 19 at%) and Y 3d signal (from 2 at% to 1 at%), indicating at least partial coverage of the substrate by an organic layer. At the same time, the C 1s contribution increases from 16 at% to 25%, and a clear Si 2p signal (2.5 at%) appears after silanization, confirming the presence of the grafted silane. The slight decrease in O 1s is consistent with surface coverage and partial masking of the oxide underneath. Although the N 1s signal is not clearly visible in the survey spectrum, the increase in carbon together with the appearance of silicon provides clear evidence of APTES immobilization on the zirconia surface.

In the XPS survey spectra (**Figure III-12**) of the control zirconia samples, the C 1s signal at 285 eV is nearly absent, indicating a very low level of surface contamination. Following functionalization with APTES, a clear C 1s peak emerges at 285 eV, accompanied by the appearance of the Si 2p signal around 100 eV (also **Figure III-14**), confirming the successful grafting of the silane layer. However, no nitrogen signal was detected. Some studies report N/Si ratios well below 1 [223,223–225], and in some cases, nitrogen is not observed at all due to its susceptibility to X-ray–induced degradation or desorption of the amino groups during analysis [226].

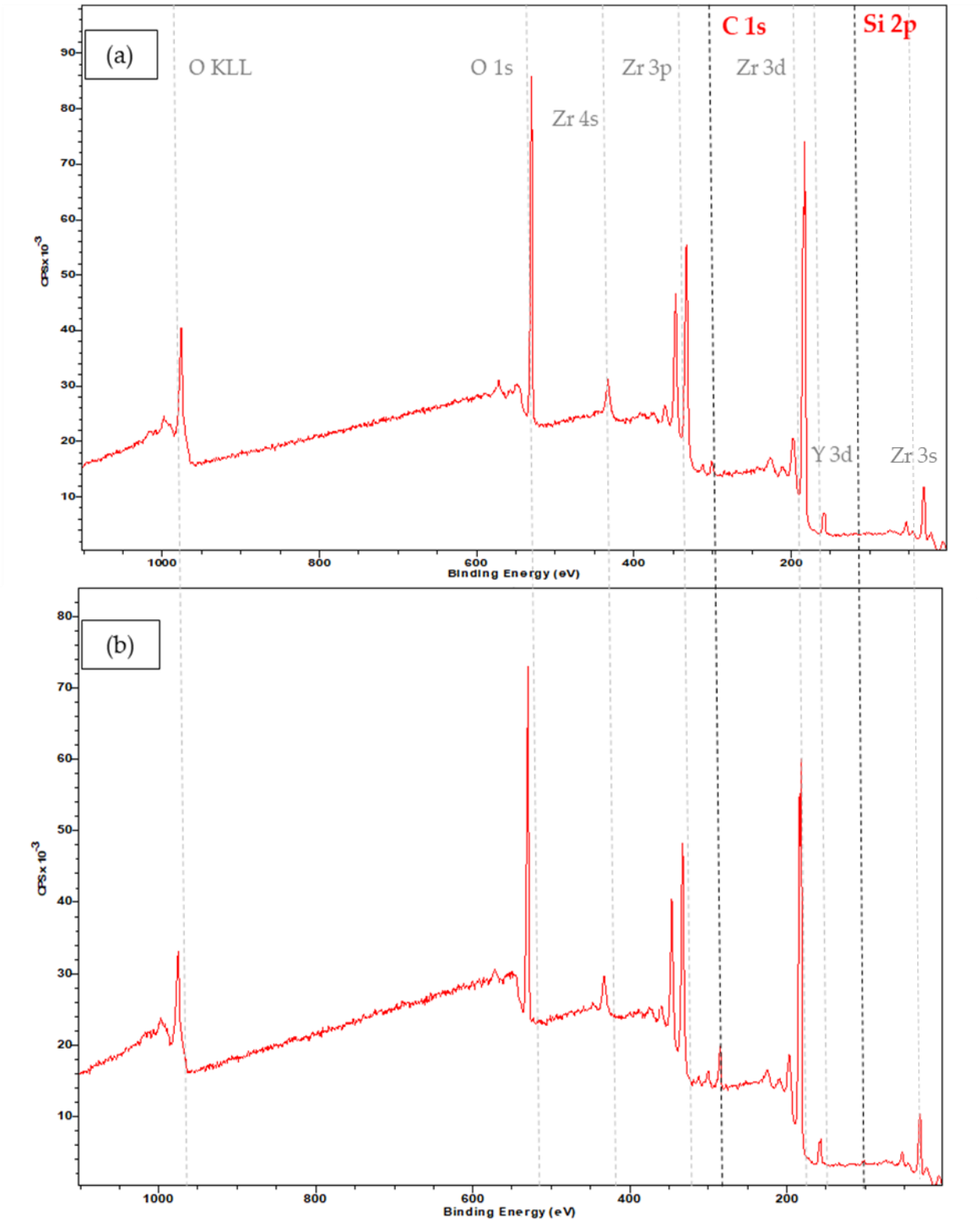

Figure III-12. XPS survey spectra of zirconia surfaces before and after APTES functionalization. (a) Bare zirconia substrate and (b) zirconia functionalized with APTES under the optimized conditions (1 mM, 2 h immersion, 110°C curing). The emergence of the C 1s peak at 285 eV and the Si 2p signal around 100 eV after treatment confirms the presence of the grafted organosilane layer.

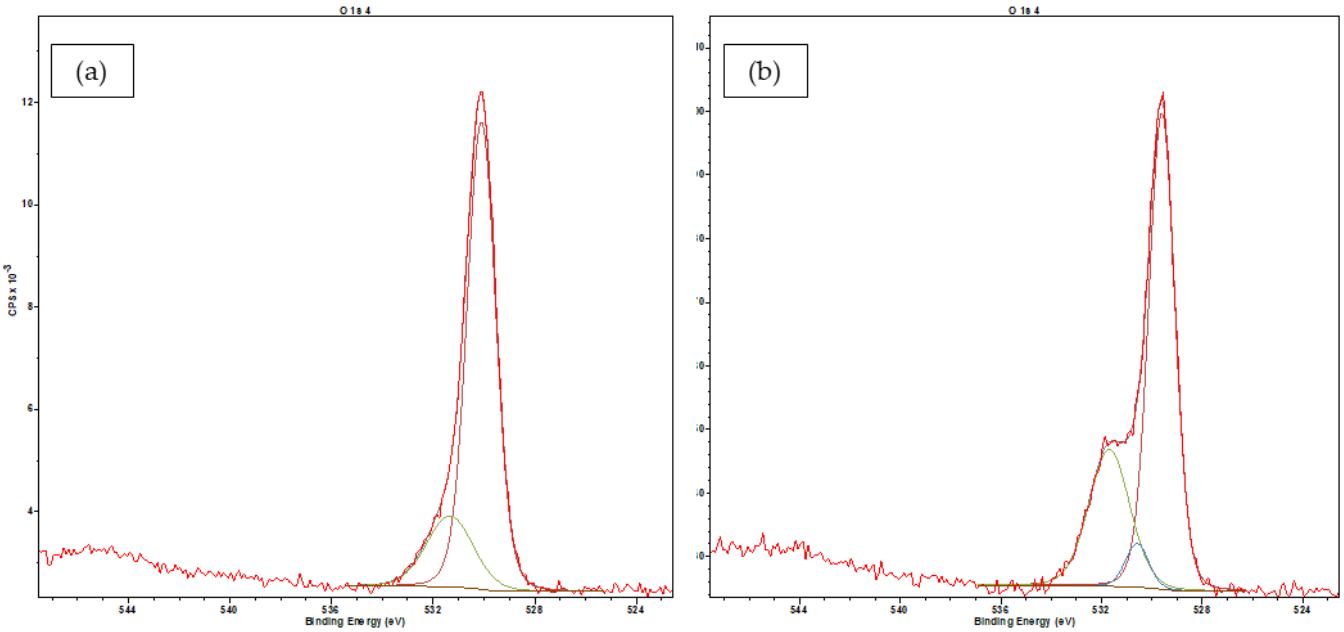

Figure III-13. High-resolution O 1s XPS spectra of zirconia surfaces before and after APTES functionalization.
(a) Bare zirconia substrate and (b) zirconia functionalized with APTES under optimized conditions (1 mM, 2 h immersion, 110°C curing). Deconvolution of the O 1s region reveals contributions from lattice oxygen (Zr–O) and surface hydroxyl or siloxane-related species. After functionalization, changes in the relative intensity of the higher binding energy component indicate the formation of Si–O–Zr and/or Si–O–Si bonds associated with the grafted silane layer.

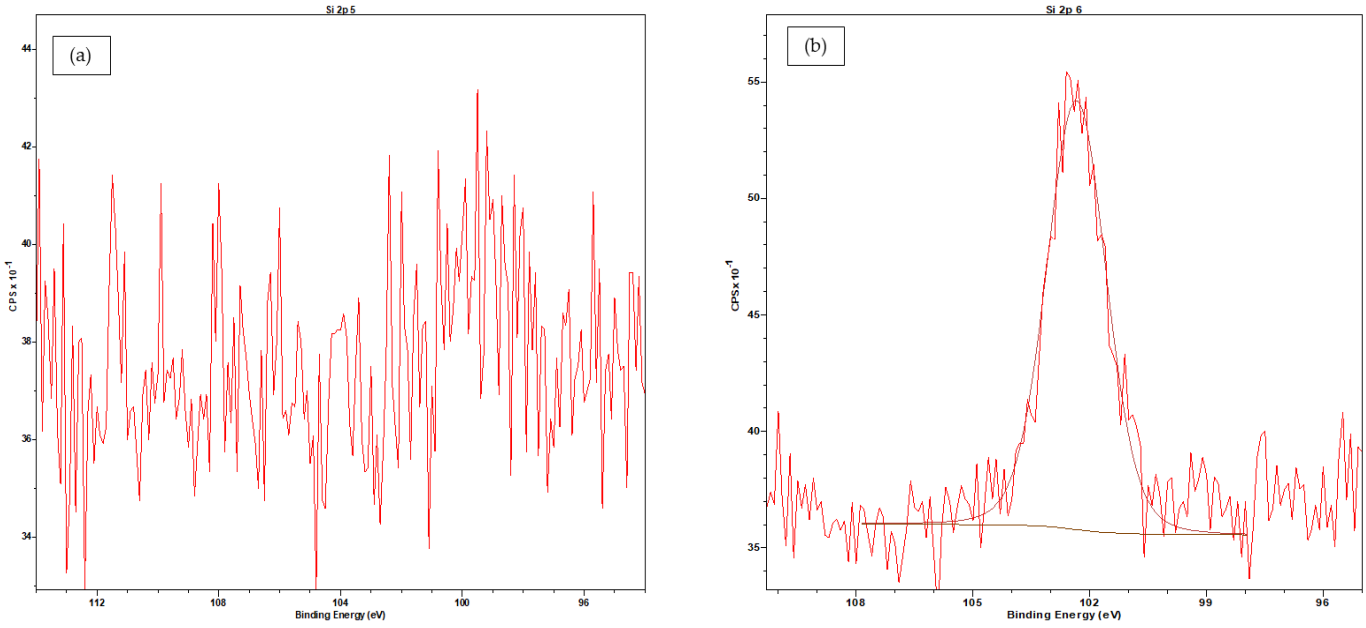

Figure III-14. High-resolution Si 2p XPS spectra of zirconia surfaces before and after APTES functionalization. (a) Bare zirconia substrate, showing no detectable Si 2p signal, and (b) zirconia functionalized with APTES under optimized conditions (1 mM, 2 h immersion, 110°C curing). The appearance of a distinct Si 2p peak around 102–103 eV after treatment confirms the presence of silicon-containing species associated with the grafted silane layer.

In **Figure III-13**, the high-resolution O 1s spectrum of the control sample (**Figure III-13a**) can be deconvoluted into two main components: lattice oxygen from zirconia (Zr–O) centered at approximately 530.0 eV, and a secondary contribution at higher binding energy (around 531.5 eV), typically attributed to surface hydroxyl groups and/or adventitious oxygen-containing species such as C–O or C=O. After APTES functionalization (**Figure III-13b**), the O 1s spectrum exhibits a clear modification of the peak shape, together with the emergence of an additional component at approximately 532.5 eV. This higher binding energy contribution is consistent with oxygen atoms in Si–O–Si and/or Si–O–M environments associated with the grafted silane layer [227].

In **Figure III-14**, the high-resolution Si 2p spectra provide additional confirmation of successful surface modification. As expected, the control sample (**Figure III-14a**) shows no detectable Si 2p signal, consistent with the absence of silicon on the polished zirconia surface. In contrast, the functionalized sample (**Figure III-14b**) exhibits a distinct Si 2p peak centered at approximately 102 eV. This binding energy is characteristic of silicon in siloxane-type environments and confirms the presence of silicon-containing species on the surface, consistent with the formation of an APTES-derived layer [227].

III.4.2. Application of the Silanization Protocol to PFPTES

The ZR-P surfaces were functionalized with the trifunctional pentafluorophenyl-terminated silane (PFPTES), intended for subsequent peptide conjugation, as described in III.2. The optimized silanization protocol previously developed for APTES was applied to ensure consistency and comparability between the two silanes. The objective of this step was to validate the applicability of the optimized silanization conditions to PFPTES and to verify that the PFP-terminated silane could form a layer on zirconia while introducing its reactivity toward nucleophilic coupling.

Since PFPTES was not soluble in ethanol, anhydrous dichloromethane (DCM) was used instead of the dried ethanol. The solvent was dried over 4 Å molecular sieves for 48 hours prior to use, and all manipulations were carried out under dry conditions to prevent premature hydrolysis of the pentafluorophenyl ester. Apart from the solvent change, the immersion, rinsing, and curing steps were kept identical to those optimized for APTES, ensuring direct comparability between the two protocols. A control sample was introduced each time. The “control” sample followed the same protocol but it was immersed in anhydrous DCM without PFPTES.

III.4.3. Characterization of PFPTES-grafted layer

III.4.3.1. *Wettability of the Silanized Surface*

The surface wettability was evaluated to assess the effect of PFPTES grafting on surface energy and to verify successful functionalization. The angle measurements are presented in **Table III-2**. The measurements are the average of 3 points on each sample with a standard deviation.

sample	**angle (°)**
control	43 ± 1
PFPTES	85 ± 2

Table III-2. Water contact angle values measured on polished zirconia disks before and after surface functionalization with PFPTES

The water contact angle measurements show a clear difference between the control sample (43 ± 1°), which was only immersed in DCM and annealed, and the PFPTES-functionalized zirconia (85 ± 2°). This represents the first significant difference observed between APTES and PFPTES functionalization under identical conditions. The WCA of APTES-functionalized disks (1 mM, 2 h immersion) ranges from 27 to 31°. This could be attributed to the larger hydrocarbon chain of PFPTES, as well as the effect of the functional group to the surface energy. Because both samples underwent the same protocol, with the only difference being the presence of the fluorinated silane, the higher contact angle of the PFPTES sample indicates that the silane treatment increases the surface hydrophobicity. This trend is fully consistent with the introduction of an organic layer, which typically reduces surface polarity, and with the expected low surface energy associated with the pentafluorophenyl group and the hydrocarbon chain of the PFPTES molecule.

However, WCA alone is insufficient to prove the presence of the pentafluoroaromatic ring on the surface; definitive chemical evidence must come from spectroscopic analysis. The relatively narrow standard deviation for both samples suggests that the modification procedure produced reproducible and homogeneous layers.

The control sample also exhibits a higher water contact angle than freshly ozone-cleaned zirconia, which is expected since immersion in DCM followed by annealing introduces slight changes to the surface chemistry compared to a freshly cleaned surface.

III.4.3.2. *Chemical Composition of the Surface*

The chemical composition of the PFPTES-modified surface was analyzed by XPS in order to confirm incorporation of the fluorinated silane. XPS measurements were performed on both the control sample and the PFPTES-functionalized zirconia prepared using the optimized protocol. The control sample consisted of a polished zirconia disk subjected to the same treatment procedure, but immersed in dichloromethane (DCM) without PFPTES.

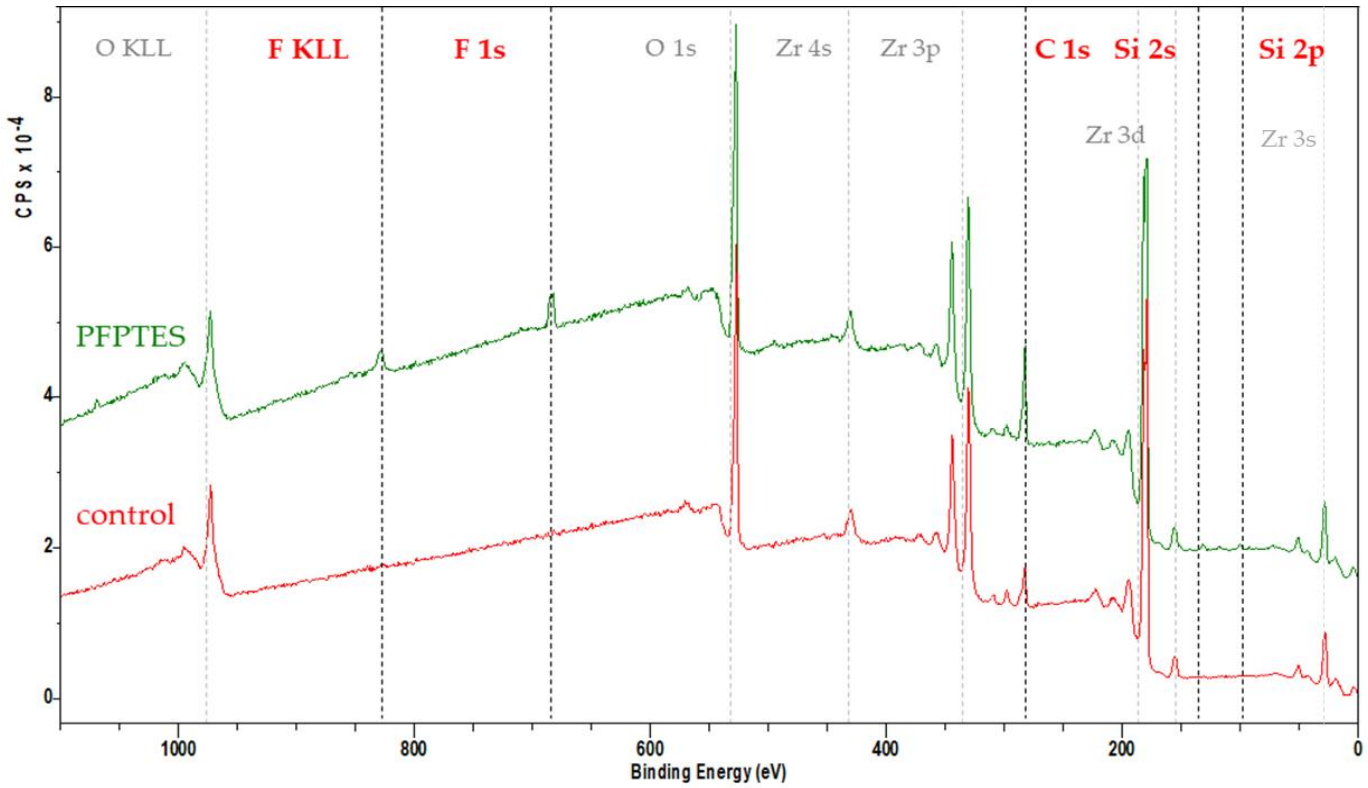

Figure III-15. Survey spectra of polished zirconia disks for the control sample (red) and after PFPTES treatment (green). Following functionalization, characteristic fluorine signals appear at F 1s (~689 eV) together with the F KLL Auger feature (~832 eV). Silicon-related peaks are observed at Si 2s (~153 eV) and Si 2p (~102–103 eV), confirming the presence of the grafted silane layer. An increase in the C 1s signal (~285 eV) is also detected, consistent with the formation of an organic fluorinated overlayer.

The XPS survey spectra (**Figure III-15**) clearly demonstrate successful surface modification after PFPTES treatment. In addition to the characteristic zirconium and oxygen signals from the substrate, new peaks appear at approximately 102 eV (Si 2p) and 686–689 eV (F 1s), corresponding to silicon and fluorine species introduced by the fluorinated silane. An increase in the C 1s signal at 285 eV is also observed, consistent with the presence of the organic overlayer. The emergence of both silicon and fluorine signals, which are absent in the control sample, confirms the successful grafting of PFPTES onto the zirconia surface.

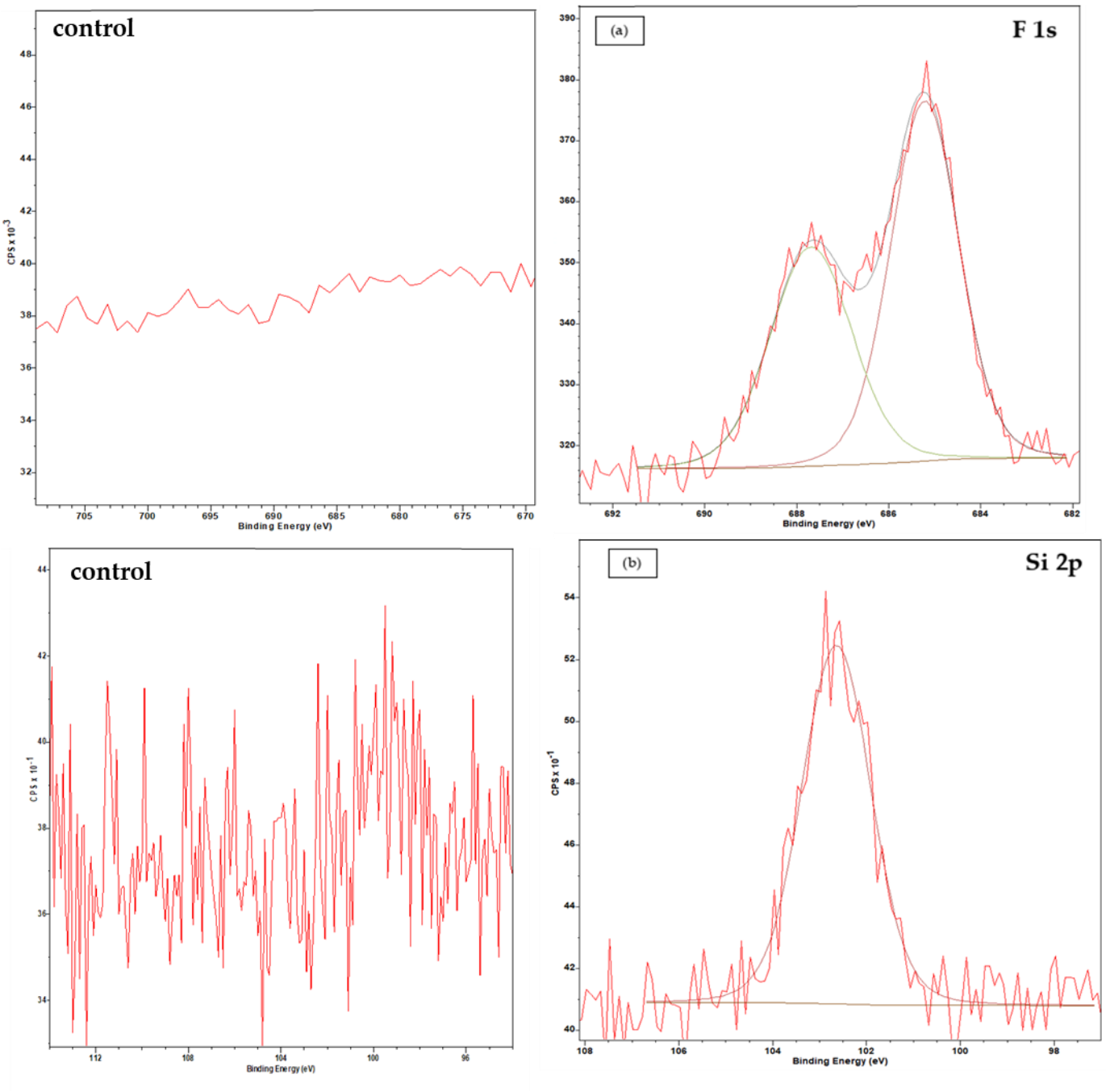

Figure III-16. High-resolution XPS spectra of PFPTES-functionalized zirconia. a) F 1s region showing components centered at approximately 685 eV and 688 eV, corresponding to inorganic fluoride species and aromatic C–F bonds from the pentafluorophenyl group, respectively. (b) Si 2p region displaying a peak at ~102–103 eV, characteristic of silicon in siloxane environments (Si–O–Si and/or Si–O–Zr), confirming covalent attachment of the PFPTES layer to the zirconia surface. Experimental conditions of **III.3.4**

A closer examination of the high-resolution spectra **(Figure III-16a**) reveals two distinct components in the F 1s region, with peaks centered at approximately 685 eV and 688 eV. The lower binding energy component (~685 eV) is characteristic of inorganic or free fluoride species (F^-). In contrast, the higher binding energy peak at ~688 eV corresponds to fluorine bound to

aromatic carbon (C–F), consistent with the pentafluorophenyl moiety of PFPTES. The presence of this component confirms the successful introduction of fluorinated organic groups onto the surface. Similar binding energies have been reported in XPS studies of fluorinated materials, where metal fluorides appear near 685 eV and organic C–F species near 688 eV [228]. The small contribution of the lower-energy component may originate from minor degradation or substitution reactions of the pentafluorophenyl group during functionalization, leading to the release of fluoride ions that remain adsorbed on the oxide surface.

In the modified samples, silicon is detected at approximately 1 at%, together with 4 at% fluorine, yielding an F/Si atomic ratio of about 4. This ratio is close to the theoretical value of 5 expected from the pentafluorophenyl group of PFPTES. The slight deviation may arise from partial attenuation effects, minor degradation under XPS irradiation, incomplete surface coverage, or uncertainties associated with quantitative analysis. Nevertheless, the presence of both silicon and fluorine in approximately stoichiometric proportion strongly supports successful grafting of the PFPTES layer. The retention of fluorine signals further indicates that the pentafluorophenyl moiety remains largely intact, which is essential for subsequent peptide conjugation. It should be noted that the total fluorine atomic percentage includes both the C–F contribution from the pentafluorophenyl group and the F^- component detected at lower binding energy.

In the Si 2p region (**Figure III-16b**), a peak centered at approximately 102–103 eV is observed, which is characteristic of silicon in siloxane environments (Si–O–Si and/or Si–O–Zr). This further supports the formation of a covalently attached silane layer on the zirconia surface. The corresponding atomic percentages are summarized in **Table III-3**.

	XPS At%	
Element	Control	PFPTES
Zr 3d	24	19
Y 3d	2	1
O 1s	54	48
C 1s	20	27
Si 2p	-	1
F 1s	-	4

Table III-3. Atomic percentages obtained from XPS survey spectra for polished zirconia before and after PFPTES treatment using the optimized protocol. The appearance of Si 2p and F 1s signals, together with the increase in C 1s and attenuation of Zr 3d and Y 3d contributions, confirms successful grafting of the fluorinated silane layer.

III.4.3.3. *Molecular-Level Evidence of Surface Functionalization*

ToF-SIMS measurements and data analysis were performed by our NOMAD partner at the University of Siegen, in both positive and negative ion modes, to monitor the chemical evolution of the ZrO_2 surface upon PFPTES functionalization. The substrates sent for analysis were ZR-P disks. A control sample was included, which was subjected to the complete experimental protocol, including solvent exposure, but without PFPTES silanization.

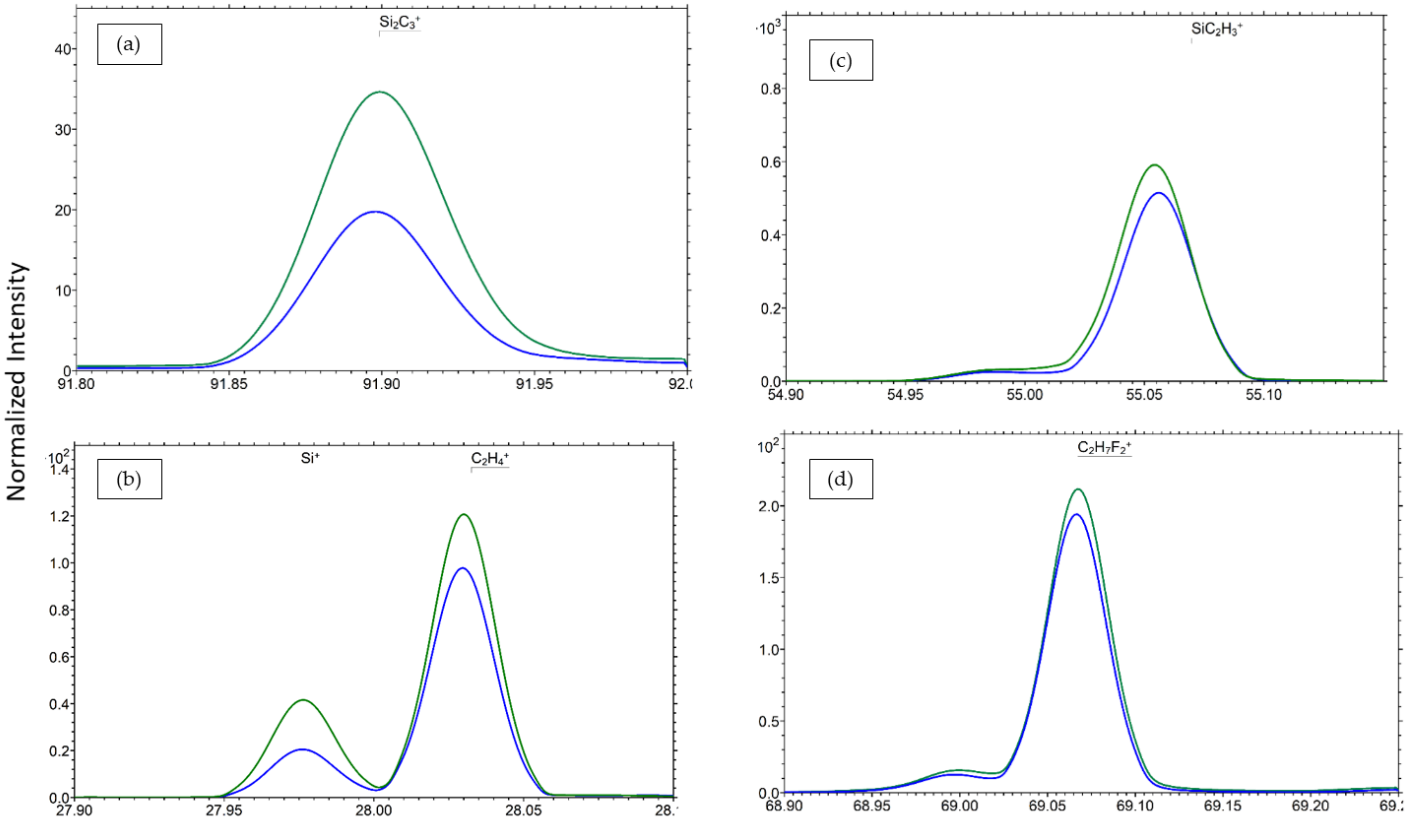

Figure III-17. (a) TOF-SIMS analysis of the $Si_2C_3^+$ fragment intensity for the control (blue) and PFPTES-functionalized (green) zirconia samples. The markedly higher signal observed for the functionalized surface reflects the presence of silane-derived silicon–carbon fragments, in contrast with the low background level of the control. (b) TOF-SIMS analysis showing the Si^+ and $C_2H_4^+$ fragment intensities for the control (blue) and PFPTES-functionalized (green) zirconia samples. Both ions display significantly higher signals on the functionalized surface compared to the control, consistent with the introduction of the organic silane layer. (c) TOF-SIMS analysis of the $Si_2H_3^+$ fragment intensity for the control (blue) and PFPTES-functionalized (green) zirconiasamples. The functionalized surface exhibits a notably higher signal than the control, reflecting the presence of silane-derived silicon-containing species. (d) TOF-SIMS analysis of the $C_2H_7F_2^+$ fragment intensity for the control (blue) and PFPTES-functionalized (green) zirconia samples. The increase in signal for the functionalized sample indicates the presence of fluorinated organic fragments associated with the PFPTES layer

The ToF-SIMS analysis provides additional evidence for PFPTES grafting on the zirconia surface (**Figure III-17**). Silicon-containing fragments such as $Si_2C_3^+$ and $Si_2H_3^+$ show consistently higher intensities for the functionalized samples compared to the control, indicating the presence

of silane-derived species at the outermost surface. Likewise, increased signals for Si^+ and $C_2H_4^+$ fragments are consistent with the introduction of an organosilane layer. The fluorinated fragment $C_2H_7F_2^+$ is also clearly more intense on the functionalized surface, confirming incorporation of fluorine-containing groups associated with PFPTES.

Although the signal differences are moderate, the coherent increase across multiple silicon- and fluorine-related fragments supports successful surface modification. Given the extreme surface sensitivity of ToF-SIMS, even relatively small increases are indicative of chemical changes at the outermost molecular layers. Furthermore, as discussed in the following chapter, ToF-SIMS analysis on additional substrates confirms the robustness and reproducibility of the PFPTES chemistry, reinforcing the conclusions drawn here.

III.4.3.4. *Spectroscopic Evidence of Chemical Bond Formation*

Although ATR-FTIR measurements can in principle be performed directly on zirconia disks, the signal originating from a nanometric silane layer is extremely weak in ATR mode. To enhance the signal-to-noise ratio and clearly identify the characteristic vibrational bands of PFPTES, a 3Y-TZP zirconia powder was functionalized under identical conditions than the disks. The main idea was that the much higher specific surface area of the powder would significantly improve the detectability of surface-bound species in transmission FTIR measurements. The activation procedure, PFPTES concentration, immersion time, and curing parameters were thus maintained consistent with those used for bulk samples. After functionalization, the powder was collected using a Millipore filtration system under vacuum, and spectra were recorded in absorbance mode.

The FTIR spectrum of the PFPTES reference compound exhibits characteristic bands associated with the pentafluorophenyl group and the silane structure (**Figure III-18**). In particular, a distinct absorption band centered at approximately 1504 cm^{-1} is observed, corresponding probably to vibrations of the pentafluorophenyl aromatic ring. Additional bands appear in the 1100–1300 cm^{-1} region and can be attributed to C–F stretching vibrations characteristic of fluorinated aromatic groups.

In contrast, the control zirconia powder does not display these aromatic or C–F features. Its spectrum is dominated by broad bands associated with the oxide surface, with no distinct absorption around 1504 cm^{-1} and no defined signals in the 1100–1300 cm^{-1} region attributable to fluorinated groups.

The PFPTES-functionalized zirconia powder exhibits spectral features that combine characteristics of both the PFPTES reference and the zirconia substrate. A band at approximately 1504 cm^{-1} appears in the modified sample, matching the aromatic vibration observed in the PFPTES reference spectrum and confirming the presence of the pentafluorophenyl moiety on the surface. In the 1100–1300 cm^{-1} region, additional bands corresponding to C–F stretching vibrations are also observed, further distinguishing the functionalized powder from the control sample. At lower wavenumbers, a broad band centered around 900–1000 cm^{-1} is present and can be attributed to Si–O stretching vibrations.

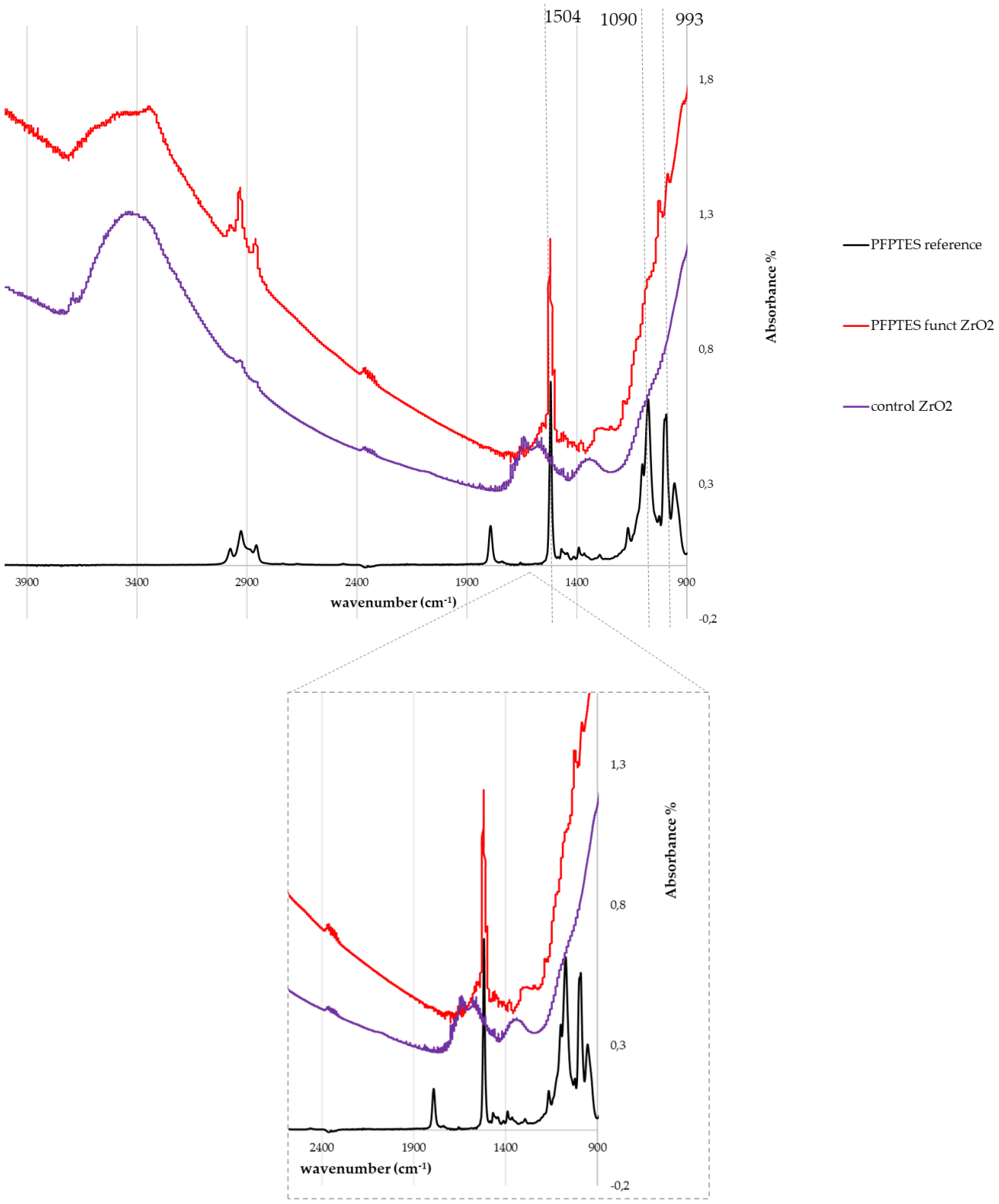

Figure III-18. ATR-FTIR spectra of the control zirconia surface (purple), PFPTES-functionalized zirconia (red), and the reference PFPTES compound (black). The functionalized surface exhibits vibrational features that correspond to those of the PFPTES reference, confirming the presence of the grafted fluorinated silane layer.

Taken together, the coexistence of aromatic ring vibrations and Si–O-related bands, combined with their correspondence to the PFPTES reference spectrum, supports successful grafting of PFPTES onto the zirconia surface. The retention of characteristic fluorinated aromatic features further indicates that the pentafluorophenyl group remains chemically intact following surface attachment.

III.5. Biological Evaluation

It is essential to verify that the surface functionalization strategy does not induce adverse effects on cell viability. Surface preparation and chemical modification may potentially introduce cytotoxic effects that could compromise the biological response. Cytotoxicity assays with MG-63 osteoblasts, as a pre-screening assessment of the intermediate PFPTES layer, and fibroblasts to evaluate the biocompatibility of the final surface, were therefore conducted to confirm that the applied surface treatments were not detrimental to cellular survival.

Cytotoxicity assay and the data analysis were initially performed internally at the I2B (Mateis) laboratory by Sandra Balvay. The intermediate PFPTES layer was specifically evaluated to verify that, in the event of exposure, it does not pose a risk to cellular viability. The results are presented in the following graphs **Figure III-19** and **Figure III-20**.

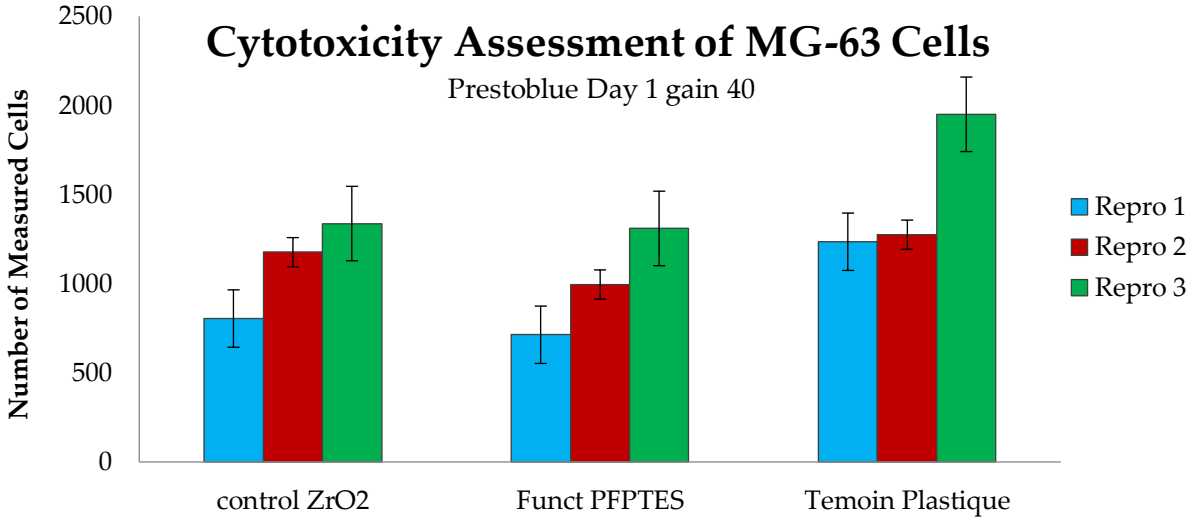

Figure III-19 Cytotoxicity assessment of MG-63 osteoblast-like cells after 24 h of direct contact with ZrO_2 surfaces. Cell metabolic activity was quantified using the PrestoBlue assay (excitation 535 nm, emission 610 nm, gain 40). PFPTES-functionalized ZrO_2 surfaces were compared to non-functionalized ZrO_2 (ZrO_2 control) and tissue culture plastic, "témoin plastique" (positive control). Data are shown for three independent replicates.

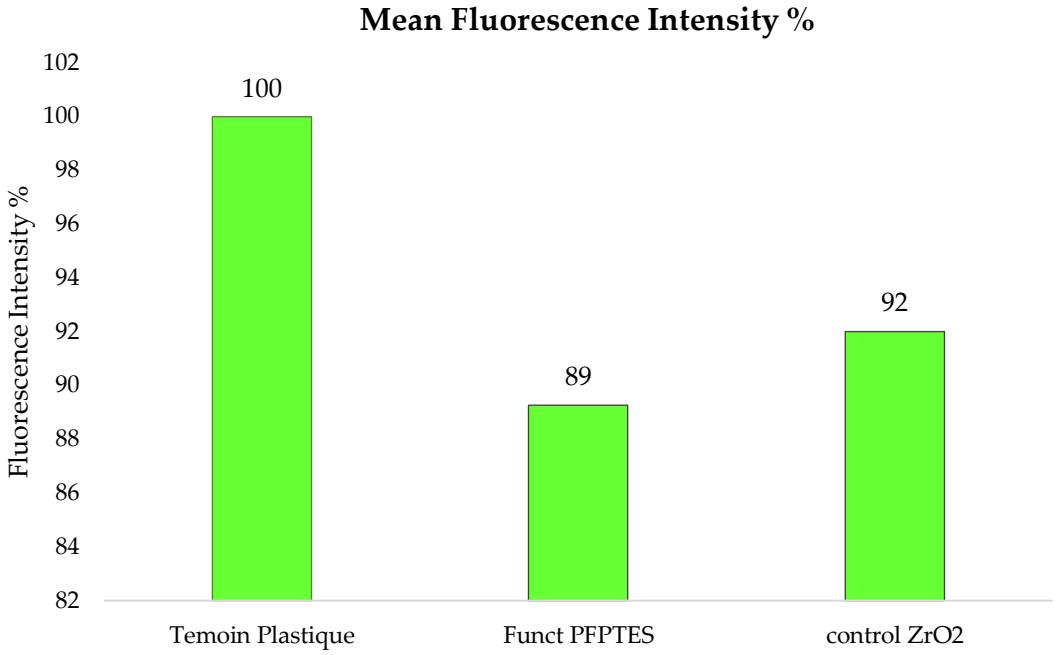

Figure III-20. Relative cell metabolic activity of MG-63 osteoblast-like cells after 24 h of direct contact with ZrO_2 surfaces, expressed as a percentage of the tissue culture plastic control (témoin plastique). Fluorescence values obtained from the PrestoBlue assay were normalized to the plastic control, set to 100%. PFPTES-functionalized ZrO_2 and non-functionalized ZrO_2 (control ZrO_2) exhibited metabolic activity levels comparable to the reference material.

Cytotoxicity of the functionalized ZrO_2 surfaces was evaluated after 24 h of direct contact with MG-63 osteoblast-like cells using the PrestoBlue assay. Absolute fluorescence measurements indicated comparable levels of cell metabolic activity on PFPTES-functionalized ZrO_2 and non-functionalized ZrO_2 controls, with values consistently lower than those measured on tissue culture plastic, used as a positive reference. The dispersion observed between replicates remained within a similar range for Control ZR-REC ZrO_2 and ZR-REC-PFPTES functionalized, indicating good experimental reproducibility.

To facilitate comparison between materials, fluorescence values were normalized to the tissue culture plastic control, set to 100%. Under these conditions, PFPTES-functionalized ZrO_2 exhibited a relative metabolic activity of approximately 89%, while non-functionalized ZrO_2 reached approximately 92%. According to ISO 10993-5 (Biological evaluation of medical devices – Part 5: Tests for *in vitro* cytotoxicity), a reduction in cell viability below 70% of the negative control indicates a cytotoxic effect, whereas materials maintaining cell metabolic activity above 70% are considered non-cytotoxic. Both tested ZrO_2 surfaces therefore meet this criterion, indicating that the presence of the PFPTES intermediate layer does not induce cytotoxic effects. Overall, both absolute and normalized data confirm the cytocompatibility of the PFPTES ZrO_2 under the tested conditions.

III.6. Conclusions

This chapter focused on the optimization and characterization of silane-based surface functionalization of zirconia substrates. The influence of key reaction parameters, including silane concentration, immersion time, curing duration, and solvent conditions, was systematically investigated in order to identify a controlled and reproducible grafting protocol.

For APTES functionalization, combined analysis using water contact angle (WCA) measurements and ADECA quantification allowed the identification of consistent trends in surface modification. Although absolute variations remained within a limited range, both techniques exhibited parallel behavior across conditions, confirming that changes in wettability reflected differences in organic surface coverage. Higher concentrations and longer immersion times tended to increase apparent amine density; however, reproducibility decreased under more concentrated conditions. In particular, 5 mM APTES showed increased variability, suggesting reduced control over condensation processes. In contrast, 1 mM APTES with 2 h immersion provided a balanced compromise between grafting density, reproducibility, and practical feasibility, and was therefore selected as the optimized condition.

The curing time study demonstrated that prolonged thermal treatment did not significantly increase accessible amine density under the selected conditions. Consequently, the shortest effective curing time was retained to maintain efficiency without compromising surface functionality.

XPS analysis confirmed successful APTES grafting through the appearance of Si 2p and increased C 1s signals, along with attenuation of substrate peaks. High-resolution spectra supported the formation of siloxane bonds at the zirconia interface.

The optimized protocol was subsequently transferred to PFPTES functionalization. XPS and ToF-SIMS analyses confirmed the incorporation of silicon and fluorine species at the surface, with an F/Si ratio close to the theoretical value expected from the pentafluorophenyl structure. ATR-FTIR measurements performed on high-surface-area zirconia powder further verified the presence of both siloxane linkages and characteristic aromatic fluorinated bands, confirming covalent attachment while retaining the functional moiety required for subsequent peptide coupling.

Finally, the biocompatibility of the intermediate layer, in case of exposure, was pre-screened in order to proceed to the biomolecule conjugation studies.

Overall, this systematic optimization established a reproducible and chemically validated silanization strategy for zirconia surfaces. The selected reaction window ensures controlled surface modification while maintaining functional group integrity, providing a robust platform for subsequent biofunctionalization steps.

Despite the comprehensive characterization performed, certain aspects of the silane layer could not be directly quantified. In particular, the exact thickness of the grafted layer and the absolute grafting density could not be determined with high precision. While XPS provided clear evidence of surface modification and allowed estimation of elemental ratios, it does not directly yield film thickness or molecular surface coverage for such ultrathin organic layers. Similarly, techniques such as ellipsometry or AFM thickness measurements were difficult to apply reliably to the current substrates and experimental configuration. Consequently, the structural model of the silane layer remains based on indirect indicators such as wettability changes, elemental composition, and functional group detection rather than direct thickness measurements.

Nevertheless, this work contributes to the field by establishing a controlled and experimentally validated protocol for silanization of zirconia surfaces under relatively mild and reproducible conditions. By systematically evaluating the influence of reaction parameters and combining complementary analytical techniques, this study clarifies how processing conditions affect both apparent amine density and reproducibility of surface modification. Furthermore, the successful transfer of the optimized conditions from APTES to PFPTES demonstrates the versatility of the approach and confirms the preservation of reactive pentafluorophenyl functionalities required for peptide grafting. Together, these results provide a reliable chemical foundation for the subsequent biofunctionalization strategies developed in the following chapters.

IV. Biomolecule Attachment

IV.1. Abstract

In this chapter, grafting of biomolecules onto silanized zirconia surfaces is presented, with a focus on the covalent attachment of RGDC peptides through nucleophilic substitution on an activated ester. The optimization of this reaction is detailed by examining the influence of peptide concentration, immersion time, and pH on grafting efficiency. The resulting bioactive layer is then thoroughly characterized using complementary surface analysis techniques in order to assess the extent of peptide immobilization, and its overall reproducibility. Preliminary *in vitro* cell studies are also reported to evaluate the biological response induced by the functionalized surfaces. Finally, the robustness of the layer to sterilization and mechanical stress was examined. This chapter therefore provides an overview of the methodology and outcomes associated with peptide conjugation onto silanized ZrO_2 for the development of biologically active implant surfaces.

IV.2. Introduction

Despite its excellent mechanical properties, chemical stability, and favorable aesthetics, zirconia (ZrO_2) remains a largely bioinert material, particularly with respect to soft tissue integration at the transmucosal region of dental implants [229]. A stable soft tissue seal around the abutment is critical for protecting the underlying bone against bacterial invasion and inflammatory processes, since insufficient epithelial or connective tissue attachment contributes to the development of peri-implant disease [230,231]. Although surface topography and wettability are well known to influence protein adsorption and subsequent cell behavior, their ability to provide specific and instructive biological signaling remains limited when used as sole modification strategies. Consequently, biofunctionalization approaches based on biomolecular cues have been widely explored to actively regulate cell–material interactions at the implant–tissue interface [232].

Among these strategies, the immobilization of short bioactive peptides has attracted particular interest due to their ability to mimic specific extracellular matrix (ECM) motifs while offering improved stability, reduced immunogenicity, and better chemical control compared to full-length proteins [233]. Peptides containing the Arg–Gly–Asp (RGD) sequence (**Figure IV-1**), an integrin-binding motif found in ECM proteins such as fibronectin, have been extensively investigated for

soft tissue applications. Studies have demonstrated that RGD-functionalized ZrO_2 surfaces significantly enhance the adhesion, spreading, and proliferation of human gingival fibroblasts compared to unmodified ZrO_2 [234]. In that study, peptide immobilization was achieved through a polydopamine-mediated strategy, in which a bio-inspired adhesive interlayer was first deposited on the zirconia surface to enable subsequent biomolecule attachment. While effective, such approaches rely on the formation of an intermediate coating whose thickness, chemical composition, and surface density may vary depending on deposition conditions.

Beyond promoting cell attachment, RGD-based functionalization has also been reported to influence early competitive interactions between host cells and bacteria, a key aspect of the "race for the surface" concept in implantology [235]. Importantly, these biological effects strongly depend on the immobilization strategy, as covalent grafting provides superior stability and reproducibility under physiological conditions compared to physisorbed biomolecules.

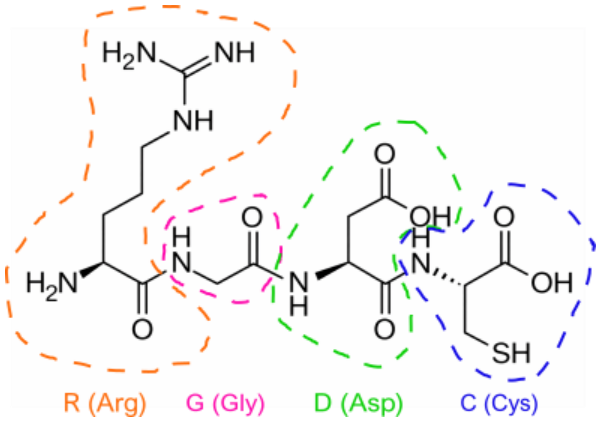

Figure IV-1. Chemical structure of the RGDC peptide (Arg–Gly–Asp–Cys), highlighting the integrin-binding RGD motif and the N-terminal primary amine used for covalent immobilization onto the activated zirconia surface.

In this chapter, we report the covalent immobilization of RGDC, an RGD-containing peptide onto ZrO_2 surfaces using a controlled and mild chemical strategy. ZrO_2 substrates were first functionalized with an activated ester moiety (**III.3.4**), enabling subsequent peptide attachment through a nucleophilic substitution reaction with the primary amine groups of the peptide. This approach was selected to enable covalent bonding under aqueous conditions compatible with biomolecule stability, while limiting undesired side reactions and preserving peptide bioactivity, through coupling of the peptide primary amine to surface-activated ester groups. The RGDC peptide was chosen as a model cell-adhesive sequence and the grafting protocol was systematically optimized by varying key reaction parameters, including peptide concentration, immersion time, and reaction pH. The efficiency of the resulting bioactive layer was assessed using complementary surface characterization techniques, allowing both qualitative and quantitative evaluation of peptide attachment. Through this systematic study, the influence of key parameters on peptide immobilization was investigated, providing a basis for defining suitable conditions for subsequent experiments.

IV.3. Materials and Methods

IV.3.1. Materials and Reagents

Ethanol (99.8%), dried ethanol (≤ 0.01% H_2O), tetrahydrofuran (THF, 99%), acetone (99.5%), 2-propanol (99.5%), dichloromethane (DCM, 99.8%), methanol (99.9%), glacial acetic acid (100%), and HEPES sodium salt hydrate were purchased from Sigma-Aldrich.

11-Pentafluorophenylundecanoatetriethoxysilane (PFPTES) was obtained from SIKEMIA (Grabels, France).

RGDC (H-Arg-Gly-Asp-Cys-OH) and FITC-labeled RGDC (H-Arg-Gly-Asp-Cys-Lys(FITC)-NH_2) peptides were purchased from Bachem (Bubendorf, Switzerland).

Deionized water (resistivity ≥ 18.2 MΩ·cm) was produced using an Elga water purification system (Veolia) and used for all aqueous solution preparations and rinsing steps.

Dichloromethane was dried prior to use by storage over activated 4 Å molecular sieves for 48 h to eliminate residual moisture that could interfere with silanization reactions. Molecular sieves were activated by heating at 250 °C for at least 12 h and cooled under reduced pressure prior to remove adsorbed water and allowed to return to room temperature under reduced pressure.

IV.3.2. Surface Preparation

IV.3.2.1. *Surface Pre-treatment*

Commercially available 3Y-TZP zirconia (ZrO_2) substrates were used throughout this study in different physical forms in order to accommodate the requirements of surface-sensitive characterization techniques and biological assays. Bulk zirconia disks, zirconia powder, and zirconia thin films deposited on glass substrates were employed depending on the experimental objective.

Bulk 3Y-TZP disks (Ø 9 mm, thickness 2 mm; provided by Anthogyr, Sallanches, France and Ø 5 mm, thickness 2 mm by DOCERAM, Dortmund, Germany) were supplied with a machined surface finish corresponding to a mean roughness of approximately 0.2 μm.

Because of a lack of sufficient samples for that study, bulk 3Y-TZP disks (Ø 11 mm, thickness 2 mm) were sintered by our NOMAD partner in KU Leuven, using TZ-3Y-E powder from Tosoh.

3-YTP zirconia powder (3 mol% yttria-stabilized ZrO_2, TZ-3Y-E from Tosoh Corporation, Japan) was used for infrared spectroscopy measurements due to its high specific surface area, allowing enhanced sensitivity to surface-bound species. The powder was chosen to be similar to

the one used for most of common dental restorations (and thus likely for the fabrication of the disks).

Zirconia thin films were also deposited on glass coverslips by reactive RF magnetron sputtering to obtain transparent substrates suitable for wound healing assays.

The different ZrO_2 substrates were prepared and functionalized following the same surface modification and peptide conjugation protocols. Unless otherwise specified, all samples were treated identically to ensure consistency and comparability of the results. The type of ZrO_2 surface used for each characterization technique is specified in the corresponding sections. The following six types of samples are later described:

1. Recycled 3Y-TZP ZrO_2 disks Ø 9mm, previously polished (see Section 2.4.2) and recycled by polishing with diamond suspensions of the following order 9µm, 3µm and 1µm for a few seconds.
2. Sintered disks using Tosoh powder (TZ-3Y-E, Tosoh Corporation, Japan), in KU Leuven, Ø 11 mm
3. 3Y-TZP disks (Ø 5mm, thickness 2mm; DOCERAM, Dortmund, Germany)
4. 3Y-TZP disks (Ø 5mm, thickness 2mm; DOCERAM, Dortmund, Germany), etched with 2% HF solution for 5min and rinsed thoroughly
5. 3 mol% yttria-stabilized ZrO_2 powder (TZ-3Y-E, Tosoh Corporation, Japan). Prior to use, the powder was debinded by calcination in air at 600 °C for 5 h.
6. ZrO_2 deposited via PVD on glass coverslides. ZrO_2 thin films were deposited onto glass substrates by reactive RF magnetron sputtering using an AC450 deposition system. In brief, prior to deposition, the substrates were thoroughly cleaned to ensure good film quality and reproducible stoichiometry. All depositions were performed at room temperature. A metallic zirconium target was sputtered in an argon/oxygen atmosphere under cold deposition conditions. The deposition was carried out using an argon flow of 50 sccm and an oxygen flow of 10 sccm, with a working pressure of 5×10^{-3} mbar and an RF power of 100 W. The deposition time was fixed at 10 min. Based on a previously calibrated deposition rate of 0.875 nm·min^{-1} for this system, the resulting ZrO_2 film thickness was estimated to be approximately 9–10 nm.

To ensure clear identification of the different ZrO_2-based substrates used throughout this study, a nomenclature was adopted (**Table IV-1**). Each sample identifier reflects both the physical form of the material (bulk disk, powder, or thin film) and its origin or surface processing history. This approach allows consistent cross-referencing of samples across experimental sections and facilitates direct comparison between surface states and processing conditions.

Sample ID	Sample type	Origin/Supplier	Geometry	Processing History
ZR-REC	Bulk ZrO_2 disk	3Y-TZP, recycled (see Chapter 2, Section 2.4.2)	Ø 9 mm	Previously polished disks (Anthogyr, ZR-P), recycled by sequential diamond polishing (9 μm → 3 μm → 1 μm, few seconds each)
ZR-KU	Bulk ZrO_2 disk	Tosoh powder, pressed and sintered at KU Leuven	Ø 11 mm	Disks sintered from Tosoh ZrO_2 powder following KU Leuven processing protocol
ZR-PW	ZrO_2 powder	TZ-3Y-E, Tosoh Corporation, Japan	powder	Calcined in air at 600 °C for 5 h
ZR-DOC	Bulk ZrO_2 disk	3Y-TZP, DOCERAM (Dortmund, Germany)	Ø 5 mm	As-received disks, no additional surface treatment
ZR-DOC-HF	Bulk ZrO_2 disk	3Y-TZP, DOCERAM (Dortmund, Germany)	Ø 5 mm	Chemically etched in 2% HF solution for 5 min, followed by thorough rinsing
ZR-PVD	ZrO_2 thin film	ZrO_2 on glass (PVD-deposited)	~10 nm thickness	Reactive RF magnetron sputtering on glass coverslides using AC450 system (Ar 50 sccm, O_2 10 sccm, 5×10^{-3} mbar, 100 W RF, 10 min deposition, room temperature)

Table IV-1. Definition, origin, geometry, and processing history of the ZrO_2-based samples used in this study. Sample identifiers are constructed to encode the material form (bulk, powder, or thin film), supplier or fabrication route, and any additional surface treatment, enabling clear and consistent referencing throughout the manuscript.

All disks, before any treatment, were cleaned with a series of solvents, for 10min each, under sonication: acetone, 2-propanol, ethanol, Milli-Q H_2O and dried under N_2 stream.

The UV–ozone cleaning was performed using a Novascan UV–Ozone Cleaner (PSD/PSDP series) operating under ambient conditions with a supplemental oxygen flow. The UV lamp operated at an irradiance of 28–32 mW/cm² at 254 nm, and the samples were treated for 30 min.

IV.3.2.2. *Silanized Surfaces Preparation*

Functionalization was performed by immersing the activated substrates (30min in UV/O_3) in a freshly prepared 1 mM PFPTES solution, in anhydrous dichloromethane (DCM), for 2 h at room temperature. The PFPTES solution was prepared immediately before use by adding the silane to dried DCM, which had been stored over 4Å molecular sieves for at least 24 h. Following immersion, substrates were removed from the solution, and subjected directly, without rinsing, to annealing at 110°C for 1 h to promote siloxane condensation and film stabilization. After annealing, samples were rinsed three times, at room temperature, with freshly dried DCM under sonication, to remove physisorbed or polymerized species and then dried under nitrogen. Functionalized substrates were stored in dry conditions to avoid the hydrolysis of the activated ester, until characterization or further use.

For experiments conducted on 3Y-TZP ZrO_2 powder (ZR-PW), the same silanization protocol was applied. Due to the powder morphology, samples were collected after immersion by vacuum filtration using a 47 mm Durapore PVDF membrane (0.45 μm), washed three times with dry DCM, and dried at 110 °C for 5 min prior to further functionalization.

IV.3.2.3. *RGDC grafting on Silanized Surfaces*

Peptide conjugation was performed on PFPTES-functionalized surfaces by immersion in a RGDC peptide solution (1 $mg \cdot mL^{-1}$, 2.2 mM) prepared in 50 mM HEPES buffer. The buffer pH was adjusted to 8 using 0.05 M NaOH. The reaction was carried out for 2 h to promote nucleophilic substitution between the peptide primary amine group and the activated pentafluorophenyl ester. After conjugation, the samples were rinsed with tetrahydrofuran (THF) to remove the pentafluorophenyl by-product, followed by sequential sonication in HEPES buffer and MilliQ water for 5 min each. The surfaces were then dried under a nitrogen stream and stored prior to characterization.

For PFPTES-functionalized ZrO_2 powder, RGDC conjugation was performed under identical conditions. Following reaction, the powder was recovered by vacuum filtration and successively washed with HEPES buffer and Milli-Q water, followed by THF and DCM, to remove unreacted peptide and reaction by-products. The functionalized powder was finally dried prior to characterization.

IV.3.3. Mechanical Stressors (Brushing) Test

IV.3.3.1. *Experimental Set-up*

A custom brushing test was performed using a mechanical testing setup (**Figure IV-2**) designed to simulate daily oral hygiene conditions. Characterization of the layer after brushing was performed using fluorescence imaging using RGDC-FITC modified samples. Consequently, to preserve the fluorescence signal of the FITC-labelled RGDC peptide, the entire setup was operated in the dark by covering the machine enclosure with an opaque cloth.

The system consisted of three toothbrushes mounted on a support connected to the mobile actuator of a BOSE 1010CCH-250-B testing machine. Each toothbrush was equipped with a joint and spring mechanism, enabling the application of a controlled axial force. Zirconia samples (ZR-DOC disks functionalized with RGDC-FITC) were mounted on a dedicated holder positioned in front of each toothbrush. The protrusion of each sample relative to the holder was measured using a mechanical comparator to ensure consistent positioning. For the experiment, the following materials were used:

- Hard toothbrushes “SIGNAL Action Anti Plaque” (68295643) (Unilever).
- Tap Water

The load applied by each toothbrush head was measured using a dynamometer and adjusted to 4 N (±1 N) by radially positioning the setup. Brushing was performed with a linear motion of 14 mm amplitude at a frequency of 3 Hz.

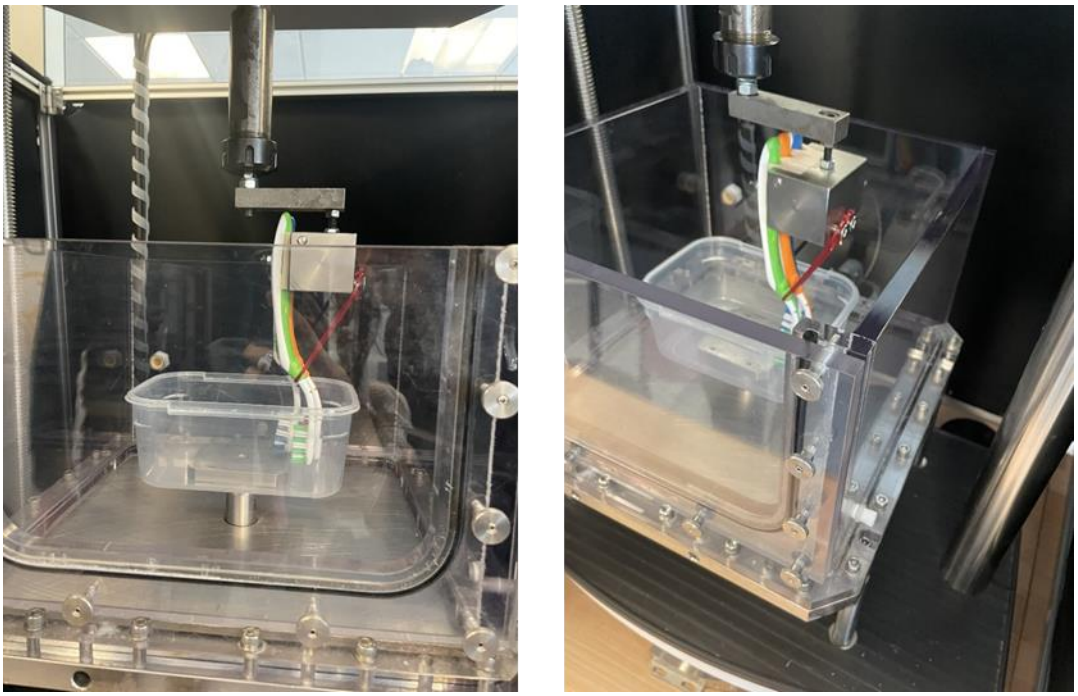

Figure IV-2 Experimental setup for the brushing test, in the facilities of our NOMAD partner, Anthogyr.

During testing, the samples were fully immersed in tap water (total volume < 1 L) to mimic the wet oral environment.

Three different brushing durations were applied: 100, 1,000, and 22,500 cycles. The highest number of cycles corresponds to approximately six months of daily tooth brushing, assuming two brushing sessions of two minutes per day.

The functionalized and brushed samples, before submitted to fluorescence characterization, were rinsed with acetone to remove residues from the surface.

Three different sample types were tested:

- 1 control sample ZR-DOC; it had gone through the cleaning process with solvents (Acetone, IPA, EtOH and DI H_2O)
- 1 RGDC-FITC modified ZR-DOC sample produced according to the optimized protocol (**IV.3.2.3**); it served as a control sample for the brushing test (before)
- 3 RGDC-FITC modified ZR-DOC sample produced according to the optimized protocol (**IV.3.2.3**); that went through the three different number of brushing cycles.

IV.3.3.2. *Fluorescence Quantification*

Fluorescence intensity was quantified using regions of interest (ROIs) defined on the acquired microscopy images. For each sample, three linear ROIs were selected, with lengths of 3.739 μm, 3.963 μm, and 4.674 μm. These line profiles were positioned consistently across all samples to ensure comparability and to account for local surface heterogeneity.

The fluorescence intensity along each ROI was extracted using LAS X software (Leica Microsystems), and the mean intensity value was calculated for each line. For each sample, the reported fluorescence intensity corresponds to the mean of these three ROI mean values, while the associated standard deviation reflects the variability between ROIs.

IV.3.4. Characterization Methods

IV.3.4.1. *X-ray Photoelectron Spectroscopy (XPS)*

For theoretical insights, see **II.3.3.2**.

A subset of the XPS measurements and analyses were performed by Dr Vincent Humblot (Franche-Comté Électronique Mécanique Thermique et Optique), using a Thermo Fisher NEXSA G2 photoelectron spectrometer, equipped with a standard AlKa monochromated source (hν = 1486.6 eV), operated at a 150 W electron beam power. The emission of photoelectrons from the sample was analyzed at a takeoff angle of 90° under ultra-high vacuum conditions of $\leq 10^{-9}$ mbar. Spectra were carried out with 150 eV pass energy for the survey scan and 50 eV pass energy for elementary high-resolution regions. Binding energies (BE) were calibrated against C 1s aliphatic carbon bonds (C–C and CH) binding energy at 284.8 eV and element peak intensities were corrected according to Scofield factors. The spectra were fitted using Casa XPS v.2.3.15 software (Casa Software Ltd, U.K.) and applying a Gaussian/Lorentzian ratio equal to 70/30. The peak areas were determined after subtraction of a Shirley background.

IV.3.4.2. *Time-of-Flight Secondary Ion Mass Spectrometry (ToF-SIMS)*

For theoretical insights, see **III.3.5.4**.

Positive and negative static SIMS spectra were acquired on a ToF-SIMS IV instrument (IONTOF GmbH) using a 25 keV Bi^+ primary ion beam. The primary ion current was on average 0.97 pA, with a pulse width below 0.8 ns. Measurements were performed under static SIMS conditions, with a primary ion dose of approximately 5×10^{11} ions·cm^{-2}, well below the static limit of 1×10^{13} ions·cm^{-2}, thereby minimizing beam-induced surface damage and associated artefacts. Spectra were collected from a 50 × 50 μm² analysis area within a 100 × 100 μm² irradiated region, with a minimum acquisition time of 30 s per spot for each polarity. Data processing was carried out using SurfaceLab 7.3. The ion-irradiated areas were considered locally modified and were not used for subsequent analyses.

IV.3.4.3. *Fourier-transform infrared spectroscopy (FTIR)*

For theoretical insights, see **III.3.5.5**

Fourier-transform infrared spectroscopy (FTIR) is a technique that identifies chemical bonds and functional groups by measuring the absorption of infrared light at specific wavelengths corresponding to molecular vibrations. In this study, FTIR was used to qualitatively identify and semi-quantitatively assess the efficacy of the silanization protocols on zirconia powder.

Fourier-transform infrared (FTIR) spectra were collected at a resolution of 2 cm^{-1} using a Nicolet 6700 FT-IR Spectrometer (Thermo Fisher Scientific) equipped with a DTGS detector. The spectrometer was used in the transmission mode.

The measurements were taken with pressed pellets using ZR-PW. Samples were prepared as self-supporting pellets by weighing 20 mg of powder, which was pressed into circular pellets of 0.7 cm diameter. The mass was checked before and after pressing (1.5 Ton) to ensure no loss. This corresponds to a surface loading of approximately 52 mg cm^{-2}, suitable for IR analysis.

The spectra presented correspond to the raw absorbance data acquired by the instrument, as the background measurement was automatically recorded before each sample acquisition and substracted by the instrument software during data collection. No additional background subtraction or post-processing was applied to the FTIR spectra.

IV.3.4.4. *Fluorescence Microscopy*

Fluorescence microscopy was used to visualize fluorescently labeled samples. The technique is based on the excitation of fluorophores at a specific wavelength and the subsequent emission of light at a longer wavelength. The emitted fluorescence was separated from the excitation light using appropriate optical filters and collected to form the image.

Fluorescence microscopy was used to visualize the presence of a fluorescent marker (FITC) attached to the RGDC peptide on the functionalized zirconia surfaces. Images were acquired using a Leica THUNDER Imager fluorescence microscope (Leica Microsystems) equipped with an integrated computational clearing system and a Leica DFC9000 GTC camera. Fluorescence was detected using a Y3 filter set, with excitation in the range of 532–558 nm, a dichroic mirror at 565 nm, and emission collected between 570 and 640 nm. Images were recorded without pixel binning using a 16-bit digitization depth (intensity range: 0–65 535 counts) and a linear gamma setting. Image acquisition was performed using a fixed exposure time of 50 ms and identical detector gain settings for all samples. Samples were observed using the same objective lens for all measurements, yielding a pixel size of 1.63 μm. For visualization purposes, the fluorescence intensity display range was adjusted at the software level to facilitate qualitative comparison between samples, while the raw image data remained unmodified. Image acquisition and processing were performed using the manufacturer's software.

The intensity was quantified using 3 ROIs per sample

IV.3.5. Biological Assays Protocols

IV.3.5.1. *Cytotoxicity Assay*

The second set of assays to evaluate the cytotoxicity using a direct-contact cell viability assay was conducted by Prof. Henny C. van der Mei and Dr. Lu Yuan at the University Medical Center Groningen, who also managed the data. Cytotoxicity was assessed after 24 h of direct contact using the PrestoBlue assay. This assay is based on the reduction of non-fluorescent resazurin into fluorescent resorufin by metabolically active cells. After removal of the culture medium, samples were rinsed twice with phenol red-free RPMI. The PrestoBlue reagent was diluted to 10% (v/v) in RPMI and added to each well. Following incubation at 37 °C for 2 h, fluorescence was measured using an INFINITE PRO 200 fluorimeter (excitation 535 nm, emission 610 nm, gain 40). Measurements were performed in triplicate for each condition, and the entire experiment was repeated three independent times. Reagent-only blanks were included for background subtraction.

Cytotoxicity evaluation was performed using human gingival fibroblasts (HGF) and human oral keratinocytes (HOK). Prior to cell seeding, zirconia implants were sterilized by immersion in 70% ethanol for 30 min, followed by three rinses with sterile demineralized water and three washes with sterile PBS to remove residual ethanol.

HGF were cultured in DMEM high glucose supplemented with 10% fetal bovine serum (DMEM-HG + 10% FBS), while HOK were maintained in DermaLife K medium, under standard conditions (37 °C, 5% CO_2). Cells were subcultured at 80–90% confluency. Detachment was performed using trypsin–EDTA (1 mL for T25 flasks, 2 mL for T75 flasks) for approximately 3 min at 37 °C. Trypsin activity was neutralized with complete culture medium, and the cell suspension was collected and centrifuged (1,000 rpm, 5 min).

Cell number and viability were determined by Trypan Blue exclusion using a Bürker–Türk counting chamber. The total cell density was calculated from the counted areas and adjusted to a final concentration of 1×10^6 cells/mL prior to seeding.

For cytotoxicity assessment, HOK were seeded at a density of 5×10^4 cells/mL and HGF at 2.5×10^4 cells/mL. Cells were seeded either in 24-well plates (1 mL per well) or directly onto the implant samples. For smaller implant formats placed in 48-well plates, a reduced seeding volume of 0.5 mL per well was used. Cells were incubated under standard culture conditions for 1 and 3 days prior to further analysis.

Cell metabolic activity was also evaluated using a CyQUANT™ XTT Cell Viability Assay (Thermo Fisher Scientific). After 1 and 3 days of culture, phase-contrast images of the cells surrounding the implants were first acquired. Samples were then transferred to fresh culture plates and incubated with freshly prepared XTT working solution for 2 h at 37 °C. Following incubation, 150 µL of the supernatant was transferred in triplicate to a 96-well plate, and absorbance was measured at 450 nm with a reference wavelength of 660 nm using a microplate

reader. Cell viability was calculated after blank correction and normalized to the control (cells cultured on tissue culture plastic), following ISO 10993-5 recommendations.

Cell morphology and cytoskeletal organization were evaluated by fluorescence microscopy after 1 and 3 days of culture. Samples were washed with PBS, fixed in 4% formaldehyde for 30 min, permeabilized with 0.2% Triton X-100 for 5 min, and blocked with 1% bovine serum albumin (BSA) in PBS. Actin filaments were stained using FITC-conjugated phalloidin (1:1000), while cell nuclei were counterstained with DAPI (1:200). After incubation for 30 min in the dark, samples were washed and imaged using a Leica Thunder fluorescence microscope. Cell density and surface coverage were subsequently quantified using Fiji (ImageJ).

IV.3.5.2. *Tube Formation Assay*

Tube formation assays were performed by Prof. Henny C. van der Mei and Dr. Lu Yuan at the University Medical Center Groningen, who also managed the data. Human umbilical vein endothelial cells (HUVECs, pooled) were cultured in EGM®-2 Endothelial Cell Growth Medium-2 under standard conditions (37 °C, 5% CO_2) and used at 70–90% confluency. Cells were detached using 0.05% trypsin–0.025% EDTA, neutralized with complete culture medium, and collected by centrifugation (1,000 rpm, 5 min). Cell number and viability were determined by Trypan Blue exclusion using a Bürker–Türk counting chamber. The cell pellet was subsequently resuspended in EGM-2 medium at the required density for tube formation experiments.

For the assay, the functionalized disks, inside 96-well plates, were coated with Matrigel to provide a basement membrane-like matrix supporting endothelial network formation. Matrigel was handled on ice to prevent premature gelation and either used directly or diluted 1:1 in cold PBS prior to coating. A total volume of 50–100 µL per well was applied, and the coated plates were incubated at 37 °C for 30–60 min to allow complete gelation.

HUVECs were seeded onto the Matrigel-coated wells at a density of 5×10^5 cells/mL (100 µL per well) and incubated under standard culture conditions. Tube formation was monitored using an IncuCyte live-cell imaging system (4× objective), with images acquired at 1 h intervals for up to 6 h. Quantitative analysis of network formation was performed according to established image analysis protocols.

Tube formation was quantitatively analyzed using ImageJ software, where nodes corresponding to branching points were identified (red dots) and meshes corresponding to enclosed network areas were quantified (yellow circles).

IV.3.5.3. *Wound Healing Assay*

Wound healing assays were performed by Prof. Henny C. van der Mei and Dr. Lu Yuan at the University Medical Center Groningen, who also managed the data. Transparent ZR-PVD substrates were used to allow direct optical monitoring of cell migration. ZrO_2 thin films were deposited onto glass coverslips by physical vapor deposition (PVD), as described in Section 4.2.5.2, and subsequently functionalized using the optimized biofunctionalization protocol.

Selected samples were additionally grafted with a fluorescently labeled peptide to verify successful surface functionalization by fluorescence microscopy.

Human gingival fibroblasts (HGF) and human oral keratinocytes (HOK) were cultured under standard conditions (37 °C, 5% CO_2) until 80–90% confluency. Cells were detached using trypsin, neutralized with fresh culture medium, and counted using a Burk–Türk counting chamber with Trypan Blue exclusion to determine viable cell density. Cells were then resuspended at defined concentrations to ensure the formation of a confluent monolayer within 24 h after seeding.

For the migration assay, cells were seeded directly onto the functionalized ZR-PVD substrates placed in multiwell plates and allowed to reach confluence. A linear wound was then created in the cell monolayer using a sterile 200 μL pipette tip. After removal of detached cells and addition of fresh culture medium, samples were incubated under standard culture conditions. Wound closure was monitored over time using live-cell imaging (IncuCyte system), and images were acquired at identical positions for each sample. The wound area at each time point was quantified using FIJI software and normalized to the initial wound area measured immediately after scratch formation to calculate the percentage of wound closure.

IV.4. Results & Discussion

In the following section, the influence of key reaction parameters is discussed in detail to assess their role in controlling the efficiency and robustness of RGDC peptide conjugation. Peptide concentration, buffer composition, and pH were varied, as they strongly affect the nucleophilic substitution reaction between the peptide amine and surface-bound pentafluorophenyl esters. RGDC was chosen as a model peptide owing to its well-established cell-adhesive properties and its frequent use in surface functionalization studies.

IV.4.1. Optimization of Peptide Conjugation Parameters

IV.4.1.1. *Concentration & Immersion Time*

RGD peptide-based surface functionalization studies have frequently reported an increase in immobilized peptide amount with increasing solution concentration, although the extent of this relationship depends on the substrate, coupling chemistry, and experimental design.

In one study, surface peptide density increased with solution concentration over a range spanning 0.01 – 4.0 $mg \cdot mL^{-1}$, with peptide immobilization performed at room temperature in aqueous solution using EDC-mediated coupling at pH 4.5 – 4.7, following an initial 30 min incubation and a subsequent reaction [236]. The authors reported a quantitative relationship between

input peptide concentration and surface density, with a pronounced increase at lower concentrations (0.01–1.0 mg·mL^{-1}) and a progressive saturation behavior at higher concentrations (1.0–4.0 mg·mL^{-1}), attributed to the occupation of available surface reactive sites. Another work employing EDC/NHS chemistry used solution concentrations from 0.05 to 0.5 mg·mL^{-1} to achieve measurable surface immobilization [237]. Additionally, RGD uptake efficiency on polymer networks was found to peak at ~2.0 mg·mL^{-1}, suggesting that higher concentrations may not always increase grafting due to limited available binding sites [237].

For metal oxide and implant-relevant surfaces such as titanium and titanium oxide, RGD and RGD-containing peptides have typically been grafted using solution concentrations in the sub-millimolar to low millimolar range. Reported concentrations most commonly fall between approximately 0.1 and 1 mM, depending on peptide sequence, coupling chemistry, and surface preparation strategy[105,238–244].

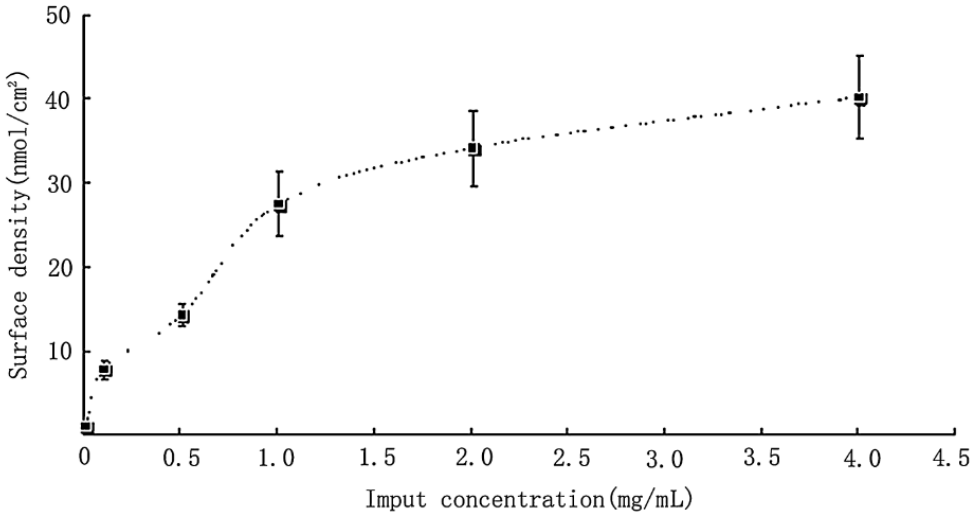

Figure IV-3. Surface density versus input concentration of RGD peptides grafted on bone cartilage, *reproduced by* [236].

In the present work, to remain within concentration ranges reported in the literature while limiting excessive peptide consumption, the lower-to-intermediate portion of these reported ranges was explored to assess whether sufficient peptide immobilization could be achieved on PFPTES-modified ZrO_2 surfaces. Accordingly, RGDC solution concentrations from 125 to 1000 μg·mL^{-1} (0.28–2.2 mM) were selected for the systematic evaluation of surface coverage and XPS-detectable peptide immobilization.

For the lowest concentration tested (0.28 mM or 125 μg·mL^{-1}), we compared two coupling strategies: conventional immersion and an evaporation-assisted method, in which a 100 μL droplet of peptide solution was deposited on the PFPTES-functionalized ZrO_2 disk and allowed to evaporate overnight under ambient conditions. This droplet evaporation approach can locally

increase peptide concentration at the interface, potentially enhancing grafting efficiency without increasing the total peptide usage. For the remaining conditions, RGDC concentrations ranged from 0.28 mM (125 μg·mL^{-1}) to 2.2 mM (1000 μg·mL^{-1}), with intermediate concentrations of 0.56 mM and 1.1 mM. Peptide coupling was performed by immersing the samples in the peptide solution for 1 h, a duration selected based on previous immobilization protocols reporting substantial surface attachment of RGD-family peptides within similar timeframes. Previous XPS-based studies have demonstrated covalent RGD peptide grafting onto oxide and silane-modified substrates with effective attachment achieved within incubation times on the order of one hour [105,245,246]. All peptide solutions were prepared in carbonate (Na_2CO_3) buffer, chosen for its compatibility with nucleophilic substitution reactions and peptide stability.

For these experiments, ZR-REC disks were functionalized following the protocol described in **IV.3.2.2**. After UV/ozone activation, peptide grafting was carried out by immersion in RGDC solutions prepared in carbonate buffer for 1 h at the indicated concentrations. Following functionalization, the disks were rinsed and dried prior to surface characterization. Control samples consisted of identically treated Zr-REC disks immersed in DCM without PFPTES and carbonate buffer without RGDC.

Table IV-2 summarizes the atomic percentages of the elements detected by XPS on the sample surfaces (ZR-REC). All values correspond to the mean of three independent measurements for each sample type.

	XPS At%					
	Control	**PFPTES**	**RGDC 500 μg/ml**	**RGDC 250 μg/ml**	**RGDC 125 μg/ml**	**RGDC 125 μg/ml (evap)**
Zr 3d	14	16± 1.7	15.7 ± 2.5	17.7 ± 1.2	16.7 ± 0.6	19.0 ± 1.4
Y 3d	1	1	1	1	1	1
O 1s	45	41.7 ± 2.1	49 ± 1.7	46.7 ± 1.5	46.3 ± 1.2	48.5 ± 0.7
C 1s	30	35.7 ± 3.8	29.7 ± 1.5	30.3 ± 1.5	31.3 ± 0.6	28.5 ± 0.7
Si 2p	-	2	2	2.0 ± 1.0	1.7 ± 0.6	2.5 ± 0.7
F 1s	-	3.7 ± 1.2	2.5 ± 0.7 (*n* = 2)	2	2.3 ± 0.6	1.5 *(n = 1)*
N 1s	-	-	0.5 (*n = 1*)	-	-	0.5 *(n = 1)*

Table IV-2. Mean atomic percentages (n = 3) obtained by XPS for ZrO_2 samples functionalized with RGDC peptides at different solution concentrations in carbonate buffer following a 1 h grafting reaction. When indicated, n = 1 or n = 2 denotes that the corresponding element was detected in only one or two of the three analyzed samples.

The relatively high fluorine atomic percentages detected after immersion in the RGDC peptide solution, combined with the absence of a detectable N 1s signal, suggest that peptide grafting under these conditions is incomplete. The N 1s was, when detected so low, that resembled background noise (**Figure IV-4**). The persistence of the F 1s signal indicates that a significant fraction of the pentafluorophenyl groups from the PFPTES layer remains unreacted, while the lack of nitrogen, which is characteristic of the peptide backbone, points to a limited surface coverage by RGDC. Together, these observations imply that nucleophilic substitution of the activated ester is not quantitative and that only partial substitution of the fluorinated moieties by the peptide occurs.

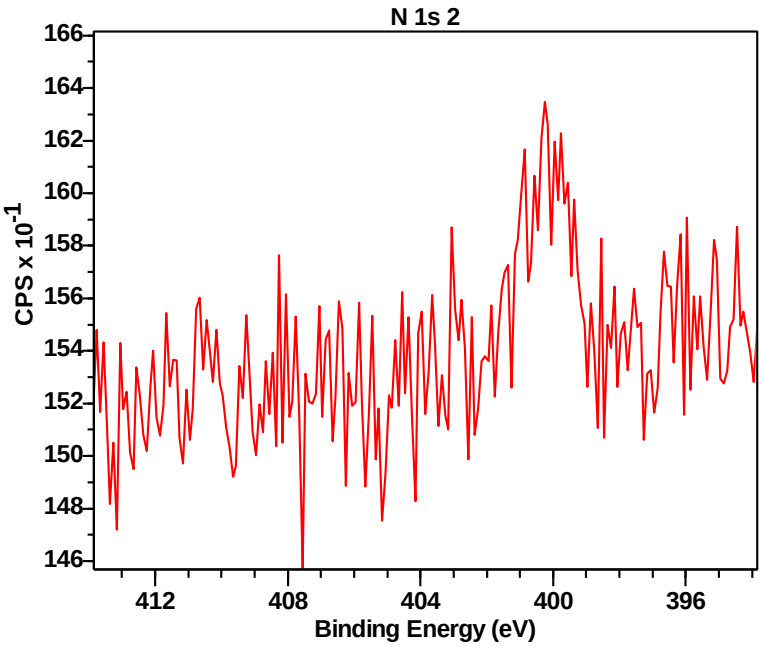

Figure IV-4. High-resolution XPS N 1s spectrum of ZR-REC samples functionalized with RGDC at 500 µg/mL (≈ 1.15 mM). The N 1s signal appears at very low intensity and close to the noise level, indicating minimal detectable nitrogen at the surface. This weak signal suggests a low peptide surface coverage and/or nitrogen concentration near the XPS detection limit under these conditions.

For these reasons, subsequent experiments were conducted under modified conditions, combining the highest peptide concentration tested (1 mg·mL^{-1}) with an extended immersion time of 2 h in order to promote the conjugation reaction. In parallel, the experimental approach was adapted to enable more practical characterization, leading to the use of powder-based model systems and FTIR spectroscopy. As discussed in later sections, the combined use of these conditions was associated with the disappearance of the F 1s signal, indicating consumption of the activated ester groups and suggesting improved peptide grafting efficiency.

These findings highlight the need for further investigation of the grafting reaction beyond solution concentration alone. Moreover, as XPS was not available as a routine method, complementary characterization strategies were required. For this reason, subsequent sections

additionally examine peptide functionalization using FTIR spectroscopy and 3-YTP powder (ZR-PW).

IV.4.1.2. *Buffer Selection and pH adjustment*

Fourier-transform infrared spectroscopy (FTIR) was employed as a complementary technique to probe chemical changes associated with surface functionalization, particularly on zirconia powder samples where the high specific surface area enhances sensitivity to surface-bound species.

Figure IV-5 shows the FTIR spectra of activated ZR-PW (control), PFPTES-functionalized surfaces, and samples exposed to the RGDC peptide under the previously discussed grafting conditions. Following silanization, several characteristic features associated with PFPTES are observed. In particular, weak bands in the 2950–2850 cm^{-1} region are attributed to alkyl C–H stretching vibrations of the silane chain, while a sharp band around ~1520 cm^{-1} is assigned to aromatic C=C stretching vibrations of the pentafluorophenyl group. Additional absorptions in the 1350–1200 cm^{-1} region are consistent with C–F stretching vibrations of the pentafluorophenyl moiety. A strong band centered around ~1010 cm^{-1} is attributed to overlapping Si–O–Si and interfacial Si–O–Zr stretching vibrations.

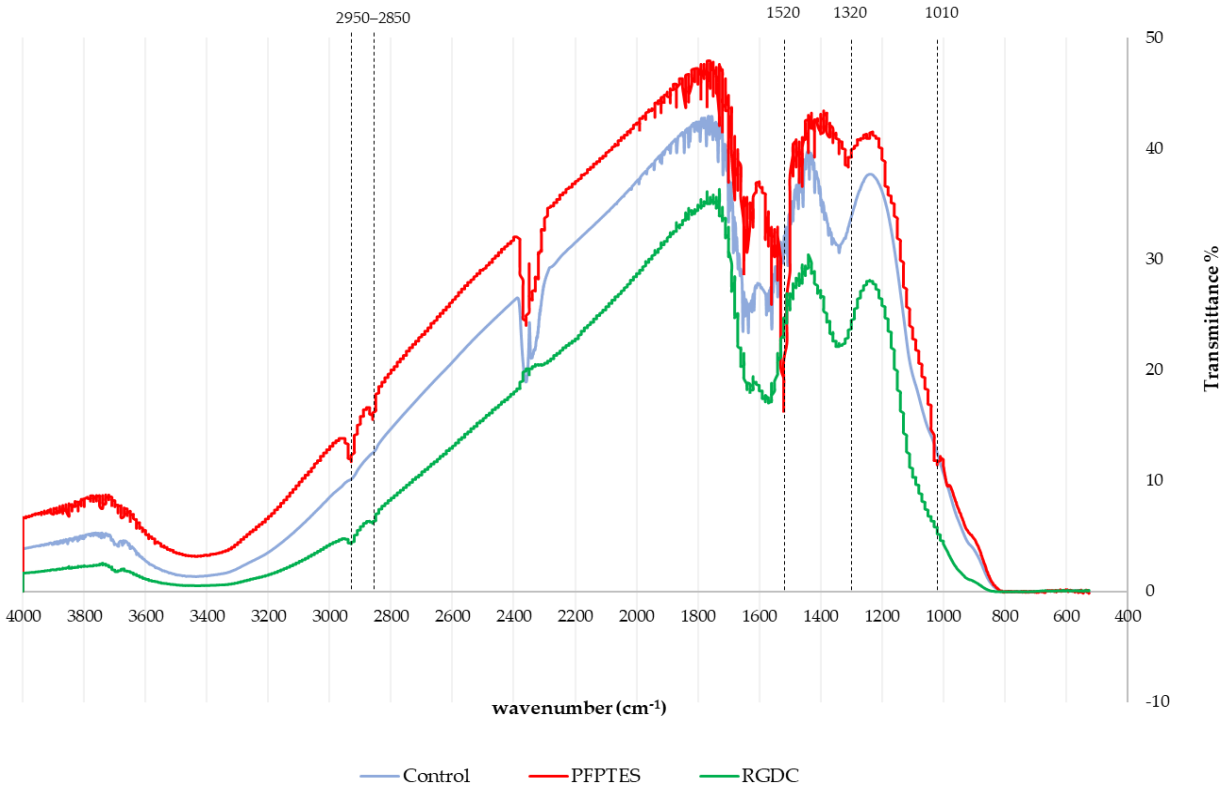

Figure IV-5. Stacked FTIR spectra of 3Y-TZP ZrO_2 powder (ZR-PW) after different surface treatments: control powder immersed in dichloromethane (DCM) and carbonate buffer (blue), PFPTES-functionalized powder after silanization in 1 mM PFPTES in anhydrous DCM (2 h) followed by 1h annealing (red), and

PFPTES-functionalized powder after exposure to RGDC peptide (1 mg·mL^{-1}, 2.2 mM) in carbonate buffer for 2 h (green).

All spectra are dominated by carbonate-related absorptions, with bands extending through the 1600–1700 cm^{-1} region.

Taken together, these FTIR results clearly confirm successful PFPTES silanization of the zirconia surface, while peptide-related vibrational features cannot be conclusively resolved at this stage. This spectrum therefore represents an initial, non-optimized condition in which RGDC grafting could not be directly evidenced by FTIR spectroscopy, motivating subsequent optimization of reaction parameters and the use of complementary characterization approaches described in the following sections. However, due to the strong affinity of zirconia for atmospheric and aqueous carbonate species, FTIR interpretation is inherently limited by overlapping absorption bands in the 1500–1700 cm^{-1} region. Consequently, FTIR results are interpreted in conjunction with XPS and ToF-SIMS data and are used here to provide supportive rather than standalone evidence of peptide grafting.

Following immersion in carbonate buffer, intense FTIR absorption bands attributable to adsorbed carbonate species were observed, indicating significant interaction between the ZrO_2 surface and carbonate ions under aqueous conditions. This observation prompted further examination of the buffer system used during peptide conjugation.

The carbonate buffer initially employed exhibited a pH of approximately 9.6. While mildly basic conditions are required to enhance the nucleophilicity of primary amines and promote their reaction with activated esters, excessively high pH values are known to accelerate competing hydrolysis reactions of activated ester functionalities and may negatively affect peptide stability [98,247]. Pentafluorophenyl esters are widely used for peptide immobilization due to their high reactivity toward amines under mildly basic conditions; however, their susceptibility to hydrolysis increases markedly at elevated pH [98,247]. As a result, although the carbonate buffer provided sufficient basicity to activate the RGDC amine functionality, its high pH likely favored partial hydrolysis of the surface-bound ester groups, thereby limiting effective peptide grafting.

Given the relatively short reaction time (2 h), the buffering strategy was therefore simplified. The peptide solution was prepared in water and its pH adjusted to approximately 8 using small aliquots of NaOH (0.05 M), a pH range commonly reported to balance efficient amine–ester coupling with minimized ester hydrolysis. The adjusted pH was verified using a calibrated pH meter prior to immersion of the PFPTES-functionalized powder. For the "control" sample, the ZR-PW was immersed in DCM and then in DI H_2O.

In **Figure IV-6**, the presence of the PFPTES layer is confirmed by the appearance of a sharp absorption band at approximately 1520 cm^{-1}, attributed to aromatic C=C stretching vibrations of the pentafluorophenyl group, as discussed previously.

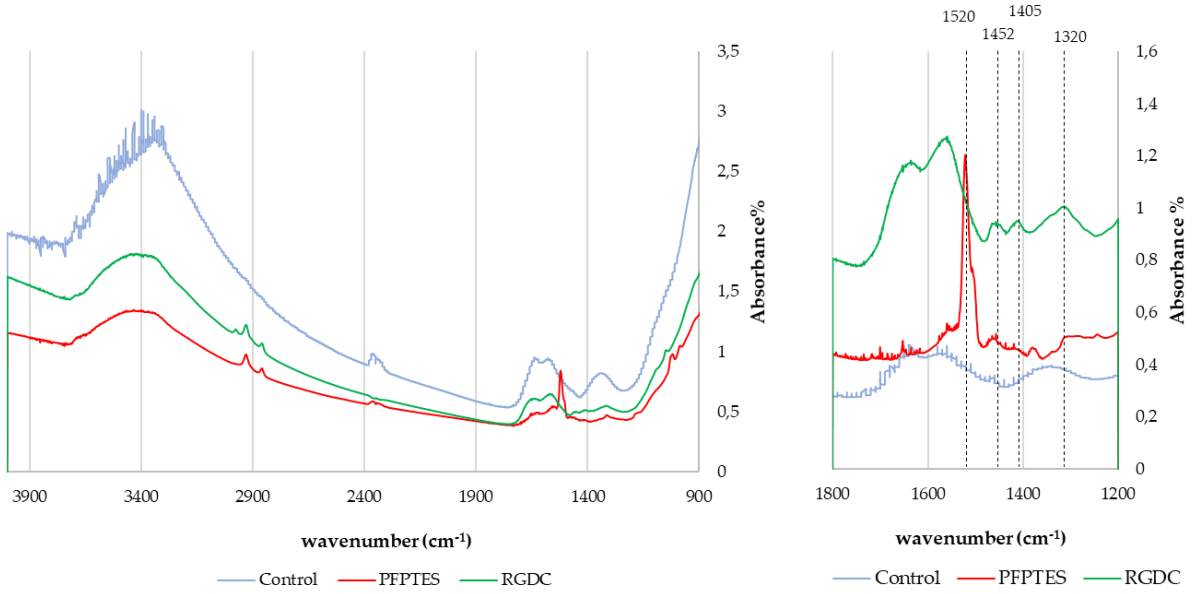

Figure IV-6. Stacked FTIR spectra of 3Y-TZP ZrO_2 powder after successive surface treatments. The control powder immersed in dichloromethane (DCM) is shown in blue, the PFPTES-functionalized powder obtained after silanization in 1 mM PFPTES in anhydrous DCM by annealing is shown in red, and the PFPTES-functionalized powder after exposure to RGDC peptide (1 mg·mL^{-1}, 2.2 mM) in DI H_2O (pH 8) for 2 h is shown in green.

Upon exposure to the RGDC peptide solution, additional absorption features are observed in the 1800–1200 cm^{-1} region. Compared to the PFPTES-functionalized sample, new bands emerge at approximately 1452, 1405, and 1320 cm^{-1}. These features are not present in the PFPTES spectrum and therefore reflect chemical or structural changes induced by peptide exposure. The bands at 1452 and 1405 cm^{-1} fall within a region commonly associated with aliphatic C–H deformation modes and symmetric stretching vibrations of carboxylate groups, consistent with the introduction of peptide-derived functionalities such as aliphatic side chains and aspartic acid residues. The band observed around 1320 cm^{-1} may include contributions from peptide backbone vibrations, including amide III–related modes involving C–N stretching and N–H bending.

An RGDC reference spectrum was not feasible due to low concentration of the solutions used. To further attribute these newly observed absorption bands, relevant literature on the functionalization of nanoparticles with RGD-derived peptides and their infrared characterization was examined. In the work of Di Pietro *et al.* [248], the authors investigated the functionalization of silver nanoparticles with an RGD-derived peptide, specifically a fluorescent cyclic RGD sequence. In the Supporting Information of this study, FTIR spectra of the hybrid AgNP/peptide systems are presented and compared with those of the free peptide and bare silver nanoparticles (**Figure IV-7**), providing useful reference features for peptide-related vibrational modes.

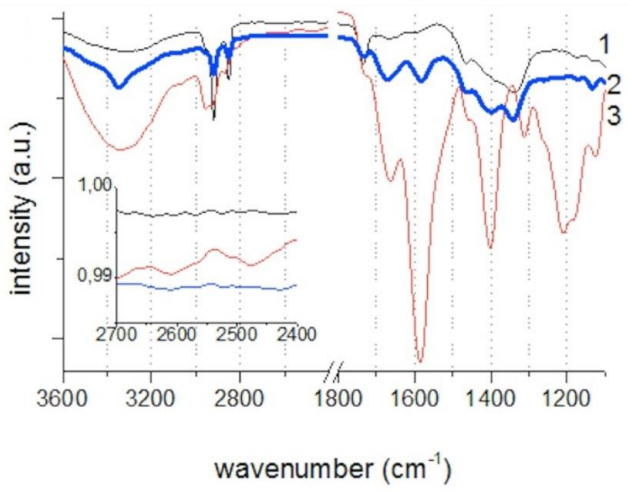

Figure IV-7. Recorded FT-IR spectra of the bare silver colloidal particles (line 1), the unbound peptide (line 3) and the AgNP- peptide systems (line 2) for $RGD(GC)_2$, *reproduced from* [248].

The FTIR spectrum of the free RGDC peptide reported by Di Pietro *et al.* exhibits characteristic absorption bands associated with peptide functionalities, including prominent features in the 1450–1400 cm^{-1} region, attributed to aliphatic C–H deformation and carboxylate-related vibrations, as well as a band near ~1320 cm^{-1} assigned to amide III–related modes involving C–N stretching and N–H bending. These bands are also observed, with modified intensity and shape, in the spectra of RGDC-functionalized silver nanoparticles, indicating their persistence upon peptide immobilization.

However, this spectral region overlaps with vibrational modes arising from surface species inherent to zirconia powders, and remains influenced by strong background absorptions. In particular, the spectral window typically associated with peptide amide vibrations is dominated by broad contributions extending from the 1600–1700 cm^{-1} region. As a result, despite the appearance of new bands following RGDC treatment, these features cannot be unambiguously assigned to peptide amide I or amide II vibrations. Nevertheless, the appearance of new absorption features following RGDC exposure indicates chemical modification of the surface, which is further investigated and corroborated using more surface-sensitive and chemically specific techniques, including ToF-SIMS, as discussed in the following sections.

Notably, the wavenumber positions of these peptide-related features are consistent with the additional bands observed in the present work (**Figure IV-8**) at approximately 1452, 1405, and 1320 cm^{-1} following RGDC exposure. While direct comparison is limited by differences in substrate chemistry and background contributions, this correspondence supports the tentative assignment of the newly observed bands to peptide-derived vibrational modes.

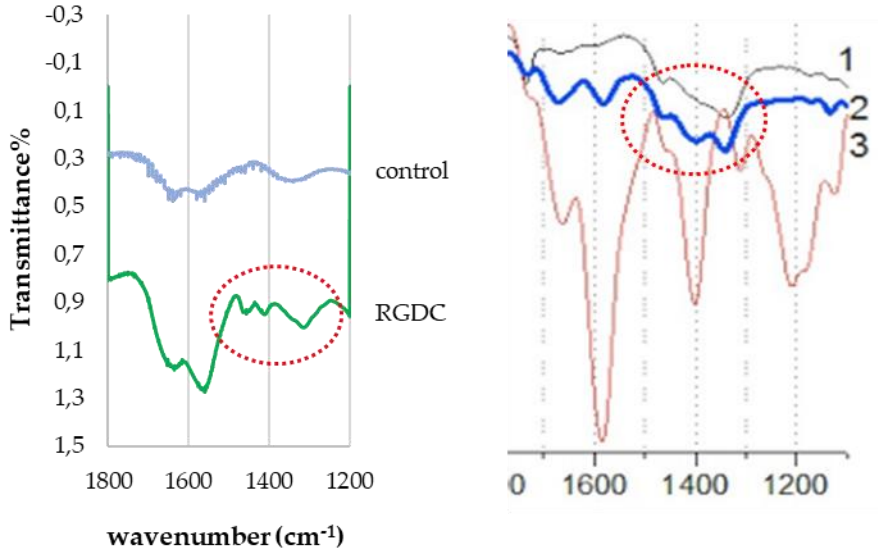

Figure IV-8. Comparison of the RGDC peptide vibrational features obtained in this work with literature FTIR spectra of the free (unreacted) RGDC peptide (line 3 in red) and RGDC-functionalized silver nanoparticles (line 2 in blue), *reproduced from* [248]. The spectrum labeled "Control" corresponds to 3Y-TZP ZrO_2 powder subjected to the complete experimental protocol in the absence of PFPTES and RGDC. The spectrum labeled "RGDC" corresponds to PFPTES-functionalized ZrO_2 powder after immersion in an RGDC peptide solution (2.2 mM) prepared in pH 8 buffer for 2 h. This comparison highlights similarities and differences in vibrational features between free, grafted, and zirconia-supported RGDC systems.

Although the characteristic amide I and amide II bands of peptides are largely obscured on ZrO_2 surfaces due to strong carbonate absorption in the 1500–1700 cm^{-1} region, peptide immobilization can nevertheless be inferred from complementary spectral changes. In particular, the attenuation or disappearance of the PFPTES-related band at ~1520 cm^{-1} after exposure to buffer or RGDC solution indicates modification of the activated pentafluorophenyl ester functionality, consistent with either nucleophilic substitution during peptide grafting or hydrolytic conversion in aqueous media.

To investigate the influence of pH on the conjugation reaction under a pH-stable environment, RGDC grafting experiments were performed in 50 mM HEPES buffer at three different pH values (7.6, 8.6, and 9.6), adjusted by the addition of small aliquots of NaOH and verified using a calibrated pH meter. FTIR spectra acquired in the 1800–1100 cm^{-1} range under each condition are presented in **Figure IV-9**. The ZR-PW sample, labeled as "control", is the powder immersed in dry DCM without the presence of silane and serves as a control for the PFPTES functionalization. Then, the ZR-PW sample, labeled as "control PFPTES", is the PFPTES functionalized powder immersed in HEPES buffer without the peptide and serves as the control for the RGDC grafting.

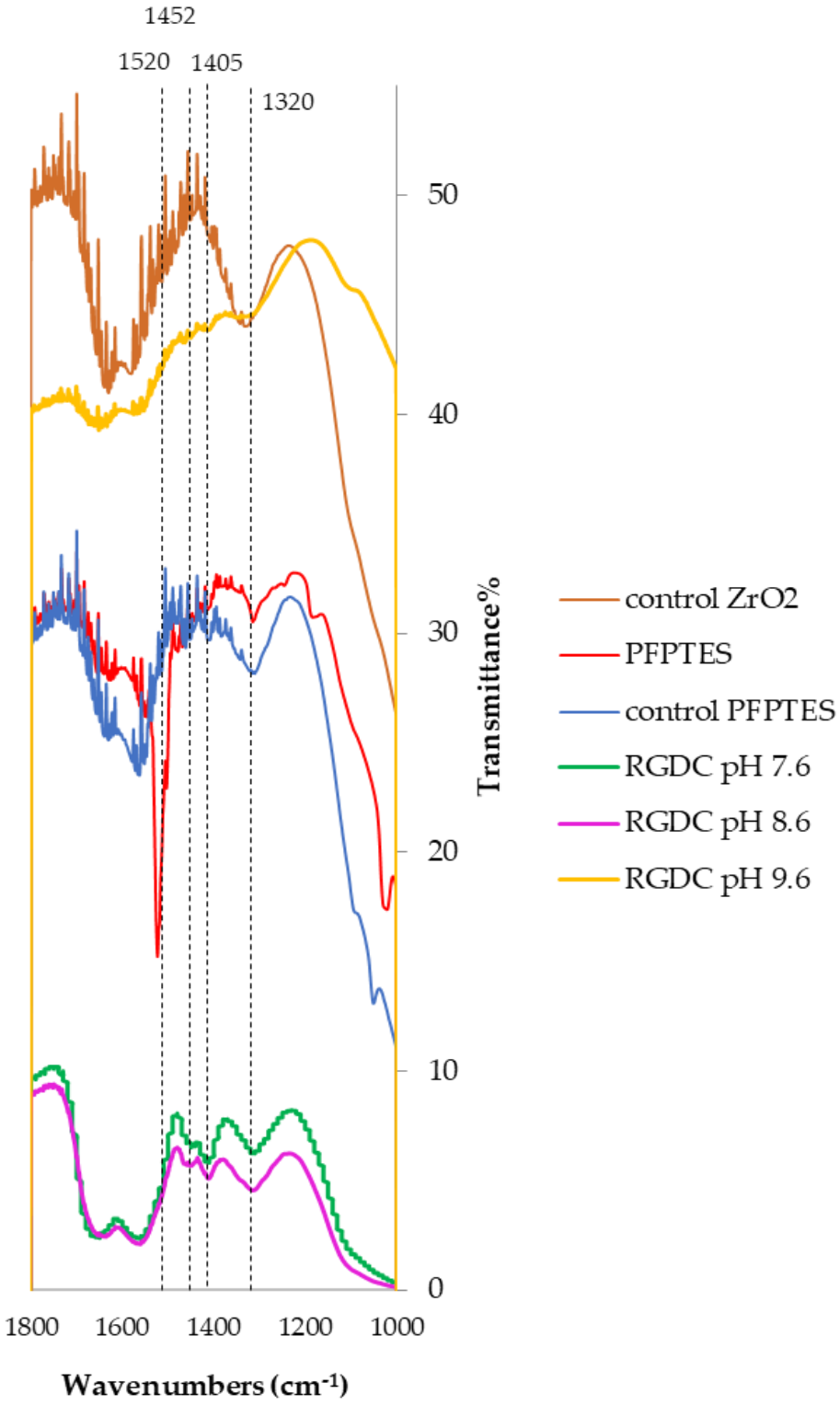

Figure IV-9. Stacked FTIR spectra of 3Y-TZP ZrO_2 powder following successive surface treatments and RGDC grafting experiments performed at different pH values. The spectrum labeled Control corresponds to ZrO_2 powder immersed sequentially in dichloromethane (DCM) and buffer without silane or peptide. The PFPTES spectrum corresponds to powder functionalized with PFPTES (1 mM in anhydrous DCM, 2 h immersion) followed by annealing at 110 °C for 1 h. The PFPTES control spectrum corresponds to

PFPTES-functionalized powder subsequently immersed in buffer in the absence of RGDC. The remaining spectra correspond to PFPTES-functionalized powders exposed to RGDC peptide solutions (2.2 mM) prepared in HEPES buffer, with the pH adjusted to 7.6, 8.6, or 9.6 using 0.1 mM NaOH. The spectra are presented to compare changes in vibrational features as a function of surface treatment and peptide grafting pH, particularly in the 1800–1100 cm^{-1} region where peptide-related modes are expected.

The attenuation of the PFPTES-related band at ~1520 cm^{-1} after exposure to buffer or RGDC solution suggests modification of the activated ester functionality, consistent with either nucleophilic substitution during peptide grafting or hydrolysis in aqueous media.

As shown in **Figure IV-9**, the FTIR spectra of RGDC-treated ZrO_2 nanoparticles exhibit additional absorption features in the 1300–1500 cm^{-1} region compared to non-grafted ZrO_2 (control) and PFPTES-treated control samples. In particular, bands centered at approximately 1452 and 1405 cm^{-1} are observed for RGDC-functionalized samples prepared at pH 7.6 and 8.6, while these features appear significantly weaker at pH 9.6. These bands are absent in the "control", "PFPTES", and "control PFPTES" samples and fall within spectral regions reported for RGDC-related vibrational modes in the literature, including free RGDC peptides and surface-bound RGD-derived peptides on nanoparticles. The reduced intensity of these features at higher pH suggests a pH-dependent modification of the peptide environment or surface coverage.

In addition, a band observed near ~1320 cm^{-1} is detected not only in RGDC-functionalized samples but also in the PFPTES control exposed to buffer, indicating that this feature is more likely associated with COOH-related vibrations arising from hydrolysis of the activated ester or the peptide itself rather than from peptide-specific amide III modes.

On this basis, subsequent experiments were carried out using HEPES buffer at a pH close to 8 (between 7.6 and 8.6), with minor adjustments using NaOH when required.

IV.4.2. Characterization of the RGDC grafted layer

While FTIR analysis supported the occurrence of the grafting reaction on powder samples, surface-sensitive analyses were carried out on ZrO_2 disks to further investigate surface functionalization. The protocols were applied to different types of substrates to examine the robustness of the chemistry.

IV.4.2.1. *Surface Chemical Composition of RGDC layer on ZR-KU substrate*

In order to investigate the elemental composition of the samples, ZR-KU disks were used and before the functionalization protocol and they were cleaned with a series of solvents before the functionalization, to remove any fabrication contamination. All the samples followed the protocols described in **IV.3.2.2** and **IV.3.2.3**, while for the control sample, it was immersed in DCM (anhyd) and HEPES buffer without the silane or peptide. The elemental composition of the surface was analyzed via XPS analysis. The atomic percentages are presented in **Table IV-3**.

	XPS At %		
Element	Control	PFPTES	RGDC
Zr 3d	22,5	22	24
Y 3d	1	1	1
O 1s	46	47	43
C 1s	25	28	29
Si 2p	**4**	3	2
F 1s	-	1	0,2
N 1s	**1,5**	**1**	2
S 2s	-	-	-

Table IV-3. Surface elemental composition (atomic percentage, At%) of ZR-KU zirconia disks determined by X-ray photoelectron spectroscopy (XPS) after successive surface treatments. Prior to functionalization, all ZR-KU disks were cleaned using a series of organic solvents to remove fabrication-related contaminants. PFPTES-functionalized and RGDC-grafted samples were prepared according to the protocols described in Sections 4.3.2.2 and 4.3.2.3. The control sample was subjected to the same solvent and buffer exposures, consisting of immersion in anhydrous dichloromethane (DCM) and HEPES buffer, but without PFPTES or RGDC.

XPS elemental analysis shows modest but systematic changes in surface composition across the different functionalization steps. The control sample already exhibits significant amounts of C 1s (25 at%), Si 2p (4 at%), and N 1s (1.5 at%) in addition to Zr and O. The presence of Si and N prior to any chemical treatment indicates intrinsic contamination or manufacturing-related residues, making both elements unreliable quantitative markers for silanization or peptide grafting.

After PFPTES functionalization, a F 1s signal appears (1 at%), while C 1s increases slightly from 25 to 28 at%. However, the Si 2p content (3 at%) remains comparable to that of the control. Considering that PFPTES contains five fluorine atoms per silicon atom, a Si:F ratio close to 1:5 would be expected if the detected silicon originated mainly from the grafted silane. Instead, the measured ratio is approximately 3:1, clearly inconsistent with the molecular stoichiometry. This confirms that most of the detected Si signal arises from the substrate rather than from PFPTES, and that Si cannot be used to quantify the silane layer. The relatively low F content further suggests a thin or low-coverage fluorinated layer. As discussed in section **III.4.3.2**, it appears that there are two fluorinated species, one attributed to the C-F of the PFP ring and the free F^-.

Following RGDC grafting, the F signal almost disappears while N increases to 2 at% and C rises to 29 at%. The reciprocal evolution of F 1s and N 1s signals is consistent with nucleophilic substitution of the activated ester by the peptide. This trend is further supported by the XPS narrow scans of the F 1s region (**Figure IV-10**), which clearly show a marked decrease in the

fluorine signal intensity after RGDC coupling compared to the PFPTES surface. No sulfur signal is detected, indicating that sulfur from the cysteine residue remains below the XPS detection limit.

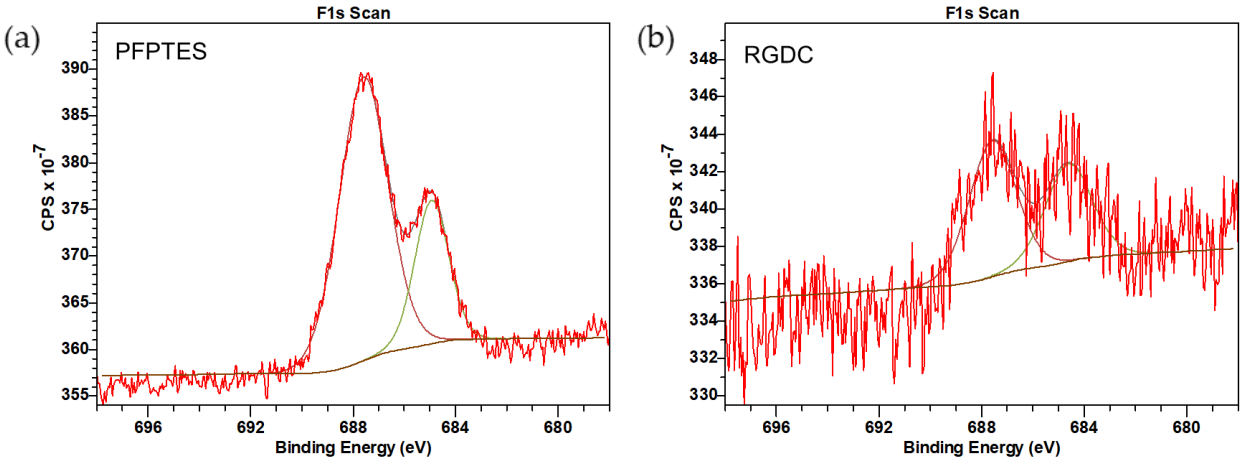

Figure IV-10. (a) High-resolution XPS F 1s spectra of PFPTES- and (b) RGDC-functionalized zirconia surfaces. The PFPTES-modified surface (a) exhibits a well-defined F 1s signal centered around ~688 eV, characteristic of the pentafluorophenyl group. After RGDC grafting (b), the F 1s signal markedly decreases to near-background level, consistent with nucleophilic substitution of the activated ester and loss of the fluorinated moiety. Peak fitting components and background are shown for the PFPTES surface, while only background-level signal is observed after peptide coupling.

Overall, although the appearance and disappearance of F and the increase in C and N qualitatively support successful surface reactions, the initial Si and N contamination and the absence of the expected 1:5 Si:F ratio render XPS non-conclusive for quantitative assessment of the grafted layers. The original chemical state of the substrate limits the reliability of this technique for accurately determining functionalization efficiency in this system.

To further substantiate the surface functionalization and overcome the limitations observed with XPS quantification, Time-of-Flight Secondary Ion Mass Spectrometry (ToF-SIMS) analyses were performed to provide more surface-sensitive chemical information.

ToF-SIMS measurements and data analysis were performed by our NOMAD partner at the University of Siegen, in both positive and negative ion modes, to monitor the chemical evolution of the ZrO_2 surface upon PFPTES functionalization and subsequent RGDC grafting. The substrates sent for analysis were ZR-KU zirconia disks. A control sample was included, which was subjected to the complete experimental protocol, including solvent and buffer exposures, but without PFPTES silanization or RGDC peptide grafting.

Figure IV-11 presents secondary ion spectra corresponding to selected substrate- and organic-related fragments acquired under identical experimental conditions for the control ZR-KU ZrO_2 surface, PFPTES-functionalized ZR-KU samples, and PFPTES + RGDC-functionalized ZR-KU samples. All ToF-SIMS spectra were normalized to the total secondary ion intensity to enable comparison of relative fragment intensities between samples.

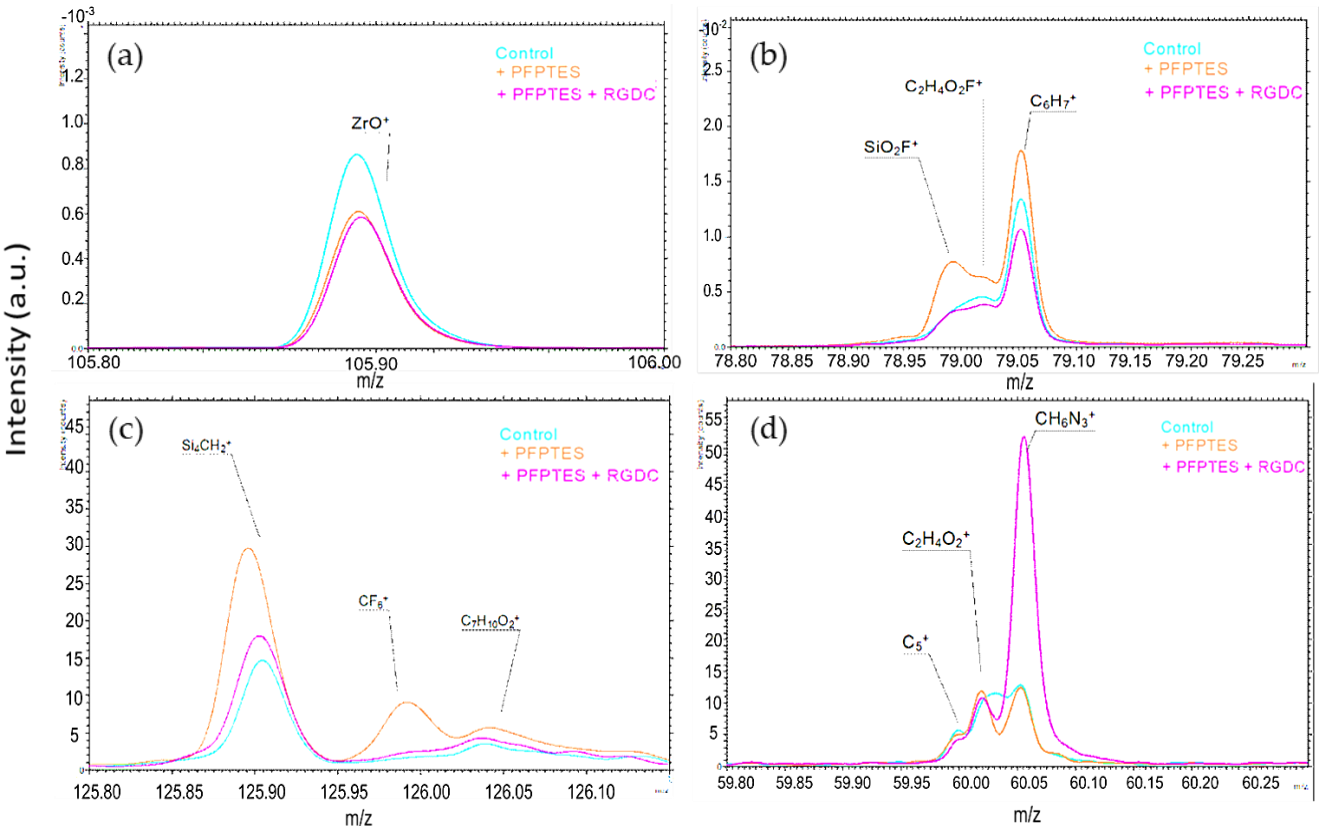

Figure IV-11. Positive ToF-SIMS spectra of selected secondary ion fragments acquired for bare Zr-KU ZrO_2, PFPTES-functionalized ZR-KU ZrO_2, and PFPTES + RGDC Zr-KU surfaces: (a) ZrO^+ substrate-related fragment, (b) carbon- and silicon-containing fragments in the low mass range, (c) organosilane- and organic-related fragments in the higher mass range, and (d) nitrogen-containing fragments characteristic of the peptide-grafted surface. All spectra were acquired under identical experimental conditions and normalized to total secondary ion counts.

In **Figure IV-11a**, the ZrO^+ (*m*/*z* 105.89) substrate-related fragment exhibits the highest relative intensity for the control surface. After PFPTES functionalization, a clear attenuation of the ZrO^+ signal is observed in the total-ion–normalized spectra, consistent with partial masking of the zirconia surface by an organic overlayer. Following RGDC grafting, the ZrO^+ intensity remains at a similarly reduced level, with no pronounced additional attenuation relative to the PFPTES-functionalized sample.

In the lower mass range (**Figure IV-11b**), a prominent peak centered at *m*/*z* ≈ 79 is observed. This signal likely arises from overlapping contributions of several fragments, including $C_6H_7^+$ (*m*/*z* 79.06), $C_2H_4O_2F^+$ (*m*/*z* 79.03), and SiO_2F^+ (*m*/*z* 78.98), which are associated with aromatic, fluorinated organic, and siloxane-derived species, respectively. The *m*/*z* ≈ 79 signal exhibits very low relative intensity on the control ZrO_2 surface, increases markedly after PFPTES functionalization, and decreases again following RGDC grafting. This evolution is consistent with the introduction of the pentafluorophenyl silane layer and its subsequent modification through nucleophilic substitution or hydrolysis during peptide conjugation, resulting in partial consumption or masking of fluorinated ester functionalities.

In the higher mass range (**Figure IV-11c**), prominent peak centered at m/z ≈ 126 is observed. This signal likely arises from overlapping contributions of several isobaric fragments, including $Si_4CH_2^+$ (m/z 125.89), CF_6^+ (m/z 125.98), and $C_7H_{10}O_2^+$ (m/z 126.04), which are associated with siloxane-derived species, fluorinated fragments of the pentafluorophenyl ester, and oxygen-containing organic functionalities, respectively. The m/z ≈ 126 signal is weak on the control ZrO_2 surface, increases markedly after PFPTES functionalization, and decreases following RGDC grafting. This evolution is consistent with the introduction of a fluorinated silane layer and its subsequent modification through nucleophilic substitution or hydrolysis during peptide conjugation, leading to partial consumption or masking of fluorinated ester groups.

Finally, in the low-mass region shown in **Figure IV-11d**, a pronounced signal centered at m/z ≈ 60 is observed following RGDC grafting. This peak arises from overlapping contributions of several fragments, including C_5^+ (m/z 60.00), $C_2H_4O_2^+$ (m/z 60.03), and the nitrogen-rich fragment $CH_6N_3^+$ (m/z 60.08). While low-intensity signals in this mass region are detected on the control and PFPTES-functionalized surfaces due to generic hydrocarbon and oxygen-containing fragments, the m/z ≈ 60 signal exhibits a marked and selective increase in the RGDC-functionalized sample. This strong enhancement is attributed primarily to the $CH_6N_3^+$ fragment, which is characteristic of arginine-containing peptides and is consistent with the presence of the RGDC sequence at the surface. In contrast to PFPTES-related fragments, which decrease following peptide grafting, the emergence of this nitrogen-containing signal provides direct molecular evidence for successful RGDC immobilization on the ZrO_2 surface.

Overall, the systematic evolution of substrate-, silane-, organic-, and nitrogen-containing secondary ion signals provides a coherent picture of the successive surface modification steps. The attenuation of ZrO_2-related signals, the emergence and partial masking of silane- and organic-related fragments, and the strong enhancement of nitrogen-containing ions after RGDC grafting collectively confirm the successful functionalization of the ZrO_2 surface and the formation of a peptide-containing outermost layer.

IV.4.2.2. *Surface Chemical Composition of RGDC layer on ZR-DOC substrate*

To evaluate the robustness and transferability of the functionalization strategy, the same PFPTES silanization and RGDC grafting protocol was subsequently applied to ZR-DOC zirconia disks. These samples were processed following the identical cleaning, silanization, and peptide conjugation steps used for ZR-KU substrates, without any modification of reaction conditions. XPS analysis was then performed to assess the surface elemental composition after each functionalization step. In this analysis, three spots were analyzed of each surface, to examine the homogeneity of the layer, as well. The corresponding XPS results are presented in **Table IV-4.**

	XPS At %		
Element	Control	PFPTES (*n = 1*)	RGDC
Zr 3d	26 ± 0,6	19	22 ± 3,6

Y 3d	1,6 ± 0,05	1	1
O 1s	50 ± 2,2	39	45 ± 2,2
C 1s	22 ± 2,3	28	26 ± 2,3
Si 2p	-	4	2 ± 0,4
F 1s	**0,08 ± 0,07**	0,4	0,8 ± 0,07
N 1s	**0,2 ± 0,06**	**0,4**	0,8 ± 0,2
S 2s	-	-	-
P 2p	**0,2 ± 0,17**	**0,7**	**0,2 ± 0,12**

Table IV-4. Surface elemental composition (atomic percentage, At%) of ZR-DOC zirconia disks determined by X-ray photoelectron spectroscopy (XPS) after successive surface treatments. Prior to functionalization, all ZR-DOC disks were cleaned using a series of organic solvents to remove fabrication-related contaminants. PFPTES-functionalized and RGDC-grafted samples were prepared according to the protocols described in Sections 4.3.2.2 and 4.3.2.3. The control sample was subjected to the same solvent and buffer exposures, consisting of immersion in anhydrous dichloromethane (DCM) and HEPES buffer, but without PFPTES or RGDC.

XPS elemental analysis of this ZR-DOC series shows similar limitations related to the initial surface state. The control surface already exhibits dominant Zr 3d (26 ± 0.6 at%) and O 1s (50 ± 2.2 at%) contributions, together with C 1s (22 ± 2.3 at%), and trace levels of F 1s (0.08 ± 0.07 at%), N 1s (0.2 ± 0.06 at%), and P 2p (0.2 ± 0.17 at%). These non-negligible background signals again indicate surface contamination, which complicates the interpretation of low-intensity elements after functionalization.

Following PFPTES treatment, Zr and O contributions decrease markedly (to 19 and 39 at%, respectively), while C increases to 28 at%, consistent with the deposition of an organic overlayer partially attenuating the substrate signal. Silicon appears at 4 at%, and both F and N increase to 0.4 at%. The detection of Si confirms silane deposition; however, as only a single PFPTES sample was measured (n = 1), and considering the background contributions observed on the control, quantitative interpretation remains limited. Moreover, the F content remains low compared to the Si signal. Given that PFPTES contains five fluorine atoms per silicon atom, a Si:F ratio close to 1:5 would be expected. Instead, the experimental ratio is approximately 10:1, again indicating that the detected Si signal is not exclusively associated with intact PFPTES molecules and that stoichiometric quantification of the silane layer is not reliable.

After RGDC grafting, Zr and O signals partially recover (22 ± 3.6 and 45 ± 2.2 at%), suggesting either a thinner overlayer or partial reorganization of the surface. Carbon slightly decreases to 26 ± 2.3 at%. Silicon decreases to 2 ± 0.4 at%, while both F and N increase to 0.8 at%. The increase in N is consistent with peptide immobilization. However, the unexpected increase in F after peptide coupling does not align with the anticipated loss of the pentafluorophenyl group during nucleophilic substitution. This behavior, together with the very low absolute F

concentrations and their presence already in trace amounts on the control, indicates that F quantification is strongly influenced by background.

Overall, although attenuation of the substrate signal and evolution of C, Si, and N contents qualitatively suggest surface modification, the presence of background contamination, low signal intensities, non-stoichiometric Si:F ratios, and values close to detection limits render XPS non-conclusive for reliable quantitative assessment of silanization and peptide grafting on this substrate. Similarly, to the KU samples, Time-of-Flight Secondary Ion Mass Spectrometry (ToF-SIMS) was therefore employed to obtain more surface-sensitive chemical information and to further support the functionalization strategy.

The functionalization protocol was repeated on ZR-DOC samples and **Figure IV-11** portrays the results on the differently treated ZrO_2 surfaces. The "control" sample once again was subjected to the complete experimental protocol, including solvent and buffer exposures, but without PFPTES silanization or RGDC peptide grafting.

Figure IV-12a shows the Zr^+ substrate-related fragment (m/z ≈ 89.91) obtained from ZR-DOC (control) samples analyzed before and after PFPTES functionalization. The control ZR-DOC surface exhibits a strong Zr^+ signal, reflecting the direct exposure of the zirconia substrate. After PFPTES treatment, a clear attenuation of the Zr^+ intensity is observed in the total-ion–normalized spectrum. This decrease indicates partial masking of the ZrO_2 surface by the silane-derived organic overlayer. The observation of a similar attenuation trend for the Zr^+ fragment on ZR-DOC as previously observed for ZR-KU substrates confirms that the PFPTES functionalization effectively modifies the surface irrespective of the zirconia substrate.

Figure IV-12b presents the positive-ion ToF-SIMS spectrum of ZR-DOC samples in the $m/z \approx 79$ region. The signal observed at this mass arises from overlapping contributions of several isobaric fragments, including SiO_2F^+ (m/z 78.92), C_5F^+ (m/z 78.99), and $C_6H_7^+$ (m/z 79.08), which are associated with fluorinated siloxane species and aromatic fragments originating from the PFPTES layer.

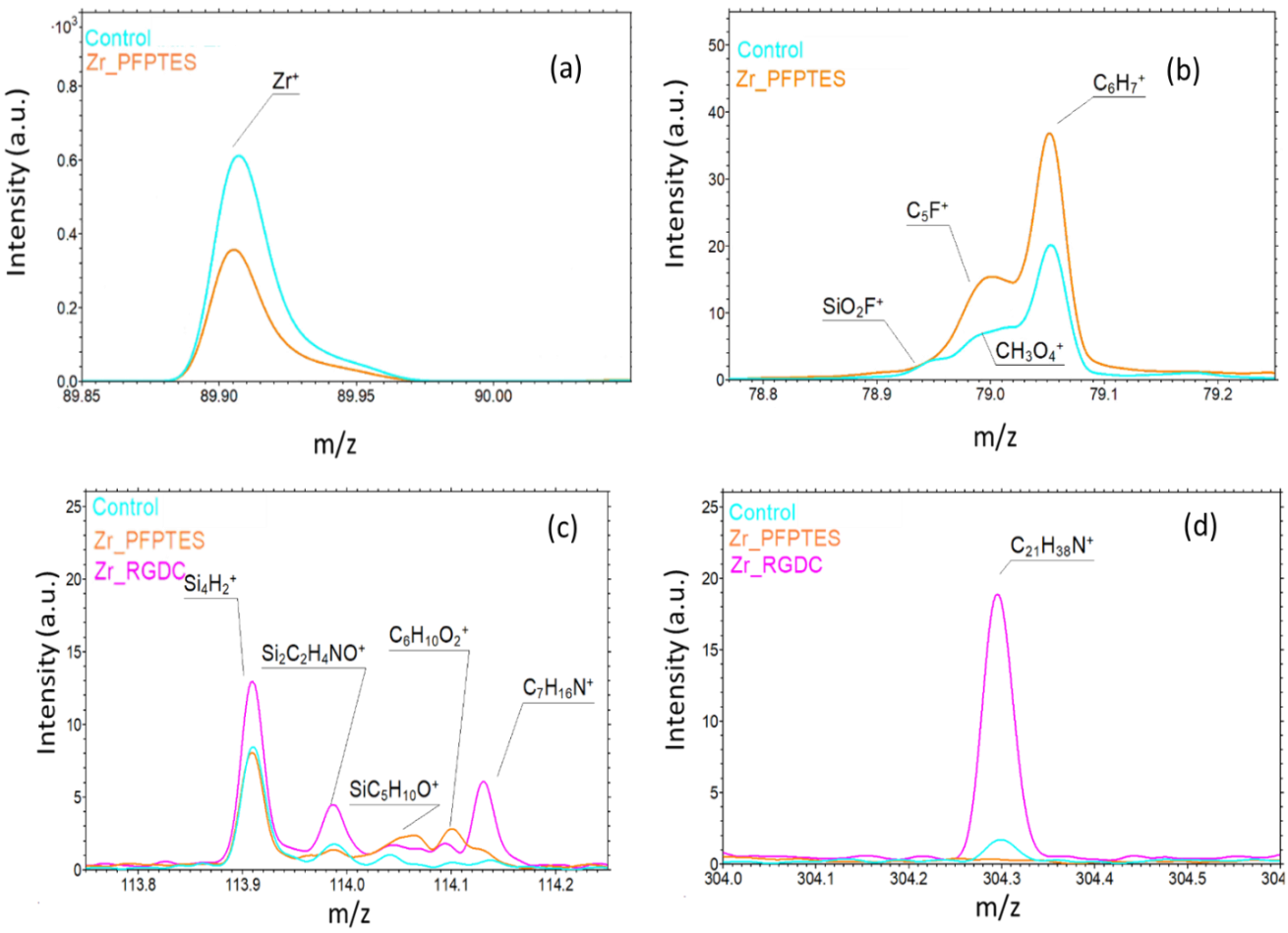

Figure IV-12. Positive-ion ToF-SIMS characterization of ZR-DOC surfaces before and after PFPTES functionalization and RGDC grafting: (a) attenuation of the substrate-related Zr^+ fragment (m/z ≈ 89.91) following PFPTES treatment; (b) fluorinated silane-related signal in the m/z ≈ 79 region; (c) enhancement of siloxane- and nitrogen-containing fragments in the m/z ≈ 114 region after PFPTES functionalization and RGDC grafting; and (d) appearance of the peptide-derived fragment $C_{21}H_{38}N^+$ (m/z ≈ 304.3) exclusively after RGDC immobilization, confirming successful peptide grafting.

Figure IV-12c shows the positive-ion ToF-SIMS spectrum of ZR-DOC samples in the m/z ≈ 113.9–114.2 region. This signal arises from overlapping contributions of isobaric fragments, including $Si_4H_2^+$ (m/z 113.90), $Si_2C_2H_4NO^+$ (m/z 113.99), $SiC_5H_{10}O^+$ (m/z 114.08), and the nitrogen-containing fragment $C_7H_{16}N^+$ (m/z 114.14). The signal is weak on the control ZrO_2 surface and increases moderately after PFPTES functionalization, reflecting siloxane-derived species. Following RGDC grafting, a clear enhancement is observed, particularly on the high-m/z side of the peak, consistent with the introduction of nitrogen-containing organic fragments and supporting successful peptide immobilization.

Figure IV-12d shows the positive-ion ToF-SIMS spectrum of ZR-DOC samples in the high-mass region around *m*/*z* ≈ 304.3. A pronounced peak corresponding to the nitrogen-containing fragment $C_{21}H_{38}N^+$ (*m*/*z* 304.3) is observed exclusively for the RGDC-functionalized surface, while only negligible signal is detected for the control and PFPTES-treated samples. The selective

appearance and high intensity of this fragment after RGDC grafting provide strong molecular-level evidence for the presence of peptide-derived species at the zirconia surface, as such high-mass nitrogen-containing ions cannot originate from the silane layer alone.

IV.4.2.3. *Fluorescent Labeling and Surface Visualization*

In this section, fluorescence microscopy was used as a complementary technique to visualize surface functionalization of ZrO_2 surfaces, providing qualitative information on the presence and spatial distribution of the grafted molecules. The same optimized grafting protocol was applied on ZR-DOC disks (**IV.3.2.2**, **IV.3.2.3**), with the RGDC peptide replaced by an RGDC peptide synthesized and labeled with fluorescein isothiocyanate (FITC). To preserve the intensity of the fluorescent signal, all experimental steps involving the labeled peptide were carried out in the dark. The corresponding fluorescence microscopy results are presented in **Figure IV-13**. A control sample consisting of ZR-DOC disk immersed in the fluorescent peptide solution was included to assess nonspecific adsorption.

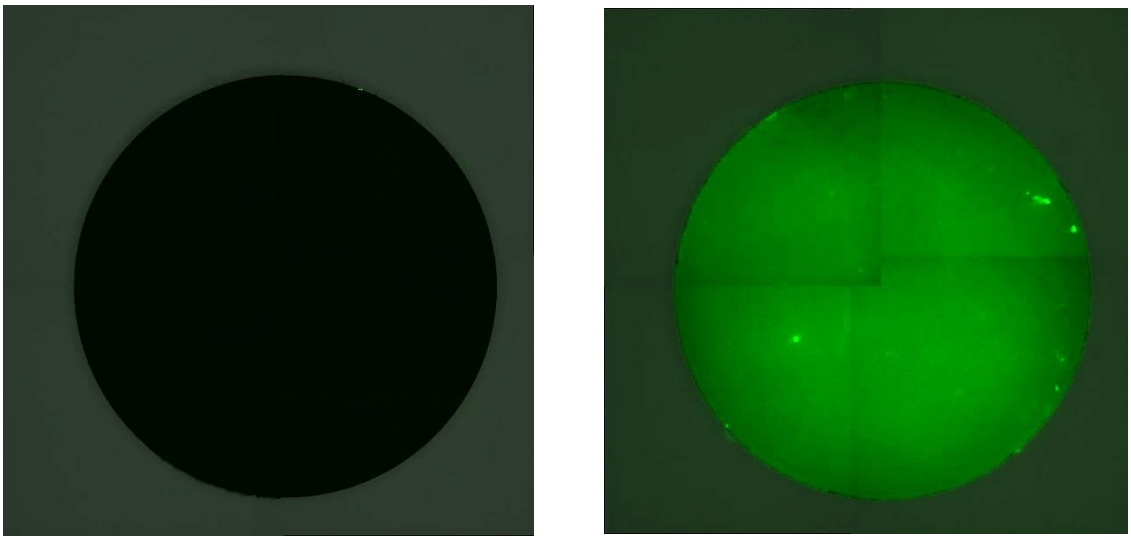

Figure IV-13. Fluorescence microscopy images of ZrO_2 disks. *Left:* control sample consisting of ZR-DOC immersed in the FITC–RGDC solution to assess nonspecific adsorption. *Right:* silanized ZR-DOC functionalized with FITC-labeled RGDC peptide using the optimized grafting protocol. Both images are displayed using the same fluorescence intensity scale.

Fluorescence microscopy revealed a clear signal on ZrO_2 disks functionalized with FITC–RGDC, whereas the control sample exhibited almost no detectable fluorescence. This marked difference suggests that the observed signal is associated with the functionalized surface rather than nonspecific adsorption. Another observation is the complete coverage of the disk with fluorescent peptide. Nevertheless, as fluorescence microscopy is a qualitative technique, it does not allow conclusions to be drawn directly regarding the density of the grafted peptide layer but it shows a full coverage of the substrate.

The average intensity of the control sample (ZR-DOC), calculated from three ROIs, was 112.1 ± 0.6, whereas the RGDC-FITC (ZR-DOC) sample exhibited a higher intensity of 290.5 ± 39.2. This increase is consistent with the fluorescence images, confirming the enhanced signal observed after RGDC-FITC functionalization.

This fluorescence-based validation was further extended to ZR-PVD substrates, which were subsequently used in the wound healing assay described in a following section (**IV.5.2**). The samples were prepared according to the protocol previously described and the control sample consists of a cover glass slide, with deposited ZrO_2 that was immersed in the peptide solution to study non-specific adsorption. The functionalized sample was treated as described in **IV.3.2.2** and **IV.3.2.3**, employing the RGDC labeled with FITC.

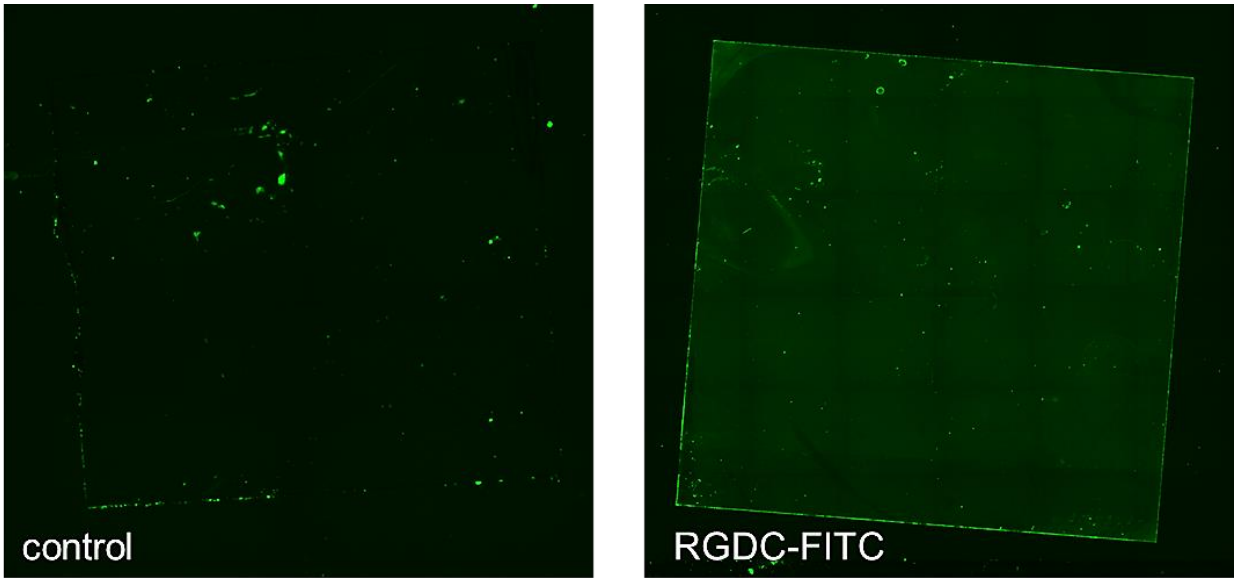

Figure IV-14. Fluorescence microscopy images of FITC-labeled RGDC-functionalized zirconia disks. The functionalized surface (right) exhibits a homogeneous green fluorescence signal across the disk area, indicating successful immobilization and spatial distribution of the peptide. In contrast, the control sample (left), consisting of a zirconia disk immersed in the fluorescent peptide solution without prior silanization, shows only weak and localized fluorescence, consistent with limited nonspecific adsorption.

As shown in **Figure IV-14**, the control sample exhibits only weak and heterogeneous fluorescence, mainly localized in isolated spots, indicating limited nonspecific adsorption of the FITC-labeled peptide on the untreated zirconia surface or contamination like dust. In contrast, the functionalized disk displays a clearly stronger and more uniform fluorescence signal over the entire surface area. This homogeneous emission supports successful immobilization of the RGDC-FITC peptide through the optimized silanization and coupling protocol.

The average intensity of the control sample (ZR-PVD), calculated from three ROIs, was 139.7 ± 1.5, whereas the RGDC-FITC (ZR-PVD) sample exhibited a higher intensity of 209.2 ± 3.3. This increase is consistent with the fluorescence images, confirming the enhanced signal observed after RGDC-FITC functionalization.

IV.4.3. Robustness to Sterilization

Beyond initial grafting efficiency, the long-term performance of biofunctionalized surfaces depends on the stability of the immobilized biomolecules when exposed to clinically relevant stressors. In the context of dental and orthopedic applications, surface-bound biomolecules must withstand both sterilization procedures applied prior to implantation and mechanical challenges encountered during service. Sterilization processes can induce chemical degradation or detachment of grafted species, while repetitive mechanical actions, such as brushing or friction, may compromise surface integrity through shear forces. Evaluating the resistance of biofunctionalized surfaces to these stressors is therefore essential to assess the robustness and translational potential of the biomolecule attachment strategy.

Although gamma (γ) irradiation is commonly used for the sterilization of dental implants, this method is not ideal for ZrO_2-based abutments or restorations. Exposure to gamma rays is known to induce discoloration of ZrO_2, leading to a darkened or black appearance that compromises one of its key advantages in dental applications, namely its favorable aesthetics [249]. As aesthetic outcomes are particularly critical in the transmucosal and visible regions of dental implants, alternative sterilization methods must be considered. For this reason, ethylene oxide (EtO) sterilization is generally used and was selected in this study, as it allows effective sterilization at low temperature while preserving the optical and structural properties of ZrO_2 surfaces.

Although ethylene oxide (EtO) sterilization is widely used due to its low-temperature compatibility with polymeric and temperature-sensitive materials, it has been reported to induce chemical modifications in proteins and amino acids. In particular, reactions between EtO and nucleophilic side chains have been described in the literature, leading to the formation of covalent adducts under certain sterilization conditions [155,250]. While such modifications are less likely at low residual EtO levels following controlled aeration, they highlight a potential chemical interaction that must be considered when sterilizing biomolecule-functionalized surfaces.

Ethylene oxide (EtO) sterilization was performed by our NOMAD partner, Anthogyr. Prior to sterilization, the samples were prepared according to the optimized protocol described in **IV.3.2.2** and **IV.3.2.3**. The samples investigated were ZR-DOC prepared under the optimized conditions. To investigate the stability of the layers to sterilization, the samples were examined before and after with ToF-SIMS analysis. The control samples submitted, before and after sterilization, were ZR-DOC, cleaned with a series of solvents.

For the effect of the sterilization method on the bioactive layer, positive and negative ToF-SIMS spectra are presented in **Figure IV-15**.

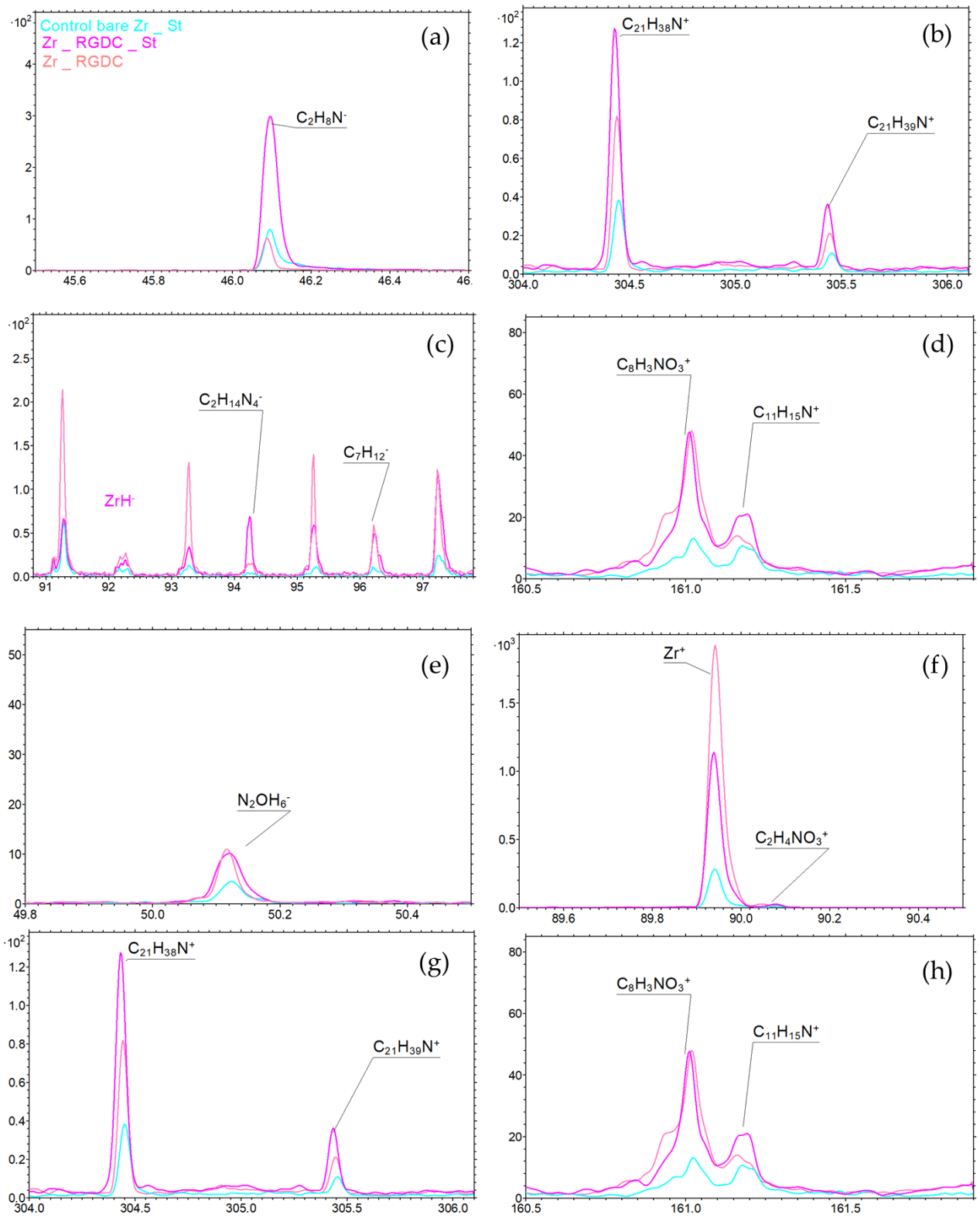

Figure IV-15 Positive (b), (d), (f), (g), (h) and negative (a), (c), (e) ToF-SIMS spectra acquired for bare Zr-DOC zirconia (control) and RGDC-functionalized surfaces (sterilized and non-sterilized), highlighting differences in surface chemical composition across selected mass regions. All spectra were acquired under identical experimental conditions and normalized to total secondary ion counts.

The negative ion fragment observed at m/z ≈ 46 ($C_2H_8N^-$) is detected in both the bare control and the RGDC-functionalized samples. However, its intensity is noticeably higher on the functionalized surfaces and further increases after sterilization. The presence of this fragment in the control indicates a contribution from background contamination, while the increase observed after functionalization and sterilization suggests that nitrogen-containing species at the surface are more readily detected following treatment.

In the high-mass region of the positive spectra (m/z ≈ 304–306), the fragments $C_{21}H_{38}N^+$ and $C_{21}H_{39}N^+$ are clearly visible for the functionalized samples, with only lower or negligible intensity in the bare control. An increase in intensity is observed after sterilization. Given their high mass and nitrogen content, these fragments are unlikely to originate from sample contamination, and their enhanced signal after sterilization could suggest improved detectability of surface-bound organic species or inhomogeneity of the grafted layer, but either way reinforcing their attribution to the grafted peptide.

In the negative mode spectra around m/z ≈ 91–97, several fragments are observed, including $C_2H_{14}N_4^-$, $C_7H_{12}^-$, and ZrH^-. The $C_2H_{14}N_4^-$ signal is clearly higher for the functionalized samples compared to the control, and it increases further after sterilization. On the other hand, $C_7H_{12}^-$ is present in all samples with only small variations, suggesting it mainly comes from general hydrocarbon contamination. The ZrH^- signal, which is related to the substrate, is detected in all cases and does not show a clear decrease after functionalization, likely due to matrix effects influencing the signal.

In the positive mode spectra around m/z ≈ 161, the fragments $C_8H_3NO_3^+$ and $C_{11}H_{15}N^+$ are observed for all samples, including the control, although at lower intensity. Both fragments show a clear increase in intensity for the functionalized samples and a further enhancement after sterilization. As these species are also present in the control, they cannot be considered fully specific, but their relative increase suggests a higher contribution from nitrogen-containing surface species after treatment.

The fragment $N_2OH_6^-$ (m/z ≈ 50) is present in all samples, including the bare control, so it is not specific to the functionalized surface. However, its intensity is higher for the functionalized samples and increases after sterilization. This suggests that sterilization affects how these nitrogen-containing species are detected, possibly by modifying the surface or improving ionization.

In the spectra around m/z ≈ 90, the Zr^+ signal is observed for all samples, as expected since it comes from the substrate. Interestingly, it is more intense for the non-sterilized functionalized sample than for the bare control, and then decreases after sterilization. This is not what would normally be expected, and is likely due to matrix effects or changes in ion yield rather than actual differences in surface coverage. The $C_2H_4NO_3^+$ fragment is also detected at low intensity in all samples, including the control, suggesting that it is not specific and may come from background contamination.

The interpretation of the ToF-SIMS results must consider the intrinsic limitations of the technique. In particular, secondary ion intensities are affected by matrix effects, meaning that the detected signal depends not only on surface concentration but also on the local chemical environment and ionization probability. As a result, ToF-SIMS is generally regarded as a semi-quantitative technique, and variations in fragment intensity cannot be directly correlated to changes in surface coverage [251,252]. In this context, the differences observed between sterilized and non-sterilized samples, as well as the unexpected behavior of substrate-related signals such as Zr^+, can be interpreted in terms of changes in ion yield and signal detectability rather than actual differences in the amount of grafted material [251–253].

IV.4.4. Robustness to Mechanical Stressors

During clinical insertion of the implant and subsequent placement of the abutment, as well as during routine oral hygiene procedures such as tooth brushing, the bioactive layer is subjected to various mechanical stresses. It is therefore essential that this layer remains stable under clinically relevant conditions. To evaluate the effect of daily tooth brushing, a dedicated experiment was conducted in collaboration with Anthogyr, with the full experimental setup described in **IV.3.3**. The following figure presents fluorescence microscopy images of the ZR-DOC surface (control_bare), the ZR-DOC functionalized with RGDC-FITC prior to brushing (control_before), and the three ZR-DOC-RGDC-FITC functionalized samples after exposure to different numbers of brushing cycles.

Based on the fluorescence images, successful grafting is first confirmed by the presence of a detectable fluorescence signal on the functionalized disks. The observed bright spots could be attributed either to locally adsorbed peptide or to contaminants emitting within the same fluorescence wavelength range.

Following the brushing experiment, the fluorescent signal remains detectable on the surface, although a gradual decrease in the number and intensity of bright spots is observed with increasing numbers of brushing cycles.

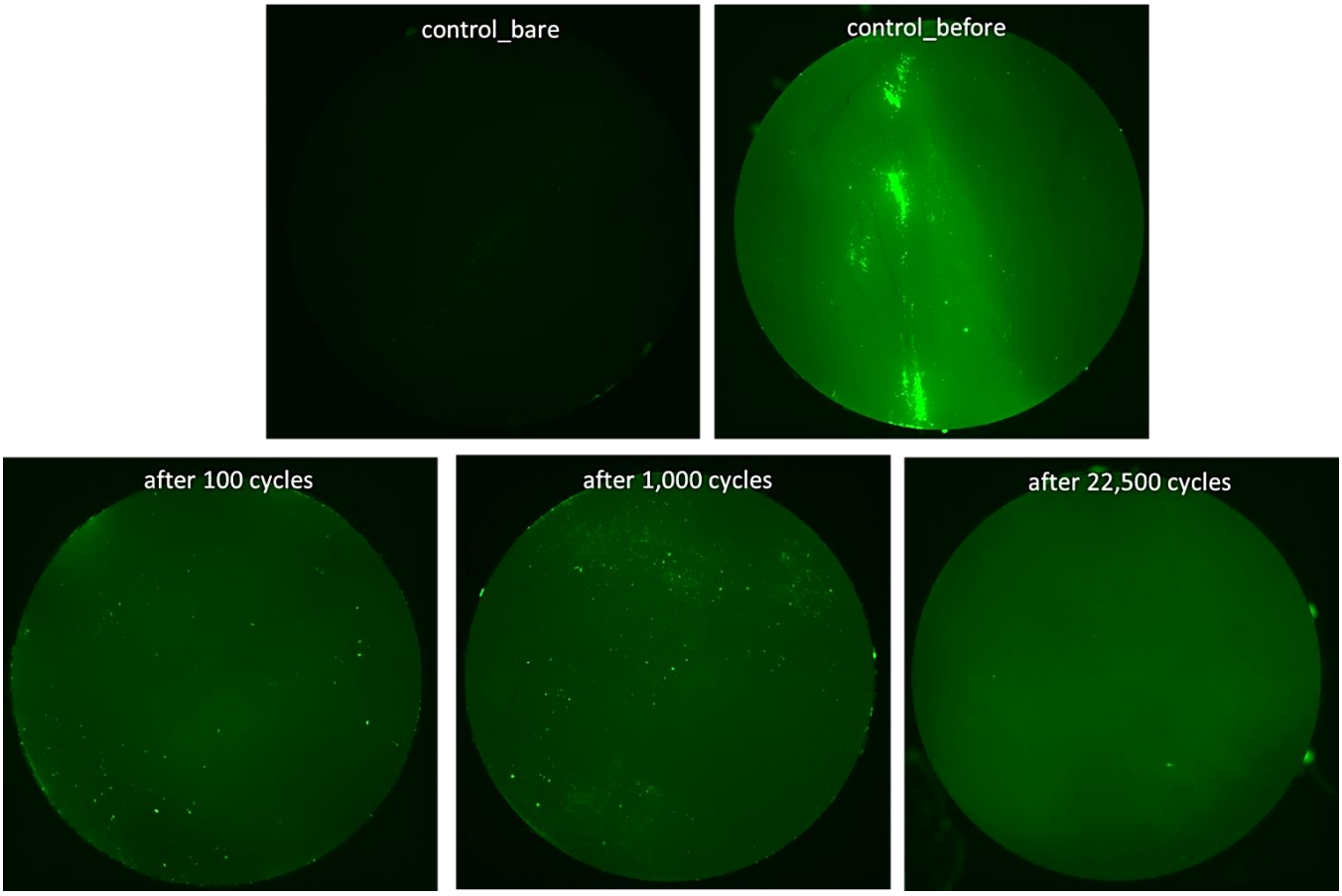

Figure IV-16 . Fluorescence microscopy images of zirconia (ZR-DOC) disks before and after simulated tooth brushing. A bare zirconia disk (control_bare) is shown as a negative control, alongside a functionalized disk prior to brushing (control_before). Functionalized samples exposed to 100, 1,000, and 22,500 brushing cycles are also presented. The decrease in fluorescence intensity reflects the progressive loss or degradation of the RGDC-FITC bioactive layer under mechanical stress, with 22,500 cycles corresponding to approximately six months of daily tooth brushing.

To quantify the effect of brushing on the stability of the RGDC-FITC layer, fluorescence intensity measurements were performed and are presented in **Figure IV-17**. For each sample, the reported value corresponds to the mean of the fluorescence intensities measured across three linear ROIs, with error bars representing the standard deviation between these measurements.

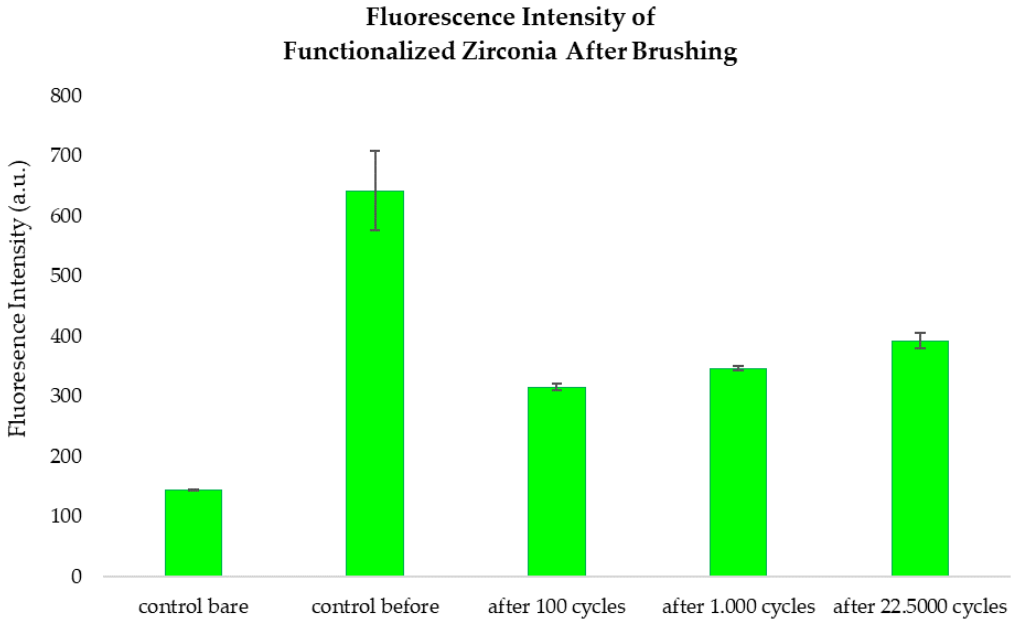

Figure IV-17 Quantitative analysis of fluorescence intensity on RGDC-FITC functionalized ZR-DOC disks before and after simulated tooth brushing. Mean fluorescence intensities were extracted from three linear regions of interest (ROIs) of 3.739 µm, 3.963 µm, and 4.674 µm in length, defined across each sample. The values represent the average intensity along each line, while error bars correspond to the standard deviation of the three ROI measurements, reflecting local surface heterogeneity. The evolution of the fluorescent signal is shown as a function of the number of brushing cycles (100, 1,000, and 22,500 cycles), in comparison to the functionalized control prior to brushing.

A relative decrease in fluorescence intensity is observed after brushing. This reduction may be attributed either to partial loss of the bioactive layer or to the removal of loosely bound contaminants or aggregated peptide. Nevertheless, the fluorescence signal remains, approximately twofold higher than that of the control, indicating that a significant portion of the bioactive layer is retained even after the full brushing cycle experiment.

IV.5. Biological Activity

While surface chemistry and stability are essential prerequisites, the ultimate objective of biomolecule grafting is to elicit a controlled and beneficial biological response. In this context, the biological activity of the functionalized ZrO_2 surfaces was evaluated to determine whether the immobilized biomolecules retained their functionality after surface attachment and exposure to relevant processing steps. Cell-based assays were therefore employed to evaluate the biological response to the biofunctionalized surfaces. Specifically, cytotoxicity and cell proliferation were assessed using human keratinocytes and gingival fibroblasts, two cell types relevant to soft tissue integration around dental implants. In addition, wound-healing assays were performed to investigate the influence of surface functionalization on cell migration behavior. These

experiments aimed to correlate the surface modification strategy with biological performance and to assess the effectiveness of the biomolecule grafting approach.

IV.5.1. Cytotoxicity Assays

To evaluate the cytotoxicity of the bioactive layer under biologically relevant conditions, additional cytotoxicity assays were performed by our NOMAD partner Dr. Lu YUAN at the University Medical Center Groningen (UMCG), within the Department of Biomaterials & Biomedical Technology. Human gingival fibroblasts were cultured on the different ZrO_2 surfaces for 1 and 3 days. Cell viability was assessed using the XTT assay. In parallel, cell morphology and spreading were evaluated by fluorescence microscopy after staining of the actin cytoskeleton with phalloidin (F-actin, green) and nuclei with DAPI (blue) (**Figure IV-18**).

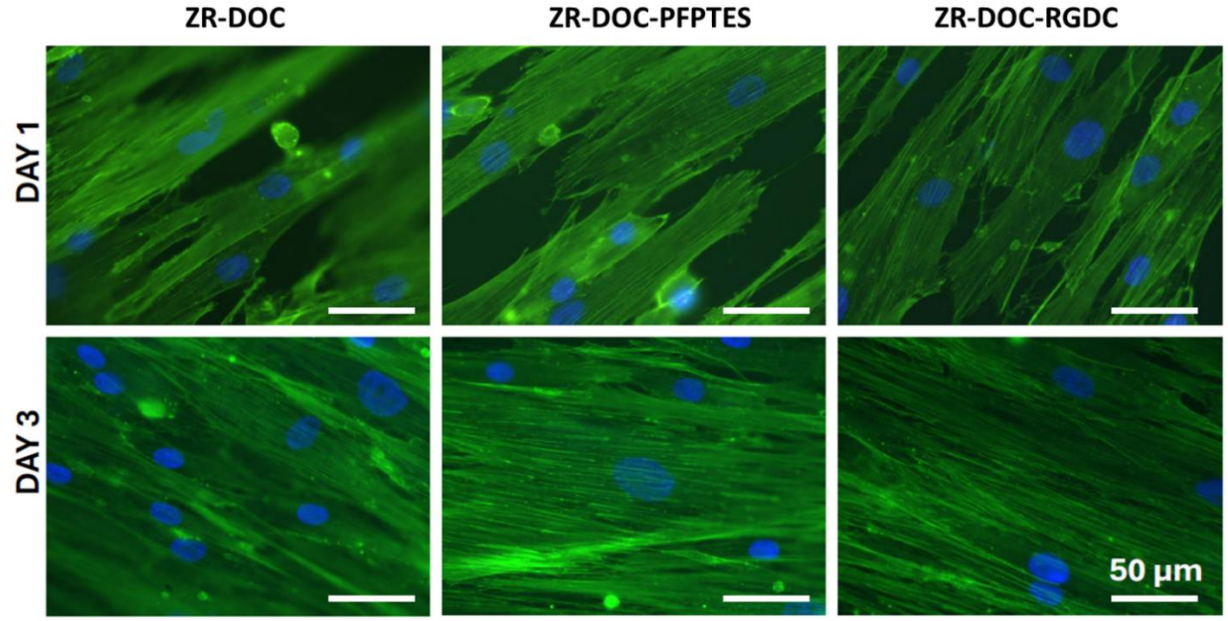

Figure IV-18 Representative fluorescence microscopy images of fibroblasts cultured on bare ZrO_2 (ZR-DOC), PFPTES-modified ZR-DOC (ZR-DOC-PFPTES), and RGDC-functionalized silanized ZR-DOC (ZR-DOC-RGD) after 1 and 3 days of culture. Actin cytoskeleton was stained with phalloidin (F-actin, green) and cell nuclei with DAPI (blue). Scale bar: 50 µm

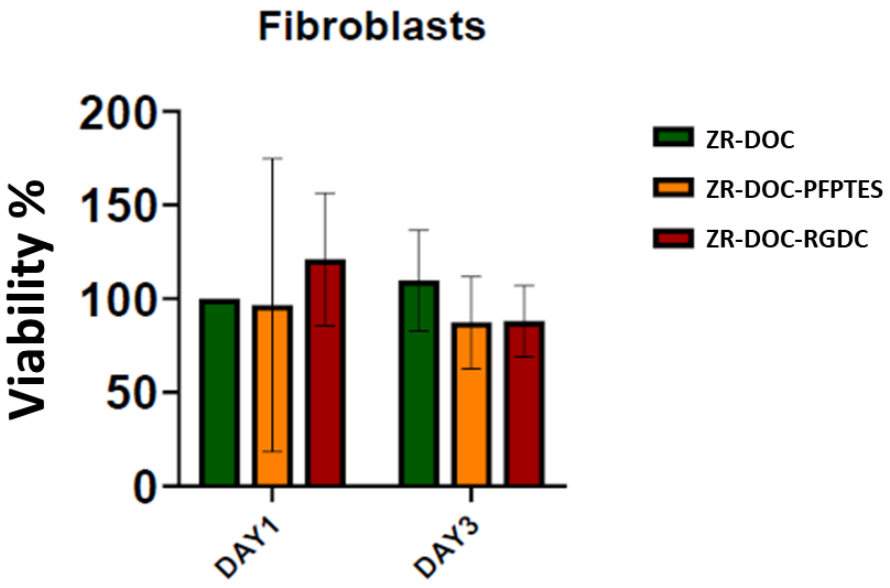

Figure IV-19. Cytocompatibility of ZrO_2 surfaces assessed using human gingival fibroblasts. Quantitative cell viability results obtained by XTT assay are shown, expressed as percentage relative to the tissue culture plastic positive control. Data are presented as mean ± standard deviation.

Fluorescence microscopy images revealed well-spread cells with organized actin cytoskeletons on all tested surfaces, including control "bare" ZR-DOC disks, PFPTES-modified ZrO_2, and RGDC-functionalized ZrO_2. Quantitative viability measurements obtained from the XTT assay (**Figure IV-19**) indicated comparable cell viability levels across all surfaces at both time points, with values remaining above the non-cytotoxicity threshold (70% of the positive tissue culture plastic reference). Together, these qualitative and quantitative results confirm that the bioactive surface modification does not induce cytotoxic effects and supports normal fibroblast adhesion and viability.

Finally, the potential cytotoxic effect of the sterilization method and HF 2% etching, was evaluated. Ethylene oxide (EtO) was selected as the sterilization technique, as gamma irradiation has been reported to induce a pronounced darkening of zirconia ceramics, turning them deep brown to black and thereby compromising their aesthetic properties. In parallel, samples etched with 2% HF were also tested to verify the cytocompatibility of the surface pre-treatment proposed for zirconia components with complex 3D geometries. These experiments were performed by our NOMAD partner Dr. Lu Yuan at the University Medical Center Groningen (UMCG), within the Department of Biomaterials and Biomedical Technology. Human gingival fibroblasts were cultured on the different ZrO_2 surfaces for 1 and 3 days ($n = 1$). One sample per surface type (n = 1) was used due to limited sample availability, as the experiment was intended to evaluate cytotoxicity rather than compare quantitative biological responses. Cell viability was assessed using the XTT assay. In parallel, cell morphology and spreading were evaluated by fluorescence microscopy after staining the actin cytoskeleton with phalloidin (F-actin, green) and the nuclei

with DAPI (blue). The results of the assay are presented in **Figure IV-20** and the fluorescent microscopy images of the tinted cells on the different surfaces, in **Figure IV-21** and **Figure IV-22.**

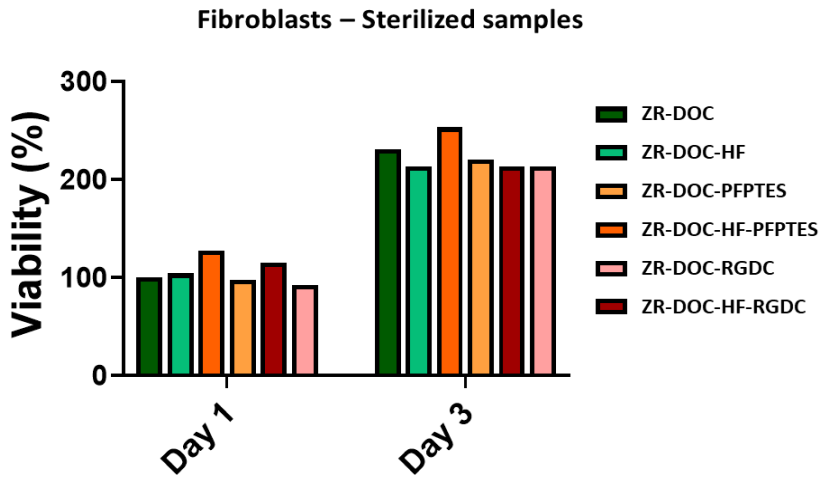

Figure IV-20 Quantitative cell viability results obtained by the XTT assay are shown, expressed as a percentage relative to the tissue culture plastic positive control. The effects of ethylene oxide (EtO) sterilization and surface pre-treatment by etching with 2% hydrofluoric acid (HF) for 5 min were also evaluated. Data are presented as mean ± standard deviation.

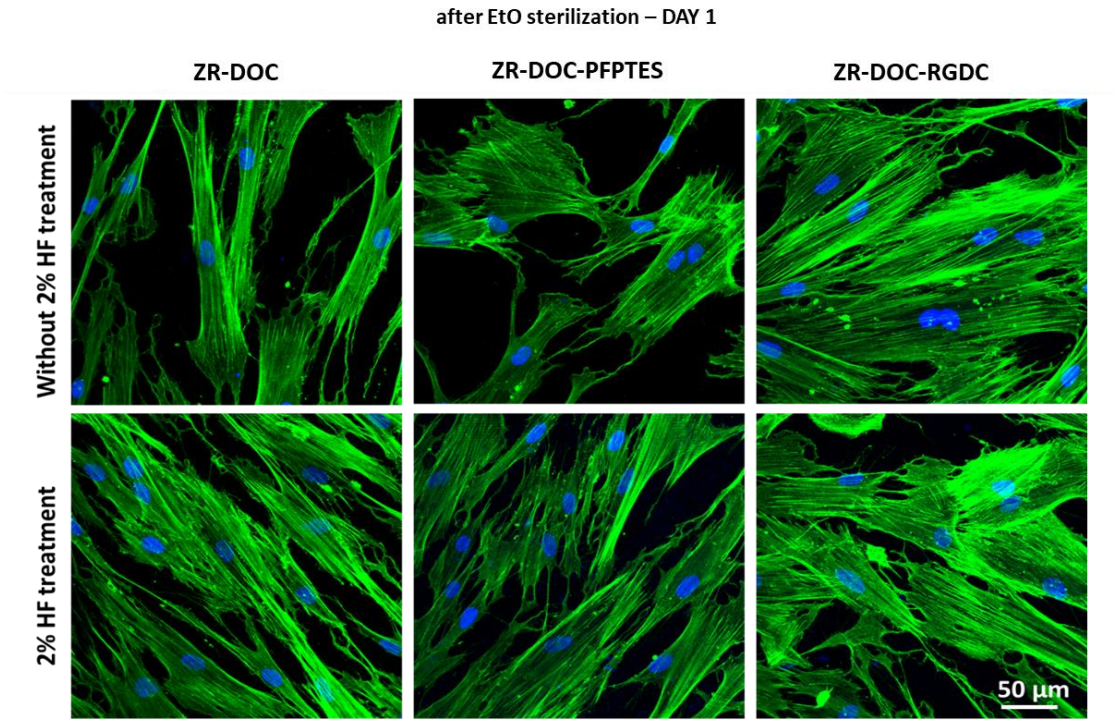

Figure IV-21 Representative fluorescence microscopy images of fibroblasts cultured on sterilized bare ZrO_2 (ZR-DOC), sterilized PFPTES-modified ZrO_2 (ZR-DOC-PFPTES), and sterilized RGDC-functionalized ZrO2 (ZR-DOC-RGDC), after EtO sterilization, and with (ZR-DOC-HF) and without HF 2% acid treatment (ZR-DOC), after 1 day of culture. Actin cytoskeleton was stained with phalloidin (F-actin, green) and cell nuclei with DAPI (blue). Scale bar: 50 µm

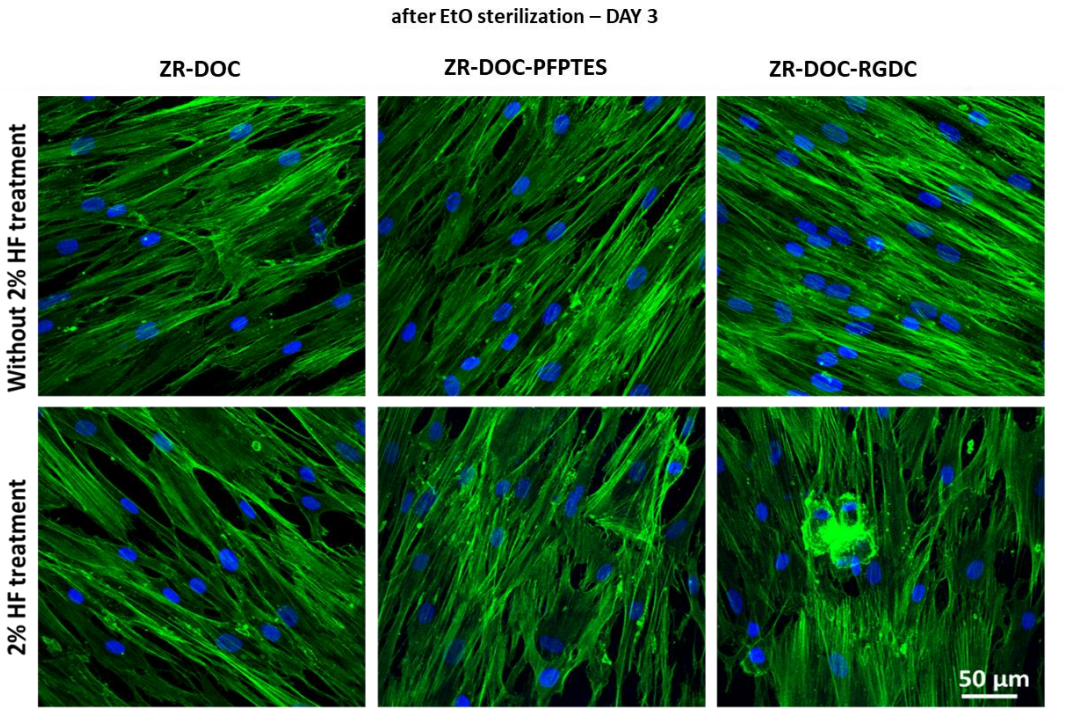

Figure IV-22 Representative fluorescence microscopy images of fibroblasts cultured on sterilized bare ZrO_2 (ZR-DOC), sterilized PFPTES-modified ZrO_2 (ZR-DOC-PFPTES), and sterilized RGDC-functionalized ZrO2 (ZR-DOC-RGDC), after EtO sterilization, and with (ZR-DOC-HF) and without HF 2% acid treatment (ZR-DOC), after 3 days of culture. Actin cytoskeleton was stained with phalloidin (F-actin, green) and cell nuclei with DAPI (blue). Scale bar: 50 µm

The XTT assay demonstrated that all investigated zirconia surfaces supported cellular metabolic activity, indicating good cytocompatibility following the different surface modification steps. Compared with the untreated ZR-DOC control, the HF-treated and functionalized surfaces exhibited similar or slightly higher XTT values, suggesting that neither the HF etching process nor the subsequent PFPTES silanization adversely affected cell viability.

Among the tested groups, the ZR-DOC-HF-PFPTES surface showed the highest metabolic activity, while the RGDC-functionalized samples maintained values comparable to those of the control and silanized surfaces. Overall, the results indicate that the surface functionalization strategy, including HF treatment, PFPTES immobilization, and subsequent RGDC grafting, preserves the biocompatibility of zirconia and provides a favorable substrate for cell growth and metabolic activity.

After 1 day of culture (**Figure IV-21**), cells exhibited the characteristic spindle-shaped fibroblast morphology and developed actin stress fibers on all surfaces, indicating successful attachment and early cytoskeletal organization. Notably, cells on the RGDC-functionalized surfaces appeared more extensively spread and displayed a denser actin network, suggesting enhanced cell-substrate interactions.

After 3 days of culture (**Figure IV-22**), cell density increased on all surfaces, reflecting continued proliferation and viability. While fibroblasts maintained a well-developed actin cytoskeleton in all groups, the RGDC-functionalized samples exhibited a more pronounced cellular alignment, with neighboring cells and actin filaments organized along a common direction. This behavior is consistent with enhanced integrin-mediated adhesion promoted by the RGD motif and may indicate a more mature adhesive phenotype. Such improved cytoskeletal organization and collective alignment are particularly relevant for peri-implant soft tissue integration, where the formation of an organized fibroblast network is expected to contribute to the establishment of a stable connective tissue seal around the abutment surface

IV.5.2. Proliferation and Wound Healing Assays

To further evaluate the biological safety of the ZrO_2 surfaces, the cytotoxicity of material extracts and of the modified surfaces were assessed using a tube formation assay with endothelial cells. The assays were performed by our NOMAD partner Dr. Lu YUAN at the University Medical Center Groningen (UMCG), within the Department of Biomaterials & Biomedical Technology.

Endothelial tube formation was assessed using extracts from the different ZrO_2 materials in order to evaluate potential cytotoxic effects related to the release of soluble components. Quantitative analysis of tube formation parameters, including the number of nodes and meshes, showed no noticeable differences between the tested conditions. In all cases, endothelial cells were able to form well-defined capillary-like networks comparable to the control.

Human umbilical vein endothelial cells were cultured in the presence of extracts obtained from the different ZrO_2 materials, prepared according to standardized extraction conditions. After incubation, the ability of the cells to form capillary-like structures was evaluated as an indicator of endothelial functionality. This assay enabled the assessment of potential cytotoxic or inhibitory effects of ZrO_2-derived extracts on endothelial cell organization and network formation.

Although slight variations in the measured parameters were observed between the different surface conditions (**Figure IV-23**), statistical analysis indicated that these differences were not significant ($p > 0.05$). In particular, while the ZR-DOC-PFPTES samples exhibited numerically higher values for some parameters at Day 3, these differences fell within the experimental variability and therefore cannot be interpreted as an improvement in angiogenic activity.

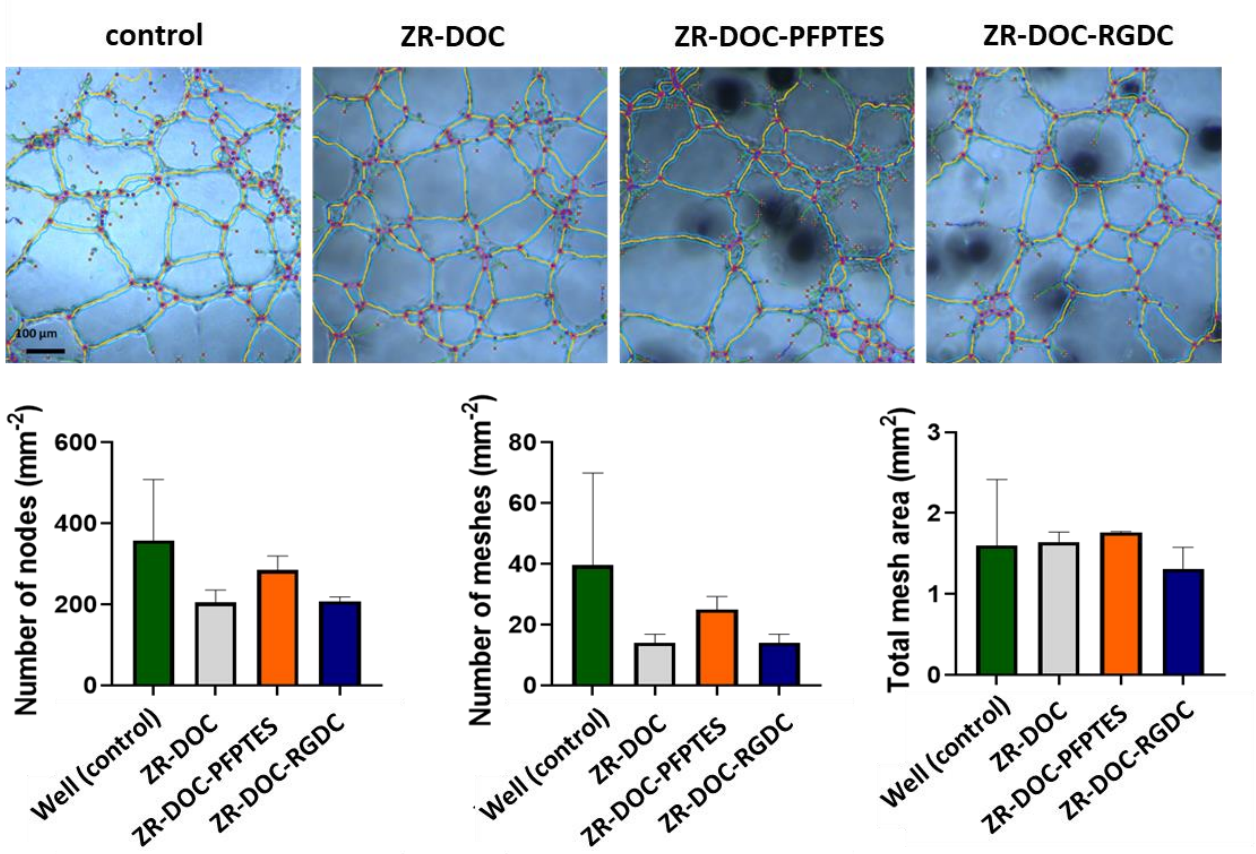

Figure IV-23. Endothelial tube formation assay performed using extracts from differently modified ZR-DOC disks. Representative optical microscopy images of human umbilical vein endothelial cells cultured with material extracts show the formation of capillary-like networks. Tube formation was quantitatively analyzed using ImageJ software, with nodes (branching points) identified in red and meshes (enclosed network areas) highlighted in yellow. Quantitative analysis of network parameters is presented below for each condition. Scale bar: 100 µm.

These results are consistent with the nature of extract-based assays, which assess only substances released from the materials into the culture medium. The absence of differences between conditions indicates that the functionalized ZrO_2 surfaces do not release toxic compounds. Overall, this assay confirms the biological safety of the developed surface modification strategy with respect to endothelial cell function.

To evaluate the wound healing properties of the biofunctionalized surfaces, a dedicated protocol was developed using transparent substrates compatible with a wound healing assay. For this purpose, ZrO_2 was deposited onto glass coverslips by physical vapor deposition (PVD), as described in **III.3.2** and subsequently functionalized using the optimized protocol. The resulting samples were additionally grafted with a fluorescently labeled peptide to verify successful surface functionalization. The results of the wound healing assay are presented in **Figure IV-24**.

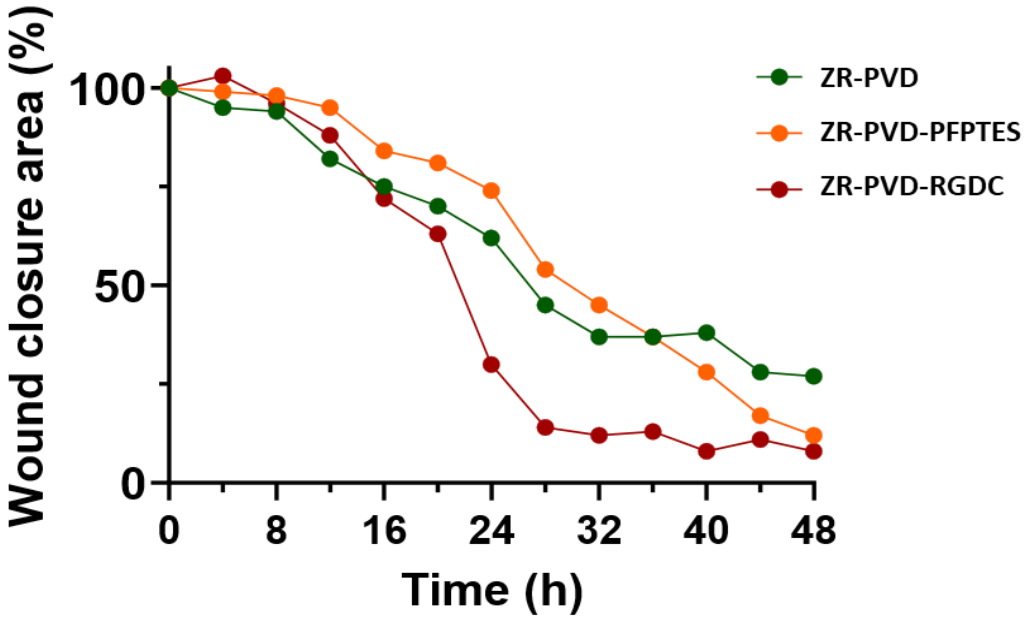

Figure IV-24. Quantitative wound healing assay results showing the evolution of wound closure over time for the different surface conditions.

Quantitative analysis of wound closure showed a time-dependent decrease in wound area for all tested conditions. A closer look at the wound healing kinetics shows that the effect of RGDC functionalization is mainly observed during the early phase of the assay. A pronounced decrease in wound area occurs on RGDC-functionalized surfaces within the first ~18 h, indicating faster initial cell migration compared to the non-functionalized controls. After this time point, the rate of wound closure slows down and becomes more similar to that observed for the other conditions. This suggests that RGDC primarily promotes early cell adhesion and migration, while later stages of wound closure are influenced by additional factors such as cell–cell interactions and surface coverage.

IV.6. Conclusion

In this chapter, the successful functionalization of the second bioactive layer (RGDC) onto silanized zirconia surfaces was demonstrated. The robustness and reproducibility of the functionalization strategy were established using multiple complementary surface and chemical characterization techniques applied to differently treated zirconia substrates. Beyond physicochemical validation, the biological performance of the engineered surfaces was assessed through cytotoxicity assays, confirming their biocompatibility. Furthermore, wound healing assays revealed that the bioactive layers tend to promote favorable cellular responses, highlighting their potential to enhance soft tissue interactions at the zirconia interface.

V. Conclusions & Perspectives

V.1. Conclusions

This thesis focused on the biofunctionalization of 3Y-TZP zirconia surfaces intended for soft tissue contact, with the objective of developing a controlled and reproducible route toward bioactive interfaces. The strategy relied on a two-step approach consisting of the formation of an organic intermediate layer followed by the covalent immobilization of a bioactive molecule, both of which were systematically optimized. Because no single technique can fully describe surface chemistry, several complementary physicochemical methods were combined. An original conjugation route based on an already activated ester was also explored in order to simplify the functionalization process. Next, a peptide was immobilized and its successful grafting was confirmed. The stability of both layers under mechanical stress and ethylene oxide (EtO) sterilization was then evaluated. Finally, the biological response of the functionalized surfaces was assessed in terms of cytocompatibility and cell adhesion. The main outcomes of this work are discussed in the following sections, which summarize the contributions of each chapter.

V.1.1. Surface Pre-treatment

This chapter was focused on the evaluation of the as-received 3Y-TZP zirconia surface and to the development of pre-treatment strategies aimed at obtaining a clean, hydroxylated and reproducible starting state prior to chemical functionalization. A comprehensive physicochemical characterization highlighted the presence of surface contaminants and demonstrated the variability of the initial surface condition. Different pre-treatment methods were therefore investigated and compared in terms of their ability to remove contamination species and activate the surface while preserving the integrity of the substrate. Polishing the surface led to a stable and reproducible surface state, providing a reliable platform for subsequent silanization and HF etching appeared to be an alternative for 3D samples. These results emphasize the critical role of surface preparation in zirconia functionalization and establish the pre-treatment step as a key parameter for ensuring the reproducibility and efficiency of the overall grafting strategy. Simultaneously, another important aspect of metal oxide functionalization, namely surface activation, was briefly investigated using WCA and XPS analyses. Water contact angle (WCA) measurements provided information on surface wettability and served as an indirect indicator of

surface cleanliness. As an example, XPS analyses were performed on two activation methods that produced hydrophilic surfaces; however, no significant differences in surface chemical composition were observed. A more informative approach would involve quantifying the subsequent functionalization step in order to estimate the density of available active sites. Nevertheless, the corresponding experiments did not yield conclusive results.

V.1.2. Silanization of Yttria stabilized zirconia

This chapter focused on the grafting of a trifunctional silane bearing a pentafluorophenyl ester moiety in order to create an already activated surface suitable for direct peptide conjugation. The silanization process was systematically optimized by investigating the influence of reaction parameters on layer formation, homogeneity and stability, while particular attention was paid to limiting uncontrolled polymerization and ensuring reproducibility. Because of the intrinsic complexity of surface chemical analysis, a combination of complementary characterization techniques was employed to confirm the successful formation of the silane layer and to assess its physicochemical properties. To accommodate this variety of characterization methods, different types of samples were used. The optimized conditions resulted in a controlled and stable functional layer exposing reactive ester groups at the interface. The optimized protocol also appeared to be transferable to other types of substrates, such as powder. By eliminating the need for a post-grafting activation step, this approach simplifies the functionalization protocol and represents a promising strategy for the development of more efficient and industry-compatible surface modification routes for zirconia-based implant components.

V.1.3. Biomolecule Attachment

This chapter addressed the covalent immobilization of the cell-adhesive RGDC peptide onto the activated zirconia surface and the evaluation of the biological response to the functionalized substrates. The peptide grafting conditions were optimized to achieve efficient coupling while preserving the bioactivity of the molecule. Surface analyses confirmed the successful immobilization of the biomolecular layer. The functionalized samples were subsequently subjected to *in vitro* biological assays in order to assess their cytocompatibility and their capacity to promote cell adhesion. The results demonstrated that the modified surfaces are biocompatible and that the presence of the RGDC layer enhances cellular attachment compared to non-functionalized zirconia. These findings validate the relevance of the developed chemical strategy for the design of bioactive zirconia surfaces intended for improved soft tissue integration.

V.2. Perspectives

Although progress has been achieved in the functionalization of zirconia surfaces for soft tissue integration, many studies reported in the literature provide only partial insight into the relationship between surface chemistry, grafting efficiency and biological response, as well as clinical relevance. In this context, the strategy developed in this work was designed to rely on well-controlled and reproducible modification steps, providing a stable platform for further investigations.

The first perspective of this project concerns the extension of the developed functionalization protocol to other bioactive molecules. In particular, the immobilization of additional cell-adhesive peptides and the comparison of their biological performance would make it possible to better understand the influence of biomolecular structure and surface density on cellular behavior.

On the other hand, RGDC was initially selected to compare conjugation techniques. As discussed in Chapter I, the presence of the cysteine residue enables the SMP-mediated reaction to occur through the thiol functionality. This would include and additional activation step, which would provide an additional parameter to compare. Under identical reaction conditions, this system therefore provides a convenient model to evaluate and compare the grafting efficiency. The grafting density of the resulting RGDC layer can thus be assessed.

Beyond the initial *in vitro* validation, further studies are required to deepen the evaluation of the cell–surface interactions on functionalized zirconia abutments. This includes a more comprehensive investigation of adhesion strength, cell spreading, proliferation and the formation of a stable soft tissue seal.

Within the framework of the NOMAD project, the antimicrobial properties of the grafted layer were also planned to be evaluated using a Robbins device and an experimental setup developed by our partners at UCM, in order to assess the dual activity of the RGD-derived peptides.

Ultimately, the clinical relevance of the developed surfaces will need to be assessed through *in vivo* experiments. In this framework, the materials elaborated during this thesis will be pursued within the NOMAD project and evaluated in animal models, representing a key step toward future clinical applications

A. Synthèse en français

A.1 Introduction

Les implants constituent aujourd'hui une solution fiable et durable pour le remplacement des racines dentaires, mais leur succès clinique à long terme dépend autant de leur stabilité mécanique que de leur intégration biologique. Si l'intégration osseuse assure l'ancrage de l'implant, l'intégration des tissus mous péri-implantaires joue un rôle essentiel en formant une barrière protectrice contre l'environnement oral. Une perte de contact au niveau des tissus gingivaux favorise l'infiltration bactérienne et l'inflammation, pouvant conduire à des Dans ce contexte, la modification de surface s'est imposée comme une stratégie clé pour améliorer les performances des implants. Au-delà des approches historiques fondées sur l'optimisation de la rugosité et de la topographie pour favoriser l'intégration osseuse, il est désormais établi que l'ingénierie des interfaces basée sur le greffage de biomolécules joue un rôle déterminant dans la modulation des réponses biologiques. Les stratégies de fonctionnalisation visent ainsi à introduire des signaux biochimiques spécifiques capables d'orienter activement l'adhésion et le comportement cellulaires.

Bien que le titane demeure le matériau de référence en implantologie, la zircone apparaît comme une alternative prometteuse, notamment pour des raisons esthétiques et de biocompatibilité. Elle présente des propriétés mécaniques suffisantes pour l'application et une intégration osseuse comparable à celle du titane. Toutefois, son inertie chimique et sa faible réactivité de surface rendent plus complexe le développement de stratégies de fonctionnalisation chimique stables et reproductibles. Les traitements de surface actuellement rapportés reposent majoritairement sur des modifications physiques ou physicochimiques.

La fonctionnalisation par immobilisation covalente de biomolécules, en particulier de peptides bioactifs, constitue une approche plus ciblée pour favoriser l'intégration tissulaire. Elle nécessite cependant des stratégies de greffage robustes et bien contrôlées. Dans cette perspective, les chimies à base de silanes représentent une voie intéressante pour introduire des fonctions réactives sur les surfaces d'oxydes, afin d'immobiliser des peptides biologiquement actifs.

L'objectif de cette thèse est de développer et caractériser une stratégie de modification chimique pour la fonctionnalisation de surfaces en zircone destinées aux piliers des implants dentaires, en vue de favoriser l'adhésion de la muqueuse gingivale. Les travaux portent sur la définition d'états de surface reproductibles, l'optimisation de protocoles de silanisation, le contrôle des paramètres influençant la formation des couches organiques, l'immobilisation covalente de peptides bioactifs, ainsi que l'évaluation de l'efficacité du greffage et de la réponse biologique associée. L'ensemble vise à concevoir des surfaces en zircone chimiquement adaptées,

capables de favoriser des interactions stables et biologiquement pertinentes à l'interface implant-tissu.

A.2 État de l'art

A.2.1 La zircone dans le contexte implantaire

La zircone (ZrO_2), et plus particulièrement la zircone tétragonale stabilisée à l'yttrium (3Y-TZP), s'est imposée comme une alternative crédible au titane en implantologie dentaire. Elle associe une ténacité élevée pour une céramique, liée au mécanisme de transformation tétragonale–monoclinique sous contrainte, à une excellente stabilité chimique et des propriétés esthétiques favorables. Les recommandations récentes de la Société Européenne d'Implantologie Céramique confirment la pertinence clinique des implants en zircone, qu'ils soient monoblocs ou en deux pièces.

Au-delà des performances mécaniques, la réussite implantaire repose toutefois sur la qualité des interactions biologiques à l'interface tissu–matériau. Si l'ostéointégration assure l'ancrage osseux, le scellement de la muqueuse gingivale autour du pilier conditionne la protection contre l'infiltration bactérienne et le développement de péri-implantites. L'ingénierie de surface constitue ainsi un levier majeur pour moduler l'adhésion cellulaire, l'organisation tissulaire et la réponse inflammatoire.

A.2.2 Structure cristalline et propriétés physicochimiques de la zircone

La zircone présente trois phases cristallines principales : monoclinique, tétragonale et cubique. En implantologie, la phase tétragonale stabilisée par l'yttrium est privilégiée pour ses propriétés mécaniques supérieures. La microstructure, notamment la taille des grains issue des conditions de frittage, influence directement la stabilité de phase, la résistance au vieillissement et l'état de surface.

Sur le plan chimique, la zircone se distingue par un caractère iono-covalent mixte des liaisons Zr–O. À la surface, des sites acides de Lewis associés aux cations Zr^{4+} et des sites basiques liés aux anions oxygène coexistent. L'adsorption dissociative de l'eau conduit à la formation de groupements hydroxyles dont la densité et la nature dépendent de la phase cristalline et de l'histoire thermique du matériau. Ces groupements –OH constituent les principaux sites d'ancrage pour les stratégies de fonctionnalisation.

Cependant, la majorité des études fondamentales sur la réactivité de la zircone concernent des poudres monocliniques utilisées en catalyse ou en chromatographie. Les connaissances spécifiques aux surfaces denses en 3Y-TZP, telles qu'utilisées en implantologie, demeurent

limitées, en particulier quant à la nature et à la distribution réelle des sites réactifs disponibles pour un greffage contrôlé.

A.2.3 Stratégies générales de biofonctionnalisation de la zircone

La biofonctionnalisation des surfaces en zircone repose généralement sur une approche en plusieurs étapes : un prétraitement visant à nettoyer et activer la surface, le greffage d'un agent de couplage formant une couche organique intermédiaire, puis l'immobilisation covalente de la biomolécule d'intérêt.

Les prétraitements peuvent être mécaniques, chimiques ou physicochimiques. Ils influencent la rugosité, l'énergie de surface et la densité en groupements hydroxyles, paramètres déterminants pour la suite des réactions.

Parmi les agents de couplage, les organosilanes sont les plus étudiés. Leur tête siliciée hydrolysable réagit avec les hydroxyles de surface pour former des liaisons Si–O–Zr, tandis que leur chaîne organique porte une fonction terminale réactive. La qualité des couches greffées dépend fortement de la structure du silane, des conditions expérimentales telles que le solvant, la teneur en eau, la concentration, la température et la durée de réaction. Les silanes multifonctionnels peuvent conduire à des réseaux réticulés plus stables, mais au prix d'un risque de polycondensation non contrôlée. La stabilité hydrolytique des liaisons hétérosiloxanes sur zircone reste par ailleurs inférieure à celle observée sur silice.

Dans la littérature d'autres approches ont été explorées pour la modification chimique d'oxides, notamment l'utilisation d'acides organo-phosphoniques ou organo-phosphates de la polydopamine issues de l'oxydation de la dopamine ou de la L-DOPA. Des agents naturels tels que la génipine ou des systèmes enzymatiques comme la transglutaminase ont également été proposés. Néanmoins, pour la zircone, ces stratégies restent peu étudiées de manière systématique et leur stabilité à long terme demeure insuffisamment documentée.

A.2.4 Chimies de couplage covalent

L'immobilisation covalente est privilégiée afin d'assurer la stabilité des biomolécules greffées. Les réactions les plus couramment utilisées impliquent des fonctions amine, carboxyle ou thiol. Ici, nous nous intéressons particulièrement à l'immobilisation des peptides.

La formation de liaisons amides via la réaction entre une amine primaire et un acide carboxylique nécessite l'activation de la fonction carboxylique. Classiquement, cette activation est réalisée en utilisant comme réactifs une carbodiimide et le N-hydroxysuccinimide (NHS). Bien que les conditions de couplage soient compatibles avec les biomolécules, cette chimie reste

sensible au pH, à la stœchiométrie et aux réactions secondaires pouvant limiter l'efficacité du greffage. Une alternative aux NHS est d'utiliser des esters pentafluorophényles.

Les réactions thiol–maleimide, reposant sur une addition de Michael, permettent un couplage sélectif sur des résidus cystéine. Toujours parmi les réactions de type « click », les cycloadditions de type 1,3 de Huisgen entre un azoture et un alcyne, offrent un contrôle élevé et une grande spécificité, mais leur application directe à la zircone reste marginale.

Dans l'ensemble, bien que ces chimies soient bien établies sur la silice ou le titane, leur adaptation à la zircone repose souvent sur des extrapolations et manque d'études comparatives systématiques.

A.2.5 Molécules bioactives pour l'ingénierie de surface

Les molécules bioactives explorées pour la zircone incluent des protéines de la matrice extracellulaire, des facteurs de croissance et des peptides courts. Parmi les peptides, il est possible de noter :

- Le motif RGD, dérivé de la fibronectine, est le plus étudié. Il favorise l'adhésion cellulaire via les intégrines et stimule la différenciation ostéogénique. Son application à la zircone a montré des effets positifs sur l'adhésion et l'activité ostéoblastique, bien que les études restent limitées,
- Des peptides dérivés de la laminine, tels que YIGSR ou des fragments de laminine-5, présentent un intérêt particulier pour l'intégration des tissus mous et la formation d'hémidesmosomes,
- Les peptides ostéoinducteurs dérivés des BMP ou d'autres séquences spécifiques ont également été évalués.

Comparativement aux protéines entières, les peptides offrent une meilleure stabilité, une synthèse contrôlée et une résistance accrue aux procédés de stérilisation, ce qui les rend particulièrement adaptés à des applications cliniques sur implants en zircone.

A.2.6 Limites et enjeux actuels

L'état de l'art met en évidence plusieurs limites majeures.

Les connaissances sur la réactivité spécifique des surfaces denses en 3Y-TZP restent partielles. Les protocoles de silanisation et de greffage sont très variables et rarement comparables d'une étude à l'autre. Enfin, peu de travaux évaluent la stabilité des couches organiques sous contraintes cliniques réelles, incluant la stérilisation et les sollicitations mécaniques par exemple lors du brossage ou de la pose de l'implant.

Ainsi, la fonctionnalisation de la zircone nécessite l'adaptation de protocoles développés pour d'autres oxydes. Elle nécessite une approche intégrée, associant contrôle rigoureux de l'état de

surface, optimisation des paramètres chimiques et évaluation de la stabilité de l'interface dans une perspective translationnelle.

A.3 Prétraitement de surface de la zircone

A.3.1 État initial des échantillons commerciaux

La caractérisation des disques de zircone tels que reçus (ZR-AR) a mis en évidence la présence de contaminations particulaires et organiques issues du procédé de fabrication et de manipulation. Les analyses par microscopie électronique et spectroscopie des photo-électrons X (XPS) ont révélé des particules riches en aluminium et en silicium, attribuées au procédé industriel comme des résidus d'aluminosilicates issus du polissage ou de l'alumine utilisée comme ajout pour améliorer le frittage et la stabilité hydrothermale.

Ces contaminants masquent partiellement le signal du substrat et sont susceptibles d'interférer avec les étapes de greffage, en particulier lors de l'utilisation de silanes. L'élimination de ces espèces est donc indispensable afin d'éviter des artefacts d'analyse et d'assurer une fonctionnalisation homogène.

L'analyse par diffraction des rayons X a confirmé que les disques présentaient majoritairement la phase tétragonale attendue pour une zircone 3Y-TZP, sans transformation monoclinique détectable à l'état initial.

A.3.2 Stratégies d'élimination des contaminants inorganiques

Deux approches principales ont été étudiées pour obtenir une surface exempte de contamination : l'attaque chimique par acide fluorhydrique (HF) et le polissage mécanique.

A.3.2.1 Attaque à l'acide fluorhydrique

L'attaque par HF a été évaluée pour différentes concentrations et durées. Les analyses XPS ont montré que le silicium était éliminé dès les conditions les plus douces, tandis que l'élimination complète de l'aluminium nécessitait des conditions plus sévères.

Cependant, l'augmentation de la concentration et du temps d'attaque induit une modification progressive de la topographie de surface, accompagnée d'une augmentation de la rugosité et d'une forte variabilité locale. Les mesures d'angle de contact ont également mis en

évidence une augmentation importante de l'hydrophilie sous conditions agressives, liée à la fois à l'évolution chimique et morphologique de la surface.

Bien que l'attaque HF permette un nettoyage efficace, elle ne garantit pas un contrôle reproductible de la rugosité pour les disques étudiés.

A.3.2.2 Polissage mécanique

Le polissage progressif a permis d'obtenir des surfaces significativement plus lisses, avec une rugosité réduite à l'échelle nanométrique. Les observations par SEM ont révélé la microstructure granulaire du matériau ainsi que la présence ponctuelle de particules d'alumine intégrées dans la matrice, cohérentes avec la composition du matériau.

Contrairement à l'état initial, les analyses XPS n'ont plus détecté de contamination en aluminium ou en silicium en surface, confirmant l'efficacité du polissage combiné au nettoyage par solvants. Cette approche a permis d'obtenir une surface propre, homogène et adaptée aux analyses de surface fines.

A.3.3 Elimination de la contamination organique et activation de surface

Au-delà de l'élimination des contaminants inorganiques, la suppression des résidus organiques et l'activation chimique (cf A 2.3) de la surface sont nécessaires pour favoriser la formation ultérieure de liaisons Si–O–Zr.

Plusieurs méthodes ont été comparées : solutions basiques, solutions oxydantes de type piranha, et traitement UV/O_3. L'efficacité des traitements a été évaluée par mesure de l'angle de contact, utilisé comme indicateur indirect de la propreté et de l'énergie de surface.

Les traitements combinant oxydation chimique ou basique et exposition UV/O_3 ont conduit aux surfaces les plus hydrophiles. Toutefois, le traitement UV/O_3 seul a été retenu pour la suite des travaux en raison de sa simplicité, de sa reproductibilité et de sa compatibilité avec un flux expérimental routinier, tout en limitant les manipulations chimiques agressives.

A noter qu'il n'a pas été possible de mettre en évidence l'effet de ces prétraitements sur la réaction de silanisation.

A.3.4 Choix de l'état de surface pour la fonctionnalisation

Les deux stratégies, attaque HF prolongée et polissage mécanique, ont permis d'obtenir des surfaces exemptes de contamination détectable. Néanmoins, le polissage a été privilégié pour l'optimisation des protocoles de greffage, car il fournit une surface lisse et reproductible permettant une interprétation fiable des mesures d'angle de contact et des analyses de surface.

Pour des géométries tridimensionnelles telles que des implants ou piliers, une attaque chimique douce peut constituer une alternative pertinente, à condition de contrôler strictement les paramètres afin de préserver la topographie souhaitée.

A.4 Silanisation de la zircone stabilisée à l'yttrium

A.4.1 Enjeux de la silanisation sur zircone

La zircone, bien qu'oxyde métallique, présente une réactivité de surface moins étudiée que la silice. L'immobilisation directe de biomolécules sur ce substrat repose essentiellement sur des interactions physiques faibles, insuffisantes pour garantir une stabilité à long terme en milieu aqueux ou biologique. L'introduction d'une couche d'interface organosiliciée constitue ainsi une étape clé pour permettre un ancrage covalent robuste.

Les organosilanes trifonctionnels possèdent une double réactivité :

– 3 groupes alkoxysilane capable de former des liaisons Si–O–Zr avec les hydroxyles de surface ou Si-O-Si avec les silanes adjacents,

– une fonction organique terminale servant de point d'ancrage pour les biomolécules.

Cependant, la formation d'une couche contrôlée dépend fortement des paramètres expérimentaux. Une hydrolyse ou une condensation mal maîtrisée peut conduire à la formation de polymères siloxanes désordonnés, compromettant la reproductibilité et l'accessibilité des fonctions terminales.

A.4.2 Optimisation du greffage de l'APTES

Le 3-aminopropyltriéthoxysilane (APTES) a été utilisé comme molécule modèle afin d'optimiser les paramètres de réaction. Son groupement amine terminal permet une quantification indirecte de la densité de greffage par la méthode colorimétrique (ADECA), facilitant le criblage des conditions expérimentales.

Une étude factorielle a été menée en faisant varier :

- La concentration en silane,
- Le temps d'immersion,
- La durée de recuit thermique.

Les résultats obtenus par mesure d'angle de contact et par quantification ADECA ont montré des tendances cohérentes : une augmentation de la concentration et du temps d'immersion tend à accroître la densité apparente d'amines en surface. Toutefois, aux concentrations élevées, une augmentation de la variabilité expérimentale a été observée, suggérant des phénomènes de condensation moins contrôlés et une possible formation partielle de multicouches

L'optimisation ne s'est donc pas limitée à la maximisation de la densité de greffage, mais a intégré un critère de reproductibilité. Les conditions retenues correspondent à une concentration modérée (1 mM) et un temps d'immersion de 2 heures, offrant un compromis équilibré entre densité de fonctions accessibles, stabilité et robustesse expérimentale.

L'étude de la durée de recuit a montré qu'un traitement thermique court 1 h à 110 °C suffisait à stabiliser la couche, sans bénéfice mesurable pour des durées plus longues. Cette observation renforce la pertinence d'un protocole compatible avec des contraintes industrielles.

A.4.3 Confirmation spectroscopique du greffage de la couche d'APTES

Les analyses XPS ont confirmé la formation d'une couche organosiliciée par :

- L'apparition du signal Si 2p,
- L'augmentation du signal C 1s,
- L'atténuation des signaux du substrat Zr 3d et Y 3d.
- L'analyse haute résolution du signal O 1s mettant en évidence la formation de liaisons siloxanes (Si–O–Zr et/ou Si–O–Si) et confirmant l'ancrage covalent du silane à la surface.
- L'absence ou la faible intensité du signal N 1s, fréquemment rapportée dans la littérature pour l'APTES sur les oxydes métalliques.

Dans l'ensemble, les résultats confirment la formation d'une couche mince, homogène compatible avec un greffage de type monocouche contrôlée plutôt qu'avec une polymérisation massive.

avec un greffage de type monocouche contrôlée plutôt qu'avec une polymérisation massive.

A.4.4 Transposition au silane activé PFPTES

Le protocole optimisé a ensuite été appliqué à un silane trifonctionnel portant un ester pentafluorophényle (PFPTES), destiné au couplage ultérieur de peptides.

Le choix d'un ester pentafluorophényle repose sur sa meilleure stabilité hydrolytique par rapport aux esters NHS classiquement utilisés. Cette stabilité accrue permet d'envisager des

réactions de couplage en conditions aqueuses tout en limitant l'hydrolyse prématurée du groupement activé.

La silanisation a été réalisée dans des conditions anhydres afin de limiter une polycondensation anarchique et afin de préserver l'intégrité de l'ester activé.

A.4.5 Caractérisation multi-technique de la couche PFPTES

Les mesures d'angle de contact ont montré une augmentation marquée de l'hydrophobicité après greffage, cohérente avec l'introduction du motif fluoré.

L'analyse XPS a révélé :

- L'apparition du signal F 1s,
- La présence du signal Si 2p,
- Une augmentation du signal C 1s,
- Une atténuation des pics Zr 3d et Y 3d relatifs du substrat.

Le rapport atomique F/Si proche de la valeur théorique. Cependant, deux contributions sont observables sur le pic F1s correspondant à un fluore de type organique (688 eV) et un fluore dont le déplacement chimique (685 eV) suggère qu'il est sur forme de fluorure.

Les analyses ToF-SIMS ont détecté des fragments caractéristiques contenant du silicium et du fluor, attestant de la présence de la couche organique dans les toutes premières couches atomiques de la surface.

Enfin, les analyses FTIR réalisées sur poudre de zircone à grande surface spécifique ont permis d'identifier les bandes vibratoires associées :

- Aux liaisons C–F (1520 cm^{-1}),
- Aux liaisons siloxanes (1000-900 cm^{-1}).

L'ensemble de ces résultats convergents démontre la formation d'une couche PFPTES covalente, chimiquement intacte et potentiellement réactive vis-à-vis des amines nucléophiles.

A.4.6 Cytocompatibilité des couches intermédiaires et bioactives

Une première étape a consisté à évaluer l'innocuité de la couche intermédiaire PFPTES, afin d'exclure tout effet cytotoxique potentiel lié à la chimie d'activation de surface. Des tests de viabilité cellulaire réalisés sur cellules ostéoblastiques de type MG-63 ont montré une activité métabolique comparable entre la zircone non modifiée et la zircone fonctionnalisée par PFPTES.

Après normalisation par rapport au témoin plastique, les valeurs de viabilité cellulaire restaient supérieures à 70 %, seuil défini par la norme ISO 10993-5 pour caractériser l'absence de

cytotoxicité. Ces résultats confirment que la couche silanisée activée ne présente pas d'effet délétère sur la survie cellulaire.

A.5 Greffage covalent du peptide RGDC sur zircone fonctionnalisée

A.5.1 Stratégie chimique et principe du greffage

Le peptide RGDC, contenant le motif RGD reconnu par les intégrines, a été choisi comme séquence modèle en raison de son rôle établi dans l'adhésion cellulaire. Contrairement aux stratégies fondées sur des couches intermédiaires polymériques (ex. polydopamine), l'approche développée repose sur une modification étape par étape :

1) Silanisation contrôlée de la surface par PFPTES,
2) Substitution nucléophile entre l'ester activé de surface et l'amine primaire du peptide.

Cette stratégie vise à garantir un ancrage covalent stable tout en conservant l' activité du peptide.

A.5.2 Optimisation des paramètres de greffage

A.5.2.1 Influence de la concentration et du temps d'immersion

Une étude paramétrique a été menée afin d'évaluer l'influence de la concentration en peptide, du pH et du temps de réaction sur l'efficacité du greffage.

Les analyses XPS réalisées après greffage à faibles concentrations (125 – 1000 $\mu g \cdot mL^{-1}$) ont montré la persistance du signal fluor (F 1s), caractéristique du groupe pentafluorophényle, associée à une détection très faible voire inexistante du signal azote (N 1s). Ces résultats indiqueraient une substitution incomplète des esters activés et donc une densité limitée de peptide immobilisé.

L'augmentation de la concentration à 1 $mg \cdot mL^{-1}$ (≈ 2,2 mM) combinée à un temps d'immersion prolongé (2 h) a conduit à une diminution marquée du signal fluoré, suggérant une consommation plus efficace des esters activés. Ces observations ont conduit à retenir ces conditions comme protocole optimisé.

A.5.2.2 Influence du tampon et du pH

Le choix du milieu réactionnel s'est révélé déterminant. L'utilisation initiale d'un tampon carbonate à pH élevé (~9,6) a favorisé l'adsorption de carbonates à la surface de la zircone et probablement accéléré l'hydrolyse compétitive de l'ester activé.

Des analyses FTIR sur poudre de zircone ont montré des modifications spectrales après exposition au peptide, mais l'interprétation était limitée par la forte contribution des carbonates dans la région des bandes amides.

Afin de limiter l'hydrolyse tout en maintenant une nucléophilie suffisante de l'amine, le greffage a ensuite été réalisé en solution aqueuse ajustée à pH ≈ 8, puis en tampon HEPES contrôlé entre pH 7,6 et 8,6. Les spectres FTIR ont montré l'apparition de nouvelles bandes dans la région 1400–1450 cm^{-1}, compatibles avec les signatures de vibrations du peptide, tandis que l'intensité du signal associé au pentafluorophényle diminuait.

Ces résultats indiqueraient que des conditions modérément basiques permettent un meilleur compromis entre réactivité et stabilité chimique. Toutefois, même si la présence du peptide à la surface de la zircone est démontrée, la formation de la liaison amide par réaction entre l'ester activé et l'amine primaire du peptide RGDC n'a pu être mise en évidence.

A.5.3 Caractérisation physicochimique du greffage du peptides RGDC

L'analyse XPS a mis en évidence des évolutions cohérentes entre les différentes étapes :

- Atténuation du signal zirconium après silanisation,
- Apparition du fluor après PFPTES,
- Diminution du fluor et augmentation de l'azote après greffage du peptide.

Toutefois, la présence de contaminations initiales en silicium et azote, ainsi que des rapports atomiques non stœchiométriques, ont limité l'interprétation des couches greffées.

Afin d'obtenir une information plus spécifique des couches superficielles, des analyses ToF-SIMS ont été réalisées.

Les résultats ont montré :

– Une atténuation des fragments caractéristiques du substrat après silanisation, confirmant la formation d'un film organique à la surface. En particulier, le fragment ZrO^+ (m/z 105,89), caractéristique du substrat zirconia, présente l'intensité relative la plus élevée pour la surface contrôle. Après fonctionnalisation par PFPTES, une diminution nette de ce signal est observée dans les spectres normalisés en ions totaux, cohérente avec un masquage partiel de la surface de zirconia par une couche organique. Après greffage du peptide RGDC, l'intensité de ZrO^+ reste à un niveau réduit similaire, sans atténuation supplémentaire marquée, indiquant que la couche organique est déjà formée après silanisation.

– L'apparition de fragments fluorés après fonctionnalisation par PFPTES, notamment des signaux centrés autour de m/z ≈ 79 et m/z ≈ 126. Le signal autour de m/z ≈ 79 peut résulter de plusieurs fragments isobares tels que $C_6H_7^+$ (m/z 79,06), $C_2H_4O_2F^+$ (m/z 79,03) ou SiO_2F^+ (m/z 78,98), associés respectivement à des fragments aromatiques, fluorés ou issus de structures siloxanes. De même, le signal autour de m/z ≈ 126 peut provenir de fragments tels que $Si_4CH_2^+$ (m/z 125,89), CF_6^+ (m/z 125,98) ou $C_7H_{10}O_2^+$ (m/z 126,04). Ces signaux, très faibles sur la surface contrôle, augmentent nettement après silanisation par PFPTES, confirmant l'introduction d'une couche organique fluorée contenant le groupement pentafluorophényl ester.

– La diminution de ces fragments fluorés après greffage du peptide, indiquant la modification chimique de la couche silanisée. Les signaux autour de m/z ≈ 79 et m/z ≈ 126 diminuent après la réaction avec le peptide RGDC, ce qui est cohérent avec une substitution nucléophile ou une hydrolyse partielle des fonctions ester pentafluorophényl lors de la conjugaison du peptide, conduisant à une consommation ou à un masquage partiel de ces groupes fluorés.

– L'émergence de fragments azotés caractéristiques du peptide, notamment un signal marqué autour de m/z ≈ 60 après greffage du RGDC. Ce signal résulte de contributions de plusieurs fragments tels que C_5^+ (m/z 60,00), $C_2H_4O_2^+$ (m/z 60,03) et surtout $CH_6N_3^+$ (m/z 60,08). Bien que des fragments hydrocarbonés et oxygénés puissent être présents à faible intensité sur les surfaces contrôle et PFPTES, l'augmentation marquée du signal à m/z ≈ 60 après greffage est principalement attribuée au fragment $CH_6N_3^+$, riche en azote et caractéristique de résidus d'arginine. Cette observation est cohérente avec la présence du peptide RGDC à la surface et constitue une preuve moléculaire directe de son immobilisation.

Dans l'ensemble, l'évolution systématique des signaux d'ions secondaires associés au substrat, au silane, aux fragments organiques fluorés et aux fragments azotés fournit une image cohérente des différentes étapes de modification de surface. L'atténuation des signaux liés au ZrO_2, l'apparition puis la diminution partielle des fragments fluorés du silane, ainsi que l'augmentation marquée des fragments azotés après greffage du RGDC confirment la fonctionnalisation progressive de la surface et la formation d'une couche externe contenant le peptide.Sur les deux types de substrats étudiés (ZR-KU et ZR-DOC), des fragments azotés de masse élevée ont été détectés exclusivement après greffage, fournissant une preuve moléculaire directe de la présence du peptide en surface.

Ainsi, contrairement à l'XPS, la ToF-SIMS a permis de confirmer de manière plus spécifique l'immobilisation du RGDC.

Le greffage a également été validé en fluorescence à l'aide d'un peptide RGDC marqué au FITC.

Les surfaces fonctionnalisées ont présenté un signal fluorescent homogène sur l'ensemble du disque, tandis que les échantillons témoins (sans silanisation préalable) n'ont montré qu'un signal faible et localisé, attribué à une adsorption non spécifique limitée.

Ces observations confirment :
– La réussite du protocole de greffage,
– La couverture homogène de la surface,
– La faible contribution de la physisorption.

A.5.4 Activité biologique des surfaces biofonctionnalisées

Au-delà de la validation physicochimique du greffage du peptide RGDC, l'objectif final de cette stratégie de biofonctionnalisation est d'induire une réponse biologique contrôlée et favorable. L'activité biologique des surfaces modifiées a donc été évaluée afin de vérifier que les biomolécules immobilisées conservent leur fonctionnalité après greffage et que la stratégie chimique développée ne génère pas d'effets indésirables.

A.5.4.1 Cytocompatibilité des couches bioactives

La cytocompatibilité de la surface finale greffée par le peptide RGDC a ensuite été évaluée à l'aide de fibroblastes gingivaux humains, cellules particulièrement pertinentes pour l'intégration des tissus mous péri-implantaires. Les analyses quantitatives (test XTT) et qualitatives (marquage de l'actine et des noyaux) ont montré :

- Une viabilité comparable entre surfaces témoins et surfaces fonctionnalisées,
- Une morphologie cellulaire normale,
- Une organisation cytosquelettique compatible avec une bonne adhésion.

Ainsi, ni la silanisation ni le greffage peptidique n'induisent d'altération de la viabilité ou de l'adhésion cellulaire, démontrant la biocompatibilité globale de la stratégie développée.

A.5.4.2 Absence de relargage cytotoxique

Afin d'évaluer d'éventuels effets liés au relargage de composés issus des surfaces modifiées, des essais sur extraits ont été réalisés à l'aide d'un test de formation de structures endothéliales (tube formation assay).

Les cellules endothéliales exposées aux extraits des différentes surfaces ont conservé leur capacité à former des réseaux capillaires organisés, sans différence notable entre conditions. Ces résultats indiquent que les surfaces fonctionnalisées ne libèrent pas de composés solubles susceptibles d'altérer la fonctionnalité cellulaire

Cette étape confirme la stabilité chimique des couches développées dans un environnement aqueux simulant des conditions biologiques.

A.5.4.3 Influence sur la migration cellulaire

Au-delà de l'innocuité, l'effet fonctionnel du greffage du peptide RGDC a été évalué à travers un test de cicatrisation in vitro (wound healing assay), réalisé sur substrats transparents

recouverts de zircone obtenue par déposition physique en phase vapeur (PVD) puis biofonctionnalisés.

L'analyse cinétique de la fermeture de la plaie montre :

- Une accélération significative de la migration cellulaire au cours des premières heures sur les surfaces RGDC,
- Une convergence progressive des vitesses de fermeture à des temps plus longs.

Ces résultats suggèrent que la présence du motif RGD favorise les phases précoces d'adhésion et de migration cellulaire, étapes critiques dans l'établissement d'un joint muqueux stable autour d'un implant. L'effet observé est cohérent avec le rôle biologique du motif RGD dans l'activation des intégrines et la modulation de l'adhérence cellule–matériau.

A.6 Conclusion

Les travaux présentés dans cette thèse ont permis de développer une stratégie chimique intégrée de biofonctionnalisation de surfaces en zircone stabilisée à l'yttrium, en vue d'applications en implantologie dentaire.

L'étude a d'abord mis en évidence l'importance déterminante de la préparation de surface, condition préalable indispensable à toute modification chimique reproductible. La maîtrise de l'état de surface, notamment par polissage et activation contrôlée, s'est révélée essentielle pour limiter les contaminations et garantir une réactivité homogène.

Une approche de silanisation optimisée a ensuite été établie, permettant l'introduction stable de fonctions réactives à la surface de la zircone. L'analyse critique des paramètres réactionnels a montré que la densité de greffage ne constitue pas l'unique critère d'optimisation : la reproductibilité, la stabilité hydrolytique et la compatibilité avec des contraintes de mise en œuvre réalistes sont tout aussi déterminantes.

Le greffage covalent du peptide RGDC via un ester pentafluorophényle activé a démontré la faisabilité d'une immobilisation contrôlée en conditions aqueuses à pH basique modéré. La combinaison de techniques complémentaires de caractérisation de surface a permis de valider la formation d'une couche peptidique stable, tout en mettant en lumière les limites analytiques associées aux substrats céramiques denses.

Enfin, l'évaluation biologique a confirmé que la couches organiques développées sont cytocompatibles et capables de moduler favorablement les interactions cellulaires précoces, en particulier la migration et l'adhésion de cellules impliquées dans l'intégration des tissus mous. Ces résultats suggèrent que la biofonctionnalisation contrôlée de la zircone constitue une voie prometteuse pour renforcer la stabilité biologique de l'interface implant–tissu.

Dans son ensemble, ce travail souligne que la transformation d'une surface bioinerte en surface bio-instructive ne repose pas uniquement sur le choix d'une molécule bioactive, mais sur la maîtrise intégrée de la préparation du substrat, de la chimie de greffage et de la validation physicochimique et biologique. Cette approche systématique ouvre des perspectives vers le développement de surfaces implantaire en zircone capables de soutenir des interactions tissulaires plus stables et durables en contexte clinique.

VI. References

1. **Gahlert, M. *et al.*** Biomechanical and histomorphometric comparison between zirconia implants with varying surface textures and a titanium implant in the maxilla of miniature pigs. *Clinical Oral Implants Research* **18**, 662–668 (2007).
2. **Tzanakakis, E.-G. C., Tzoutzas, I. G. & Koidis, P. T.** Is there a potential for durable adhesion to zirconia restorations? A systematic review. *The Journal of Prosthetic Dentistry* **115**, 9–19 (2016).
3. **Nakamura, K., Kanno, T., Milleding, P. & Ortengren, U.** Zirconia as a dental implant abutment material: a systematic review. *The International Journal of Prosthodontics* **23**, 299–309 (2010).
4. **Padhye, N. M., Calciolari, E., Zuercher, A. N., Tagliaferri, S. & Donos, N.** Survival and success of zirconia compared with titanium implants: a systematic review and meta-analysis. *Clinical Oral Investigations* **27**, 6279–6290 (2023).
5. **Halim, F. C., Pesce, P., De Angelis, N., Benedicenti, S. & Menini, M.** Comparison of the Clinical Outcomes of Titanium and Zirconia Implant Abutments: A Systematic Review of Systematic Reviews. *Journal of Clinical Medicine* **11**, 5052 (2022).
6. **Piascik, J. R., Wolter, S. D. & Stoner, B. R.** Development of a novel surface modification for improved bonding to zirconia. *Dental Materials* **27**, (2011).
7. **Alagiriswamy, G. *et al.*** Surface characteristics and bioactivity of zirconia (Y-TZP) with different surface treatments. *Journal of Pharmacy and Bioallied Sciences* **12**, S114–S123 (2020).
8. **Canullo, L. *et al.*** Influence of abutment material and modifications on peri-implant soft-tissue attachment: A systematic review and meta-analysis of histological animal studies. *The Journal of Prosthetic Dentistry* **125**, 426–436 (2021).
9. **Kimura, Y., Matsuzaka, K., Yoshinari, M. & Inoue, T.** Initial attachment of human oral keratinocytes cultured on zirconia or titanium. *Dental Materials Journal* **31**, 346–353 (2012).
10. **Yasuno, K., Kakura, K., Taniguchi, Y., Yamaguchi, Y. & Kido, H.** Zirconia Implants with Laser Surface Treatment: Peri-Implant Bone Response and Enhancement of Osseointegration. *Journal of Hard Tissue Biology* **23**, 93–100 (2014).
11. **Han, J. *et al.*** Laser surface texturing of zirconia-based ceramics for dental applications: A review. *Materials Science and Engineering: C* **123**, 112034 (2021).
12. **Brezavšček, M. *et al.*** The Effect of UV Treatment on the Osteoconductive Capacity of Zirconia-Based Materials. *Materials* **9**, 958 (2016).
13. **Xie, H. *et al.*** Effects of Acid Treatment on Dental Zirconia: An In Vitro Study. *PLOS ONE* **10**, e0136263 (2015).
14. *Zirconia: New Advances, Structure, Fabrication and Applications*. (IntechOpen, Erscheinungsort nicht ermittelbar, 2023).
15. **Falahchai, M., Neshandar Asli, H., Daneshvar, M. & Hendi, A.** Effect of different surface treatments on retention and fracture strength of zirconia crowns over Ti-base zirconia abutments. *Heliyon* **10**, e40164 (2024).

16. **Chopra, D., Jayasree, A., Guo, T., Gulati, K. & Ivanovski, S.** Advancing dental implants: Bioactive and therapeutic modifications of zirconia. *Bioactive Materials* **13**, 161–178 (2022).
17. **Jia, S. *et al.*** Challenges of Soft Tissue Integration Around Dental Implants and Strategies Based on Material Surface Modification. *Advanced Materials Interfaces* **12**, 2500025 (2025).
18. **Rydzek, G. *et al.*** Electrochemical nanoarchitectonics and layer-by-layer assembly: From basics to future. *Nano Today* **10**, 138–167 (2015).
19. **De Rochebrune, G. R. *et al.*** Grafting of phosphonylated polymers onto 3D printed polycaprolactone scaffolds improves osteoblasts proliferation and calcium mineralization in-vitro. *Reactive and Functional Polymers* **206**, 106103 (2025).
20. **Treccani, L., Yvonne Klein, T., Meder, F., Pardun, K. & Rezwan, K.** Functionalized ceramics for biomedical, biotechnological and environmental applications. *Acta Biomaterialia* **9**, 7115–7150 (2013).
21. **Zhang, B. *et al.*** Surface functionalization of zinc oxide by carboxyalkylphosphonic acid self-assembled monolayers. *Langmuir* **26**, 4514–4522 (2010).
22. **Pujari, S. P., Scheres, L., Marcelis, A. T. M. & Zuilhof, H.** Covalent Surface Modification of Oxide Surfaces. *Angewandte Chemie International Edition* **53**, 6322–6356 (2014).
23. **Hardan, L. *et al.*** Peptides in Dentistry: A Scoping Review. *Bioengineering* **10**, 214 (2023).
24. **Morra, M.** Biochemical modification of titanium surfaces: Peptides and eCM proteins. *European Cells and Materials* **12**, 1–15 (2006).
25. **Kohal, R., Att, W., Bächle, M. & Butz, F.** Ceramic abutments and ceramic oral implants. An update. *Periodontology 2000* **47**, 224–243 (2008).
26. **Garvie, R. C., Hannink, R. H. & Pascoe, R. T.** Ceramic Steel? in *Sintering Key Papers* (eds Sōmiya, S. & Moriyoshi, Y.) 253–257 (Springer Netherlands, Dordrecht, 1990).
27. **Saridag, S., Tak, O. & Alniacik, G.** Basic properties and types of zirconia: An overview. *World Journal of Stomatology* **2**, 40 (2013).
28. **Chevalier, J.** What future for zirconia as a biomaterial? *Biomaterials* **27**, 535–543 (2006).
29. **Deville, S., Chevalier, J. & Gremillard, L.** Influence of surface finish and residual stresses on the ageing sensitivity of biomedical grade zirconia. *Biomaterials* **27**, 2186–2192 (2006).
30. **Kosmač, T., Oblak, C., Jevnikar, P., Funduk, N. & Marion, L.** The effect of surface grinding and sandblasting on flexural strength and reliability of Y-TZP zirconia ceramic. *Dental Materials* **15**, 426–433 (1999).
31. **Kosmač, T., Oblak, Č. & Marion, L.** The effects of dental grinding and sandblasting on ageing and fatigue behavior of dental zirconia (Y-TZP) ceramics. *Journal of the European Ceramic Society* **28**, 1085–1090 (2008).
32. **Piconi, C. & Maccauro, G.** Zirconia as a ceramic biomaterial. *Biomaterials* **20**, 1–25 (1999).
33. **Spinelli, M. S. *et al.*** Zirconia Toughened Alumina (ZTA) Powders: Ultrastructural and Histological Analysis. *International Journal of Immunopathology and Pharmacology* **24**, 153–156 (2011).
34. **Catlow, C.** Defect processes and electrical properties of metal oxide ceramics. 99–108 (1977).
35. **Rahaman, M. N.** *Ceramic Processing and Sintering*. (CRC Press, 2017).
36. **Subbarao, E. C.** Advanced ceramics—an overview. *Sadhana* **13**, 1–11 (1988).
37. **Fabris, S.** A stabilization mechanism of zirconia based on oxygen vacancies only. *Acta Materialia* **50**, 5171–5178 (2002).

38. **Korhonen, S. T., Calatayud, M. & Krause, A. O. I.** Stability of Hydroxylated (1̄11) and (1̄01) Surfaces of Monoclinic Zirconia: A Combined Study by DFT and Infrared Spectroscopy. *The Journal of Physical Chemistry C* **112**, 6469–6476 (2008).
39. **Busca, G.** The Surface Acidity and Basicity of Solid Oxides and Zeolites. in *Metal Oxides* (ed. Fierro, J.) vol. 108 247–318 (CRC Press, 2005).
40. **Jung, K. T. & Bell, A. T.** Effects of Zirconia Phase on the Synthesis of Methanol over Zirconia Supported Copper. *Catalysis Letters* **80**, 63–68 (2002).
41. **Nawrocki, J., Rigney, M., McCormick, A. & Carr, P. W.** Chemistry of zirconia and its use in chromatography. *Journal of Chromatography A* **657**, 229–282 (1993).
42. **Yamaguchi, T., Nakano, Y. & Tanabe, K.** Infrared Study of Surface Hydroxyl Groups on Zirconium Oxide. *Bulletin of the Chemical Society of Japan* **51**, 2482–2487 (1978).
43. **Trunschke, A., Hoang, D. L. & Lieske, H.** In situ FTIR Studies of High-temperature Adsorption of Hydrogen on Zirconia. *Journal of the Chemical Society, Faraday Transactions* **91**, 4441-4444 (1995).
44. **Elassal, Z. *et al.*** Synthesis and FT–IR study of the acido–basic properties of the V2O5 catalysts supported on zirconia. *Arabian Journal of Chemistry* **4**, 313–319 (2011).
45. **Audry, F. *et al.*** Infrared Study and Quantum Calculations of the Conversion of Methylbutynol into Hydroxymethylbutanone on Zirconia. *Journal of Catalysis* **168**, 471–481 (1997).
46. **Korhonen, S. T., Calatayud, M. & Krause, A. O. I.** Stability of Hydroxylated (1̄11) and (1̄01) Surfaces of Monoclinic Zirconia: A Combined Study by DFT and Infrared Spectroscopy. *The Journal of Physical Chemistry C* **112**, 6469–6476 (2008).
47. **Su, Y., Cui, H., Li, Q., Gao, S. & Shang, J. K.** Strong adsorption of phosphate by amorphous zirconium oxide nanoparticles. *Water Research* **47**, 5018–5026 (2013).
48. **Ridder, M. D., Welzenis, R. G. V. & Brongersma, H. H.** Surface cleaning and characterization of yttria-stabilized zirconia. *Surface and Interface Analysis* **33**, 309–317 (2002).
49. **Atsu, S. S., Kilicarslan, M. A., Kucukesmen, H. C. & Aka, P. S.** Effect of zirconium-oxide ceramic surface treatments on the bond strength to adhesive resin. *The Journal of Prosthetic Dentistry* **95**, 430–436 (2006).
50. **Liu, D., Pow, E. H. N., Tsoi, J. K.-H. & Matinlinna, J. P.** Evaluation of four surface coating treatments for resin to zirconia bonding. *Journal of the Mechanical Behavior of Biomedical Materials* **32**, 300–309 (2014).
51. **Aboushelib, M. N., Kleverlaan, C. J. & Feilzer, A. J.** Selective infiltration-etching technique for a strong and durable bond of resin cements to zirconia-based materials. *The Journal of Prosthetic Dentistry* **98**, 379–388 (2007).
52. **Oluwabi, A. T. *et al.*** Influence of Post-UV/Ozone Treatment of Ultrasonic-Sprayed Zirconium Oxide Dielectric Films for a Low-Temperature Oxide Thin Film Transistor. *Materials* **13**, 6 (2019).
53. **Caravaca, C. *et al.*** Direct silanization of zirconia for increased biointegration. *Acta Biomaterialia* **46**, 323–335 (2016).
54. **Meillan, M. *et al.*** Mixed Self-Assembled Monolayers with Internal Urea Group on Silica Surface. *ChemistrySelect* **2**, 11868–11874 (2017).
55. **Jeon, S., Andrade, J. & De Gennes, P.** Protein—surface interactions in the presence of polyethylene oxide: I. Simplified theory. *Journal of Colloid and Interface Science*, 149–158 (1990).

56. **Dugas, V., Demesmay, C., Chevolot, Y. & Souteyrand, E.** Use of organosilanes in biosensors. *Use of Organosilanes in Biosensors* 1–85 (2010).
57. **Wang, L., Schubert, U. S. & Hoeppener, S.** Surface chemical reactions on self-assembled silane based monolayers. *Chemical Society Reviews* **50**, 6507–6540 (2021).
58. **Haensch, C., Hoeppener, S. & Schubert, U. S.** Chemical modification of self-assembled silane based monolayers by surface reactions. *Chemical Society Reviews* **39**, 2323–2334 (2010).
59. **Brzoska, J. B., Azouz, I. B. & Rondelez, F.** Silanization of Solid Substrates: A Step Toward Reproducibility. *Langmuir* **10**, 4367–4373 (1994).
60. **Howarter, J. A. & Youngblood, J. P.** Optimization of silica silanization by 3-aminopropyltriethoxysilane. *Langmuir* **22**, 11142–11147 (2006).
61. **Zalipsky, S.** Chemistry of polyethylene glycol conjugates with biologically active molecules. *Advanced Drug Delivery Reviews* **16**, 157–182 (1995).
62. **Fiorilli, S. *et al.*** Vapor-phase self-assembled monolayers of aminosilane on plasma-activated silicon substrates. *Journal of Colloid and Interface Science* **321**, 235–241 (2008).
63. **Duleba, D., Denuga, S. & Johnson, R. P.** Reproducibility and stability of silane layers in nanoconfined electrochemical systems. *Physical Chemistry Chemical Physics* **26**, 15452–15460 (2024).
64. **Rouvière, L. *et al.*** Silane-Based SAMs Deposited by Spin Coating as a Versatile Alternative Process to Solution Immersion. *Langmuir* **38**, 6464–6471 (2022).
65. **Matinlinna, J. P., Lung, C. Y. K. & Tsoi, J. K. H.** Silane adhesion mechanism in dental applications and surface treatments: A review. *Dental Materials* **34**, 13–28 (2018).
66. **Plueddemann, E. P.** *Silane Coupling Agents*. (New York, 1991).
67. **Arkles, B.** Tailoring Surfaces with Silanes. *Chemtech* **7**,.
68. **Hong, G. *et al.*** Improving osteogenic activity of Y-TZP (Yttria-stabilized tetragonal zirconia polycrystal) surfaces by grafting of silanes with different end groups. *Applied Surface Science* **570**, (2021).
69. **Thompson, J. Y., Stoner, B. R., Piascik, J. R. & Smith, R.** Adhesion/cementation to zirconia and other non-silicate ceramics: Where are we now? *Dental Materials* **27**, 71–82 (2011).
70. **Nawrocki, J. *et al.*** Part II. Chromatography using ultra-stable metal oxide-based stationary phases for HPLC. *Journal of Chromatography A* **1028**, 31–62 (2004).
71. **Geibel, C. *et al.*** Controllable organosilane monolayer density of surface bonding using silatranes for thiol functionalization of silica particles for liquid chromatography and validation of microanalytical method for elemental composition determination. *Journal of Chromatography A* **1653**, (2021).
72. **Silva, C. R., Airoldi, C., Collins, K. E. & Collins, C. H.** A new generation of more pH stable reversed phases prepared by silanization of zirconized silica. *Journal of Chromatography A* **1191**, 90–98 (2008).
73. **Kern, M. & Wegner, S. M.** Bonding to zirconia ceramic: adhesion methods and their durability. *Dental Materials* **14**, 64–71 (1998).
74. **Özcan, M. & Vallittu, P. K.** Effect of surface conditioning methods on the bond strength of luting cement to ceramics. *Dental Materials* **19**, 725–731 (2003).
75. **Sciasci, P., Abi-Rached, F. O., Adabo, G. L., Baldissara, P. & Fonseca, R. G.** Effect of surface treatments on the shear bond strength of luting cements to Y-TZP ceramic. *The Journal of Prosthetic Dentistry* **113**, 212–219 (2015).

76. **Blatz, M. B., Vonderheide, M. & Conejo, J.** The Effect of Resin Bonding on Long-Term Success of High-Strength Ceramics. *Journal of Dental Research* **97**, 132–139 (2018).
77. **Comino-Garayoa, R., Peláez, J., Tobar, C., Rodríguez, V. & Suárez, M. J.** Adhesion to zirconia: A systematic review of surface pretreatments and resin cements. *Materials* **14**, (2021).
78. **Li, X. *et al.*** Different surface treatments and adhesive monomers for zirconia-resin bonds: A systematic review and network meta-analysis. *Japanese Dental Science Review* **60**, 175–189 (2024).
79. **Zhou, Z. *et al.*** Enhancing osteoblast bioactivity through SDSSD peptide-immobilized on the surface of zirconia implants. *Materials Letters* **307**, (2022).
80. **Palkowitz, A. L. *et al.*** Functionalization of a zirconia surface by covalently immobilized fibronectin and its effects on resistance to thermal, acid, and mechanical exposure. *Journal of Biomedical Materials Research - Part B Applied Biomaterials* **112**, (2024).
81. **Queffélec, C., Petit, M., Janvier, P., Knight, D. A. & Bujoli, B.** Surface Modification Using Phosphonic Acids and Esters. *Chemical Reviews* **112**, 3777–3807 (2012).
82. **Boissezon, R., Muller, J., Beaugeard, V., Monge, S. & Robin, J.-J.** Organophosphonates as anchoring agents onto metal oxide-based materials: synthesis and applications. *RSC Advances* **4**, 35690 (2014).
83. **Spori, D. M. *et al.*** Influence of alkyl chain length on phosphate self-assembled monolayers. *Langmuir* **23**, 8053–8060 (2007).
84. **Bou Orm, N. *et al.*** Design of Hybrid PAH Nanoadsorbents by Surface Functionalization of ZrO2 Nanoparticles with Phosphonic Acids. *Nanomaterials* **11**, 952 (2021).
85. **Forato, F. *et al.*** Comparison of Zirconium Phosphonate-Modified Surfaces for Immobilizing Phosphopeptides and Phosphate-Tagged Proteins. *Langmuir* **32**, 5480–5490 (2016).
86. **Asaad, S. *et al.*** New Carbamoyl Surface-Modified ZrO2 Nanohybrids for Selective Au Extraction from E-Waste. *Molecules* **28**, 2219 (2023).
87. **Hiltunen, O.-M. *et al.*** Selective separation of Am(III)/Eu(III) using heterocyclic bistriazolyl phosphonate grafted zirconia and titania solid phase extractants. *RSC Applied Interfaces* **2**, 279–291 (2025).
88. **Marcinko, S. & Fadeev, A. Y.** Hydrolytic Stability of Organic Monolayers Supported on TiO_2 and ZrO_2. *Langmuir* **20**, 2270–2273 (2004).
89. **Hsu, S. K. *et al.*** Enhancing the bioactivity of yttria-stabilized zirconia immobilized with adhesive peptide using L-dopa as cross-linker. *Thin Solid Films* **620**, 145–149 (2016).
90. **Liebscher, J. *et al.*** Structure of Polydopamine: A Never-Ending Story? *Langmuir* **29**, 10539–10548 (2013).
91. **Ball, V., Frari, D. D., Toniazzo, V. & Ruch, D.** Kinetics of polydopamine film deposition as a function of pH and dopamine concentration: Insights in the polydopamine deposition mechanism. *Journal of Colloid and Interface Science* **386**, 366–372 (2012).
92. **Ju, K.-Y., Lee, Y., Lee, S., Park, S. B. & Lee, J.-K.** Bioinspired Polymerization of Dopamine to Generate Melanin-Like Nanoparticles Having an Excellent Free-Radical-Scavenging Property. *Biomacromolecules* **12**, 625–632 (2011).
93. **Lee, H., Dellatore, S. M., Miller, W. M. & Messersmith, P. B.** Mussel-Inspired Surface Chemistry for Multifunctional Coatings. *Science* **318**, 426–430 (2007).
94. **Ejima, H., Richardson, J. J. & Caruso, F.** Metal-phenolic networks as a versatile platform to engineer nanomaterials and biointerfaces. *Nano Today* **12**, 136–148 (2017).

95. **Yu, J. *et al.*** Mussel protein adhesion depends on interprotein thiol-mediated redox modulation. *Nature Chemical Biology* **7**, 588–590 (2011).
96. **Liu, M. *et al.*** Surface modification of zirconia with polydopamine to enhance fibroblast response and decrease bacterial activity in vitro: A potential technique for soft tissue engineering applications. *Colloids and Surfaces B: Biointerfaces* **136**, 74–83 (2015).
97. **Yang, Z. *et al.*** Biofunctionalization of zirconia with cell-adhesion peptides: Via polydopamine crosslinking for soft tissue engineering: Effects on the biological behaviors of human gingival fibroblasts and oral bacteria. *RSC Advances* **10**, 6200–6212 (2020).
98. **Hermanson, G. T.** *Bioconjugate Techniques*. (Academic Press, 2013).
99. **Fischer, M. J. E.** Amine Coupling Through EDC/NHS: A Practical Approach. in *Surface Plasmon Resonance* (eds Mol, N. J. & Fischer, M. J. E.) vol. 627 55–73 (Humana Press, Totowa, NJ, 2010).
100. **Nakajima, N. & Ikada, Y.** Mechanism of Amide Formation by Carbodiimide for Bioconjugation in Aqueous Media. *Bioconjugate Chemistry* **6**, 123–130 (1995).
101. **Totaro, K. A. *et al.*** Systematic Investigation of EDC/sNHS-Mediated Bioconjugation Reactions for Carboxylated Peptide Substrates. *Bioconjugate Chemistry* **27**, 994–1004 (2016).
102. **Mädler, S., Bich, C., Touboul, D. & Zenobi, R.** Chemical cross-linking with NHS esters: a systematic study on amino acid reactivities. *Journal of Mass Spectrometry* **44**, 694–706 (2009).
103. **Kumar, S., Sharma, J. G., Maji, S. & Malhotra, B. D.** A biocompatible serine functionalized nanostructured zirconia based biosensing platform for non-invasive oral cancer detection. *RSC Advances* **6**, 77037–77046 (2016).
104. **Kim, H., Lee, Y. H., Kim, N. K. & Kang, I. K.** Bioactive Surface of Zirconia Implant Prepared by Nano-Hydroxyapatite and Type I Collagen. *Coatings* **12**, (2022).
105. **Porté-Durrieu, M. C. *et al.*** Development of RGD peptides grafted onto silica surfaces: XPS characterization and human endothelial cell interactions. *Journal of Biomedical Materials Research* **46**, 368–375 (1999).
106. **Rouvière, L. *et al.*** Self-assembly of amino-terminated monolayers depending on the chemical structure. *New Journal of Chemistry* **2023**, 47 (2023).
107. **Sugawara, S. *et al.*** Establishment of epithelial attachment on titanium surface coated with platelet activating peptide. *PLoS ONE* **11**, (2016).
108. **Tack, L., Schickle, K., Böke, F. & Fischer, H.** Immobilization of specific proteins to titanium surface using self-assembled monolayer technique. *Dental Materials* **31**, 1169–1179 (2015).
109. **Werner, S. *et al.*** The effect of microstructured surfaces and laminin-derived peptide coatings on soft tissue interactions with titanium dental implants. *Biomaterials* **30**, 2291–2301 (2009).
110. **Durrieu, M. C. *et al.*** Grafting RGD containing peptides onto hydroxyapatite to promote osteoblastic cells adhesion. *Journal of Materials Science: Materials in Medicine* **15**, 779–786 (2004).
111. **McRae, S. *et al.*** Pentafluorophenyl Ester-Functionalized Phosphorylcholine Polymers: Preparation of Linear, Two-Arm, and Grafted Polymer–Protein Conjugates. *Biomacromolecules* **13**, 2099–2109 (2012).
112. **Lawrence, J. & Emrick, T.** Pentafluorophenyl Ester-Functionalized Nanoparticles as a Versatile Platform for Selective and Covalent Inter-nanoparticle Coupling. *ACS Applied Materials & Interfaces* **8**, 2393–2398 (2016).

113. **Ślósarczyk, A. T., Ramapanicker, R., Norberg, T. & Baltzer, L.** Mixed pentafluorophenyl and o-fluorophenyl esters of aliphatic dicarboxylic acids: efficient tools for peptide and protein conjugation. *RSC Advances.* **2**, 908–914 (2012).
114. **Migneault, I., Dartiguenave, C., Bertrand, M. J. & Waldron, K. C.** Glutaraldehyde: Behavior in Aqueous Solution, Reaction with Proteins, and Application to Enzyme Crosslinking. *BioTechniques* **37**, 790–802 (2004).
115. **Cheung, D. T. & Nimni, M. E.** Mechanism of Crosslinking of Proteins by Glutaraldehyde I: Reaction with Model Compounds. *Connective Tissue Research* **10**, 187–199 (1982).
116. **Pinto, R. V., Gomes, P. S., Fernandes, M. H., Costa, M. E. V. & Almeida, M. M.** Glutaraldehyde-crosslinking chitosan scaffolds reinforced with calcium phosphate spray-dried granules for bone tissue applications. *Materials Science and Engineering: C* **109**, 110557 (2020).
117. **Shi, J. *et al.*** *In vitro* genotoxicity evaluation and metabolic study of residual glutaraldehyde in animal-derived biomaterials. *Regenerative Biomaterials* **7**, 619–625 (2020).
118. **Hoz, M. F. T. de la *et al.*** RGD-functionalization of anodized zirconium as a potential strategy for biomedical application: An in vitro study. *Surface and Coatings Technology* **433**, (2022).
119. **Lee, T.-J., Chau, L.-K. & Huang, C.-J.** Controlled Silanization: High Molecular Regularity of Functional Thiol Groups on Siloxane Coatings. *Langmuir* **36**, 5935–5943 (2020).
120. **Vistas, C. R., Águas, A. C. P. & Ferreira, G. N. M.** Silanization of glass chips—A factorial approach for optimization. *Applied Surface Science* **286**, 314–318 (2013).
121. **Mercurio, M. *et al.*** Ag-Decorated Titania Nanoparticles for Antibacterial Applications. *ACS Applied Nano Materials* **7**, 21124–21140 (2024).
122. **Ambrožić, G. *et al.*** Building organosilica hybrid nanohemispheres via thiol-ene click reaction on alumina thin films deposited by atomic layer deposition (ALD). *Journal of Colloid and Interface Science* **560**, 303–311 (2020).
123. **Kumar, N. & Upadhyay, L. S. B.** Enzyme Immobilization over Polystyrene Surface Using Cysteine Functionalized Copper Nanoparticle as a Linker Molecule. *Applied Biochemistry and Biotechnology* **191**, 1247–1257 (2020).
124. **Northrop, B. H., Frayne, S. H. & Choudhary, U.** Thiol–maleimide "click" chemistry: evaluating the influence of solvent, initiator, and thiol on the reaction mechanism, kinetics, and selectivity. *Polymer Chemistry* **6**, 3415–3430 (2015).
125. **Renault, K., Fredy, J. W., Renard, P.-Y. & Sabot, C.** Covalent Modification of Biomolecules through Maleimide-Based Labeling Strategies. *Bioconjugate Chemistry* **29**, 2497–2513 (2018).
126. **Smith, M. E. B. *et al.*** Protein Modification, Bioconjugation, and Disulfide Bridging Using Bromomaleimides. *Journal of the American Chemical Society* **132**, 1960–1965 (2010).
127. **Baldwin, A. D. & Kiick, K. L.** Tunable Degradation of Maleimide–Thiol Adducts in Reducing Environments. *Bioconjugate Chemistry* **22**, 1946–1953 (2011).
128. **Sun, Y. *et al.*** Thiol Michael addition reaction: a facile tool for introducing peptides into polymer-based gene delivery systems. *Polymer International* **67**, 25–31 (2018).
129. **Shen, G., Horgan, A. & Levicky, R.** Reaction of N-phenyl maleimide with aminosilane monolayers. *Colloids and Surfaces B: Biointerfaces* **35**, 59–65 (2004).
130. **Xiao, S. J. *et al.*** Immobilization of the cell-adhesive peptide Arg–Gly–Asp–Cys (RGDC) on titanium surfaces by covalent chemical attachment. *Journal of Materials Science: Materials in Medicine* **8**, 867–872 (1997).

131. **Agrahari, A. K. *et al.*** Cu(I)-Catalyzed Click Chemistry in Glycoscience and Their Diverse Applications. *Chemical Reviews* **13**, 7638-7956 (2021).
132. **Li, H., Aneja, R. & Chaiken, I.** Click Chemistry in Peptide-Based Drug Design. *Molecules* **18**, 9797–9817 (2013).
133. **Pola, R., Braunová, A., Laga, R., Pechar, M. & Ulbrich, K.** Click chemistry as a powerful and chemoselective tool for the attachment of targeting ligands to polymer drug carriers. *Polymer Chemistry* **5**, 1340–1350 (2014).
134. **Anseth, K. S. & Klok, H.-A.** Click Chemistry in Biomaterials, Nanomedicine, and Drug Delivery. *Biomacromolecules* **17**, 1–3 (2016).
135. **Ghosal, K., Bhattacharyya, S. K., Mishra, V. & Zuilhof, H.** Click Chemistry for Biofunctional Polymers: From Observing to Steering Cell Behavior. *Chemical Reviews* **124**, 13216–13300 (2024).
136. **Nwe, K. & Brechbiel, M. W.** Growing Applications of "Click Chemistry" for Bioconjugation in Contemporary Biomedical Research. *Cancer Biotherapy and Radiopharmaceuticals* **24**, 289–302 (2009).
137. **Ahmad Fuaad, A., Azmi, F., Skwarczynski, M. & Toth, I.** Peptide Conjugation via CuAAC 'Click' Chemistry. *Molecules* **18**, 13148–13174 (2013).
138. **Tang, W. & Becker, M. L.** "Click" reactions: a versatile toolbox for the synthesis of peptide-conjugates. *Chem. Soc. Rev.* **43**, 7013–7039 (2014).
139. **Sletten, E. M. & Bertozzi, C. R.** From Mechanism to Mouse: A Tale of Two Bioorthogonal Reactions. *Accounts of Chemical Research* **44**, 666–676 (2011).
140. **Kim, E. & Koo, H.** Biomedical applications of copper-free click chemistry: *in vitro*, *in vivo*, and *ex vivo*. *Chemical Science* **10**, 7835–7851 (2019).
141. **Koo, H. *et al.*** Bioorthogonal Copper-Free Click Chemistry In Vivo for Tumor-Targeted Delivery of Nanoparticles. *Angewandte Chemie* **124**, 12006–12010 (2012).
142. **Colombo, M. *et al.*** Site-Specific Conjugation of ScFvs Antibodies to Nanoparticles by Bioorthogonal Strain-Promoted Alkyne–Nitrone Cycloaddition. *Angewandte Chemie International Edition* **51**, 496–499 (2012).
143. **Meghani, N. M., Amin, H. H. & Lee, B.-J.** Mechanistic applications of click chemistry for pharmaceutical drug discovery and drug delivery. *Drug Discovery Today* **22**, 1604–1619 (2017).
144. **Meißler, M., Wieczorek, S., Ten Brummelhuis, N. & Börner, H. G.** Synthetic Aspects of Peptide– and Protein–Polymer Conjugates in the Post-click Era. in *Bio-inspired Polymers* (eds Bruns, N. & Kilbinger, A. F. M.) 1–30 (The Royal Society of Chemistry, 2016).
145. **McKay, C. S. & Finn, M. G.** Click Chemistry in Complex Mixtures: Bioorthogonal Bioconjugation. *Chemistry & Biology* **21**, 1075–1101 (2014).
146. **Dworzak, M. R. *et al.*** Rapid post-synthetic modification of porous coordination cages with copper-catalyzed click chemistry. *Chemical Communications* **59**, 8977–8980 (2023).
147. **Šarić, I. *et al.*** In-situ multi-step pulsed vapor phase surface functionalization of zirconia nanoparticles via copper-free click chemistry. *Applied Surface Science* **539**, 148254 (2021).
148. **Chen, J. Y., Sun, Y. S., Nguyen, D. T., Liu, C. F. & Huang, H. H.** Surface characterizations and cell growth of rough zirconia surfaces immobilized with different BMP-2 concentrations using natural crosslinker genipin. *Materials and Design* **223**, (2022).
149. **Facchiano, A. & Facchiano, F.** Transglutaminases and their substrates in biology and human diseases: 50 years of growing. *Amino Acids* **36**, 599–614 (2009).

150. **Griffin, M., Casadio, R. & Bergamini, C. M.** Transglutaminases: Nature's biological glues. *Biochemical Journal* **368**, 377–396 (2002).
151. **Chau, D. Y. S., Collighan, R. J., Verderio, E. A. M., Addy, V. L. & Griffin, M.** The cellular response to transglutaminase-cross-linked collagen. *Biomaterials* **26**, 6518–6529 (2005).
152. **Palkowitz, A. L., Rüger, S., Ziegler, M., Buhl, E. M. & Fischer, H.** Transglutaminase enables highly hydrolytically and proteolytically stable crosslinking of collagen on titanium surfaces and promotes osteogenic differentiation of human mesenchymal stem cells. *Journal of Biomedical Materials Research Part A* **112**, 812–824 (2024).
153. **Nair, M., Johal, R. K., Hamaia, S. W., Best, S. M. & Cameron, R. E.** Tunable bioactivity and mechanics of collagen-based tissue engineering constructs: A comparison of EDC-NHS, genipin and TG2 crosslinkers. *Biomaterials* **254**, (2020).
154. **Elkhodiry, M. A. *et al.*** Isolating and expanding endothelial progenitor cells from peripheral blood on peptide-functionalized polystyrene surfaces. *Biotechnology and Bioengineering* **116**, 2598–2609 (2019).
155. **Chen, L. *et al.*** Chemical Modifications of Therapeutic Proteins Induced by Residual Ethylene Oxide. *Journal of Pharmaceutical Sciences* **104**, 731–739 (2015).
156. **Pierschbacher, M. D. & Ruoslahti, E.** Cell attachment activity of fibronectin can be duplicated by small synthetic fragments of the molecule. *Nature* **309**, 30–33 (1984).
157. **Oyman, G. *et al.*** Peptide-modified conducting polymer as a biofunctional surface: Monitoring of cell adhesion and proliferation. *RSC Advances* **4**, 53411–53418 (2014).
158. **Swan, E. E. L., Popat, K. C. & Desai, T. A.** Peptide-immobilized nanoporous alumina membranes for enhanced osteoblast adhesion. *Biomaterials* **26**, 1969–1976 (2005).
159. **Mobasseri, R., Tian, L., Soleimani, M., Ramakrishna, S. & Naderi-Manesh, H.** Peptide modified nanofibrous scaffold promotes human mesenchymal stem cell proliferation and long-term passaging. *Materials Science and Engineering C* **84**, 80–89 (2018).
160. **Zhao, B. *et al.*** Improvement of Adhesion and Spreading of Human Gingival Fibroblasts to RGD-grafted Titanium Surface. *Journal of Hard Tissue Biology* **15**, 65–68 (2006).
161. **Auernheimer, J. *et al.*** Titanium implant materials with improved biocompatibility through coating with phosphonate-anchored cyclic RGD peptides. *ChemBioChem* **6**, 2034–2040 (2005).
162. **Zang, S. *et al.*** RGD and rhBMP-7 immobilized on zirconia scaffold with interweaved human dental pulp stem cells for promoting bone regeneration. *Materials and Design* **232**, (2023).
163. **Minguela, J. *et al.*** Peptidic biofunctionalization of laser patterned dental zirconia: A biochemical-topographical approach. *Materials Science and Engineering C* **125**, (2021).
164. **Kapp, T. G. *et al.*** A comprehensive evaluation of the activity and selectivity profile of ligands for RGD-binding integrins. *Scientific Reports* **7**, (2017).
165. **Lyons, J. C.** The effects of fibronectin and the rgd binding sequence on gingival fibroblasts in an in vitro wound healing mode. *Doctoral dissertation, Augusta University* (2004).
166. **Kämmerer, P. *et al.*** Immobilisation of linear and cyclic RGD-peptides on titanium surfaces and their impact on endothelial cell adhesion and proliferation. *European Cells and Materials* **21**, 364–372 (2011).
167. **Hsu, S. K. *et al.*** Biomolecular modification of zirconia surfaces for enhanced biocompatibility. in *Thin Solid Films* vol. 572 91–98 (Elsevier B.V., 2014).
168. **Fernandez-Garcia, E. *et al.*** Peptide-functionalized zirconia and new zirconia/titanium biocermets for dental applications. *Journal of Dentistry* **43**, 1162–1174 (2015).

169. **Chen, J., Wang, L., Shi, L., Ren, L. & Wang, Y.** Local co-delivery and release of antimicrobial peptide and RGD using porous TiO_2. *RSC Adv.* **4**, 27630–27633 (2014).
170. **Afami, M. E. *et al.*** Multicomponent Peptide Hydrogels as an Innovative Platform for Cell-Based Tissue Engineering in the Dental Pulp. *Pharmaceutics* **13**, 1575 (2021).
171. **Hamdan, F., Bigdeli, Z., Asghari, S. M., Sadremomtaz, A. & Balalaie, S.** Synthesis of Modified RGD-Based Peptides and Their in vitro Activity. *ChemMedChem* **14**, 282–288 (2019).
172. **Edwards-Gayle, C. J. C. *et al.*** Self-Assembly, Antimicrobial Activity, and Membrane Interactions of Arginine-Capped Peptide Bola-Amphiphiles. *ACS Applied Bio Materials* **2**, 2208–2218 (2019).
173. **Chen, C. Y., Jang, W., Kim, D. M., Nagai, M. & Nagai, S.** Establishment of Biomimetic Soft Tissue Integration with the Surface of Zirconia Fused with Platelet-Activating Peptide. *Materials* **15**, (2022).
174. **Herbst, T. J., McCarthy, J. B., Tsilibary, E. C. & Furcht, L. T.** Differential effects of laminin, intact type IV collagen, and specific domains of type IV collagen on endothelial cell adhesion and migration. *The Journal of cell biology* **106**, 1365–1373 (1988).
175. **Tamura, R. N. *et al.*** Coating of titanium alloy with soluble laminin-5 promotes cell attachment and hemidesmosome assembly in gingival epithelial cells: potential application to dental implants. *Journal of Periodontal Research* **32**, 287–294 (1997).
176. **Vallée, A. *et al.*** Alumina-zirconia composites functionalized with laminin-1 and laminin-5 for dentistry: Effect of protein adsorption on cellular response. *Colloids and Surfaces B: Biointerfaces* **114**, 284–293 (2014).
177. **Massia, S. P., Rao, S. S. & Hubbell, J. A.** Covalently immobilized laminin peptide Tyr-Ile-Gly-Ser-Arg (YIGSR) supports cell spreading and co-localization of the 67-kilodalton laminin receptor with alpha-actinin and vinculin. *Journal of Biological Chemistry* **268**, 8053–8059 (1993).
178. **Fittkau, M. H. *et al.*** The selective modulation of endothelial cell mobility on RGD peptide containing surfaces by YIGSR peptides. *Biomaterials* **26**, 167–174 (2005).
179. **Hsu, C. M., Sun, Y. S. & Huang, H. H.** Enhanced Cell Response to Zirconia Surface Immobilized with Type I Collagen. *Journal of Dental Research* **98**, 556–563 (2019).
180. **Teng, F. *et al.*** Bone Tissue Responses to Zirconia Implants Modified by Biomimetic Coating Incorporated with BMP-2. *The International Journal of Periodontics & Restorative Dentistry* **39**, 371–379 (2019).
181. **Sun, Y.-S., Lin, Y.-A. & Huang, H.-H.** Using Genipin to Immobilize Bone Morphogenetic Protein-2 on Zirconia Surface for Enhancing Cell Adhesion and Mineralization in Dental Implant Applications. *Polymers* **12**, 2639 (2020).
182. **Lee, H. J., Kwon, Y.-D. & Lee, S. C.** Surface engineering of zirconia with abaloparatide and nano-hydroxyapatite for synergistic osteogenic activity. *Macromolecular Research* **33**, 277–287 (2025).
183. **Yoon, S. J., Yang, D. H., Kim, E.-C., Noh, K. & Lee, D.-W.** *In Vitro* Osteogenic Differentiation Enhanced by Zirconia Coated with Nano-Layered Growth and Differentiation Factor-5. *Journal of Nanoscience and Nanotechnology* **16**, 280–286 (2016).
184. **Piest, C., Strunskus, T., Polonskyi, O., Wille, S. & Kern, M.** Efficacy of Plasma Treatment for Decontaminating Zirconia. *The Journal of Adhesive Dentistry* **20**, 289–297 (2018).
185. **Denry, I. & Kelly, J. R.** State of the art of zirconia for dental applications. *Dental Materials* **24**, 299–307 (2008).

186. **Lohbauer, U., Zipperle, M., Rischka, K., Petschelt, A. & Müller, F. A.** Hydroxylation of dental zirconia surfaces: Characterization and bonding potential. *Journal of Biomedical Materials Research - Part B Applied Biomaterials* **87**, 461–467 (2008).
187. **Piascik, J. R., Swift, E. J., Thompson, J. Y., Grego, S. & Stoner, B. R.** Surface modification for enhanced silanation of zirconia ceramics. *Dental Materials* **25**, 1116–1121 (2009).
188. **Chen, L., Suh, B. I., Kim, J. & Tay, F. R.** Evaluation of silica-coating techniques for zirconia bonding. *American Journal of Dentistry* **24**, 79–84 (2011).
189. **Bagus, P. S. & Freund, H.-J.** X-ray photoelectron spectroscopy as a useful tool to study surfaces and model systems for heterogeneous catalysts: A review and perspective. *Surface Science* **745**, 122471 (2024).
190. **Zinelis, S., Thomas, A., Syres, K., Silikas, N. & Eliades, G.** Surface characterization of zirconia dental implants. *Dental Materials* **26**, 295–305 (2010).
191. **Yang, B. *et al.*** Influence of contamination on bonding to zirconia ceramic. *Journal of Biomedical Materials Research Part B: Applied Biomaterials* **81B**, 283–290 (2007).
192. **Łagodzińska, P., Dejak, B. & Konieczny, B.** The Influence of Alumina Airborne-Particle Abrasion on the Properties of Zirconia-Based Dental Ceramics (3Y-TZP). *Coatings* **13**, 1691 (2023).
193. **Danilenko, I. *et al.*** Effect of alumina added by mechanical mixing and co-doping on the densification mechanisms of zirconia nanoparticles at the initial stage of sintering. *Results in Physics* **19**, 103495 (2020).
194. **Karthigeyan, S. *et al.*** Surface modification techniques for zirconia-based bioceramics: A review. *Journal of Pharmacy And Bioallied Sciences* **11**, 131 (2019).
195. **Conner, C. *et al.*** Surface Evaluation of a Novel Acid-Etching Solution for Zirconia and Lithium Disilicate. *Materials* **18**, 2912 (2025).
196. **Flamant, Q. & Anglada, M.** Hydrofluoric acid etching of dental zirconia. Part 2: effect on flexural strength and ageing behavior. *Journal of the European Ceramic Society* **36**, 135–145 (2016).
197. **Kim, H.-E., Lim, M.-J., Yu, M.-K. & Lee, K.-W.** Changes in Bond Strength and Topography for Y-TZP Etched with Hydrofluoric Acid Depending on Concentration and Temperature Conditions. *Medicina* **56**, 568 (2020).
198. **Kim, J.-E. *et al.*** Effect of Acid Mixtures on Surface Properties and Biaxial Flexural Strength of As-Sintered and Air-Abraded Zirconia. *Materials* **14**, 2359 (2021).
199. **Kohli, R.** UV-Ozone Cleaning for Removal of Surface Contaminants. in *Developments in Surface Contamination and Cleaning* 71–104 (Elsevier, 2015).
200. **Gong, J. *et al.*** Effects of UV/O_3 and O_2 plasma surface treatments on the band-bending of ultrathin ALD-Al_2O_3 coated Ga-polar GaN. *Journal of Applied Physics* **135**, 115303 (2024).
201. **Sim, Y.-K. *et al.*** A one-step method for covalent bond immobilization of biomolecules on silica operated in aqueous solution. *Chemical Science* **9**, 7981–7985 (2018).
202. **Weetall, H. H.** Preparation of immobilized proteins covalently coupled through silane coupling agents to inorganic supports. *Applied Biochemistry and Biotechnology* **41**, 157–188 (1993).
203. **Banjanac, K. *et al.*** Epoxy-silanization - tool for improvement of silica nanoparticles as support for lipase immobilization with respect to esterification activity: Immobilization of lipase on epoxy modified silica nanoparticles. *Journal of Chemical Technology & Biotechnology* **91**, 2654–2663 (2016).

204. **Pujari, S. P., Scheres, L., Marcelis, A. T. M. & Zuilhof, H.** Covalent surface modification of oxide surfaces. (2014).
205. **Ahangaran, F. & Navarchian, A. H.** Recent advances in chemical surface modification of metal oxide nanoparticles with silane coupling agents: A review. *Advances in Colloid and Interface Science* **286**, 102298 (2020).
206. **Baldin, E. K. K. *et al.*** Effect of sterilization processes on the properties of a silane hybrid coating applied to Ti6Al4V alloy. *Journal of Materials Research* **33**, 161–177 (2018).
207. **Brochier Salon, M.-C. & Belgacem, M. N.** Hydrolysis-Condensation Kinetics of Different Silane Coupling Agents. *Phosphorus, Sulfur, and Silicon and the Related Elements* **186**, 240–254 (2011).
208. **Kosovari, M. *et al.*** Silanization Strategies for Tailoring Peptide Functionalization on Silicon Surfaces: Implications for Enhancing Stem Cell Adhesion. *ACS Applied Materials and Interfaces* **16**, 29770–29782 (2024).
209. **Pańtak, P., Czechowska, J. P. & Zima, A.** The influence of silane coupling agents on the properties of α-TCP-based ceramic bone substitutes for orthopaedic applications. *RSC Advances* **13**, 34020–34031 (2023).
210. **Bhairamadgi, N. S. *et al.*** Hydrolytic and Thermal Stability of Organic Monolayers on Various Inorganic Substrates. *Langmuir* **30**, 5829–5839 (2014).
211. **Jiang, J., Cao, J., Wang, W. & Xue, J.** How silanization influences aggregation and moisture sorption behaviours of silanized silica: analysis of porosity and multilayer moisture adsorption. *Royal Society Open Science* **5**, 180206 (2018).
212. **Koniev, O. & Wagner, A.** Developments and recent advancements in the field of endogenous amino acid selective bond forming reactions for bioconjugation. *Chemical Society Reviews* **44**, 5495–5551 (2015).
213. **Hilvano, E. G. V., Liang, M.-C., Piane, J. J. & Nacsa, E. D.** Direct electrochemical synthesis of pentafluorophenyl esters *via* oxyl-radical-promoted nucleophilic aromatic substitution. *Organic & Biomolecular Chemistry* **23**, 6373–6385 (2025).
214. **Lockett, M. R., Phillips, M. F., Jarecki, J. L., Peelen, D. & Smith, L. M.** A Tetrafluorophenyl Activated Ester Self-Assembled Monolayer for the Immobilization of Amine-Modified Oligonucleotides. *Langmuir* **24**, 69–75 (2008).
215. **Coussot, G. *et al.*** A rapid and reversible colorimetric assay for the characterization of aminated solid surfaces. *Analytical and Bioanalytical Chemistry* **399**, 1061–1069 (2011).
216. **Qiao, B., Wang, T.-J., Gao, H. & Jin, Y.** High density silanization of nano-silica particles using γ-aminopropyltriethoxysilane (APTES). *Applied Surface Science* **351**, 646–654 (2015).
217. **Di Iorio, D. & Huskens, J.** Surface Modification with Control over Ligand Density for the Study of Multivalent Biological Systems. *ChemistryOpen* **9**, 53–66 (2020).
218. **Sypabekova, M., Hagemann, A., Rho, D. & Kim, S.** Review: 3-Aminopropyltriethoxysilane (APTES) Deposition Methods on Oxide Surfaces in Solution and Vapor Phases for Biosensing Applications. *Biosensors* **13**, 36 (2022).
219. **Caravaca, C. *et al.*** Direct silanization of zirconia for increased biointegration. *Acta Biomaterialia* **46**, 323–335 (2016).
220. **Watanabe, H., Saito, K., Kokubun, K., Sasaki, H. & Yoshinari, M.** Change in surface properties of zirconia and initial attachment of osteoblastlike cells with hydrophilic treatment. *Dental Materials Journal* **31**, 806–814 (2012).

221. **Arnfinnsdottir, N. B., Chapman, C. A., Bailey, R. C., Aksnes, A. & Stokke, B. T.** Impact of Silanization Parameters and Antibody Immobilization Strategy on Binding Capacity of Photonic Ring Resonators. *Sensors* **20**, 3163 (2020).
222. **Yang, J. *et al.*** Effect of APTES- or MPTS-Conditioned Nanozirconia Fillers on Mechanical Properties of Bis-GMA-Based Resin Composites. *ACS Omega* **5**, 32540–32550 (2020).
223. **Acres, R. G. *et al.*** Molecular Structure of 3-Aminopropyltriethoxysilane Layers Formed on Silanol-Terminated Silicon Surfaces. *The Journal of Physical Chemistry C* **116**, 6289–6297 (2012).
224. **Cabeça, R. *et al.*** Patterned functionalization layer for sub-μL DNA solid-phase immobilization and hybridization. *Sensors and Actuators B: Chemical* **149**, 432–438 (2010).
225. **Howarter, J. A. & Youngblood, J. P.** Optimization of Silica Silanization by 3-Aminopropyltriethoxysilane. *Langmuir* **22**, 11142–11147 (2006).
226. **Saad, A., Abderrabba, M. & Chehimi, M. M.** X-ray induced degradation of surface bound azido groups during XPS analysis. *Surface and Interface Analysis* **49**, 340–344 (2017).
227. **Casula, G., Fantauzzi, M., Elsener, B. & Rossi, A.** XPS and ARXPS for Characterizing Multilayers of Silanes on Gold Surfaces. *Coatings* **14**, 327 (2024).
228. **Karayaylali, P. *et al.*** The Role of Diphenyl Carbonate Additive on the Interfacial Reactivity of Positive Electrodes in Li-ion Batteries. *Journal of The Electrochemical Society* **167**, 040522 (2020).
229. **Hisbergues, M., Vendeville, S. & Vendeville, P.** Zirconia: Established facts and perspectives for a biomaterial in dental implantology. *Journal of Biomedical Materials Research Part B: Applied Biomaterials* **88B**, 519–529 (2009).
230. **Schwarz, F., Derks, J., Monje, A. & Wang, H.** Peri-implantitis. *Journal of Clinical Periodontology* **45**, (2018).
231. **Berglundh, T. & Lindhe, J.** Dimension of the periimplant mucosa: Biological width revisited. *Journal of Clinical Periodontology* **23**, 971–973 (1996).
232. **Hamraoui, A.** Cell adhesion and surface interactions: A comprehensive review of surface energy, wettability, and topography effects. *AIP Advances* **15**, 090702 (2025).
233. **Hersel, U., Dahmen, C. & Kessler, H.** RGD modified polymers: Biomaterials for stimulated cell adhesion and beyond. *Biomaterials* **24**, 4385–4415 (2003).
234. **Yang, Z. *et al.*** Biofunctionalization of zirconia with cell-adhesion peptides: Via polydopamine crosslinking for soft tissue engineering: Effects on the biological behaviors of human gingival fibroblasts and oral bacteria. *RSC Advances* **10**, 6200–6212 (2020).
235. **Grischke, J. *et al.*** Keratinized mucosa width is associated with severity of peri-implant mucositis. A cross-sectional study. *Clinical Oral Implants Research* **30**, 457–465 (2019).
236. **Hou, X., Hu, Y. & He, J.** Isotopic Tracing for Calculating the Surface Density of Arginine–glycine–aspartic acid-containing Peptide on Allogeneic Bone. *Orthopaedic Surgery* **5**, 51–55 (2013).
237. **Psarra, E. *et al.*** In Situ Monitoring of Linear RGD-Peptide Bioconjugation with Nanoscale Polymer Brushes. *ACS Omega* **2**, 946–958 (2017).
238. **Kantlehner, M. *et al.*** Surface Coating with Cyclic RGD Peptides Stimulates Osteoblast Adhesion and Proliferation as well as Bone Formation. *ChemBioChem* **1**, 107–114 (2000).
239. **Ferris, D.** RGD-coated titanium implants stimulate increased bone formation in vivo. *Biomaterials* **20**, 2323–2331 (1999).
240. **Schuler, M. *et al.*** Biomimetic modification of titanium dental implant model surfaces using the RGDSP-peptide sequence: A cell morphology study. *Biomaterials* **27**, 4003–4015 (2006).

241. **Elmengaard, B., Bechtold, J. E. & Søballe, K.** *In vivo* effects of RGD-coated titanium implants inserted in two bone-gap models. *Journal of Biomedical Materials Research Part A* **75A**, 249–255 (2005).
242. **Elmengaard, B., Bechtold, J. E. & Søballe, K.** In vivo study of the effect of RGD treatment on bone ongrowth on press-fit titanium alloy implants. *Biomaterials* **26**, 3521–3526 (2005).
243. **Rammelt, S. *et al.*** Coating of titanium implants with collagen, RGD peptide and chondroitin sulfate. *Biomaterials* **27**, 5561–5571 (2006).
244. **Xiao, S. J. *et al.*** Immobilization of the cell-adhesive peptide Arg-Gly-Asp-Cys (RGDC) on titanium surfaces by covalent chemical attachment. *Journal of materials science: Materials in Medicine* **12**, 867-872 (1997).
245. **Mertgen, A.-S. *et al.*** A low-fouling, self-assembled, graft co-polymer and covalent surface coating for controlled immobilization of biologically active moieties. *Applied Surface Science* **584**, 152525 (2022).
246. **Massia, S. P. & Stark, J.** Immobilized RGD peptides on surface-grafted dextran promote biospecific cell attachment. *Journal of Biomedical Materials Research* **56**, 390–399 (2001).
247. **Wilchek, M. & Bayer, E. A.** [2] Introduction to avidin-biotin technology. in *Methods in Enzymology* vol. 184 5–13 (Elsevier, 1990).
248. **Di Pietro, P. *et al.*** Silver nanoparticles functionalized with a fluorescent cyclic RGD peptide: a versatile integrin targeting platform for cells and bacteria. *RSC Advances* **6**, 112381–112392 (2016).
249. **Han, A., Tsoi, J. K. H., Matinlinna, J. P., Zhang, Y. & Chen, Z.** Effects of different sterilization methods on surface characteristics and biofilm formation on zirconia in vitro. *Dental Materials* **34**, 272–281 (2018).
250. **Rickert, C. A., Bauer, M. G., Hoffmeister, J. C. & Lieleg, O.** Effects of Sterilization Methods on the Integrity and Functionality of Covalent Mucin Coatings on Medical Devices. *Advanced Materials Interfaces* **9**, 2101716 (2022).
251. **Vickerman, John C., and David Briggs,** *ToF-SIMS: Materials Analysis by Mass Spectrometry*. (SurfaceSpectra Limited, Manchester, 2013).
252. **Vickerman, J. C.** Secondary ion mass spectrometry–basic concepts, instrumental aspects, applications and trends. A. Benninghoven, F. G. Rüdenauer and H. W. Werner, Wiley, New York, 1987, 1277 pages. *Surface and Interface Analysis* **10**, 435–435 (1987).
253. **D. Briggs, M. P. Seah** Practical surface analysis. 1: Auger and x-ray photoelectron spectroscopy. in (Wiley, Chichester, 1996).